FORMULATION AND MANUFACTURE OF PHARMACEUTICALS BY FLUIDIZED-BED IMPREGNATION OF ACTIVE PHARMACEUTICAL INGREDIENTS ONTO POROUS EXCIPIENTS

by

PLAMEN I. GRIGOROV

A dissertation submitted to the

School of Graduate Studies

Rutgers, The State University of New Jersey

In partial fulfillment of the requirements

For the degree of

Doctor of Philosophy

Graduate Program in Chemical and Biochemical Engineering

Written under the direction of

Fernando J. Muzzio and Benjamin J. Glasser

Approved by:

_____

_____

_____

_____

New Brunswick, Ney Jersey

May 2018

ABSTRACT OF THE DISSERTATION

Formulation and manufacture of pharmaceuticals by fluidized-bed impregnation of active pharmaceutical ingredients onto porous excipients

By PLAMEN I. GRIGOROV

Dissertation Directors:

Fernando J. Muzzio and Benjamin J. Glasser

It takes a tremendous amount of research and development in order to put a new drug on the market or to make an existing medicine cheaper and therefore more affordable to many people around the world. This is mainly due to the complexity of the whole process itself (discovery, safety studies, drug substance development, drug product development, clinical trials, scale-up and manufacture), the ever increasing requirements from regulatory agencies (regarding drug quality, safety and efficacy) and the growing demand for cheaper, more affordable drugs.

Drug product development (or drug formulation) is one of the main stages of pharmaceutical development, where the final dosage form is set and optimized. There are many requirements imposed on the final dosage form, including (but not limited to) the following: route of administration, size, taste, stability, drug substance uniformity, dissolution kinetics, cost, scalability, etc. Those requirements are set by the

pharmacokinetics/pharmacodynamics of the drug or its physical properties, safety requirements, market projections, customer preference and agency guidance. In an effort to satisfy all requirements, the formulation methods are becoming more complex, often including several unit operations and many additives and excipients. The pharma industry is constantly on the search of more efficient and cheaper formulation methods.

This work presents and studies a new manufacturing method for solid dosage forms using fluidized bed (FB) impregnation, which could eliminate many of the challenges during solid dosage manufacturing. The main difference between impregnation and dry blending is the placement of the active pharmaceutical ingredient (API) inside a porous carrier. This makes the final material flow properties independent of the physical properties of the API. The method consists of spraying an API solution in appropriate solvent onto a carefully chosen porous excipient in a fluidized state. The solution penetrates the porous carrier due to capillary forces and the solvent is evaporated soon after that. Impregnation and drying occur simultaneously, which could potentially make this impregnation method suitable for continuous implementation. Carefully choosing the operating conditions allows impregnation to occur without introducing spray drying or spray coating of the API.

This work looks closely into the main requirements for successful API impregnation, establishes methodology for equipment and materials selection and identifies appropriate excipients suitable for impregnation. A toolbox of analytical methods for the full characterization of the impregnated product was developed and presented. Fluidized bed impregnation proof-of-concept was demonstrated using preliminary experiments. A case study with a model drug provided a more complete look into fluidized bed impregnation

and established its benefits over conventional methods. It was demonstrated that FB impregnation can significantly improve the blend uniformity of the final formulation, independent on the drug load. The application of the impregnation technique was expanded to other drugs and excipients to demonstrate its robustness as a formulation method. It was found that FB impregnation can significantly improve dissolution kinetics of poorly soluble APIs by carefully choosing the excipient. Co-impregnation with additives led to further improvements in the dissolution profiles. Particle imaging using energy dispersive X-ray spectroscopy was used to characterize the internal distributions of the impregnated APIs within the porous matrix. Finally, a multi-scale mathematical modeling approach was developed that allows the calculation of some important process parameters. An impregnation simulation on a single-particle demonstrated the effect of several material properties on the API distribution inside the excipient.

Acknowledgements

Table of Contents

List of Tables

List of Figures

Chapter 1 .   Introduction

1.1   Background

Approximately 65% of all prescription drugs are manufactured as solid dosage forms [1], which includes tablets and capsules. In both cases, the final formulation consists of an excipient (or mixtures of excipients) and an active pharmaceutical ingredient (API), which is homogeneously distributed throughout the excipient powder. For very potent drugs, the amount of API in the solid dosage form can be as low as 0.1% by weight, or in some cases, even lower [2]. This very low API loading poses one of the biggest challenges in pharmaceutical product development: the control of dose uniformity. Low API content variability in the blend (or equivalently, a high level of blend homogeneity) are highly desired and strictly enforced by the U.S. Food and Drug Administration (FDA). Current guidelines developed by the FDA require API content variability in finished products to have relative standard deviation (RSD) of no higher than 6 %, with lower being better [3]. Typically, the leading source of product content variability is poor blend uniformity. In the commonly available approaches for blend uniformity control (for example, direct blending followed by wet or dry granulation) as the API concentration decreases, the variability of the blend increases, which makes it very difficult to meet FDA's requirements for low drug loadings. Therefore, a process or method that is able to tightly control API variability in blends, regardless of drug loadings, is very desirable.

According to the current Biopharmaceutics Classification System (BCS) adopted by the U.S. Federal Drug Administration (FDA), drug substances are categorized into four main classes, based on their solubility and permeability [4]. Two of those classes (BCS classes

II and IV) are characterized with low solubility. The trend in the past decade has been towards a steady increase in the number of active pharmaceutical ingredients (APIs) belonging to BCS classes II and IV. It has been estimated that up to 60% of new chemical entities fall in the low solubility class, compared to 39% for marked drugs [5]. This trend towards decrease in API solubility is undoubtedly one of the main hurdles for formulators today, as they continuously strive to develop novel formulations capable of effectively delivering the drug into the blood stream. Most formulation methods used to increase solubility (and ultimately the bioavailability) of the APIs include size-reduction techniques (bottom-up or top-down approaches) [6-8] or altering their solid form (salts, co-crystals and amorphous forms of the API) [9-12]. As a consequence of the above modifications, the API often exhibits poor flow properties with negative impact on downstream processing (blending, tableting, capsulation) often resulting in a complex formulation process (multiple excipients, roller compaction, granulation, milling). Universal manufacturing method capable of improving dissolution kinetics of poorly soluble drugs regardless of their nature, if existed, would provide huge advantage in drug product development.

Another important aspect of pharmaceutical process development is the final product cost. As pharmaceutical companies strive to develop more affordable drugs, any possible elimination of lengthy and expensive unit operations becomes commercially advantageous. One group of such unit operations is associated with the control of API attributes (size, size distribution, shape, bulk density, crystal form, etc.). These unit operations can include crystallization control and various milling and de-lumping steps. The need for control of API attributes is solely dictated by the drug product development

and usually is associated with desired improvements in blend uniformity or release profile. Having a formulation process that can make these and other steps unnecessary will provide a large advantage to pharmaceutical companies and the whole industry.

One method for manufacturing that could address all of the above challenges in drug substance and product development is impregnation of porous carriers. By definition, impregnation is the process of filling the internal void structure of a porous carrier with a chemical substance. Impregnation is a well-known process, which currently is generally used in supported catalyst preparation. Benefits of impregnation to catalyst manufacture include high uniformity of the dispersed active component (Ni, Pt, Pd, Co, etc.) within the support (typically alumina or silica), chemical and mechanical stabilization of the substrate, increase in total active surface area and reduction in the amount of the catalyst metal (usually very expensive). There are two types of impregnation, namely dry (or capillary) impregnation and wet (or diffusional) impregnation [13-16]. As the name suggests, during dry impregnation the support is initially dry and the driving force for impregnation is capillarity. Liquid solution is drawn inside the carrier due to capillary forces. Similarly, during wet impregnation, the support is initially wetted with pure solvent and the driving force for impregnation is the concentration gradient. An important outcome of the impregnation process is the resulting catalyst profile in the supported particles. There are four distinct types of catalyst profiles: uniform, egg-shell, egg-white and egg-yolk. These generally depend on the nature of the interactions (physical or chemical) between the support and catalyst. Several authors have shown that the catalyst profile established during impregnation can be significantly altered during the drying

phase [13, 15, 17]. Mathematical models describing catalyst profile control during drying have also been developed [18-20].

1.2   Impregnation methods

Impregnation of APIs onto porous excipients has been gaining attention only in the past several years. Research activities in this area have been focused primarily on altering (increasing or decreasing) of the dissolution profile of the API. Many of today's drugs are poorly soluble in water and ways to increase their solubility are becoming more attractive. Impregnation is a process that by design offers a unique approach for improving the API's dissolution rate [21, 22]. The increase in release kinetics comes from the fact that drug molecules are deposited in small pores, which increases the effective surface area for dissolution. In some cases, drug molecules are deposited in the form of an amorphous solid [23, 24] or as a molecular dispersions [21, 22, 25], which also has an effect of dissolution. Impregnation also offers a possibility for controlled-release formulations [25, 26].

There are three main types of impregnation techniques commonly used for loading of porous carriers with APIs. The most common of the three is the dry impregnation method, also known as incipient wetness impregnation [21, 22, 26, 27]. This method usually involves mixing of a dry porous carrier with an API solution in appropriate organic solvent and the subsequent evaporation of the solvent by drying (usually under vacuum). Although it is simple and easily achieved in the lab environment, one drawback of this method is that the final drug loading depends on its solubility in the organic solvent. If the solubility of the API is low then several impregnation-drying cycles could be needed in order to obtain the targeted drug loading in the carrier.

Another technique for impregnation gaining academic attention involves super critical CO_2 as the impregnation media [25, 28, 29]. Due to its low viscosity and ability to swell many polymers, super critical CO_2 is particularly useful when impregnating APIs into biocompatible polymeric carriers. Its use is advantageous since it is non-toxic and easy to remove from the final product. However, the method often has as a drawback due to limited drug solubility in the supercritical CO_2. Another drawback of this method is the relatively high capital cost if it is to be implemented on commercial scale.

A third, not very popular technique for impregnation is the melt method [21, 23, 30]. As the name suggest, the drug and porous carrier are mixed together and then heated above the melting point of the API. Being in a liquid form, the API penetrates inside the porous support drawn by capillary forces. There are two main drawbacks of this method. First, due to the usually high viscosity of many molten APIs, penetration within the porous matrix is slowed down. Second, not too many APIs are chemically stable in a molten state in order to undergo impregnation.

A fourth method for impregnation, which has not being widely utilized, involves dry impregnation of porous carriers in a fluidized bed (FB). It has been successfully demonstrated for the preparation of supported metal catalysts [31-33]. Applied to pharmaceutical formulation the method involves three steps, which occur simultaneously in a continuous fashion: 1) API solution in appropriate solvent is sprayed onto a porous excipient in a fluidized state; 2) the API solution penetrates the porous carrier driven by capillary forces and 3) the carrier particles loaded with API solution dry as they move around the bed. The benefits of performing impregnation in a fluidized bed are several. It eliminates the need for a separate drying step, which otherwise would lead to more

powder handling. Impregnation and drying steps occur continuously with a constant increase in API loading. As a result, the final API loading is controlled by the duration of the FB impregnation process and it is not limited by the API solubility in the solvent. Fluidized bed processing provides an excellent powder mixing with minimal shear forces exerted on the particles. Mass and heat transfer are the highest in a fluidized state, leading to an efficient drying and solvent removal.

1.3   Fluidized bed processing

Powder fluidization is a state that is achieved when air stream (or other gas) is passed through a bed of solid particles. At the initial state, when the air velocity is low, the fluid passes through the gaps within the static powder bed. If the velocity is increased, some of the solid particles start to move causing the static bed to expand. Further increase in air velocity causes the drag force exerted on the particles by the fluid to increase. A point is reached when the drag force becomes equal to the weight of the particles. This is the moment when the powder bed becomes fluidized and the gas velocity equals to what is known as "minimum fluidization velocity" [34]. If the velocity is increased further, channeling and bubbling of the gas take place, producing more vigorous moving of solid particles. Fluidized powder beds exhibit several liquid-like properties: light objects can float in the fluidized bed, surface remains horizontal when the bed is tilted, powder can flow out of the bed if there is an opening, and there is a pressure drop across the bed's height. Not every powder can be fluidized and different powders can exhibit different fluidization behaviors. The ability of a powder to be fluidized depends on its particle size and density and the density of the fluidizing gas. The Geldart chart distinguishes four groups of powders classified based on their fluidization properties [35]. Group A

powders are ideal for fluidization. They exhibit the highest bed expansion and a wider range of non-bubbling fluidization. Solid mixing and gas back mixing is the highest with no spouting (air forms a channel opening where particles flow up and fall on the outside). Powders belonging to group B are on average larger and/or with higher densities. They exhibit moderate bed expansion with bubbles forming immediately after reaching minimum fluidization velocity. Solid mixing and gas back mixing is moderate comparing to group A, with spouting only present for very shallow beds. Croup C consists of cohesive powders which are extremely difficult to fluidize. The powders in this group either lift up as plugs (in small beds) or form channels where the air passes through without moving any particles. These materials are usually of very small particle size with very strong electrostatic forces between them. The inter-particle forces are higher than the force exerted by the gas, resulting in a very poor fluidization and very low particle mixing. Group D powders are those with large and very dense particles. Their fluidization is characterized with low bed expansion and low particle and gas mixing. Spouting occurs even for deep beds. Based on their general fluidization properties, the preferred powders for fluid bed processing belong to groups A and B. Although group C particles can be engineered to fluidize as group A powders through coating with nanoparticles [36], their fluidization in general is very difficult. Group D powders can be fluidized, however due to the significantly reduced particle mixing their use may be limited depending on the particular application. Various fluidization regimes are exhibited depending on the class of powders and the fluidization velocity: smooth, bubbling, slugging, turbulent, fast and pneumatic conveying [37, 38]. The choice of the regime could vary between smooth, bubbling or turbulent depending on the particular

application. If minimizing particle entrainment and maximizing gas throughput are desirable for example, as it is in the case of catalyst regeneration or particle drying, then turbulent fluidization is the preferred flow regime [39].

Fluidized bed processing has been widely used in the chemical industry for a variety of applications including coal gasification, catalyst cracking, various chemical synthesis, coal combustion, etc., [34]. One of its main applications is for drying of various chemical, biochemical, biological and food products [40-44]. Fluidized bed processing was first introduced to the pharmaceutical industry by Wurster in 1950s, who developed a method for fluidized bed coating of tablets and small particles [45]. Soon after, fluidized bed processing was applied successfully to powder granulation [46, 47]. Both of these pharma applications consist of powder fluidization coupled with spraying of a liquid solution, where wetting and drying are two processes occurring continuously. The outcome of the process (granulation or coating) depends on the processing conditions and material (powder and solution) properties. The research, application and commercialization of fluid bed process processing in the pharmaceutical industry expanded significantly in the 1980s [48]. Recent innovations of fluidized bed technology, which can be seen as modifications to coating and granulation, include spray encapsulation and pelletizing (direct, layering, spheronization) [49-51]. Other pharmaceutical applications of fluidized bed processing include powder mixing and drying [51-53].

Fluidized bed equipment for pharmaceutical applications can be categorized in three main groups, depending on the position of the spray nozzle: top spray, bottom spray (Wurster type) and tangential spray [50]. Top spray units are primarily used for

granulation, while bottoms spray systems are typically used for powder, granules or tablet coating [54]. Tangential spray models combine fluidized bed operation with a rotating bottom plate and are primarily used for pelletizing, producing denser, more spherical and less porous pellets compared to granulation [55, 56]. Fluidized bed designs can vary depending on the desired mode of operation: batch or continuous [57]. There are other types of fluidized bed systems specifically designed for difficult-to-fluidize powders: vibrated, agitated, centrifugal and rotating fluidized bed systems [58]. Fluidized bed processors can vary depending on the type of spray nozzle used: hydraulic, rotating, ultrasonic or two-fluid (air atomizing) nozzles [55, 57]. The key components of any fluidized system can be summarized as: control system, air handling unit, product chamber, air expansion chamber, exhaust filters, exhaust blower, air distribution plate, spray nozzle and liquid solution delivery system [57]. In order to meet current environmental regulations, closed-loop systems utilizing solvent recovery through vapor condensation are necessary part for any fluidized bed process using organic solvents [56].

Fluidized bed processing has several advantages over other drying or mixing systems, which include high degree of powder mixing, uniform bed temperature, large gas/solid contact surface area and rapid heat and mass transfer [34, 59]. These lead to the following characteristics of fluidized bed processing: uniform liquid distribution over solid particles during granulation/coating, ability to dry heat sensitive materials and shorter drying times. Processing parameters affecting any fluidized bed process are several and include: type/configuration/geometry of equipment (chamber, nozzle, etc.), liquid spray rate, atomizing gas pressure, drying gas flow rate, drying gas temperature and drying gas solvent/moisture content. The selection of these parameters is typically done

experimentally on a small scale. Process scale-up is performed via successful pilot runs in larger equipment where the following are usually kept constant: fluidization velocity of the drying gas, droplet size of the sprayed liquid and the ratio of spray rate to drying capacity [57].

1.4   Organization of the dissertation

The goal of the work presented in this dissertation is to introduce the fluidized bed impregnation technique to pharmaceutical manufacturing, to develop the methodology necessary for its successful implementation and to display its potential benefits over current manufacturing practices for solid dosage forms. Effects of material properties, processing conditions and equipment characteristics are studied to understand their effect on the impregnation process as a whole and on the performance of the resulting impregnated formulation. Detailed analysis of all requirements needed for the successful implementation of impregnation to the pharmaceutical manufacturing is presented (Specific Aim I). An array of analytical tools necessary for the complete characterization of the impregnated product is discussed next. Preliminary FB impregnation runs are carried out to demonstrate the applicability of the method to pharmaceutical manufacturing. A case study of FB impregnation with a complete analysis of the product firmly establishes the feasibility and benefits of FB impregnation to solid dosage formulations. The method of FB impregnation is further expanded to other APIs and excipients to demonstrate its robustness (Specific Aim II). Several benefits of FB impregnation are established, including its potential for improving dissolution kinetics of poorly soluble drugs. The co-impregnation of APIs and additives is shown to be easily achieved in FB mode. Additional benefits, such as the ability to obtain and stabilize the

amorphous form of APIs, are discussed in detail. Information regarding the spatial distribution of impregnated APIs is revealed by performing an X-ray spectroscopy analysis on impregnated particles (Specific Aim III). Different particle embedding techniques and methods for obtaining cross-sections are presented. Using first engineering principles, a multi-scale mathematical modeling approach for FB impregnation is developed and discussed in detail (Specific Aim IV). Calculations of processing parameters and API impregnation profiles within the particle are presented. Model predictions are compared with experimentally determined API distributions. Effect of material properties on the API profile is demonstrated via mathematical simulations of several different impregnation study cases.

The work in this dissertation is accomplished in the four specific aims as follows:

- Specific Aim I: Proof of Concept – Establishing appropriate materials, equipment, processing methods and analytical techniques necessary to achieve successful FB impregnation of an API (Chapter 2).

- Specific Aim II: Expanding FB Impregnation to different APIs and excipients. Improving dissolution kinetics of poorly soluble APIs (Chapter 3).

- Specific Aim III: Cross-sectional analysis of impregnated excipient particles by energy dispersive X-ray spectroscopy (Chapter 4).

- Specific Aim IV: Establishing basic framework for mathematical modeling of FB impregnation process in a porous medium (Chapter 5).

Chapter 2 .   Proof of concept – Establishing appropriate materials, equipment, processing methods and analytical techniques necessary to achieve successful FB impregnation of an API

2.1   Introduction

Solid dosage formulations for oral administration are usually in the form of tablets or capsules. The choice of the particular formulation depends on many factors: chemical and physical properties of the drug, rate of absorption, condition of the patient, manufacturing cost and others. The actual tableting or capsule filling processes are universally applicable to most APIs, however the process to produce a final powder blend suitable for tablet compression or capsule filling can be very API-specific. This process can include any (or combination) of the following pharmaceutical unit operations: blending, granulation, roller compaction, milling, spray drying and hot-melt extrusion. The particular combination of processing steps depends on the API's physical and chemical properties, the final drug loading in the dosage form or the target release profile (immediate or controlled). The abovementioned manufacturing methods have been used in the pharmaceutical industry on a commercial scale for many years and there is significant amount of knowledge and experience to allow acceptable process/product control [60, 61].

On the contrary, impregnation processing has never being used on a clinical or commercial scale in the pharmaceutical industry. It has attracted some attention in recent pharmaceutical research, however using lab methods, which could impose some

limitations upon scale up. These methods involved simple procedures designed for lab use only. Typical impregnation techniques involved: 1) mixing of carrier with API solution (or melt) and 2) subsequent drying of the wet carrier by any means possible (oven drying, roto-vapor drying, etc.) [21, 22, 27]. Limited attributes of the final impregnated powder were tested (usually dissolution profile and physical state of the API) without any robustness evaluation of the impregnation method. Impregnating excipients by immersing then into an API solution followed by filtration is not a preferred large scale manufacturing method. Using this process would lead to unnecessary API losses and increased cost of the final formulation. In order to eliminate API losses, a preferred impregnation method would include spraying a pre-determined amount of API solution onto the excipient. The amount of the API solution should be less than or equal to the total internal pore volume of the carrier in order to eliminate the need of filtration. This impregnation process could be carried out in any powder handling equipment which provides good mixing and good dispersion of the liquid phase before it comes in contact with the solid. For example, any type of powder mixers (V-blenders, double-cone blenders, etc.), granulators or fluidized beds would be a good candidate. Since drying is part of the impregnation process, the ideal equipment should be able to offer this capability as well, in order to minimize powder handling. It becomes obvious that fluidized bed dryers/granulators/coaters could be a great choice, since they can provide both mixing and drying at the same time. The benefits of potential impregnation methods can only be evaluated through a comprehensive study focusing of key product attributes, which need to be identified.

In the case of a fluidized bed dryer, liquid impregnation and drying will occur at the same time. In order to ensure that impregnation of the carrier is achieved, a special care is needed when choosing the processing conditions with impact on product quality. There could be four distinct outcomes when an API solution is sprayed onto a porous carrier which is fluidized by a hot gas. In particular one can: i) spray dry the solution to generate API particles, or ii) coat the carrier with the API solution and dry the solution to produce carrier coated with API, iii) coat the carrier with solution and granulate the carrier to produce agglomerated granules of carrier, or iv) impregnate the pores of the carrier with API solution and subsequently dry this solution to produce carrier impregnated with API. There are three main process parameters that determine the outcome of the fluidized bed operation: i) the spray rate (R_s) that the API solution is introduced into the system (in mass/time or volume/time), ii) the drying rate (R_d) that the solvent is evaporated/vaporized (in mass/time), and iii) the impregnation/penetration rate (R_i) i.e. time for the solution to move into the pores of the particles from their surface (in mass/time or volume/time). There are four different regimes of operation depending on the particular combination of those different rates:

1. Spray drying: $R_s \ll R_d$ and $R_i \ll R_d$. If the drying rate is much larger than the spray rate and impregnation rate then the API solution will not even reach the particles; instead the solution will dry in the air leading to spray dried API particles.

2. Coating: $R_i < R_s < R_d$. If the spray rate is larger than impregnation rate then there is either coating or granulation depending on the drying rate. This is because the API solution is sprayed onto the carrier faster than it is able to penetrate into the

pores of the particles and as a result, a layer of API solution develops on the surface of the particles. If the drying rate is greater than the spray rate then the API solution will dry on the surface of the carrier leading to a carrier coated with API.

3. <u>Granulation I: $R_i < R_d < R_s$.</u> API solution will coat and then bind particles. If the spray rate is faster than the impregnation rate then we have either coating or granulation depending on the drying rate. This is because the API solution is sprayed onto the carrier faster than it is able to penetrate into the pores of the particles and as a result, a layer of API solution develops on the surface of the particles. If the drying rate is less than the spray rate then the API solution will remain as liquid on the surface of the carrier leading to granulation.

4. <u>Impregnation: $R_i > R_d \geq R_s$.</u> If the drying rate and spray rate are less than the impregnation rate then API solution will penetrate or impregnate the carrier. In order to ensure that the API solution does not exceed the pore volume of the carrier one additional requirement is that the drying rate be greater than or equal to the spray rate. If the spray rate is larger than the drying rate then the API solution will accumulate in the pores and eventually exceed the pore volume leading to granulation. For this reason the spray rate must be less than or equal to the drying rate for impregnation to occur for all times.

5. <u>Granulation II: $R_i > R_s > R_d$.</u> If the drying rate and spray rate are less than the impregnation/penetration rate then API solution will penetrate or impregnate the carrier. If the spray rate is larger than the drying rate then the API solution will accumulate in the pores and eventually exceed the pore volume. When this

occurs there will be free liquid on the surface of the carrier and this will eventually lead to granulation of the carrier.

In order to ensure successful impregnation in FB mode, these three parameters need to be evaluated and appropriate process conditions selected. The impregnation rate is solely determined by the nature of the porous carrier with its unique pore size distribution and by the wetting properties (contact angle with solid) of the solvent used. The spray and drying rates are processing parameters that can be easily controlled. Choosing suitable process conditions can be achieved empirically by performing a series of one-factor-at-time (OFAT) pure-solvent experiments, although it is preferred to have a mathematical tool for estimation of a good starting point for impregnation.

This chapter investigates the possibility of performing impregnation of active pharmaceutical ingredients onto porous excipients via fluidized bed processing. The chapter explores FB impregnation's benefits to pharmaceutical solid dosage forms manufacturing and its advantages over other potential large-scale impregnation methods. Basic processing conditions are established for a successful FB impregnation: equipment set-up, process parameters and basic properties for excipients, APIs and solvents. As part of this chapter, an experimental proof-of-concept is used to demonstrate the feasibility of FB impregnation using a model drug and a common excipient. An array of analytical methods is identified and applied to fully describe and study the resulting impregnated formulations.

2.2 Materials and equipment selection

In order for an impregnation process to be 1) successful and 2) commercially viable, a special consideration needs to be taken when choosing the method for impregnation, the equipment to be used, the excipient to be impregnated and the solvent used to solubilize the API. To help establish the connection between the different aspects of the impregnation method and the desired final product, a cause and effect analysis was performed, illustrated by the fishbone diagram given in Figure 2-1 and elaborated in the discussion below.

2.2.1 Excipient Properties

Regardless of the equipment used or the particular details of the impregnation method, the ideal excipient candidate for impregnation should have the following properties:

1) To be porous - to possess high internal surface area, which is the most important property for successful impregnation:

   - By definition, impregnation is the process of imbuing or saturating with something, diffusion of some element through a medium or substance. If the chosen excipient does not possess any internal porosity, deposition of an API inside of it will be impossible.

2) To be a common and widely available excipient such as fillers or diluents (not lubricants, glidants, etc.):

   - While there are many novel excipients currently under research in academia, only limited number have been approved by the three main drug governing agencies: FDA (US), EMA (Europe) and PMDA (Japan). For a drug formulation method to be immediately commercially viable, it must

use an approved excipient. Novel excipient could also be of commercial interest for a specific reason, however their approval could take some time. Excipients generally used as fillers or diluents in solid dosage formulations are preferred for impregnation for one main reason: their performance for tablet/capsule preparation is well understood, which allows the impregnated excipient to be easily formulated in either of the solid dosage forms.

3) To have good flowability:

- Successful FB impregnation is only possible, if the porous excipient is easily fluidizable. The ideal excipient candidate for FB impregnation should belong to groups A and B, according to Geldart's chart [35].

- Regardless of which solid dosage form is chosen (tablet or capsule) the production process will involve a powder filling step of either the tablet press or capsule filling machine. In order to produce tablets/capsules with small weigh variation, the filled powder must possess good flow properties. This will allow the impregnated excipient to be directly formulated into tablets/capsules without the addition of other flow-improving excipients.

4) To have a narrow particle size distribution (PSD):

- Producing solid dosage forms with high drug uniformity is a constant battle during drug product development. Particle size segregation is among one of the phenomena affecting content uniformity. It is almost unavoidable when an API and excipient are mixed together to form a

physical mixture. If however the formulation is comprised by an impregnated excipient, size segregation will be affected solely by the size distribution of that excipient. Therefore, an excipient with narrow particle size distribution is preferred for impregnation.

5) To be insoluble in a variety of organic solvents in order to minimize dissolution and granulation during impregnation:

- The main step of any solvent impregnation method consists of filling the porous medium with a solution of the desired impregnant into an appropriate solvent. As complex organic molecules, most of the APIs are soluble in organic solvents (such as methanol, ethanol, acetone, etc.) and few of them are soluble in water. If the excipient is solubilized by the solvent, that may have an effect on its internal structure and could cause its collapse. Excipient solubility in the solvent could also cause formation of granules during the impregnation process, which is highly undesirable as it may have an effect on powder flowabiluty, content uniformity, release profile and many more.

6) To be physically stable under impregnating conditions (stable physical form, mechanically stable):

- Solvent impregnation of excipients involves contact with solvents, mechanical mixing, and exposure to elevated temperatures during drying. During these unit operations the ideal excipient should be able to preserve its physical form (e.g. if excipient is in amorphous form, it should not spontaneously crystallize during impregnation). Also, the excipient should

be unchanged mechanically throughout the impregnation process (e.g. if excipient is in granular form, collapse or attrition of the granules should not be present).

Screening was performed on numerous possible candidates based on all of the above criteria for impregnation. Table 2-1 lists four excipients with a summary of their important properties and Figure 2-2 shows scanning electron microscope pictures for these four excipients. Based on the presented properties, two excipients were chosen as candidates for impregnation development: $CaHPO_4$ and Neusilin®.

2.2.2   Solvent properties

Regardless of the equipment used or the nature of the API and excipient, the solvent used for impregnation should have the following properties:

1) To solubilize to some extend the API to be impregnated

- Solvent impregnation relies on the solvent to carry the API inside the porous excipient. Therefore some solubility is required for successful impregnation. As it will be shown later, this solubility does not have to be high in order to achieve higher loadings.

2) To be safe for pharmaceutical use

- Solvents are classified into three groups by the ICH-Q3C Industry Guidelines [62] according to their toxicity and environmental effects. Any Class 1 solvent should not be used for pharmaceutical manufacturing. Solvents from Class 2 could be used provided they are removed from the final product below specified levels, which must be detectable by adequate

analytical methods. Solvents from Class 3 are considered less toxic and have higher allowable limits than Class 2 solvents.

3) To be easily evaporated

- Solvent impregnation relies on two processes to take place in order to be successful: permeation of the API solution into the porous carrier and drying of the solvent used to carry the API inside the excipient. If the impregnation method is to be practically viable, it must use a solvent that is easily evaporated (with low boiling point). Otherwise the process will be prolonged and in certain cases may not be economical.

4) To wet the excipient

- As mentioned above, impregnation relies on permeation of the API solution into the porous matrix of the excipient. If the API solution does not wet the excipient it will not penetrate inside the pores and there will be no impregnation. In almost all cases the wettability of these API solutions is determined solely on the wettability of the pure solvents. In general, the wettability is determined by the contact angle between the solid and solvent and for good wettability the contact angle must be between 0 and 90 degrees (the closer to 0 degrees, the higher the wettability).

Three solvents were identified as good candidates for impregnation development (see Table 2-2). The majority of APIs usually will have some solubility in either of the three solvents: methanol, ethanol and acetone. Other solvents could also be used for impregnation if the API does not have solubility in any of these tree solvents, provided their boiling point is relatively low (for example tatrahydrofuran with $T_b=66^{\circ}C$).

2.2.3   API Properties

If an API is to be considered as a good candidate for FB impregnation development, there are few requirements that need to be fulfilled:

1) To be stable under FB impregnation conditions.

   - Temperature in the FB will vary depending on solvent used, liquid spray rate and drying gas flow and temperature. The API should be thermally stable under these drying conditions.

2) To be soluble to some extend in the solvent used

   - Solvent impregnation relies on the solvent to carry the API inside the porous excipient. Therefore some solubility is required for successful impregnation. As it will be shown later, this solubility does not have to be high in order to achieve higher loadings.

3) To be inert with respect to the porous carrier

   - The API will be deposited inside the porous network of the solid excipient. Ideally the drug and excipient should not display any chemical interaction. If there is, the interaction cannot lead to any degradation of the API over time.

2.2.4   Impregnation method requirements

These are general requirements for the impregnation method that are necessary to make it more attractive for large scale implementation:

1) To be able to achieve wide range of API loadings

- During the imbibing step of the impregnation process, the maximum solvent uptake is limited by the porosity of the excipient. The amount of API in the solution is limited by its solubility. Therefore, the maximum achievable API loading for a given excipient (fixed porosity) during a single imbibing/drying cycle is limited by the API's solubility. The ultimate impregnation method should be able to achieve higher API loadings that are only limited by the porosity of the excipient and not the API's solubility. This could be achieved if the imbibing/drying cycles are repeated continuously until desired impregnation loading is reached.

2) To be able to run in existing equipment

- If the impregnation method requires a specially designed equipment, that will make the process less desirable for process development and especially for large scale production and commercialization. Not requiring a new capital investment will make the impregnation method much more attractive to pharmaceutical companies.

3) To be easy to implement

- Overall, the process should be easy to implement, without too many additional steps or unit operations and should be easy to control with minimum number of critical process parameters.

2.2.5   Equipment requirements

The ideal equipment for solvent impregnation should be able to deliver the following general requirements:

1) To provide good powder mixing

- As mentioned in the introduction section, the API content uniformity is an important characteristic of any drug product with strict requirements set by the FDA. In order to achieve high blend uniformity during impregnation, the equipment used should be able to provide adequate mixing between the excipient and the impregnating API solution.

2) To impose low shear forces during mixing

- Preserving excipient particles during impregnation is highly desirable as they will have an impact on the final product's flow properties. Therefore, attrition should be minimized during mixing.

3) To have drying capabilities

- In order to streamline the impregnation process and make it commercially feasible, the equipment where the impregnation is taking place should also have drying capabilities. This will allow all individual steps of the impregnation process (mixing, solution infiltration and drying) to be carried out in the same piece of equipment.

Analysis of all equipment and method requirements listed above points to one very logical solution – an impregnation in a fluidized bed (FB) dryer. This method of impregnation has never been used for preparation of pharmaceuticals and can provide many advantages over classical methods. The fluidized state of solids has been studied for many decades and vast amount of data already exists. Fluidized beds are unique in providing a set of several important capabilities:

- Extremely high contact area between fluid and solid

- High levels of mixing, within the solid itself and between solid and sprayed fluid.

- Relatively low levels of shear forces are exerted to the solid

- High rate of particle-particle collisions

Fluidized beds have been applied across various applications such as reactors, combustion chambers, dryers, coaters and granulators. The relative high drying rate characteristic of a fluidized bed dryer coupled with the high degree of mixing and low levels of shear can make it the perfect equipment for impregnation. Spraying an API solution onto a porous excipient in a fluidized state will ensure an even distribution of the solution and the API. If fluidization is done using a pre-heated gas it will result in a continuous impregnation process where the spraying/penetration/drying cycles take place simultaneously. This is a great advantage over traditional methods where the above steps are performed one at a time.

The fluidized bed dryers (also designed for granulation and coating) chosen for impregnation development are shown in Figure 2-3. Both are lab units, capable of handling up to 500 grams in the small scale unit (Mini Glatt) and up to 3 kg (Glatt GPCG 1) in the larger unit. Both have modular structure and flexible configuration, which makes them ideal for impregnation with minimal retrofitting. Most importantly, they provide an easy and accurate monitoring and control over process parameters such as drying gas temperature and flow rate, atomization pressure and liquid flow rate, pressure drop across filter element and blow back control.

2.3 Analytical methods selection for full characterization of impregnated excipients

Fluidized bed impregnation of excipients with APIs is a novel approach for the manufacture of pharmaceutical products. As such, the resulting product should be characterized completely from every angle in order to fully understand its physical properties (microscopic and bulk), its pharmacokinetic performance, the governing principles behind its manufacturing process and the resulting potential benefits to the patient. There is a multitude of questions that needs to be answered:

1) Was impregnation successfully achieved or other side processes are observed (spray drying, coating or granulation)?

2) In what physical form (crystalline or amorphous) is the API deposited inside the porous carrier?

3) What is the average drug loading of the impregnated excipient?

4) What is the API content/blend uniformity of the impregnated excipient?

5) Is there attrition during FB impregnation?

6) How the flow properties of the impregnated excipient change during impregnation and how they compare to the pure excipient?

7) How the internal pore structure changes upon impregnation?

8) How does impregnation affect/change the dissolution kinetics of the API compared to a physical blend?

9) Can impregnated excipients be directly compressed into tablets?

In order to unequivocally answer all of the above questions, appropriate analytical techniques and test methodology must be developed and applied. Description of all

analytical tests and methods employed in the characterization of all FB impregnated materials presented in this work is given in the following discussion.

2.3.1 Microscopy

A picture is worth a thousand words. In order to visually capture the appearance of individual impregnated particles, the powerful scanning electron microscopy (SEM) technique was utilized. SEM pictures of the impregnated excipients can help answer immediately the following:

- Was there agglomeration?

- Was there coating?

- Is the original shape of the excipient particles preserved during FB impregnation?

All SEM pictures in this work were made using a Hitachi table-top scanning electron microscope TM-1000 or Hitachi SU5000 Schottky Field-Emission scanning electron microscope.

2.3.2 Differential scanning calorimetry (DSC)

DSC is a very powerful analytical tool for understanding the physical form of any solid state material. It can determine whether the solid is in crystalline or in an amorphous state. It measures the heat energy input into the solid vs. its temperature change and it can easily detect endothermic (melting) or exothermic (crystallization) events. The absence of any thermal event suggests the material is in its amorphous state. The technique is very sensitive, it can differentiate between different crystal forms of the same material and it can determine melting temperatures, decomposition temperatures, glass transition temperatures or heat of fusion. DSC results could be used to calculate relative amounts of

crystalline vs. amorphous content. All DSC analysis was carried out on a differential scanning calorimeter Q100 by TA Instruments.

2.3.3   Powder X-ray diffraction (p-XRD)

Similar to DSC, p-XRD is a solid state analytical tool used to determine the crystalline or amorphous nature of any material. It measures the X-ray diffraction pattern produced, which is unique for every crystalline material. The absence of individual distinguishable peaks in the XRD scan suggests the presence of an amorphous material. XRD is used in combination with DSC to confirm the crystalline/amorphous state of the impregnated material. Powder diffraction data was obtained using a LabX XRD-6000 X-ray diffractometer (Shimadzu) with a graphite monochromator and diffracted beam generated by Cu tube.

2.3.4   Specific surface area (SSA) and Pore-Size Distribution

Porous materials are characterized with a large specific surface area, most of which is due to the internal pore structure of the solid matrix. The SSA area correlates with the sizes of the internal pores and their distribution. Measuring SSA and pore size distribution for any excipient before and after impregnation can reveal information regarding the impregnation process. Specific surface area (in m^2/g) was determined by the BET standard method (5-point N_2 adsorption). Cumulative pore size distribution (in cm^3/g) was determined using the BJH adsorption isotherm (42-point N_2 adsorption). All nitrogen adsorption measurements were recorded at -196 ^{o}C on a TriStar[®] 3000 instrument (Micromeritics Instrument Corp.).

2.3.5   High pressure liquid chromatography (HPLC)

Determining the actual drug loading of an impregnated excipient with very high accuracy is very important for several reasons. First, it will allow the calculation of the API uniformity/variability within the impregnated excipient. This is an important property of any drug product and is tightly regulated by regulatory agencies by imposing maximum allowable limits. The API content variability is determined by collecting multiple small samples from the impregnated batch (size of sample is also important), determining the API loading in each sample accurately and then calculation the relative standard deviation (RSD) from the mean value (in %). The smaller the % RSD is for a particular batch, the smaller the variability (or higher the uniformity) is for that batch. Second, accurate measure of the API loading will allow for a comparison between the actual loading and the targeted drug loading (API input during the impregnation process). This is very important from a mass balance stand point and could be very useful in investigating how the impregnation process performs. Lastly, through comparative studies it can help answer the question if the API absorbs onto the excipient or simply is deposited inside its pores. This is also important aspect as it may affect API release kinetics.

Analyzing the API content was made possible with the help of high pressure liquid chromatography (HPLC). This is an analytical method which has the capability of separating multiple organic compounds and determining their concentration in a solution with extremely high accuracy. The concentration is calculated based on the individual compound UV absorbance using a calibration curve constructed using solutions with known concentration. The calibration curve represents peak area vs. known

concentration. The linearity of the calibration curve must be very high (usually above R^2 ≥ 0.999) to ensure high accuracy. This is achieved by constructing calibration curves around the anticipated concentrations to be analyzed.

Overall, the method developed for API content analysis consists of several steps:

1) Estimate API concentration and prepare two standard solutions using pure API in a pure solvent with concentrations slightly above and below the anticipated sample concentration.

2) Run these two standard solutions and construct a calibration curve including the origin. Calculate R^2 to make sure linearity meets the requirements of 0.999 or above.

3) Take at least 10 small samples from the impregnated excipient, place them in volumetric flasks and fill to the mark with a solvent which provides good API solubility (usually the solvent used for impregnation). Place flask in sonication bath and sonicate for at least 30 min to ensure a complete dissolution of the API.

4) Run HPLC analysis for each sample using at least two injections to determine the HPLC peak area.

5) Using the calibration curve, calculate the API content for each sample/injection. Then calculate the mean, the standard deviation and the % RSD for the entire batch.

2.3.6 Particle size distribution (PSD)

Every excipient is friable to some degree. For the impregnation method to be commercially viable, it must be able to preserve the original physical properties of the

excipient almost unchanged. Therefore, an important question to be answered is how the particle size changes due to the impregnation process. Is there attrition of the excipient and to what degree? Is there agglomeration of the excipient particles? All these can be answered by measuring PSD of the excipient before and after the impregnation process. Many analytical techniques are available today for particle size distribution analysis of powders. Some low-tech options include sieve analysis, microscope counting or particle image analysis. More elaborate analytical methods include laser diffraction analysis or dynamic light scattering. All of the PSD analyses involved with this work were performed using Beckman Coulter LS 13320 laser diffraction particle size analyzer.

2.3.7   Shear cell testing

Almost every drug product formulation process for solid dosage forms involves at some point mixing of powders (APIs and excipients). The physical behavior of the powder blend depends on many factors: physical properties of the individual powders, processing methods and conditions, additives, etc. The properties of the final drug product (tablets or capsules) are greatly influenced by the flow behavior of the powder blend used in their preparation. Poor flowability of the blend can affect the quality of the solid dosage form (high variability of API content) or the productivity of the manufacturing process (tablet capping, partially fill capsules). Therefore it is very important to assess what is the effect of the manufacturing method on the flow properties of the final powder blend. Powder flow properties and their evaluation is currently an area with dynamic research activities. Many methods have been developed for the analysis of powder flow: angle of response, Carr's compressibility index or Hausner ratio, flow through an orifice, dynamic powder testing, testing by gravitational displacement rheometer or shear cell [63, 64]. Powder

flow properties in this work were characterized by the shear cell test method using FT4 rheometer [65].

2.3.8   Dissolution testing

The main function of any drug product is to deliver the API it contains into the gastrointestinal (GI) tract by dissolution into the gastric fluids. The process of dissolving the API is in turn affected by many factors: environmental (pH and temperature of gastric fluid), properties of the API (solubility, crystal form) or properties of the solid dosage form (additives, tablet hardness, capsule properties). Therefore, measuring the dissolution profile is an important part of the full characterization of any drug product. The test is usually performed in vitro according to a prescribed procedures by the United States Pharmacopeia (USP) [66]. The test measures the % of API that dissolves as a function of time. The USP distinguishes two types of drug formulations based on their release time: immediate release (usually 80% of API released in less than 30min) or extended release (usually 80% of API released in several hours). All dissolution testing were performed in Varian's Vankel VK-7010, 8-spindle, 8-vessel USP dissolution apparatus with an automated UV-vis measurement.

2.3.9   Tableting and compressibility testing

The main difference between traditional blend methods for preparation of solid dosage forms (physical blending of API and excipients) and the impregnation method studied in this work is the location of the active ingredient. In the former, the API particles are located between the excipient particles, while in the latter the API is located inside the excipient. In order to study the effect of impregnation on the properties of the final tablets, a comprehensive tableting and compressibility testing was designed and

implemented. Individual tablets of pure and impregnated excipients were prepared using a tablet press replicator and compaction simulator (Presster™). Tablet thickness and hardness was then measured and compared.

2.4   Preliminary impregnation study

Two methods were tested: 1) classical dry-impregnation method and 2) the novel fluidized-bed impregnation method. These methods of impregnation were tested with the following goals:

- Proof of concept - achieve successful impregnation of API into porous excipient
- Perform analysis on the impregnated product
- Assess advantages/disadvantages of each method and identify potential improvements

2.4.1   Dry impregnation

The classical dry impregnation method consists of a single impregnation/drying cycle. The impregnation process can be carried out in any suitable powder mixer, where the liquid spray can be introduced safely. The wet, impregnated powder is then usually transferred in an oven to complete the drying of the carrier solvent. In this preliminary study, a conventional granulator was used to perform the impregnation part and a vacuum oven to dry the excipient. The conceptual design of the granulator is shown in Figure 2-4. The excipient powder was placed in the granulator's chamber where it was continuously mixed by the agitator. The chopper is designed to help break any large wet agglomerates and improve blend uniformity. The API solution was pulverized by the spray nozzle and introduced in the chamber in the form of fine mist. The type of spray nozzle was a single-

fluid, which uses only the kinetic energy of the liquid interring the nozzle. The liquid transfer was achieved using a peristaltic pump.

The API used in this test was acetaminophen (APAP) and the carrier solvent was methanol. The excipient used was EMCOMPRESS® - an anhydrous form of $CaHPO_4$. The processing conditions are given in Table 2-3. The amount of excipient used was chosen to ensure contact with the chopper once placed in the granulator. The speed of the agitator was chosen to ensure adequate mixing of the powder. The chopper speed was set at the lowest setting – 10% of the maximum speed of 3600 rpm. This was necessary to minimize attrition/breakage of particles that could occur during the impregnation process. A methanol solution of APAP was prepared by saturating the API in the solvent at room temperature. This resulted in a maximum concentration of about 93 mg/ml. The addition rate used was the minimum attainable that could still produce an adequate pulverization of the API solution. The maximum amount of solvent for impregnation cannot exceed the total pore volume, otherwise agglomeration will be observed. Therefore it was decided to have the total volume of API solution to be 90% of the total pore volume of the excipient. The calculation for the solvent volume, based on literature values for porosity ε and true density ρ_{true} [67], is given by equation (2-1):

$$V(solution) = \frac{\varepsilon * weight(CaHPO_4)}{\rho_{true}} * \frac{1}{(1-\varepsilon)} * 0.9 \qquad (2\text{-}1)$$

The wet, impregnated excipient was dried under full vacuum at 35°C for full 24 hrs. The dried impregnated excipient (ten samples of about 0.5 grams each) was analyzed by HPLC to determine the average APAP loading and blend uniformity. Analytical results are shown in Table 2-3. The actual API loading was slightly lower than the theoretical,

which was calculated based on amount of APAP solution and concentration that was sprayed in. This suggests that there was some small loss associated with this impregnation method and equipment. Most likely the loss was to the internals of the granulator which gets coated during the impregnation process. Although still acceptable, the measured blend uniformity was at the high end for any commercial drug product, as the limit set by the FDA is no more than 6 %RSD.

The SEM pictures of the impregnated $CaHPO_4$ are shown in Figure 2-5. Close examination of the images reveals the existence of some excipient particle agglomeration. This can be explained by the inherent uneven distribution of API solution during impregnation and the fact that the solution volume is close to the maximum that can be absorbed by the powder. Some particles will end up with higher wetness then others and may even have solution at the surface after the impregnation process. Therefore, during drying some agglomeration is to be expected.

The agglomeration of particles was also confirmed by PSD measurements. Figure 2-6 shows comparison of PSD analysis performed on pure $CaHPO_4$ and dry impregnated $CaHPO_4$. Clearly the impregnated powder exhibits broadening of the size distribution, with a shift towards the larger sizes. Due to the higher shear forces exhibited on the powder by the agitator and chopper blades during impregnation, some attrition of particles was observed, which then agglomerate to form bigger size aggregates.

2.4.2 Fluidized bed impregnation

An existing fluidized bed dryer and granulator, Glatt GPCG 1, was modified slightly and turned into impregnation equipment. The nozzle was lowered to make sure it is

completely submerged into the fluidized powder bed during operation. This is to ensure that the solution droplets will immediately collide with solid particles and there will be no spray drying taking place during impregnation. The FB dryer was also equipped with two storage vessels: one for pure solvent and second for API solution, which was placed on a scale to measure the solution mass flow rate. A schematic of the FB impregnation set up is depicted in Figure 2-7.

The same excipient, solvent and API were used as in the dry impregnation experiment. The amount of the excipient was chosen so it could reach the bottom of the spray nozzle. This will ensure complete immersion of the nozzle when the bed is fluidized. The impregnation process begins by fluidizing the powder. The velocity of the fluidizing air was increased beyond the minimal fluidization velocity to achieve turbulent regime of fluidization. Then the heater was turned on and the desired inlet temperature was set. When the bed temperature reached close to the solvent's boiling point (about $60^{\circ}C$), the pure solvent spray was started along with the atomization gas. Pure solvent was sprayed in the bed until steady state was reached: that is for a set inlet temperature, inlet gas flow rate, spray rate and fluidization gas pressure, the product temperature does not change. If any of those parameters needed adjustments, a new steady state needs to be reached. Proper blow back interval must be set on the filter element in order to eliminate powder build up. If this is not controlled properly, it may cause fouling of the filter element and eventually seizing of the fluidization process. Once steady state was attained, the liquid feed was switched to the API solution without any interruption to the fluidization process. The API solution was sprayed in until the desired drug loading was reached by monitoring the total amount of solution. Once loading was achieved, the spray was again

switched to pure solvent for several minutes to rinse the internals of all tubing and nozzle. At the end, all spraying was stopped and the material was allowed to dry in a fluidized state for appropriate time, after which it was cooled down and discharged. Two preliminary FB experiments were carried out and the results are presented below.

2.4.2.1   Preliminary FB experiment #1

All process parameters for this experiment are shown in Table 2-4. A total of three samples were taken during the entire impregnation process. After the second sample, the spray rate was increased over three times and kept constant until the end of the experiment. Each sample was analyzed by HPLC to determine average APAP loading. The results are presented graphically in Figure 2-8. The increase of APAP loading (theoretical and actual) are plotted vs. time. The actual trend of drug loading vs. time is in a close agreement with the theoretical loading until the second sample. The final sample shows a discrepancy: the actual measured loading was more than the theoretical loading (calculated based on initial weight of excipient and total amount of API sprayed in). This result is only possible if for some reason the excipient was being lost during the FB impregnation process. There was a small amount of physical loss incurred during impregnation due to sampling and opening of the equipment for various reasons (to clear a nozzle clog due to pump failure, to check for powder build up on nozzle, etc.). A careful examination of the FB's internals also revealed some product loss through the filter element and through the bottom distribution plate. It was realized that the distribution plate was not properly sized to handle small particles, and every time the process was stopped (due to sampling, etc.) small amount would fall through the screen due to the head pressure exerted by the bulk powder above. It was also discovered that

the filter element was not sized properly. A smaller size distributor plate and filter elements were procured and installed for subsequent tests.

Particle size distribution was measured on the final impregnated material to assess for any potential changes due to any of the following: particle attrition, particle agglomeration or even spray drying. Comparison of PSD measurements for pure and impregnated $CaPO_4$ is displayed in Figure 2-9. Both distributions are positioned almost perfectly on top of each other. There is no evidence of particle agglomeration (creation of large particles) or of spray drying (which would have been represented by its own distinct peak somewhere in the 0-100 micron range). There is very small shift to the left, suggesting possibly some level of particle attrition. This small shift is no near the PSD change observed during the dry impregnation experiment (Figure 2-6), reinforcing the argument that powder fluidization exerts smaller shear compared to agitated operations and it is more suited for powder mixing. Figure 2-10 shows SEM pictures of impregnated $CAHPO_4$ at the three different stages of impregnation. These pictures reveal particles that are identical to the pure excipient, without any signs of breakage, agglomeration or API coating.

2.4.2.2   *Preliminary FB experiment #2*

All process parameters for this experiment are shown in Table 2-5. A total of three samples were taken during the entire impregnation process. The spray rate was kept constant until the end of the experiment. The amount of excipient and API solution concentration was kept the same as experiment #1. The inlet gas velocity was reduced compared with experiment #1 in an effort to minimize particle attrition even further. Lower fluidization gas flowrate results in a reduction of the mixing intensity, which leads

to a reduced particle attrition. For the same exact reason the atomization pressure was also reduced. The atomization gas enters the fluidization bed countercurrent (downward) to the movement of the particles (upward), which could also affect mixing and attrition. In order to ensure the same drying capability, the inlet temperature of the fluidizing gas was increased.

Each sample was analyzed by HPLC to determine average APAP loading. The results are presented graphically in Figure 2-11, where the increase of APAP loading (theoretical and actual) are plotted vs. time. The actual loading results trend as expected with time and are in close agreement with the theoretical for all three samples. This is an improved performance over FB experiment #1 and is due to the modifications of the fluidized bed, smaller size distribution plate and filter element for exit gas. Similarly to experiment #1, the PSD was measured and compared to that of the pure excipient in order to assess for any attrition, agglomeration or spray drying. The data comparison is presented in Figure 2-12 and reveals almost identical size distributions for before and after the impregnation (final sample). This result demonstrates the lower attrition levels achieved in FB compared to other methods of powder mixing.

Figure 2-13 shows SEM pictures of the impregnated $CAHPO_4$ from the three different samples taken during the entire impregnation. These pictures reveal particles identical to the pure excipient, without any signs of breakage and agglomeration. However, they reveal something different from experiment #1. The SEM pictures for samples #2 and #3 show the existence of some "darker" particles (circled in red). The concentration of those dark particles was low as they did not appear randomly dispersed throughout the rest of the particles but rather had to be searched for. Close examination of those particles

revealed that this is a sign of API coating. This coating is non-existent for sample #1, which suggests that something happened inside the fluidized bed and caused the coating to occur for samples #2 and #3.

Coating of particles occurs via two distinct mechanisms. The first one involves very fast drying rates. This happens when the inlet gas temperature is high enough to cause evaporation of solvent as soon as the droplet reaches the surface of the particle, without allowing the solution to completely penetrate the particle. Given the fact that the drying temperature used in the experiment was not very high, only about 20°C higher than the boiling point of methanol (66°C), it is not very likely that fast drying was the reason for the observed results. The second mechanism via which coating could be observed is through a complete saturation of the particles with liquid. If a particle is completely filled with an API and does not possess any residual porosity, the sprayed liquid will dry on the surface. This could happen if the particle is consistently being filled entirely with API solution, every time it goes through the wetting zone of the FB impregnator. At some point during the process, the particle will be completely filled with an API and the next time when it gets wet, it will result in a surface deposition of the API. It is believed that this is the main reason for the observed coating, as two main differences were observed with this experiment (compared with experiment #1):

1. During this experiment, the inlet gas velocity and atomization gas pressure were reduced compared with the first experiment. This caused a reduction in the relative mixing inside the bed. Less intense mixing would results in a longer wetting time – the period spent by the particle in the spray zone. This longer wetting time would result in some particles being completely soaked with an API

solution. If this repeatedly happens to the same particle, it will eventually result in complete filling with an API and over time the particle would appear coated.

2. Several times during the experiment, the nozzle clogged and the impregnation process had to be stopped. In order to unclog the nozzle and proceed with the impregnation process, the nozzle had to be taken apart and rinsed with solvent. When the unit was open to service the nozzle, it was observed that there was a coating of wet powder (few millimeters thick) that was formed around and in the front of the nozzle. While this caused the clogging of the nozzle, it also had resulted in wetting this layer of powder first before the spray could get to the rest of the fluidized bed. The appearance of this coating of wet powder on the nozzle was a direct result of the reduced mixing inside the bed (as described above). This nozzle coating and clogging was not observed during the first experiment.

2.4.2.3   Summary

Dry impregnation of porous excipient with an API was achieved in a common granulator, followed by drying in a conventional vacuum oven. The API loading level per impregnation/drying cycle is limited to the solubility of the API in the carrier solvent and the porosity of the carrier, which in the present study was around 6 %. Higher loadings are possible by either repeating the entire process or by increasing the solution concentration (higher temperature, different solvent). Certain degree of agglomeration and attrition was observed with dry impregnation. This can be minimized by changing the following parameters: reducing the amount of solution sprayed per cycle and/or reducing the shear in the granulator. Improving the blend uniformity could be achieved by improving atomization of the solution and/or improving powder mixing.

Fluidized bed impregnation was successfully achieved using a Glatt FB granulator/dryer with minimal modifications. The process was easy to implement and run and was capable of achieving higher loadings of API compared to the conventional dry impregnation method. This is made possible due to the simultaneous occurrence of the wetting and drying steps during FB impregnation. The only process parameter that determines final API loading is the time of impregnation and the total porosity of the excipient. Special care should be taken when setting the processing parameters that control the FB impregnation process: spray rate, drying gas flow rate and temperature, atomization pressure, API concentration, etc. Fluidized bed impregnation offers other important advantage: it leaves unchanged the excipient particles as attrition is minimized significantly and agglomeration is almost nonexistent. Fluidized bed impregnation will be studied in more detail in the sections to follow.

2.5   Case study – Fluidized bed impregnation of anhydrous calcium phosphate with acetaminophen

2.5.1   Methods and procedures

Based on the preliminary experiments, the final procedure developed for the fluidized bed impregnation of excipients consists of the following several steps:

1. Charge fluidized bed dryer with excipient until the top spray nozzle is reached. During fluidization, the nozzle needs to be located within the powder bed in order to eliminate spray drying.

2. Start fluidized bed dryer and set the inlet gas temperature to desired value.

3. Begin spraying pure solvent. Continue spraying until steady state is achieved (constant product temperature).

4. Once steady state is achieved, begin spraying API solution. Continue spraying until desired loading is achieved.

5. Switch back to spraying pure solvent for specific time.

6. Dry product for specified time, cool down and unload.

The excipient used was EMCOMPRESS® - an anhydrous form of $CaHPO_4$. Three impregnation studies involving APAP and $CaHPO_4$ are presented in this study. The aim of these studies was to achieve three different APAP loadings within the excipient: medium (9-10 wt%), low (0.9-1.0 wt%) and ultra-low (0.09-0.1 wt%). All of these experiments were executed following the above procedure. Details on the experiments in terms of amounts of APAP and excipient, concentration of APAP solution, spray time and processing parameters, such as inlet and product temperatures, are given in Table 2-6.

All experimental conditions were kept constant with the exception of the APAP solution concentration, which was varied accordingly in order to achieve the target loading in the same amount of time. Spraying pure solvent after the APAP solution is an important part of the impregnation procedure, as it allows for any amounts of deposited APAP on the surface of the particles (in case they are any) to be re-dissolved and deposited within the excipient. At the end of each experiment, the impregnated material was dried until product temperature reached 60 ^{o}C, after which the heat was turned off and contents of the fluidized bed were cooled down to room temperature. Milling of the impregnated materials was performed on a 2" lab scale pin mill. The material was fed to the mill using

a vibratory feeder. Feed rate used was around 10 g/min. Mill speed used was 10,000 rpm. Capsule filling was performed on a semi-automatic CAP 8 machine. Equipment settings used during filling were: 90° auger, rotary table at maximum speed, rectifier at maximum speed. Two batches of 450 capsules were filled with each material. Only the second batch was used for blend uniformity and dissolution analysis.

2.5.2   Results and discussion

2.5.2.1   Proof of impregnation

There are four possible outcomes of the proposed fluidized bed process, with only one (impregnation) being the desired one. The three undesired outcomes are spray drying of the API, spray coating of the excipient and agglomeration/granulation of the excipient. This section tries to answer the question "Was the excipient impregnated?" This issue is examined by conducting three types of physical analysis on the impregnated blends: scanning electron microscopy, specific surface area and pore size distribution and finally, by testing the drug loading.

Spray drying of the API is easily ruled out by HPLC analysis on the impregnated materials, which is performed to determine the final drug loading (see complete details in next section "Drug loading and blend uniformity"). The loading of the API, as discussed below, was determined for various particle size fractions (obtained by mechanically sieving the powders) and then averaged. In the event that the API was spray dried, three possible outcomes could be observed: (1) collecting all the spray-dried API with the smallest particle size fraction (below 53 μm) during sieving (the size of droplets produced, hence final API particles, are on average less than 20 μm due to the nozzle and

atomization pressure used during impregnation). (2) Losing most (or all) of the spray dried API through the outlet filter, which has size of about 50 μm. (3) Having spray-dried API particles attached to the surface of the carrier. If scenario (1) was true, then all of the API must show with the lowest size fraction (below 53 microns) with almost no API in the upper fractions. If scenario (2) was true, then the amount of API analyzed should be considerably lower than the target loading (or even zero). If scenario (3) was true, then there should be clear evidence in the SEM pictures of excipient particles attached to spherical API particles (spherical because of API spray-drying). Neither the first nor the second scenarios take place, as it is evident from Figure 2-14. All size fractions receive appropriate amounts of API (see explanation in next section "Drug loading and blend uniformity") and the average loading (calculated based on data in Figure 2-14 and Table 2-7) is consistent with the total sprayed amount of API during processing (see data in Table 2-6). There is no loss of API and all of it is distributed throughout the excipient. The third scenario is examined by analyzing SEM pictures of impregnated $CaHPO_4$ (Figure 2-15), which clearly shows that this last scenario does not occur either. Therefore, spray drying of API solution during fluidized bed impregnation process can be ruled out with a high level of confidence.

Spray coating is the second undesired outcome during the impregnation process. Based on data from the preliminary runs, the process parameters (product temperature, inlet temperature) and the overall procedure are chosen carefully in order to promote impregnation and suppress coating. In order to rule out spray coating, we first examine all impregnated powders under the microscope. Figure 2-15 shows SEM pictures of various size fractions of impregnated $CaHPO_4$ along with pure $CaHPO_4$. Thorough examination

of all pictures (full set of pictures not shown) did not yield any visual sign of coating. All impregnated particles look almost identical to pure $CaHPO_4$. In the event of coating, the rough surface of the particles should have been smoothed and gaps/crevices filled up by the applied layer of API (as was seen in Figure 2-13). SEM pictures also clearly indicate that there is no agglomeration/granulation of the excipient.

Although SEM pictures demonstrate absence of spray drying and surface coating, in order to firmly establish the proof of impregnation, all powders (impregnated and pure) were further tested for their total surface area and pore size distributions. A relatively porous material, in theory, should possess high total surface area, in the order of few a m^2/g as a minimum. On the contrary, a completely non-porous material with particles of several microns usually has total surface area below 1 m^2/g. Simple calculation shows that for uniformly distributed spheres, 2 μm in diameter with a true density of 2.96 g/ml (true density of $CaHPO_4$ anhydrous [67]) the total surface area should be around 0.5 m^2/g. Therefore, examining and comparing changes in specific surface area and pore size distribution for pure and impregnated $CaHPO_4$ should give a useful indication of impregnation vs. coating. In the case of spray coating, which requires the drying process to be much faster than impregnation, all particles would receive a layer of (most likely amorphous) API. This layer would block the internal surface of the particles from the N_2 gas during surface area measurements and the corresponding SSA would be comparable to that of a non-porous material.

However, this is not the case as it is evident from Figure 2-16 and Table 2-8, which summarize SSA and pore size distribution measurements for pure and impregnated $CaHPO_4$ (8.87% and 0.99% loading). Measurements for the lowest loading of 0.1% were

performed but not included since they did not show any difference compared to pure excipient. For each size fraction shown on Figure 2-16, we observe a decrease in SSA and total pore volume (for micropores and mesopores with d_{pore}<120nm) proportional to the level of loading (see next section "Drug loading and blend uniformity" for discussion on loading). In neither case do we detect SSA values indicating spray coating of particles. Even for the size fraction with the highest loading (below 53 μm, Table 2-8) there is still high residual porosity, as indicated by the corresponding SSA of 6.3 m^2/g. Therefore, from all this data, it can be concluded with significant confidence that the carrier particles are impregnated and that spray coating is not evident. The proposed FB impregnation process does indeed promote impregnation of particles when process conditions are chosen carefully.

2.5.2.2   Drug loading and blend uniformity

It was shown already (Table 2-8) that variations in the API uptake by different size fractions of the excipient were observed during impregnation (as indicated by differences in surface area and pore volume at the end of impregnation). In order to better assess the drug loading, the final product was sieved and HPLC analysis was performed on each fraction. The results were shown in Figure 2-14. The average loading was calculated based on these results and on the mass fractions of each size group in the blend (data shown in Table 2-7). There is an emerging pattern, characteristic for all three materials – the API loading is inversely related to the size of the particles being impregnated. This is not surprising and can be explained in terms of the flux of API solution across the external surface (not to be mistaken with total surface area, which also includes internal surface area) of the particles. During fluid bed impregnation, this flux is constant for all

size particles if one assumes a well-mixed system. The difference comes from the fact that particles of pure $CaHPO_4$ (as in any other powder) have a PSD, which in mathematical terms translates to differences in the external surface-to-volume (or surface-to-mass) ratio of different size particles. Therefore, a constant flux of material causes particles with high surface-to-volume ratio (i.e., smaller particles) to receive a larger mass fraction of solution for a given time.

From this data it can be concluded that the PSD of the excipient is an important characteristic, which determines the final drug loading (or variation thereof) during FB impregnation. Having a porous carrier with a narrower PSD will result in less variation in the drug loading across size groups. It will also allow for higher drug loadings to be achieved. For example, Figure 2-14 (top left) shows that for the size group of "below 53 μm" the loading is 21.06%, when the average loading is only 8.87%. A narrower PSD allows achieving the highest loading possible without overfilling the smallest size particles. This highest theoretical loading will depends on the porosity of the excipient and the true densities of the API and excipient.

Any given pharmaceutical formulation has to be assessed in terms of its blend uniformity – that is how well the API is dispersed throughout the excipient. The blend uniformity for the impregnated materials presented in this study was assessed by first formulating them into hard gelatin capsules without any other additives. These capsules (having around 0.50-0.55 grams of impregnated powder) were then taken and ten of them were randomly chosen for HPLC analysis. The absolute amount of API in each capsule was determined and its concentration (in terms of weight %) calculated. The blend uniformity was calculated as % relative standard deviation (%RSD) from the mean value of the

concentration. The results from this analysis for all three impregnated materials are presented in Table 2-9 along with the empty capsule weight variability (measured on 50 randomly chosen capsules). Drug content uniformity (also presented) was calculated as % relative standard deviation from the mean value of the API's absolute amount in each capsule. All results for blend uniformity are around 1% RSD or less which indicates a highly uniform pharmaceutical blend. There are larger variations in drug content uniformity which are primarily due to the capsule weight variability.

In general, highly uniform blends are difficult to achieve, especially when working with low drug loadings. This is primarily due to inadequate mixing of the ingredients and size segregation of the particles (API and excipient). In such cases, conventional formulation techniques call for additional unit operations, such as wet or dry granulation, in order to help achieve targeted blend uniformity. What we have shown here are highly uniform blends, achieved with a single unit operation without any special control of API physical properties. The API (and its physical properties) does not play a role in determining the uniformity of the blend, as it is located inside the excipient particles. However, there is still a chance for size segregation due to the inherent PSD of the excipient particles. As it was shown already, various size groups have different drug loadings and if they are segregated, they will affect the final blend uniformity. In order to further improve homogeneity of the impregnated materials we examined the effects of size reduction. Milling of the impregnated powders was done on a lab scale pin mill using mild conditions (low range of milling speeds). The resulting powders were used again to fill hard gelatin capsules and then tested by HPLC for drug content. All blend uniformity

results on the milled materials are summarized in Table 2-10. Particle size distributions are discussed in one of the next sections.

For all three impregnated materials, there was further improvement of blend uniformity, which in some cases led to reductions in the RSD of 50% or more. Again, variation in drug content uniformity is mainly due to the weight variability of the filled capsules. The variability of the filled capsule's weight is primarily due to the semi-automatic fashion in which they were filled (variation between experiments such as hopper fill level). These results underline the importance of the PSD of the excipient being impregnated. Using an excipient with narrow PSD will allow not only for higher drug loading but also produce more uniform dispersion of the API.

2.5.2.3   *Physical state of the impregnated API*

The proposed impregnation method could be viewed as a slow evaporative process during which the API precipitates/crystallizes out of solution as it is being deposited within the mesoporous and microporous structure of the excipient. The question that remains is in what physical form the drug molecules are deposited inside the carrier? There are three possible outcomes: crystalline material, amorphous material or solid molecular dispersions. Factors that determine the actual physical form of the impregnated drug include: the nature of the API (some form amorphous state easier than others), the solvent system and the internal structure of carrier matrix (pore size and distribution). Whether crystalline or amorphous material is deposited will depend on the first two factors while the formation of a molecular dispersion will be influenced by the third one. Solid molecular dispersion is a state of matter, similar to amorphous, in which the intermolecular interactions are broken up and the molecules are individually separated

and dispersed throughout the pores. This scenario is possible since equilibrium thermodynamics predict that crystallization should be completely suppressed below a certain critical pore diameter. Surface energy contributions in this case over-compensate the energy advantage associated with crystallization. The critical diameter typically amounts to a few nanometers [23]. In larger size pores the state of matter will be either amorphous or crystalline, depending on the nature of the API, solvent or processing conditions. It is possible by controlling the pore size to prevent the crystallization of the amorphous material [23], or to preferentially obtain one crystal form vs. another [30]. In all cases there will be a shift of the bulk API's melting point to lower values depending on the size of the pores. This is due to the well-known phenomenon of confinement-induced melting point depression. The new melting point can be estimated using the Gibbs-Thompson equation given below [68]:

$$T_m(d) = T_m^\infty - 4\sigma_{S1}T_m^\infty/(d_P\Delta H_m\rho_C)$$ (2-2)

where $T_m(d)$ is the depressed melting point for pores with diameter d, T_m^∞ is the bulk melting point, σ_{S1} is the surface tension between crystal and liquid phases, ΔH_m is the heat of melting and ρ_C is the bulk density of the solid phase.

Differential scanning calorimetry (DSC) is a very powerful analytical tool used to investigate the physical state of solids. In the case of an amorphous material or molecular dispersion, there won't be any visible endotherm or exotherm peaks. When only a crystalline material is present, the exothermic peak (amorphous) will be absent. If the crystalline solid is confined to small pores (as it was explained already) there will be a shift of the melting peak to a lower value. All three impregnated materials were analyzed

using DSC, however only the ones with 8.87% and 0.99% loadings are presented here (Figure 2-17).

The DSC scans for 0.1% impregnated material did not show any thermal events, most likely due to the fact that the actual API amount in the DSC scans was below the limit of detection for this analytical technique. In the case of 8.87% loading (Figure 2-17-left), the amount of impregnated API was enough to give a very clear DSC signal with high intensity. Due to the difference in APAP loading, DSC scans of all size groups were taken. For all size groups there is a clear shift in the melting point of APAP from its bulk melting point of 169.02^{o}C (crystalline form I [69]). This is a clear indication of the small confinement of APAP molecules, which is another proof of impregnation. These melting point shifts are within a temperature range of 150-170°C, well in agreement with already evaluated shifts for APAP form I in pore sizes ranging from 20 to 100 nm [30]. All melting peaks show some broadening as well due to the inherent pore size distribution within the excipient. The melting peak for the size group of 53 μm and below shows some overlap with the bulk melting point. This could be an indication of complete filling up of the macropores (d_{pore}>120nm), which as suggested by *Chevalier et al* [27] in the case of CaHPO$_4$ granules and Ibuprofen, is about 22%. In the case of 0.99% loading (Figure 2-17-right), the amount of impregnated API was at the borderline of limit of detection for the DSC instrument. Therefore only the size fractions with the highest loadings are presented along with a scan for the pure CaHPO$_4$ excipient. The pattern is the same as outlined above (broadening and shifting to lower temperatures) although it is clear that the peaks are weaker, getting near the limit of detection. Sensitivity of the DSC

technique (along with the actual API loading) should be considered if it will be used to characterize impregnated materials.

Figure 2-18 shows the differential pore size distribution for the same material (8.87% loading). From this data it can be confirmed that most of the impregnation is taking place within the pore size range of 10-100 nm, as was suggested earlier. There might be some small amount of APAP in smaller pores (<5 nm) in the form of molecular dispersion as suggested from the same plot. Powder XRD analysis was also performed to confirm the physical form of impregnated $CaHPO_4$. Tests were performed only on the high loaded material due to detection limitations associated with this technique. Figure 2-19 shows XRD scans for various size groups and for pure $CaHPO_4$ and pure APAP form I as comparison. The figure does not show the full range of scans (2θ of 10°-50°) for the sake of clarity. Acetaminophen Form I can be confirmed by several peaks around 2θ of 15°-25°. These also confirm the crystalline nature of the deposited API.

2.5.2.4 Particle size distribution

Every excipient is friable to some degree. In order for the FB impregnation method to be commercially viable, it must be able to preserve the original physical properties of the excipient almost unchanged. Therefore, an important question to be answered is how the particle size changes due to the continuous fluidization during the impregnation process. Total fluidization time in all of the experiments, which includes impregnation time plus the initial start-up and final drying, was in the order of 4 hours. Particle size distribution data for pure $CaHPO_4$ and for various impregnated $CaHPO_4$ lots is shown on Figure 2-20. Comparing PSD data for pure and impregnated samples (un-milled) proves that the changes in size are not significant. There is some small amount of fines generated due to

attrition that takes place during the process. Additional, more detailed experiments are needed to determine if these fines are generated constantly throughout the process or only at the beginning of the fluidization, when the particles are still dry and not loaded with API. It could be argued that having a drug impregnated within, could further mechanically stabilize the particles (see section "Tableting and compressibility study").

Figure 2-20 also compares PSDs of impregnated $CaHPO_4$ before and after milling. As it was shown in section "Drug loading and blend uniformity", milling was used to further improve blend uniformity of the impregnated materials. One way of explaining this experimental fact, as it is evident from the PSD data, is that reduction in size of the big particles (the ones with low drug loading) significantly decreases size segregation tendencies. Using harsher milling conditions will cause all particles to be further normalized in size, which in turn will additionally reduce size segregation. This, however, needs to be balanced with the need to maintain good powder flow properties, which in general tend to worsen as the particles size gets smaller.

2.5.2.5   *Shear cell measurements*

Flow properties of pharmaceutical blends are an important factor affecting their formulation into final products (capsules or tablets). One of the main advantages of excipient impregnation with APIs is the ability to preserve the original flow properties of the pure excipient. In this section we examine this issue by analyzing and comparing shear cell data collected on pure and impregnated $CaHPO_4$. Figure 2-21 (yield locus) shows shear cell testing results of shear stress (τ) vs. normal stress (σ) for pure and milled and un-milled impregnated $CaHPO_4$ (8.87% and 0.99%) as described in 2.3.7.

Mohr stress circle analysis (not shown) was employed to calculate the values of major principal stress ($\sigma 1$) and unconfined yield strength (σc) from which the critical flow factor ($ffc=\sigma 1/ \sigma c$) was then calculated. The value of σc depends on the compacting stress in the bulk solid $\sigma 1$, and the relationship $\sigma c=f(\sigma 1)$ is called a flow function, a characteristic that is dependent on the powder properties. The value of cohesion (τc) was approximated as an intercept of linearized yield locus with the τ-axis (shear stress). Changes in flow properties can be assessed by comparing the results for cohesion and critical flow factor. In general, the smaller the cohesion is, the better powders flow [70]. Similarly, the bigger the critical flow factor, the better the flow.

All results from the Mohr stress circle analysis are presented in Table 2-11. Measured cohesion values are relatively low and decrease from τc=0.432 for pure $CaHPO_4$ to τc=0.349 for 0.99% impregnated $CaHPO_4$ and finally to τc=0.173 for 8.87% impregnated $CaHPO_4$. This data shows that all powders are free flowing, as suggested by the low cohesion values. Cohesion decreases with increasing amount of API impregnated within the excipient, as suggested by the direction of change for the value of τc. The same trend can be concluded from the calculated ffc values. Although more testing is needed to firmly establish the above conclusions (impregnation is improving powder flow), the claim that impregnation preserves the original flow properties of the pure excipient can be confirmed with a high degree of certainty. As expected, milling increase cohesion and reduces flowability, however in this case the change is very small.

Often, flow properties are correlated to the Hausner ratio, a dimensionless number defined as the ratio of tapped density to bulk density of a powder. The Hausner ratio is viewed as an indirect measure of bulk density, size and shape, surface area, moisture and

cohesiveness of materials - all important physical properties of a powder that affect its flowability. Table 2-12 shows results for bulk and tapped densities for all materials presented in this paper – pure $CaHPO_4$, impregnated $CaHPO_4$ and impregnated and milled $CaHPO_4$.

The data suggests a slight change in Hausner ratios from pure to impregnated excipient. This could be attributed to generation of fines during fluidization and impregnation because of attrition. Change in Hausner ratio to higher values for milled & impregnated $CaHPO_4$ is expected, as the particle size is intentionally reduced. The higher value for $CaHPO_4$ milled & impregnated to 0.99% (last in Table 2-12) could be attributed to the slightly smaller particles size as suggested by Figure 2-20. This is most likely due to slight differences in feed rate during milling.

From all the data in Table 2-12 it can be also concluded (as stated previously) that impregnation preserves the flow properties of pure excipient. It could be further stated that milling could be performed in a way that will slightly change bulk properties, yet still yield a free-flowing material with very high blend uniformity, ideal for further formulation.

2.5.2.6   Tableting and compressibility study

All impregnated materials presented in this case study were formulated in the form of filled hard gelatin capsules, which were in turn used to assess blend uniformity (see section "Drug loading and blend uniformity") and dissolution profile (see next section "Dissolution profile"). This formulation was chosen for its ease of manufacture and availability of appropriate equipment. It was interesting, however, to investigate the

behavior of these materials if they were to be tableted, and to evaluate the resulting tablets. In order to achieve this with limited amounts of available materials, tablets were made using the Presster^{TM}, which is a tablet press replicator and compaction simulator. Materials used for tablet preparation included: pure $CaHPO_4$, impregnated $CaHPO_4$ (8.87% and 0.99%) and physical blends of $CaHPO_4$ and APAP with loadings 7.25% and 14.00%. All tablets produced for the comparison study were made with identical weight of 0.92g and shape (1cm flat face die) without the introduction of any additive. Several tablets from each material were made by varying the compression force. Tablets were then measured for their thickness and hardness. Severe fracturing was observed for tablets made of pure $CaHPO_4$ and impregnated $CaHPO_4$ to 0.99%. In some case only the thickness was measured since the tablet was structurally compromised and hardness measurement would not have been accurate. Therefore an incomplete set of data is presented for these two materials.

Figure 2-22 (left) shows the results of tablet thickness vs. compression force. First thing to notice is that pure and impregnated (0.99%) $CaHPO_4$ behave almost identically, which is to be expected. There is not enough APAP loaded inside the excipient to cause any significant change. Secondly, the tablet thickness for impregnated 8.87% $CaHPO_4$ is lower than the one for the physical blend of similar loading (blend 7.25%). This is also to be expected as the API does not occupy the space between excipient particles (as it is the case with physical blends) but rather the space inside them (due to impregnation) resulting in smaller overall volume. This is another indirect proof of impregnation.

Figure 2-22 (right) shows the results of tablet hardness vs. compression force. Pure $CaHPO_4$ is not shown as all tablets produced have shown severe fracturing and capping,

making hardness measurements meaningless. The case was almost identical with material impregnated to low loading (0.99%) $CaHPO_4$, hence only a few tablets were produced successfully. Regardless of their APAP content, the two physical blends exhibited almost identical tablet hardness. However, impregnated $CaHPO_4$ with 8.89% loading shows much higher tablet hardness for the same compression force than the two blends. This suggests that APAP, when impregnated inside excipient particles, acts as a strong binder. The impregnation process strengthens the excipient particles within, making the tablet stronger.

2.5.2.7   Dissolution profile

The main purpose of any pharmaceutical product is to appropriately deliver an API into the body. This is achieved by dissolving the API in the GI track from where it gets absorbed into the blood stream. Therefore, the dissolution profile becomes an important characteristic of any pharmaceutical formulation and measuring it, an integral part of any drug product development. The in vitro release profile of APAP from impregnated blends with 8.87% and 0.99% loading was studied. All measurements were performed in accordance with the USP method for APAP filled capsules: apparatus I, basket method, phosphate buffer with pH=5.8. According to the USP method for acetaminophen (capsules or tablets), the release of the API should take 30 min or less. Impregnated $CaHPO_4$ to 0.1% loading was not tested due to detection limitations of the instrument. It should be mentioned that at these conditions the excipient remained un-dissolved throughout the test. All gelatin capsules disintegrated after about a minute and this time was factored in the final results.

Figure 2-23 (left) shows release profile for milled and un-milled impregnated $CaHPO_4$ to 8.87% APAP. Both dissolution profiles meet the USP requirement of 80% release in 30 min or less. The data shows slightly faster release for milled material. Release of 80% of APAP in the milled case is around 7 min vs. 9 min for the un-milled case. Figure 2-23 (right) shows release profile for milled and un-milled impregnated $CaHPO_4$ to 0.99% APAP. Again the USP requirement for APAP release is quickly met for both materials. For these two cases data suggests slightly faster dissolution for un-milled CaHPO4. The required 80% release of APAP is achieved in about 7 min for un-milled vs. 10 min for milled $CaHPO_4$.

2.6   Conclusions

This chapter presented a detailed study on the proposed new method for formulation and manufacture of pharmaceuticals - fluidized bed impregnation of APIs onto porous excipients. The proposed method has operational simplicity and offers several advantages over conventional techniques. The study involved acetaminophen as the model drug and anhydrous dibasic calcium phosphate as the porous excipient, but the method presented here can be used for many other drugs and carriers with minimum modification. Further study using different APIs and excipients to establish that claim is needed.

Fluidized bed impregnation can be summarized as the combination of three distinct processes taking place simultaneously. These include fluidization of the porous carrier, spraying API solution within the bed, which quickly penetrates the excipient due to capillary forces, and drying of the porous particles causing the API to be deposited within. Final API loading is not limited by its solubility in the organic solvent. Lower solubility could be compensated with longer run times to achieve targeted loadings.

This study helped to establish the following claims about impregnating APAP into anhydrous $CaHPO_4$ utilizing fluidized bed:

- Successful proof of concept.

- Ability of the process to deliver final product with high blend uniformity (as expressed in % RSD), independent of the API loading

- Milling of the impregnated material further improves blend uniformity.

- Physical state of impregnated APAP inside porous excipient is crystalline

- FB impregnation process by design preserves the final bulk physical properties and flow properties of the impregnated materials compared to those of the pure excipient

- Impregnated APAP acts as a binder during tableting, making harder tablets when compared to physical blends

- FB impregnation does not slow down the dissolution profile of APAP

- FB impregnation is a fast, one-step process that is able to deliver final pharmaceutical material ready for formulation into capsules (or tablets).

Implementing fluidized bed impregnation in drug manufacturing could allow for significant cost savings due to elimination of several unit operations. These include steps to control API attributes (secondary crystallization, milling), steps to control flow properties of final blends (mixing with various additives) or steps to control blend uniformity (wet or dry granulation, roller compaction) as depicted in Figure 2-24. Fluidized bed impregnation by design does not depend on the nature of the API but rather on the nature of the excipient used. Proper design of the porous excipient (high SSA)

could potentially have a big effect on the dissolution kinetics of the impregnated API.

These claims require further study.

2.7   Figures for Chapter 2
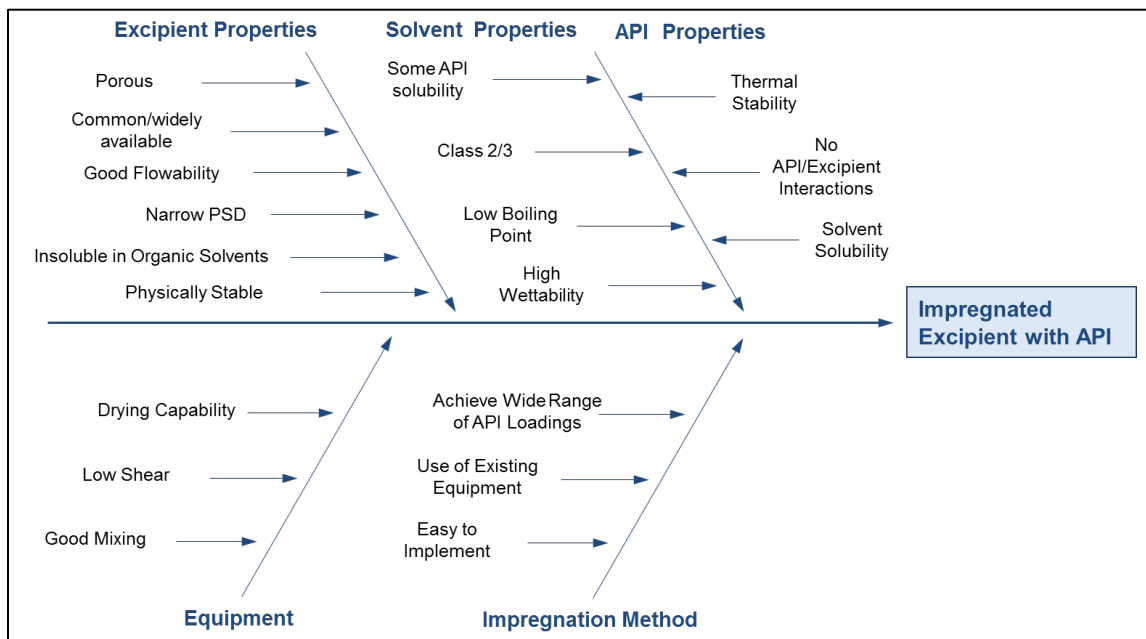
Figure 2-1: Factors influencing API impregnation of excipients
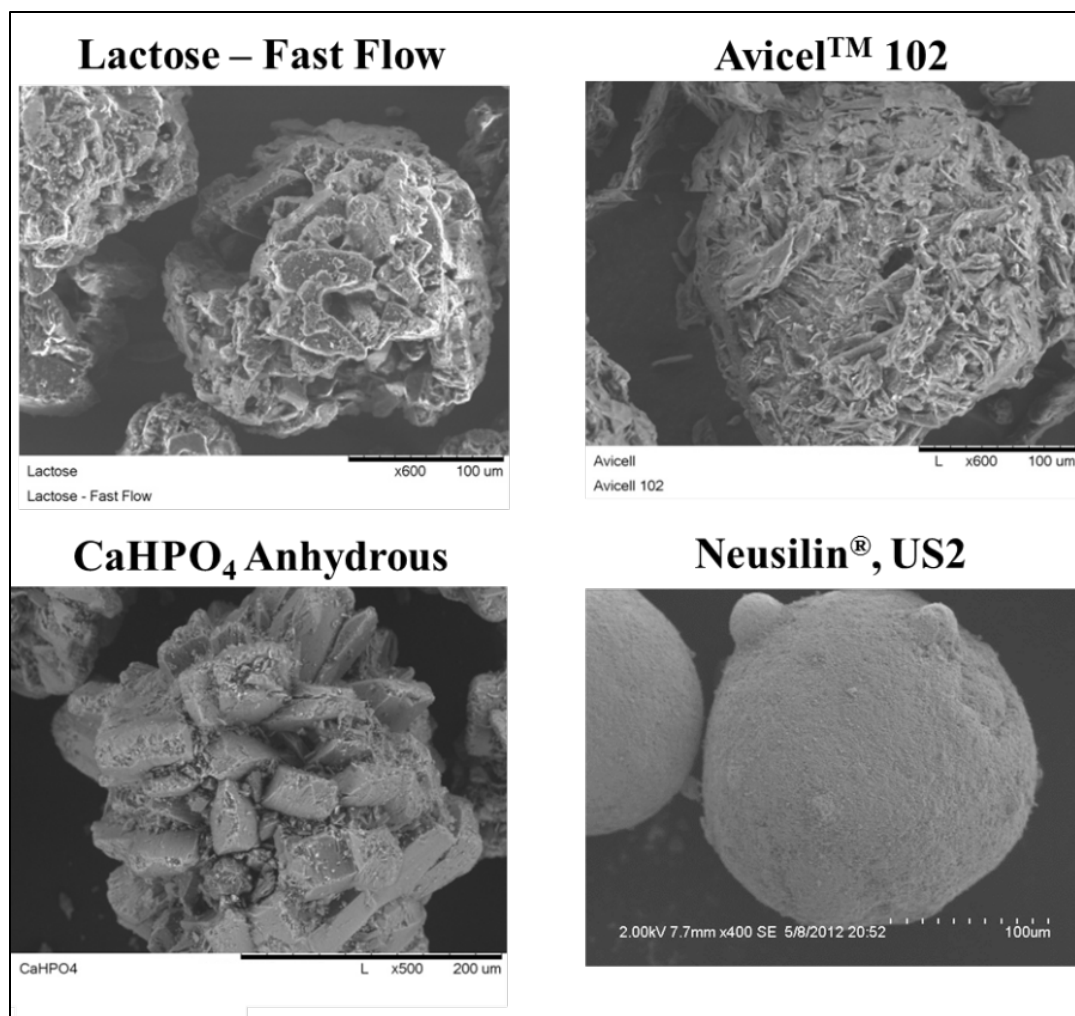
Figure 2-2: SEM pictures of common excipients.

Figure 2-3: Fluidized bed dryers chosen for impregnation development: Glatt GPCG 1 - 3kg scale (left) and Mini Glatt – 500g scale (right).
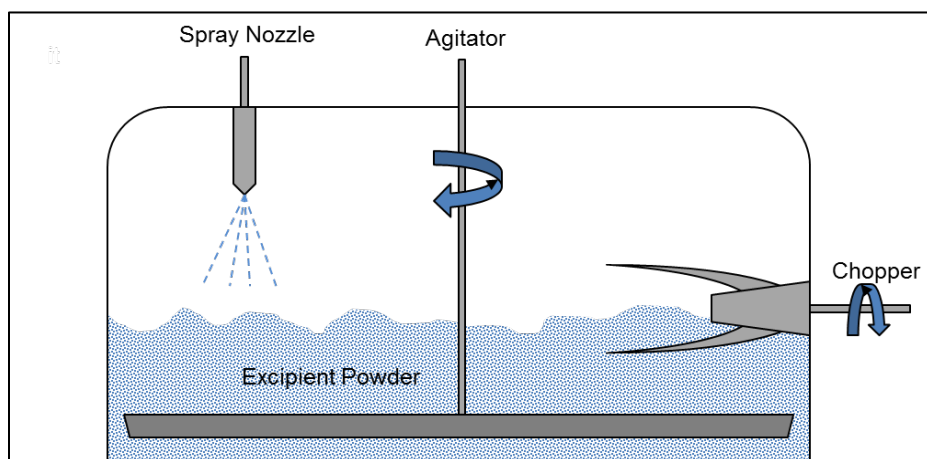
Figure 2-4: Conventional granulator used for dry impregnation
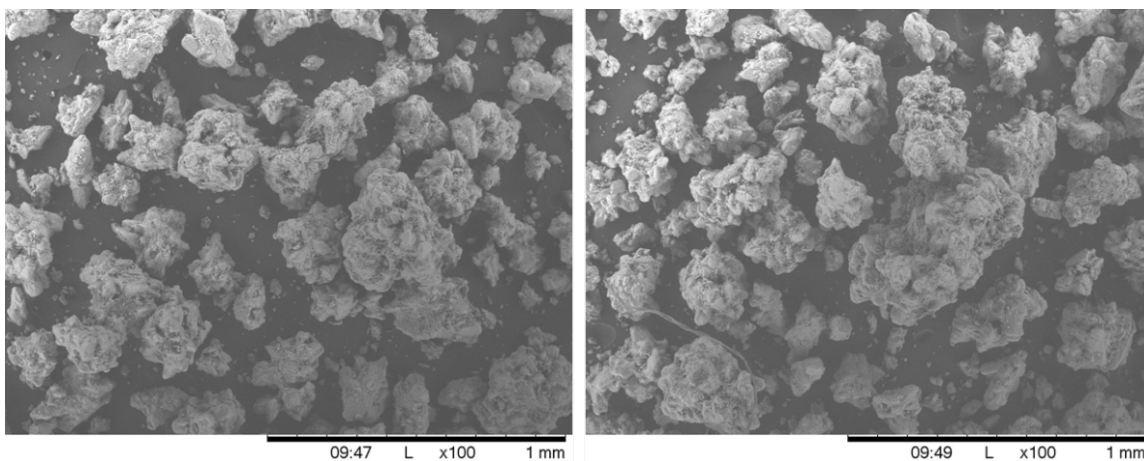
Figure 2-5: SEM pictures - dry impregnation of CaHPO$_4$ in a granulator.
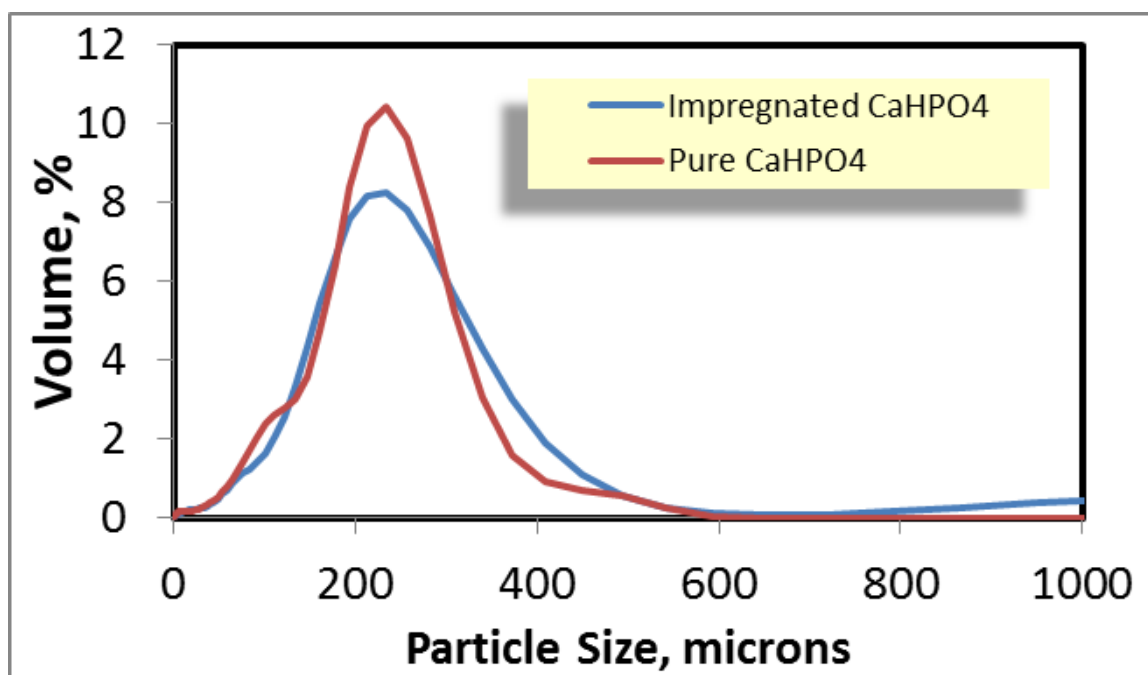
Figure 2-6: Dry impregnation, PSD
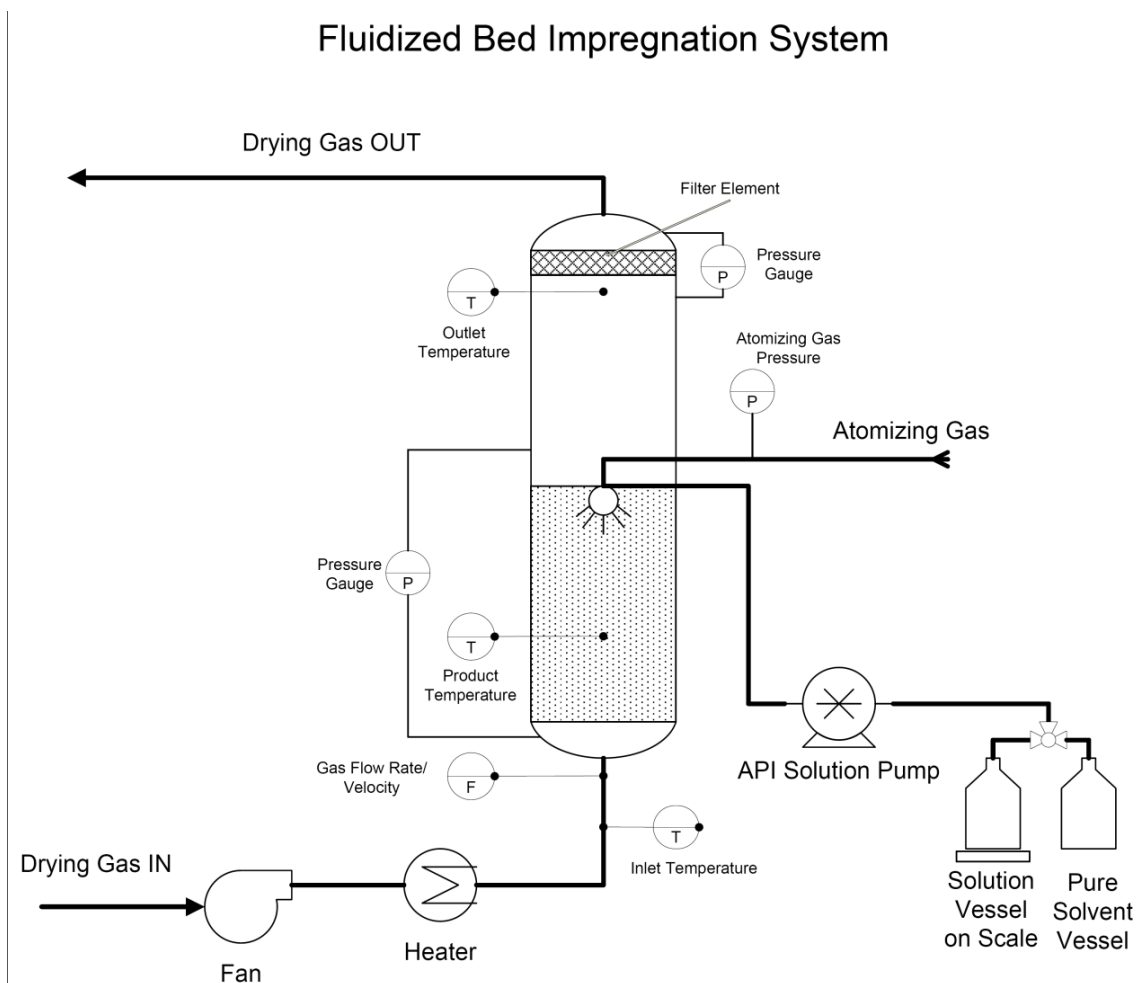
Figure 2-7: Fluidized bed impregnation set up.
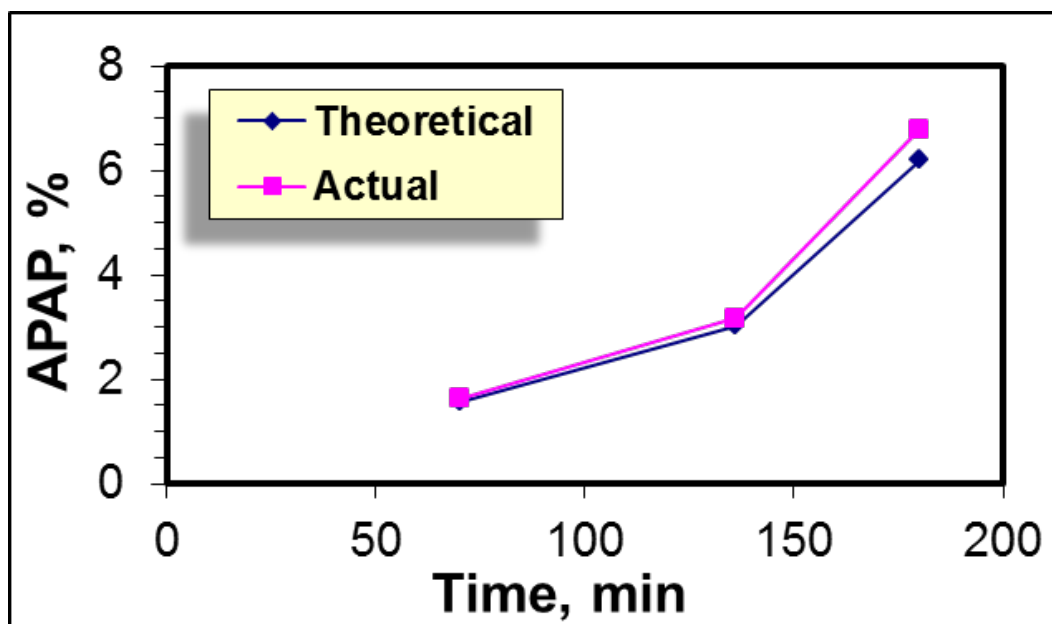
Figure 2-8: Preliminary FB experiment #1 - theoretical and actual APAP loading vs. time.
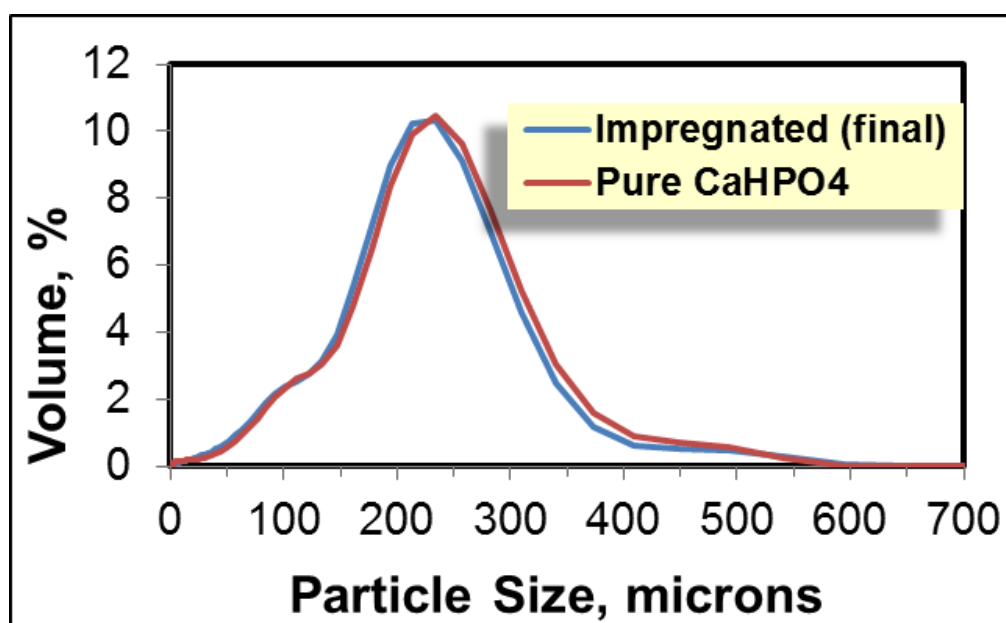
Figure 2-9: Preliminary FB experiment #1 - particle size distribution.
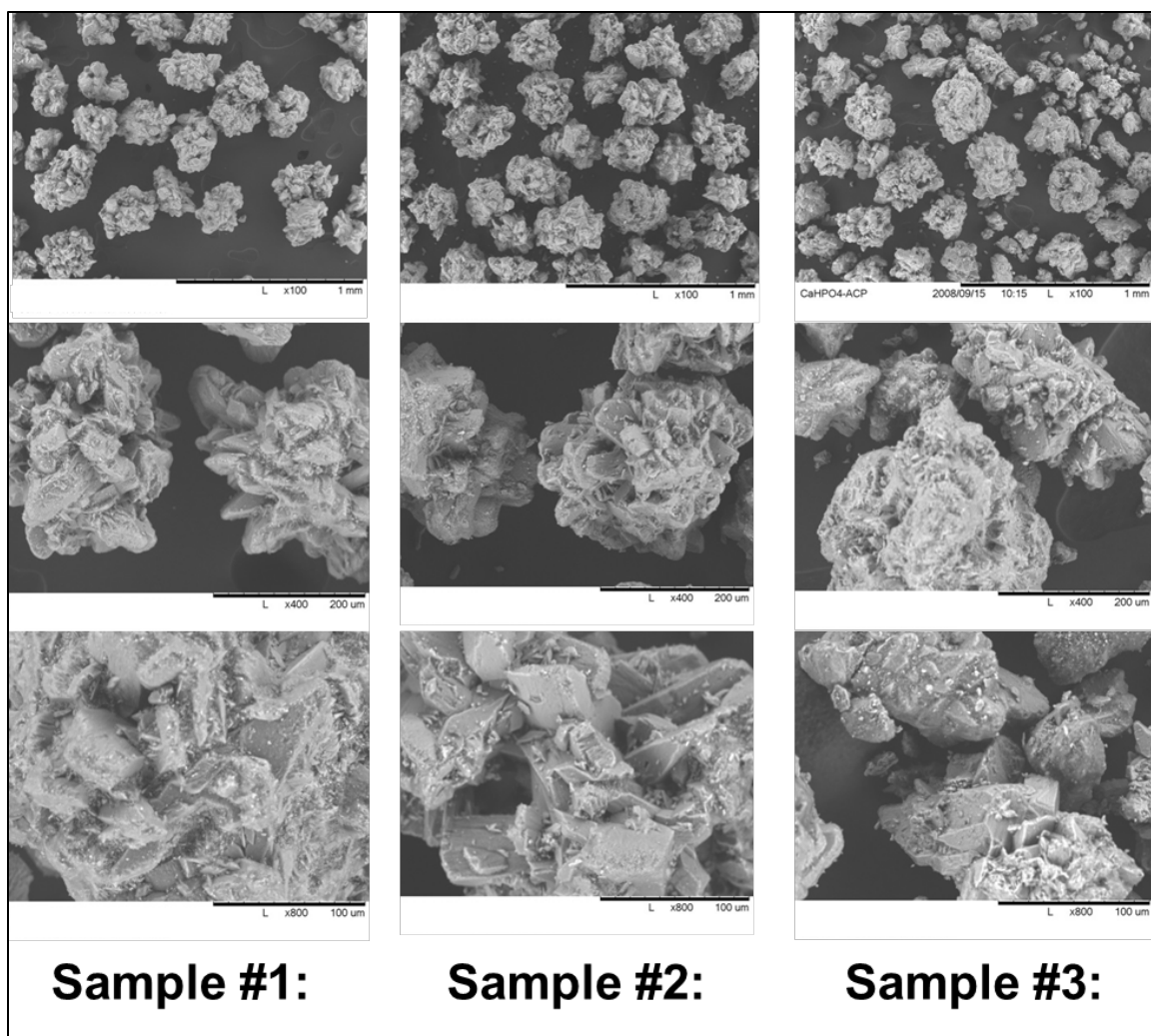
Figure 2-10: Preliminary FB experiment #1 - SEM pictures of impregnated product.
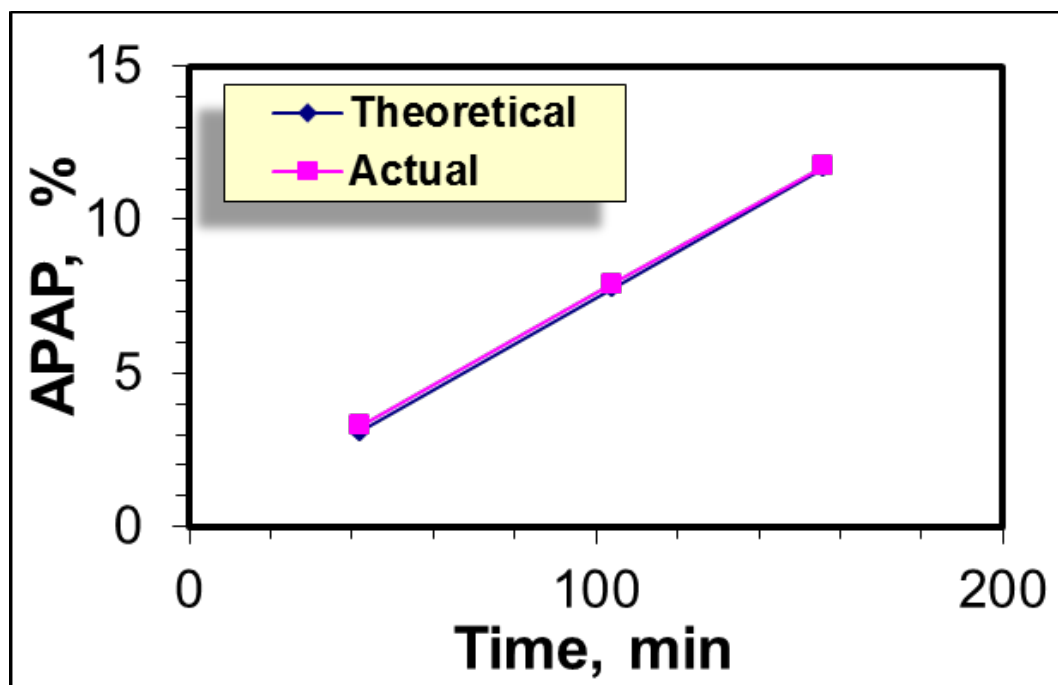
Figure 2-11: Preliminary FB experiment #2 - theoretical and actual APAP loading vs. time.
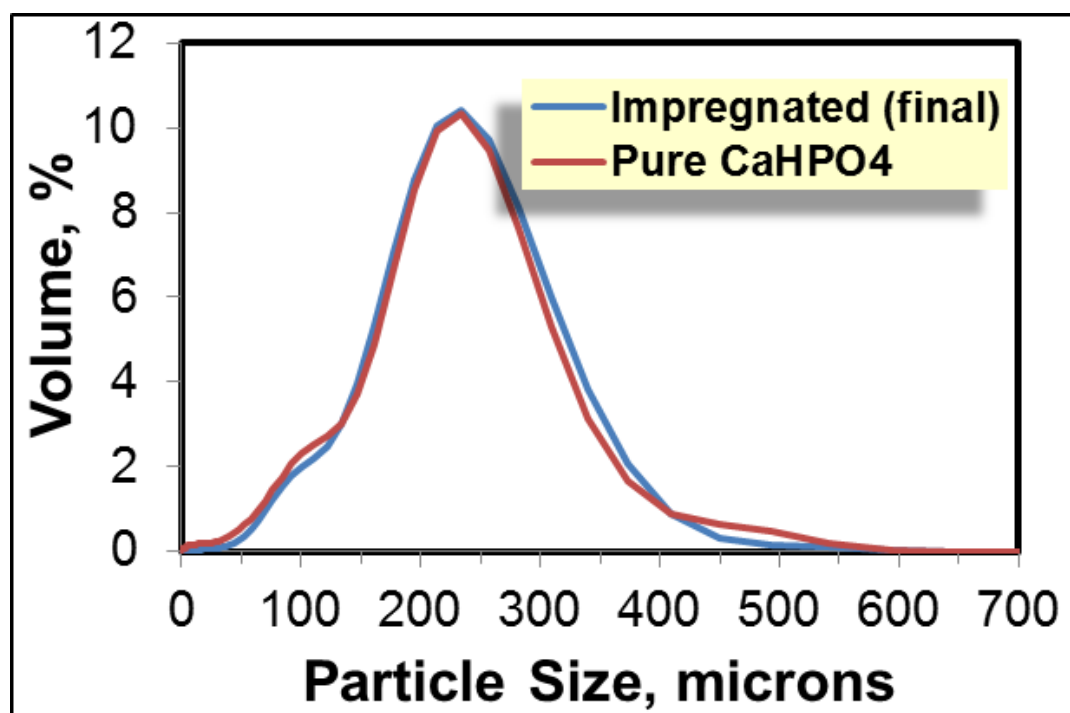
Figure 2-12: Preliminary FB experiment #2 - particle size distribution.
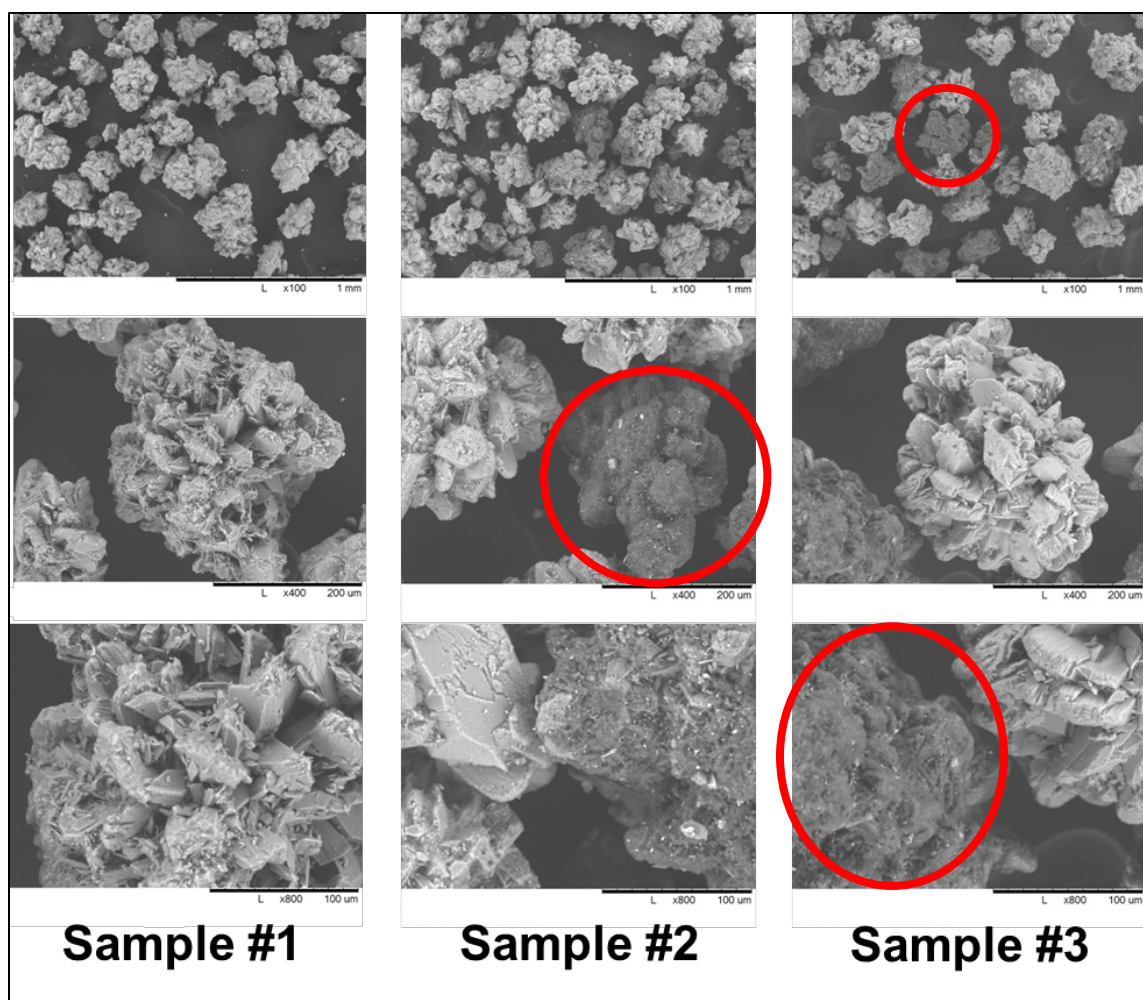
Figure 2-13: Preliminary FB experiment #2 - SEM pictures of impregnated product.
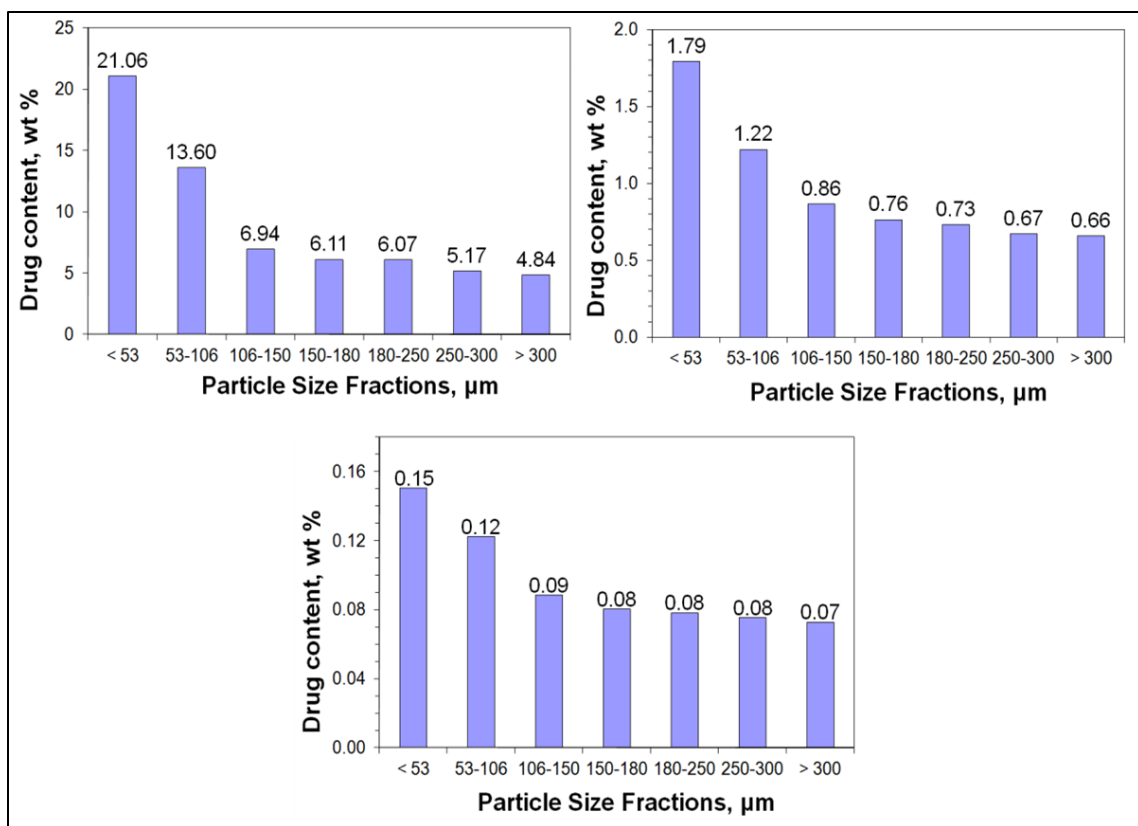
Figure 2-14: APAP loading across different size fractions for three average loadings: 8.87% (top left), 0.99 (top right) and 0.10% (bottom).
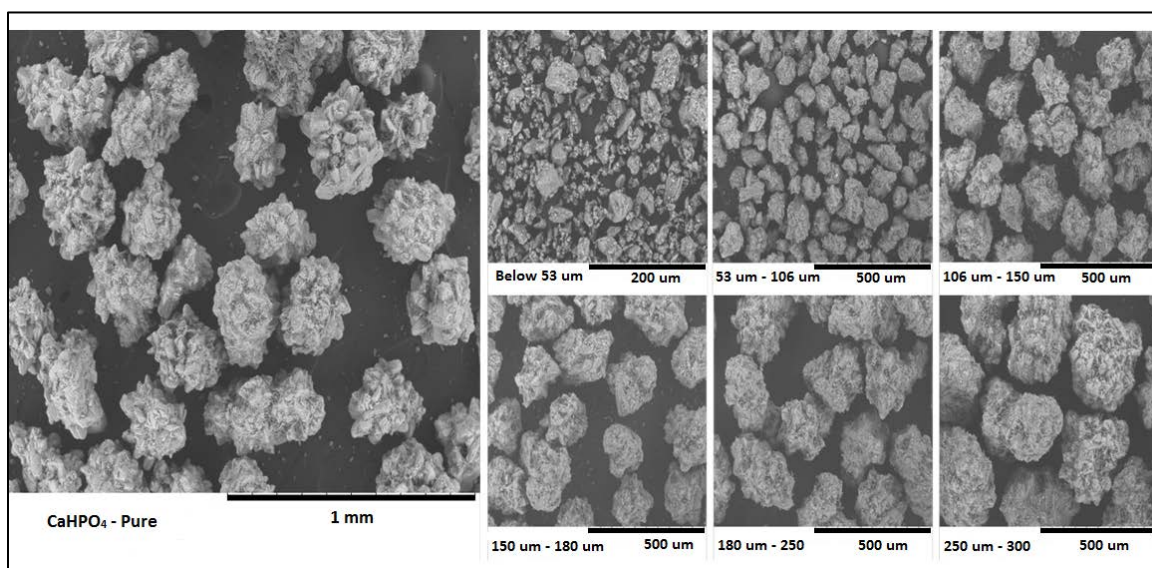
Figure 2-15: SEM pictures of pure CaHPO₄ (left) and various size fractions of impregnated CaHPO₄ (right).
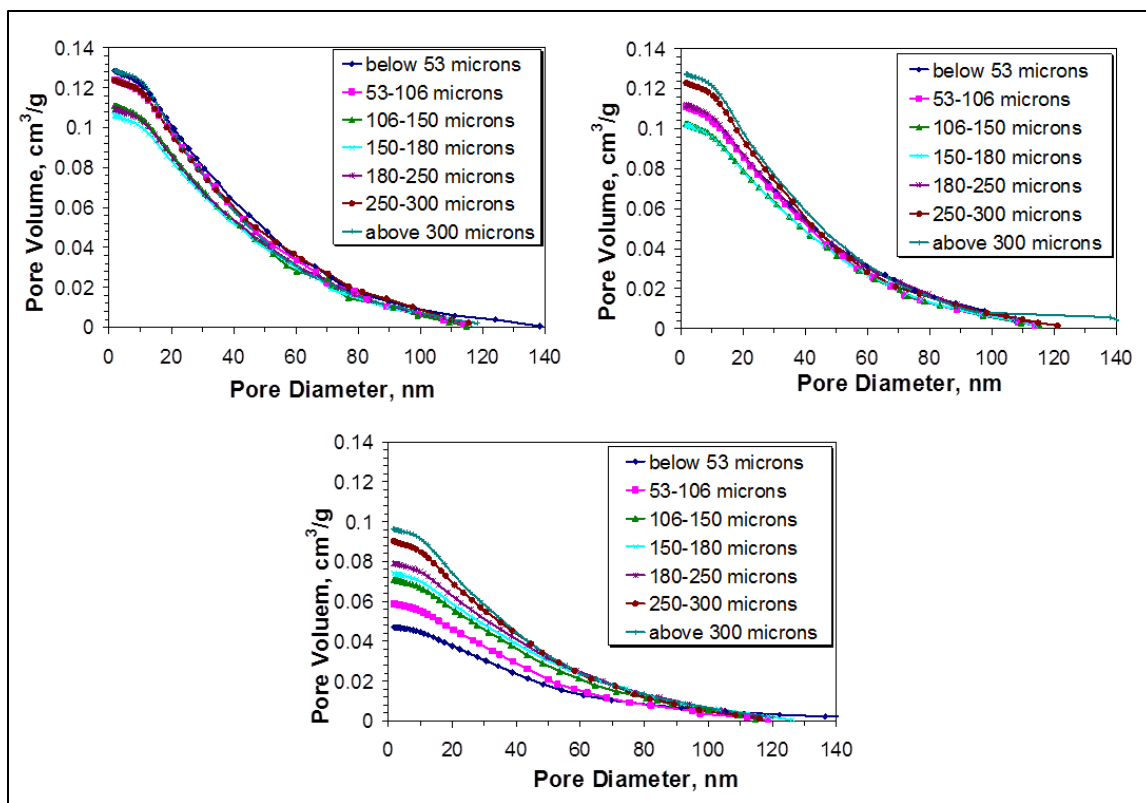
Figure 2-16: Cumulative pore size distributions (for pores with d_{pore} < 120nm) for various sieved fractions of pure (top left) and impregnated CaHPO$_4$ (top right – 0.99%, bottom – 8.87%).
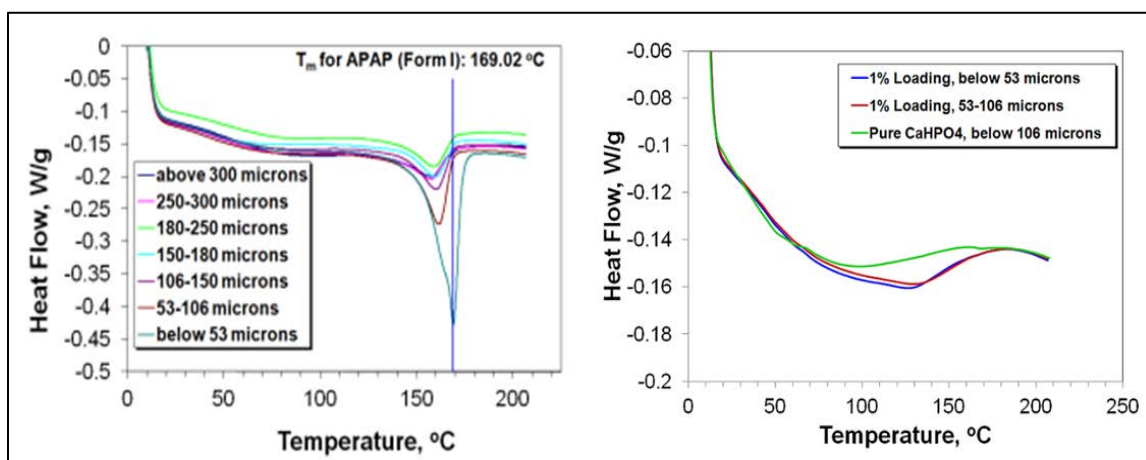
Figure 2-17: DSC test results for impregnated CaHPO$_4$ (left - 8.87% loading; right - 1% loading and pure CaHPO$_4$).
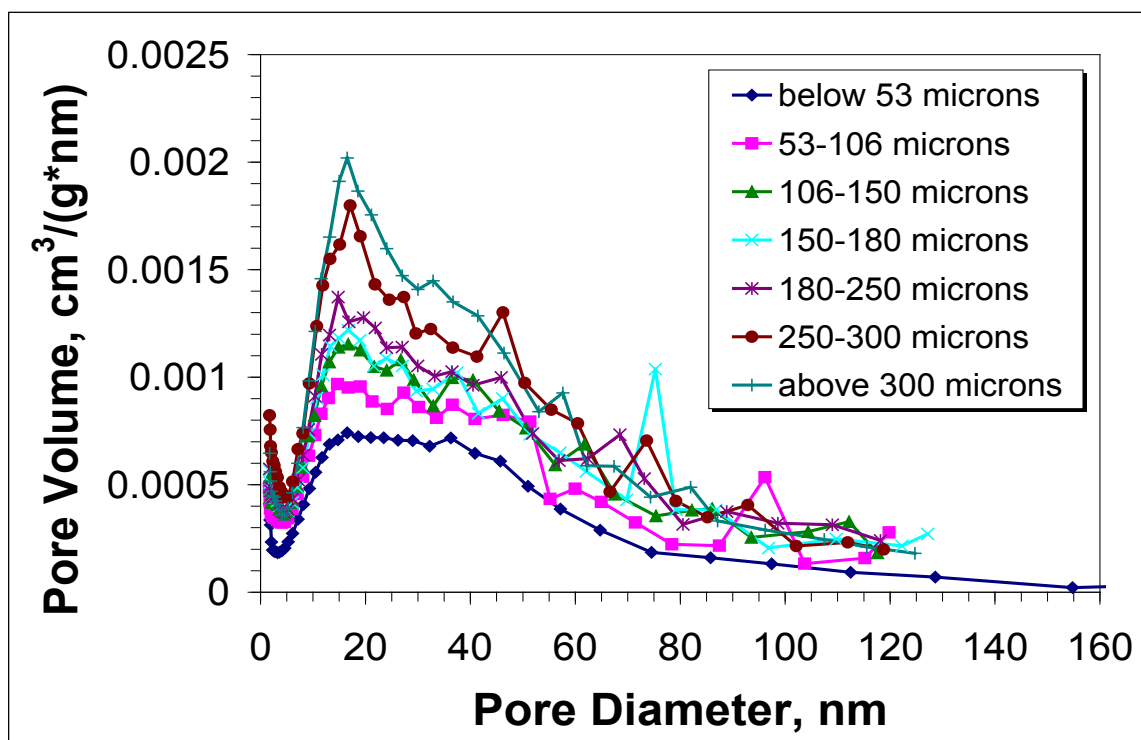
Figure 2-18: Differential pore volume distribution (for pores with $d_{pore} < 120nm$) for various size fractions of impregnated $CaHPO_4$ (8.87% loading).
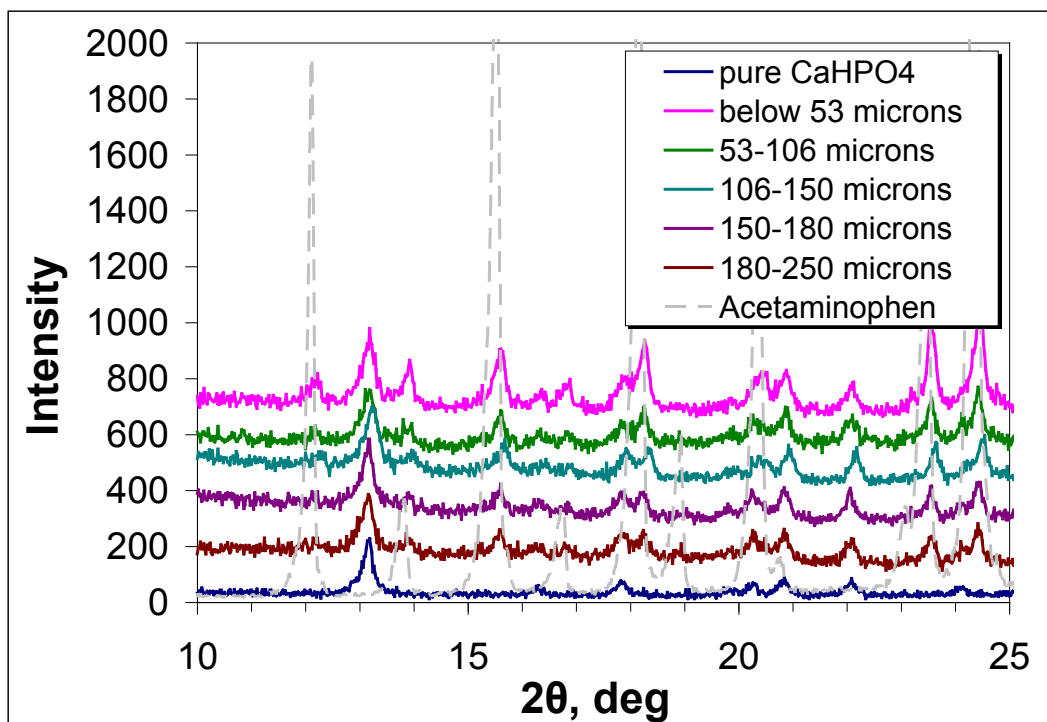
Figure 2-19: . XRD pattern comparison between pure CaHPO₄, various size fractions of impregnated CaHPO4 (8.87% loading) and pure APAP.
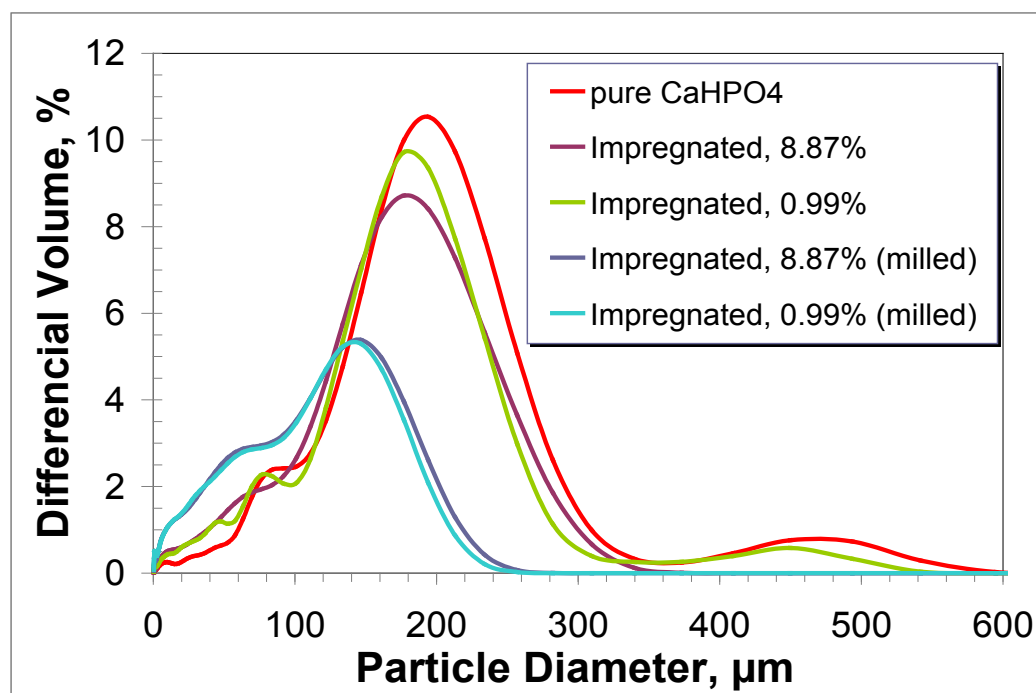
Figure 2-20: PSD measurements of pure, impregnated and impregnated & milled CaHPO$_4$.
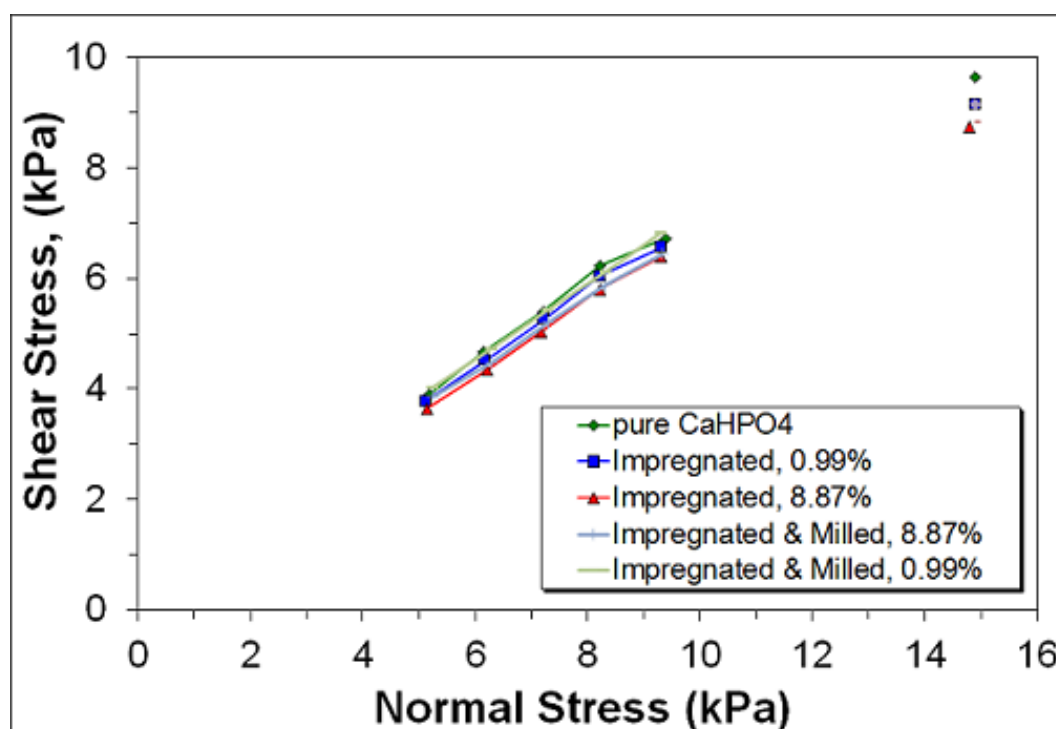
Figure 2-21: Shear cell measurements by FT4 of pure and impregnated CaHPO$_4$.
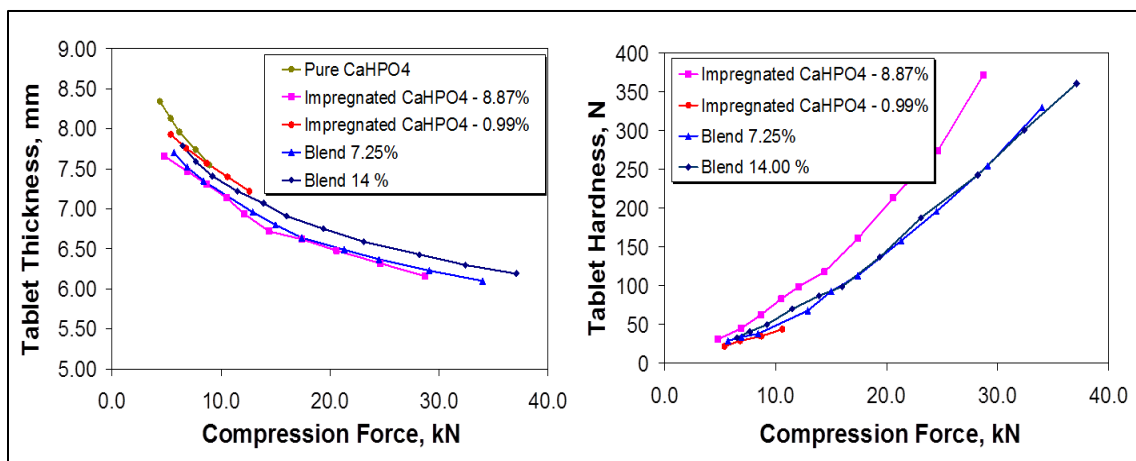
Figure 2-22: Tablet thickness vs. compression force (left) and tablet hardness vs. compression force (right) for tablets made of pure CaHPO$_4$, impregnated CaHPO$_4$ (high and low drug loading) and various blends of CaHPO$_4$ with APAP.
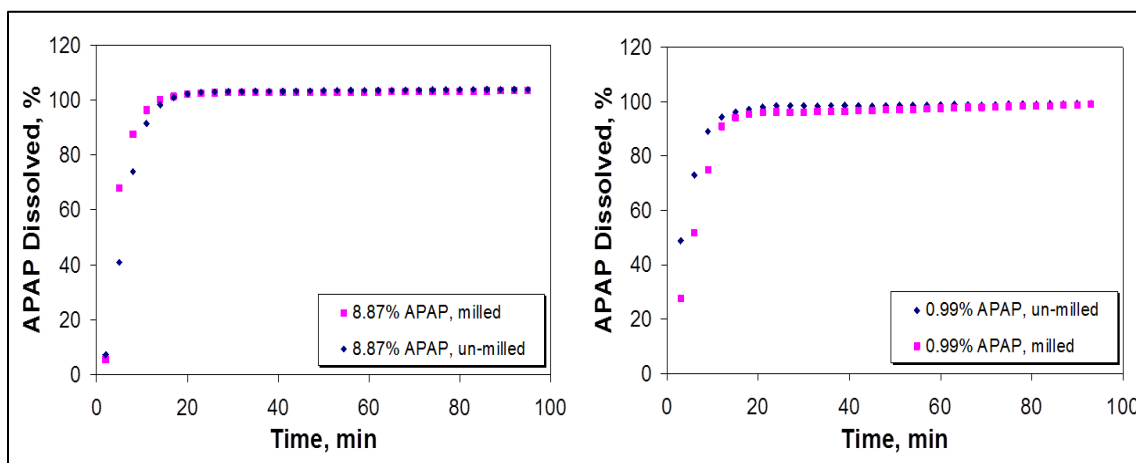
Figure 2-23: Dissolution profiles of gelatin capsules filled with impregnated CaHPO$_4$ (un-milled and milled) with APAP to 8.87% loading (left) and 0.99% loading (right) in aqueous media with pH 5.8 (phosphate buffer).
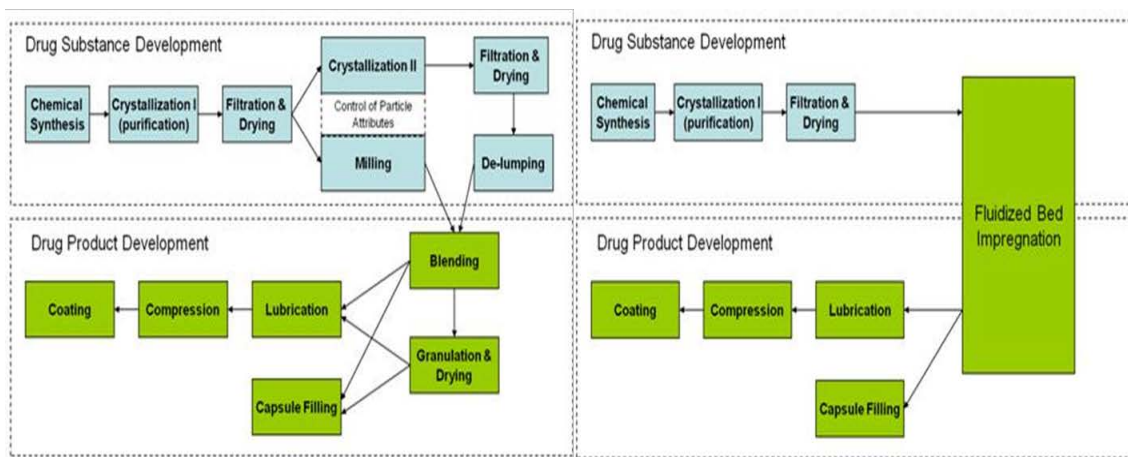
Figure 2-24: Summary of typical unit operations involved in the manufacture of solid dosage pharmaceuticals by conventional methods (left) and if fluidized bed impregnation is introduced (right).

2.8   Tables for Chapter 2

Excipient	Pros	Cons
Lactose-Fast Flow	Good Flowability Poor solubility in some solvents Narrow particle size distribution	Unstable physical form (amorphous) Low surface area (0.18 m^2/g)
Avicel^{TM} 102	Good flowability Non soluble in most solvents Stable physical form	Low surface area (0.89 m^2/g) Wide particle size distribution
CaHPO₄ (Anhydrous)	Excellent flowability Non-soluble in organic solvents Stable physical form Narrow particle size distribution High surface area (15-17 m^2/g)	None
Neusilin® (US2 grade)	Excellent flowability Non-soluble in organic solvents Narrow particle size distribution Very high surface area (300-350 m^2/g)	None

Table 2-1: Comparison of potential excipient candidates for FB impregnation

Solvent	ICH Class	Boiling Point
Methanol	Class 2 solvent	65°C
Ethanol	Class 3 solvent	78°C
Acetone	Class 3 solvent	56°C

Table 2-2: Potential solvents for FB impregnation

Process Conditions/Material Properties	
Mass of CaHPO$_4$, g	360
Porosity of CaHPO$_4$, %	68
True Density of CaHPO$_4$, g/ml	2.959
Agitator Speed, rpm	104
Chopper Speed, rpm (% of maximum=3600rpm)	360 (10)
APAP concentration in methanol, mg APAP/ml solution	92.72
Addition Rate, ml/min	5
Total Volume Added: ml	233
Drying Temperature, ^{o}C	35
Results	
Loading (theoretical), % (wt. APAP/wt. Pure CaHPO$_4$)	6.00
Loading (actual), %, (wt. APAP/wt. Pure CaHPO$_4$)	5.72
Blend Uniformity, % RSD	5.67

Table 2-3: Processing conditions used for dry impregnation in a granulator

Common Processing Parameters	Experiment #1		
Weight of CaHPO$_4$, g	3000		
APAP Concentration in Methanol, g(APAP)/g (solution)	0.155		
Inlet Gas Velocity, m/s	1.2		
Atomization Pressure, bar	2.0		
Inlet Temperature, ^{o}C	70-80		
Product Temperature, ^{o}C	35-40		
Processing Parameters/Results	**Samples**		
	#1	**#2**	**#3**
Spray Rate, (g solution)/min	4.3	4.3	13.9
Spray Time, min	70	136	180
Theoretical Loading, % w(API)/w(pure CaHPO$_4$)	1.56	3.03	6.20
Measured Loading, % w(API)/w(pure CaHPO$_4$)	1.63	3.16	6.79

Table 2-4: Preliminary FB experiment #1: Processing conditions and results.

Common Processing Parameters	Experiment #2		
Weight of CaHPO$_4$, g	3000		
APAP Concentration in Methanol, g(APAP)/g (solution)	0.1555		
Inlet Gas Velocity, m/s	0.9		
Atomization Pressure, bar	1.0		
Inlet Temperature, ^{o}C	88		
Product Temperature, ^{o}C	45-46		
Processing Parameters/Results	**Samples**		
	#1	**#2**	**#3**
Spray Rate, (g solution)/min	14.2	14.6	14.5
Spray Time, min	42	104	156
Theoretical Loading, % w(API)/w(pure CaHPO$_4$)	3.11	7.82	11.80
Measured Loading, % w(API)/w(pure CaHPO$_4$)	3.40	8.02	11.75

Table 2-5: Preliminary FB experiment #2: Process conditions and results.

Processing Parameters/Results	#1	#2	#3
Weight of CaHPO$_4$, g	3900	3900	3900
APAP Solution Concentration, mg/ml	128.15	14.40	1.44
Spray Rate, ml/min	17	17	17
Spray Time, min	160	160	160
Inlet Gas Velocity, m/s	1.3-1.5	1.3-1.5	1.3-1.5
Atomization Pressure, bar	2	2	2
Inlet Temperature, ^{o}C	85	85	85
Product Temperature, ^{o}C	43-45	43-45	43-45
Theoretical Loading, % w(API)/w(pure CaHPO$_4$)	8.94	1.00	0.1
Measured Loading, % w(API)/w(pure CaHPO$_4$)	8.87	0.99	0.1

Table 2-6: Experimental conditions, process parameters and corresponding APAP loading for three different impregnation experiments in fluidized bed.

Particle Size μm	Weight Fraction, %		
	Run #1	Run #2	Run #3
below 53	1.65	10.42	11.25
53-106	32.57	25.16	24.29
106-150	13.19	17.36	19.54
150-180	6.80	12.90	16.58
180-250	43.86	32.41	26.78
250-300	1.35	1.05	1.05
above 300	0.58	0.69	0.51

Table 2-7: Weight fraction for all particle size groups in impregnated CaHPO$_4$, runs 1, 2 and 3.

	BET Surface Area, m^2/g			Total Pore Volume, ml/g		
Particle size, μm	Pure CaHPO$_4$	Impregnated 8.87%	Impregnated 0.99%	Pure CaHPO$_4$	Impregnated 8.87%	Impregnated 0.99%
below 53	17.9961	6.3476	15.5627	0.1227	0.0449	0.1029
53-106	17.5024	8.2280	16.1061	0.1177	0.0554	0.1049
106-150	15.9307	9.8040	14.8991	0.1053	0.0657	0.0963
150-180	15.3127	10.1691	14.7922	0.0989	0.0683	0.0952
180-250	15.5947	10.8102	15.3162	0.1022	0.0742	0.1050
250-300	17.2800	13.3033	18.1248	0.1141	0.0850	0.1184
above 300	18.6128	13.5981	18.3431	0.1210	0.0909	0.1218

Table 2-8: Total surface area and total pore volume (for pores with d$_{pore}$ < 120nm) for various sieved fractions of pure and impregnated CaHPO$_4$.

APAP Loading, % (wt APAP/wt pure CaHPO$_4$)	Blend Uniformity %RSD	Capsule Total Weight Variability %RSD	Drug Content Uniformity %RSD
8.87%, un-milled	1.05	2	1.73
0.99%, un-milled	0.7	1.52	1.18
0.01%, un-milled	0.99	0.79	1.01

Table 2-9: Blend uniformity, capsule total weight variability and drug content uniformity of capsules filled with un-milled CaHPO$_4$, impregnated to different levels of APAP.

APAP Loading, % (wt APAP/wt pure CaHPO$_4$)	Blend Uniformity %RSD	Capsule Total Weight Variability %RSD	Drug Content Uniformity %RSD
8.87%, un-milled	0.54	1.19	1.65
0.99%, un-milled	0.56	1.73	1.91
0.01%, un-milled	0.42	2.25	2.79

Table 2-10: Blend uniformity, capsule total weight variability and drug content uniformity of capsules filled with milled CaHPO$_4$, impregnated to different levels of APAP.

Material	UYS, kPa	MPS, kPa	C	ffc
Pure CaHPO$_4$	1.64	26.5	0.432	16.2
Impregnated, 0.99%	1.32	25.2	0.349	19.1
Impregnated, 8.87%	0.652	24.2	0.173	37.1
Milled & Impregnated, 8.87%	1.76	24.5	0.481	13.9
Milled & Impregnated, 0.99%	1.72	24.8	0.455	14.4

Table 2-11: Mohr stress circle analysis results for shear cell measurements from Figure 2-21 showing: UYS (σc) – unconfined yield strength, MPS ($\sigma 1$) – major principle stress, C (τc) – cohesion, ffc ($\sigma 1/ \sigma c$) – critical flow factor.

Material	Bulk Density g/ml	Tapped Density g/ml	Hausner Ratio
pure CaHPO₄	0.735	0.871	1.19
Impregnated, 8.87%	1.010	1.228	1.22
Impregnated, 0.99%	0.951	1.179	1.24
Milled & Impregnated, 8.87%	0.982	1.262	1.29
Milled & Impregnated, 0.99%	0.930	1.276	1.37

Table 2-12: Bulk densities, tapped densities and Hausner ratios for pure and impregnated CaHPO₄ (milled and un-milled).

Chapter 3 .   Expanding FB impregnation to different APIs and excipients. Improving dissolution kinetics of poorly soluble APIs.

3.1   Introduction

The successful implementation of any potential large-scale method for pharmaceutical manufacturing depends on its level of applicability across various APIs. If a method is very API-specific, then its use will be limited. As suggested by the results presented in Chapter 2, the FB impregnation process should not be dependent on the nature of the API, as long as the API solution can wet the porous excipient. Establishing this claim requires more experimental studies involving other model drugs and solvents. Having a formulation process independent of the API nature could be an enormous advantage to drug product development. Many of today's solid dosage formulation methods require the implementation of a variety of "tricks" (addition of different additives/excipients, roller compaction or granulation of the powder blend) in order to deal with cohesive APIs or low drug loadings. It was also suggested in Chapter 2 that release kinetics of poorly soluble APIs could be improved if impregnation is used as the formulation method. It is a well-known fact that the dissolution rate of any solid material is proportional to the total surface area available for dissolution. In principle, if a high porosity excipient is uniformly impregnated with a drug, the total API surface area available for dissolution will be significantly increased, resulting in faster dissolution kinetics.

API solubility has a direct effect on the drug's bioavailability and therefore its efficacy. The absorption of BCS Class II and IV compounds and the resulting blood concentration-time profile depends on the rate-limiting step, which can be one of the following:

permeability limited, dissolution limited and solubility limited [71, 72]. Permeability enhancement of poorly permeable drugs is usually achieved by using absorption improving agents [73]. Improving the rate (for dissolution limited) and the extent of dissolution (for solubility limited) will directly increase the bioavailability of poorly-soluble compounds [71]. According to the Nernst-Brunner/Noyes-Whitney equation, the dissolution rate for any API is proportional to the surface area available for dissolution [74]. Since surface area is inversely proportional to the particle size, increasing the dissolution rate can be achieved through size reduction techniques (e.g. milling). Solubility of any substance is a thermodynamic property, which among other environmental factors (solvent nature, pH and temperature) depends strongly on the chemical or physical structure of the substance itself (e.g. salts, crystalline or amorphous solids, solvates, co-crystals). Many variations of these two main techniques for improving dissolution rate and increasing solubility are employed in today's development efforts for marketed drug formulations.

Depending on the approach used, all methods for particle size reduction today can be divided into two main categories, the "top-down" or "bottom–up" methods. As the name suggests, methods with the "top-down" approach start with larger particle size and use milling to reduce the size to the desired level. There are several methods in this group, depending on the final size produced, or the specific technique employed. One of the most widely used methods today for improving dissolution kinetics by size reduction is micronization, i.e. milling techniques using jet mills (dry method) or rotor-stator colloid mills (wet method) [6]. In the case of Fenofibrate for example (a poorly-soluble API), micronization with excipients in a jet mill showed to achieve more than 10-fold increase

in dissolution at 30 minutes compared to un-milled formulation [75]. While micronization typically can achieve particle size reduction between 1-5 μm, other techniques can deliver sub-micron particles. Nano-milling summarizes a group of techniques capable of delivering particles in the nanometer range (below 500nm), where the size reduction is performed in a liquid media, often in a presence of surfactants or polymers [76, 77] as stabilizers to prevent the Ostwald ripening effect [78]. There are two basic nano-milling technologies used for producing drug nanocrystals in the form of nano-suspensions: pearl/ball milling and high-pressure homogenization. Both technologies have been the base for several patents, commercial drug products (Rapamune®, Emend®) or drugs in various clinical stages [79]. Methods utilizing the "bottom up" approach produce the desired particle size during a specially designed crystallization/precipitation processes. Such processes typically involve mixing a concentrated API solution in a good solvent (S) with a known anti-solvent (AS), preferably in a high-shear environment (high-shear mixers, impinging jets, high-pressure homogenizers, etc.) resulting in enormous super-saturation and the formation of very small particles. The final size and solid form (crystalline or amorphous) usually depends on the nature of the API and the solvent/anti-solvent system, mixing intensity, the S/AS ratio and temperature. The size and form also depends on the type of additives (polymers, surfactants) used in order to stabilize the particles [7].

Altering the solid form of an API can offer significant improvement in the bioavailability of the final formulation through an increase in the true (for salts) or the apparent or kinetic solubility (for amorphous solids and co-crystals) of the drug [9, 10]. Salts of APIs are not always possible to form (if the API is neutral) and will not always lead to

solubility enhancement due to their inherent dissociation in the GI tract. Pharmaceutical co-crystals are difficult to make due to the fact that their potential existence is not always evident, therefore making their discovery a difficult task. On the contrary, amorphous solids are easier to make for most of the APIs in discovery or on the market. The increase in apparent solubility that they offer compared to their crystalline counterpart could be significant, but varies depending on the particular API [11, 12, 80]. There are various manufacturing methods for producing amorphous APIs and the following are examples of the most commonly used: spray drying, freeze drying, amorphous precipitation and hot melt extrusion. Since amorphous materials are associated with high disorder in the solid matrix, these materials are not in their thermodynamically stable state and most of them (those which possess crystalline form) tend to re-crystallize over time. Therefore, stabilization of the amorphous solid is the most important characteristic of the final drug formulation. There are numerous variations of amorphous stabilization methods, but all of them rely on creating solid dispersions and can be divided into three main categories: 1) Eutectic mixtures of a crystalline excipient and an amorphous drug; 2) Solid solutions of drug in a crystalline excipient; 3) Glass solution systems consisting of an amorphous carrier where the drug can be either molecularly dispersed or form an amorphous precipitate into the carrier [81, 82]. Amorphous stabilization in a polymer matrix is the most popular method used to date and an extensive amount of studies have been reported [82-85]. Stabilization in other small molecules (such as citric acid, sugars, urea, or nicotinamide) [86, 87] or using other drugs [88] have also been reported.

In the past decade, new techniques for improving dissolution kinetics of poorly soluble drugs using mesoporous carriers have been gaining interest [89]. Mesoporous carriers

possess very large total surface area (above 300 m^2/g) and pore sizes in the range of 2 to 50 nm. Loading these porous carriers with APIs leads to a new class of drug formulations with enhanced dissolution profiles. The improvement in dissolution is due to two main reasons: 1) the large surface area over which the drug is dispersed becomes its effective surface area for dissolution; 2) the extremely small pores in many cases prevent the API molecules from crystallization and effectively preserving the amorphous form of the drug, leading to increased solubility [88, 90]. This combination of large surface area and small pores can lead to advantages in these formulations for dissolution enhancement compared to any of those mentioned so far. There are three impregnation techniques for effectively loading drug substances into porous excipients. As mentioned already, the most common of the three is the dry impregnation method, also known as incipient wetness impregnation [21, 26, 91]. This method involves mixing of a dry porous carrier with an API solution in appropriate organic solvent and the subsequent evaporation of the solvent by drying. It is simple and easily achieved in the lab environment but its commercial implementation is not straightforward. A drawback of the method is the drug loading dependency on its solubility in the organic solvent and for low-soluble APIs, several impregnation-drying cycles must be carried to achieve high drug loading. Another technique for impregnation gaining academic attention involves super critical CO$_2$ as the impregnation media [92, 93]. Its use is advantageous since it is non-toxic and easy to remove from the final product. Drawbacks of the method include limited drug solubility in the supercritical CO$_2$ for many APIs and its relatively high capital cost for commercial scale implementation. A third technique for impregnation is the melt method [21, 23]. The drug is mixed with a porous carrier and heated above its melting point, at which

point drawn by capillary forces the API penetrates inside the porous support. The main drawbacks of this method include slow penetration within the porous matrix due to the high viscosity of molten APIs and their thermal instability in molten state.

The work presented in this chapter investigates the versatility of the FB impregnation method when other APIs and excipients are used. Using an experimental case study, the work investigates the following: 1) applicability of FB impregnation method regardless of the nature of the API; 2) influence of excipient properties on final impregnated formulation and 3) benefits of FB impregnation to poorly-soluble APIs and their formulation.

3.2   Fluidized bed impregnation using other APIs

The following investigations display the feasibility of FB impregnation with different APIs. Two sub studies are presented involving Griseofulvin and Ibuprofen as the test drugs. The analytical testing is limited, presenting only tests that reconfirm important claims about FB impregnation (proof of impregnation, blend uniformity, SEM pictures, DSC data, and dissolution data).

3.2.1   Impregnation with Griseofulvin

Fluidize bed impregnation was achieved using Griseofulvin as the model drug. The excipient used was anhydrous $CaHPO_4$. The aim of this study was to confirm that FB impregnation can achieve high blend uniformity regardless of API loading. Two impregnation runs were conducted with target drug loadings of 0.1% and 1.0%. All experimental parameters are shown in Table 3-1. Due to the limited solubility of the API in methanol, in order to achieve the 1% target loading, acetone was used as the

impregnating solvent for Run #2. Since acetone is more volatile (lower latent heat of vaporization) and has a lower boiling point than methanol (56°C vs. 66°C for methanol) the inlet gas temperature had to be reduced accordingly. This in turn resulted in lower product temperature for that run.

Impregnated product was analyzed by HPLC to determine average loading and blend uniformity of Griseofulvin (Table 3-2). The actual loading is very close to the target loading (within 6% of target). Discrepancies are mainly due to small physical loss of API and excipient during this lab scale process. This data shows that the manufacturing process is quantitative. Target loading can be easily achieved if actual loses are well characterized as a function of the equipment/scale used. Performance is expected to be improved at larger scale where these losses will be minimized.

Table 3-2 also shows blend uniformity of Griseofulvin in the impregnated product. The %RSD values for these low drug loadings are well below the industry target of 6%RSD and show once again the advantage of FB impregnation. These results re-confirm the claim that impregnation can achieve high blend uniformities regardless of the API loading. These results also confirm the ability of FB impregnation to achieve high drug uniformity independently of the API nature. In addition Table 3-2 shows blend uniformity results for milled product (pin-milled at 10,000 rpm). It is clear that mild milling of the product further increase the homogeneity, which is a confirmation of another claim made previously. It is usually very difficult to achieve such high blend homogeneities for such low loadings using conventional methods of formulation.

The product from both runs was sieved through various mesh size sieves and separated into different particle size groups. Each of these groups was analyzed to determine drug loading content and results are shown in Figure 3-1. Results confirm the expected trend – smaller particles receive higher drug loading during impregnation. Figure 3-2 shows SEM pictures of various size fractions of the impregnated $CaHPO_4$ material. No visible difference was observed when compared to pure excipient. There were no signs of API coating or particle agglomeration.

3.2.2   Impregnation with Ibuprofen

In order to further display the applicability of fluidized bed impregnation to various APIs, a study using Ibuprofen as the model drug is presented next. The impregnating solvent used is again methanol due to the high solubility of Ibuprofen in it. All processing conditions were kept the same as in the previously discussed cases (as with acetaminophen in Chapter 2) and are given in Table 3-3. Target loading was set at 10% in order to be able to perform DSC measurements and test the physical form of the API inside the carrier. As pointed out in Chapter 2, the impregnation process could lead to the formation and deposition of an amorphous API inside the excipient.

The impregnated product was analyzed by HPLC to determine average loading and homogeneity of the impregnated Ibuprofen. Blend uniformity of the milled material (pin-milled at 10,000 rpm) was also measured. All results are presented in Table 3-4. Again, there is a good agreement between the target and the actual loading. As with all presented studies so far, the small discrepancy can be attributed to some physical losses of excipient and API during impregnation (API loss to internals of vessels, excipient loss through filter element). Other factors that could be attributing to this difference are purely

analytical adjustments that have not being factored in calculating the theoretical loading. Such details include the initial moisture content of the excipient (measured between 0.92wt% to 1.05 wt%) and the purity of the API used for impregnation (usually above 99%). For simplicity during the entire study, these adjustments have not been applied.

Ibuprofen-impregnated $CaHPO_4$ was sieved and separated into seven different particle size groups. DSC analysis was run on all of these groups to determine the physical form of the API inside the carrier. The complete data set is presented in Figure 3-3. The data reveals once again the expected trend seen in the case with APAP (Figure 2-17). Endotherm peaks characteristic of melting crystalline Ibuprofen (melting point 77^oC-79^oC) [94, 95] are evident for all size groups. There is a visible shift of all peaks towards lower temperature, indicating that Ibuprofen is confined to small spaces, consistent with the Gibbs-Thompson equation (2-2). The peak broadening is also an indication of the small confinement (pores) containing Ibuprofen.

Ibuprofen is poorly water soluble drug and belongs to BSC class II drugs. Therefore, an increase in the dissolution rate of ibuprofen should increase its bioavailability. It has been suggested that impregnation could also be capable of affecting the dissolution rate of the impregnated API. Because the impregnated API is deposited in the small pores of the excipient, the effective surface area available for dissolution is significantly increased. This in turn should have an effect on the dissolution rate of the drug. Studies have shown that un-milled crystalline Ibuprofen (particle size of 10-50 microns) dissolves 80% of its original amount in about 40 minutes, when tested at 37^oC in a phosphate buffer aqueous media [94]. As part of this study, several dissolution tests were performed in order to understand the advantages (or luck of) that impregnation formulations of Ibuprofen have

to offer. Two sets of final Ibuprofen formulations were prepared: 1) gelatin capsules filled with ibuprofen impregnated $CaHPO_4$ without any other additives and 2) gelatin capsules filled with a physical blend (with the same API loading) prepared by mixing pure $CaHPO_4$ and micronized ibuprofen powder (with d_{50}=2.0 microns, d_{90}=4.5 microns, d_{98}=7.5 microns). Milled Ibuprofen was used because usually micronization is the most utilized conventional technique for improving dissolution of poorly soluble drugs. The total weight of powder contents in the capsule was on average of 420-430 mg.

The first dissolution test using the two Ibuprofen formulations was performed according to the published USP dissolution method, which is using aqueous medial buffered with potassium phosphate at pH of 7.2. The results are shown in Figure 3-4 and reveal that there is not a big difference between impregnated (80% of drug dissolved in about 9 minutes) and micronized formulation (80% of drug dissolved in about 6 minutes). These results also suggest that impregnation as a formulation method can offer a significant improvements in dissolution kinetics compared to un-milled crystalline Ibuprofen (80% of drug dissolved in about 40 minutes) [94].

Because of its chemical properties coming from its chemical structure (free acid) the solubility of Ibuprofen decreases significantly with lowering the pH of the dissolution medium [96]. This property was used to further study and understand the process of dissolution. Due to the reduced thermodynamic solubility, it is expected to observe a slowdown in dissolution kinetics of the API. The same two formulations described above were tested in an acidic aqueous media with pH of 2.0 containing 0.01N hydrochloric acid. The results are displayed in Figure 3-5 and reveal an interesting fact of the dissolution process. The micronized formulation is faster at the beginning and slows

down for the last 20% of the remaining undissolved drug. On the contrary, dissolution of the impregnated API is slower at the beginning but overall it reaches 100% dissolution faster than the micronized API. This can be explained by the physical location of the drug particles and their PSD. Micronized Ibuprofen dissolves faster at the beginning due to the initial fast dissolution of the micron and submicron particles. As they deplete, the dissolution rate is controlled by the remaining larger particles (2-10 microns), which exhibit much slower dissolution rate. Impregnated $CaHPO_4$ also contains small particles of Ibuprofen but they are located inside the excipient. Although their size is much smaller, the dissolution medium needs to reach their location within the insoluble excipient in order to dissolve the drug, which then needs to diffuse out in order to be detected in the bulk solution. This diffusion process is slower than dissolving free flowing submicron particles, but on average is faster than dissolving larger API particles.

3.2.3   Summary

The studies presented in this section helped establish the following claims regarding FB impregnation:

1. Demonstrated further expansion of the applicability of the impregnation process to other APIs.

2. Confirmed that FB impregnation is feasible with other solvents.

3. APIs with relatively low melting point (such as Ibuprofen) can be also successfully impregnated in fluidized bed.

4. Showcased once again the ability of FB impregnation process to achieve very high blend uniformity regardless of the API loading, its nature or that of the solvent used.

5. Demonstrated a potential benefit to dissolution kinetics of poorly soluble APIs.

The ability of a formulation process to improve dissolution kinetics of poorly soluble APIs has an enormous practical importance to the manufacture of pharmaceuticals. It can bring benefits to the patient (faster acting drugs) and the overall cost of the final dosage form (reduce effective loading of the API or overall manufacturing cost). This potential ability of FB impregnation process is further investigated in the next two sections.

3.3 Improving dissolution kinetics of pharmaceuticals by FB impregnation of APIs onto porous excipients

This section extends the study on fluidized bed impregnation and investigates its capabilities for improving dissolution kinetics of poorly soluble drug substances. The API under investigation is Fenofibrate, a well-known cholesterol-lowering drug discovered in 1975 and available under several marketed names, both generic and brand formulations (Fenoglide[®], Lofibra[®], Lipofen[®], Tricor[®], Triglide[®], Antara[®]) [97]. Fenofibrate is a lipophilic compound, poorly absorbed and practically insoluble in water with solubility independent of the medium pH [98]. Formulation efforts in the past two decades towards improving Fenofibrate bioavailability had led to the development of several enabled marketed formulations utilizing micronization and nano technologies. Micronization was initially the technology of choice for increasing bioavailability by reducing particle size and increasing surface area [99]. Improved formulation based on micronization technology coupled with microcoating techniques onto hydrophilic polyvinyl pyrrolidone excipient particles emerged soon after with an improved bioavailability [100]. Further improvements were made possible by introduction of the IDD-P[®] technology (insoluble drug delivery micro-particle) utilizing phospholipid agents that modify surface properties

to prevent re-aggregation, which resulted in improved bioavailability independent of food [101]. Nanotechnology pushed the bioavailability limits even further by utilizing nano-milling with spray coating of resulting nano-suspensions onto various excipients [102, 103] which led to the development of one of the most effective Fenofibrate formulation currently on the market (TriCor®) [104]. This section investigates the benefits of fluidized bed impregnation manufacturing method for making Fenofibrate formulations, which are then compared to the TriCor® tablet. The excipient used for the FB impregnation study is Neusilin®, a synthetic amorphous form of magnesium alumino-metasilicate. Neusilin® comes in many grades (powder vs. granules, neutral vs. alkaline with various bulk densities and water content) and in general exhibits very high surface area and excellent flow properties [56]. These properties make this excipient an excellent choice for fluidized bed impregnation and a great candidate for dissolution improvement of poorly soluble substances. The advantage of using Neusilin® is showcased by comparing dissolution kinetics of impregnated formulations prepared from Neusilin® and anhydrous calcium phosphate used previously. The chapter end with comparison of dissolution kinetics between the FB impregnation formulation and the 48mg TriCor® tablet.

3.3.1   Materials and methods

Several impregnation experiments involving Fenofibrate, Neusilin® and $CaHPO_4$ are presented in this study. The aim of these studies was to achieve several different Fenofibrate loadings within the excipient, ranging from 1 wt% to 40 wt% loading (defined as wt API/wt pure excipient). All of these experiments were executed following the already established procedure in Chapter 2. In order to ensure impregnation,

appropriate process conditions needs to be selected. Choosing suitable process conditions could be achieved empirically, by performing a pure solvent run. The procedure for empirical determination of process conditions consists of three main steps: 1) a mild drying temperature is chosen by setting the inlet gas temperature to 10-20°C higher than the boiling point of the solvent used; 2) spray rate is chosen such that it does not affect the fluidization of the powder; 3) ensure that product fluidization remains constant (without FB flooding) during a steady-state operation of at least 30-60 min. If FB flooding is observed (fluidization stops due to wet powder), the spray rate and/or drying temperature should be re-adjusted. It should be noted again the importance of the location of the spray nozzle during impregnation. Its position should be such that when the excipient is fully fluidized, the tip of the nozzle is immersed inside the powder bed. This further diminishes the chance for spray drying to occur by reducing the droplet's flight time between the nozzle and excipient particles. Details on the experiments in terms of amounts of Fenofibrate and excipient, concentration of API solution, spray time and processing parameters, such as inlet and product temperatures, are given in Table 3-5.

Impregnation experiments with low Fenofibrate loadings were manufactured using the Glatt GPCG 1 fluidized bed dryer at a larger scale (runs 1 and 2). All other impregnations were carried out in the Mini-Glatt fluidized bed dryer (runs 3 through 7). In all experiments, the inlet temperature was kept constant at 80°C. For runs 1 and 2, the spray time and spray rate were kept constant, while for experiments 3 through 7 the concentration and spray rate were kept constant. Spraying pure solvent after the Fenofibrate solution is an important part of the impregnation procedure, as it allows for any amounts of deposited Fenofibrate on the surface of the particles to be re-dissolved

and deposited within the excipient. At the end of each experiment, the impregnated material was dried until the product temperature reached 50 ^{o}C, after which the heat was turned off and contents of the fluidized bed were cooled down to room temperature. Milling of the impregnated Neusilin® powders was performed on a 2" lab scale pin mill. The material was fed to the mill using a vibratory feeder. The feed rate used was around 3 g/min. The mill speed used was 10,000 rpm and 20,000 rpm. Characterization of all impregnated powders was done in a similar fashion as described already in Chapter 2.

3.3.2   Results and discussion

3.3.2.1   *Average loading and blend uniformity*

Table 3-6 summarizes all impregnation experiments presented in this study in terms of excipient used, target/actual API loadings, blend uniformity and equipment used. The first two impregnation experiments were larger scale, using the Glatt GPCG 1 fluidized bed dryer, while the rest were at smaller scale, using the MiniGlatt unit. The target loading was achieved for all runs, regardless of the level and scale. The small discrepancies between actual and target loading can be attributed to any of the following: variations in solution preparation, analysis or material weighing; small product loss of fines through the FB filter element; loss in charge lines or solution vessels. One of the main benefits of impregnation, established in Chapter 2, is the ability to achieve very high blend uniformity of the final drug product, regardless of the API loading. The results in Table 3-6 once more demonstrate this inherent capability of the FB impregnation manufacturing method. All impregnation runs display very high blend uniformity as indicated by the % RSD (relative standard deviation), which in all cases is way lower than the FDA limit of 6% RSD. These results reinforce the claim previously made, that

FB impregnation achieves high blend uniformity regardless of the % loading and nature of the API. It should only depend on the nature of the excipient used, as it can be seen from the data between $CaHPO_4$ and Neusilin® (runs 1 and 2). The difference there could be attributed to the difference in powder fluidization and potentially mixing patterns, due to the differences in the excipients' bulk density and particle size. Nevertheless, achieving below 1.5% RSD for a drug product containing 1% of API in one processing step is usually a difficult proposition.

SEM pictures of pure and impregnated Neusilin® at 30% Fenofibrate loading are presented in Figure 3-6. Comparison of the pictures reveals the unchanged physical appearance of the Neusilin® particles upon impregnation. SEM picture for other loadings (not shown), provide the same conclusion. The images do not show the presence of particle agglomeration. Close examination of the particle surface also confirms that particle coating with API is not occurring during processing. The third undesired outcome, spray drying, is easily ruled out by comparing the PSDs between pure and impregnated Neusilin®. In the discussion to follow it will be shown that the particle size of Neusilin® remains practically constant during impregnation, with the small exception of the disappearance of a little hump around 400μm, which could be explained by the breakage of a few large agglomerates of pure Neusilin® particles during fluidization (see Figure 3-11 for PSD). If Fenofibrate was indeed spray dried within the excipient particles, this should have produced a bi-modal distribution with a secondary peak around 20μm (or less), which is the usual average size of spray dried particles. All of the above observations are consistent with the impregnation of Fenofibrate into Neusilin®.

3.3.2.2 Physical state of the drug molecules inside the carrier

Figure 3-7 and Figure 3-8 are intended to display the changes that are taking place inside the porous excipient during the impregnation process. Figure 3-7 shows the specific surface area (SSA), defined as total surface area per unit mass of excipient, as it changes with increasing the drug loading inside the carrier. Pure Neusilin[®] has a SSA of more than 350m^2/g, which is one of the main properties that make this excipient an excellent choice for impregnation. As expected, the SSA decreases as Fenofibrate loading is increased, due to filling of the internal pores of Neusilin[®]. The total pore volume in the particles also decreases proportionally to the drug loading. Simple extrapolation of the trends reveals that even higher loadings than the one present should be easily achievable. For example, Neusilin[®]-Fenofibrate formulations with 50%-60% drug loadings should be possible, still possessing residual high internal surface area (50-100 m^2/g). This residual high SSA is one of the important factors for the improvement in dissolution kinetics that impregnation of API in Neusilin[®] has to offer, as will be discussed later in the text. Figure 3-8 shows how the internal pore structure changes during impregnation. The predominant pore sizes in Neusilin[®] are those in the range of 0-20 nm. These pores are the ones filled during the impregnation process, proportionally with the actual drug loading (given in Table 3-6). Extrapolation of the total pore data can be performed to show that if the entire structure of Neusilin[®] is to be impregnated with Fenofibrate, the resulting API loading could reach about 85-90%.

In order to investigate the physical state of impregnated Fenofibrate inside Neusilin[®] particles, each of the impregnated samples were tested using differential scanning calorimetry (DSC). This analytical technique is capable of detecting thermal effects upon

sample heating/cooling, due to (but not limited to) the following: melting, re-crystallization, drying, glass transition, chemical reactions, etc. Based on the shape of the DSC signal it is possible to distinguish different polymorph crystal forms or between crystalline and amorphous materials. For example, the DSC curve of a pure crystalline Fenofibrate is expected to have an endotherm around its melting point. As Figure 3-9A suggests, the melting of pure Fenofibrate is $81.62^{\circ}C$. On the contrary, a straight DSC curve indicates the absence of thermal effects, which suggests that no physical transformation is taking place. Figure 3-9B-C shows DSC scans for impregnated Neusilin[®] with Fenofibrate loadings between 10-40%. The DSC scans for the 30% and 40% case (Figure 3-9C) show a similar to the pure Fenofibrate endotherm, which indicates a melting of the impregnated API. There is a small trend of decreasing the melting point of Fenofibrate from $81.62^{\circ}C$ (pure) to $78.92^{\circ}C$ (40% loading) to $78.56^{\circ}C$ (30% loading). As described in *Aim 1*, this is due to the well-known phenomenon of confinement-induced melting point depression. The new melting point can be estimated using the Gibbs-Thompson equation [68] (see Eq. 1) and it depends mainly on the confinement's pore size (for the same API and excipient). In both cases the melting points are very close to that of pure Fenofibrate, indicating that that the drug is in crystalline form. The decreasing trend in melting points as a function of API loading is most likely associated with the pore size distribution of the filled pores: the higher the loading the higher number of pores being impregnated with API, hence the broader the pore size distribution of the filled pores. Since the peak intensity is expected to be proportional to the amount of API in the testing DCS pan, it is expected to have weaker DSC peaks with lower API loadings, as it is indeed the case for 30% loadings. The DSC

scans for the 10% and 20% loadings (Figure 3-9B) show an almost straight line, although close examination reveals an offset starting at about 45°C. This indicates that there is still a thermal event (albeit very small) taking place, most likely due to melting. The reason why there is no visible endothermic peak could be attributed to the limit of detection associated with the DSC analytical technique. In the cases with low loading (< 20%), due to the very low bulk density of Neusilin$^®$, the sample size tested in each case is between 10-15mg of impregnated powder. This means that the actual amount of Fenofibrate available for the test is below 2.5mg, which is at the equipment's limits to produce a visible peak when tested with an inert material such as Neusilin$^®$. In addition, because the API exists as nanocrystals, the majority of which are formed in very small pores (in the range of 0-20nm, Figure 3-8) of the excipient, the enthalpy of fusion is further reduced [105, 106].

Much more interesting is the case of Neusilin$^®$ impregnated with 40% Fenofibrate and co-impregnated with 1% sodium lauryl sulfate (SLS). Figure 3-9D shows the DSC curve for this case, which is a straight line with no visible thermal effects. The limit of detection is clearly not the reason for the missing peaks, since it was already shown that the 40% Fenofibrate loading can be easily detected by the instrument. The absence of API is also ruled out since it was shown already that the loading was confirmed by an HPLC analysis. The only logical explanation for the DSC curve is that the whole amount of impregnated Fenofibrate is in an amorphous state. All amorphous materials are characterized with a higher energy state due to the molecular disorder and lack of a defined melting point. As the API solution is sprayed onto the excipient during impregnation, the concentration of Fenofibrate gradually increases due to the continuous

drying and at some point the solution becomes super-saturated. We hypothesize that this initiates a spontaneous nucleation causing the formation of crystalline Fenofibrate inside the pores of the excipient. These crystals continue to grow as impregnation progresses. In the presence of SLS, due to intermolecular bonding between Fenofibrate and the surfactant, the spontaneous nucleation is hindered, resulting in the precipitation of an amorphous API. The prevention of this spontaneous nucleation is further aided by the very small pore size of the impregnated excipient. It is interesting to note that the addition of SLS leads to a decrease in the pore volume distribution – compare the 40% target loading with and without 1% SLS in Figure 3-8. This behavior can be explained by the solid form change of the API. The higher degree of disorder, characteristic of amorphous materials, results in larger specific volume compared to the crystalline state. This larger specific volume causes more internal pores to be filled with the same amount of API when SLS is introduced, therefore generating the behavior seen in Figure 3-8. Amorphous materials are generally not stable and tend to crystallize out by releasing the extra energy associated with the transition to lower energy level. Figure 3-9D also shows the DSC scan for the same impregnated material (40% Fenofibrate, 1% SLS) taken about 1.5 years after the impregnation. The absence of any thermal events (or peaks) and nearly identical curves (on top of each other) indicate that the amorphous state of Fenofibrate is preserved successfully in the small Neusilin® pores over this long period of time. The amorphous state of the API due to the addition of SLS is also confirmed by the XRD data presented in Figure 3-10, where pure Neusilin®, pure Fenofibrate and impregnated Neusilin® at 40% loadings with and without SLS are compared. The XRD scans clearly show the disappearance of all peaks characteristic of crystalline Fenofibrate when SLS is

introduced, confirming the amorphous state of the impregnated API. The ability to impregnate Neusilin® with amorphous Fenofibrate has significant effect on the solubility and dissolution kinetics of the final drug product and will be discussed later in this paper. The ability to stabilize the amorphous form of the API in the impregnated excipient makes FB impregnation very attractive for drug product development, as this is the main challenge in today's amorphous drug formulations.

3.3.2.3   Overall physical properties of the impregnated excipient

One of the main advantages of FB impregnation that have been establish already in *Aim 1* was its ability to produce a drug formulation blend, which is almost indistinguishable in terms of its bulk physical properties from the pure excipient used in the formulation. One of the most important bulk physical properties of the formulated powder includes its particle size distribution (PSD) and flow properties. Figure 3-11 displays the PSD of pure and impregnated Neusilin® at various Fenofibrate loadings. It is evident from the data that the size of the excipient particles remains almost unchanged during the impregnation process regardless of the impregnation level. This is expected since the API is deposited inside the carrier particles and an increase in size is not expected. Also, powder fluidization generally is a process exerting very low shear on the processed material and unless the excipient is very brittle, decrease in particle size is not observed.

Flow properties of pharmaceutical blends are an important factor affecting their formulation into final products (capsules or tablets). One of the main advantages of excipient impregnation with APIs is the ability to preserve the original flow properties of the pure excipient. In an attempt to compare flow properties and determine the degree of change during processing, shear cell measurements were carried out on several

impregnated Neusilin® formulations (un-milled and milled) and compared to pure Neusilin®. The value of cohesion (τc) was taken to be the intercept of the linearized yield locus with the shear stress (vertical axis). Changes in flow properties can be assessed by comparing the results for cohesion. In general, the smaller the cohesion, the better powders flow [70].

Figure 3-12 (yield locus) shows shear cell testing results of shear stress (τ) vs. normal stress (σ) for pure and impregnated Neusilin® (30% loading) for both un-milled and pin-milled at 10,000 and 20,000 rpm. The results clearly indicate that impregnation has very little effect on the flow behavior of the excipient, as the yield locus for both impregnated and pure Neusilin® are almost identical. In fact, the critical flow factor (ffc) for both impregnated and pure Neusilin® could not be calculated (using Mohr stress circle analysis), indicating excellent flow properties. This once again confirms previous statement that impregnation preserves flow behavior independent of drug loading. As expected, upon milling the powders become more cohesive, which worsens with increasing the mill speed. For comparison, measured cohesion values increase from $\tau c = 0.25 \text{kPa}$ for pure Neusilin® to $\tau c = 1.28$ kPa for impregnated Neusilin® milled at 10,000rpm (30% API loading) and to $\tau c = 1.45$ kPa for impregnated Neusilin® milled at 20,000rpm (30% API loading). The primary reason for this increase in cohesion is the reduction in particle size. In addition, the creation of new surface during milling could result in the exposure of the impregnated API, increasing the surface interactions and leading to more cohesive behavior. Mohr stress circle analysis (not shown) was employed to calculate the values of major principal stress ($\sigma 1$) and unconfined yield strength (σc) from which the critical flow factor ($ffc = \sigma 1 / \sigma c$) was then calculated. For comparison,

calculated ffc values for impregnated Neusilin[®] milled at 10,000rpm (30% API loading) and impregnated Neusilin[®] and milled at 20,000rpm (30% API loading) were 5.47 and 4.64 respectively, which indicates that both powders are characterized as "easy flowing" (4<ffc<10) [107].

3.3.2.4   *Dissolution profiles*

It is of interest to examine the dissolution kinetics that could be realized by utilizing API impregnation as a formulation process. Neusilin[®] was chosen as the carrier for impregnation here due to its very large SSA. To prove the relationship between large SSA and dissolution kinetics of the poorly soluble API of choice (Fenofibrate), the dissolution profiles of impregnated Neusilin[®] and $CaHPO_4$ were compared. Figure 3-13A shows that impregnated Neusilin[®] due to its large SSA (356 m^2/g) exhibits faster dissolution by achieving 80% dissolved API at about 3 minutes vs. 26 minutes for impregnated $CaHPO_4$ (SSA of 15 m^2/g). It should be noted that impregnation of Fenofibrate onto $CaHPO_4$ still offers dissolution improvements over typical physical mixture (blend of API and excipient), where the 80% dissolution mark is achieved in about 50 minutes (Figure 3-14). Since the dissolution tests presented in Figure 3-13A were only powder tests, a comparison study was performed to determine effect of capsule filling on API release. Figure 3-13B shows that filling of impregnated powders in capsules (size 0) results in a decrease of dissolution kinetics. For Neusilin[®], the powder test shows 4 minutes release for 80% of the API, while the capsule tests shows 8 minutes. For $CaHPO_4$, the powder test shows 24 minutes release for 80% of the API, while the capsule tests shows 39 minutes. The decrease is less pronounced for Neusilin[®], establishing enhanced dissolution kinetics over $CaHPO_4$.

Figure 3-14 shows comparison of dissolution profiles (powder test) of impregnated Neusilin® at various loadings and that of a physical blend. All impregnated powders with loading less than 40% exhibit faster drug release than the blended formulation. As the impregnated API loading is increased inside the carrier, the release kinetics is decreased. At 10% loading, 80% of the API is released in about 5 minutes, while at 40% loading the same amount of API is released in almost 50 minutes, approaching the behavior of the physical blend. This is to be expected and can be explained by the higher degree of pore saturation achieved as the API loading is increased. As it was shown already in Figure 3-7, the SSA of impregnated Neusilin® decreases with drug loading, ultimately affecting the release profile. Despite the fact that the impregnated API is distributed over a large internal surface area (even for 40% loading the SSA remaining is still very high, about $160m^2/g$), the drug release is governed by diffusion through the pores on the external surface of the carrier particles (which are insoluble in the dissolution media). If the excipient was also soluble in the dissolution media, it should be expected that the release kinetics will be larger than observed here (for the same SSA) and less dependent on drug loading.

It has been established already (Aim 1) the benefit that milling of impregnated powders has on the content uniformity of the final formulation. In this study we continue to investigate the effect of milling, but this time the focus is on its influence on the dissolution kinetics. Figure 3-15 displays release kinetics of Fenofibrate from impregnated Neusilin® which was pin-milled at 10,000rpm and 20,000rpm. Several conclusions can be drown from those results. Comparing milled (10,000rpm) Neusilin® (30% and 40% loadings) to un-milled at the same loadings (Figure 3-14) the clear

advantage of size reduction is evident. Drug release is increased from 18 minutes and 48 minutes for un-milled to 3 minutes and 9 minutes for milled Neusilin® (30% and 40% loadings respectively). By reducing the size of impregnated Neusilin® particles the release is increased due to shortening the overall path for drug diffusion. This theory is further supported by comparing release kinetics of impregnated Neusilin® (30% loading) milled at two different speeds. As expected, more intense milling results in faster release due to the smaller particle size of the formulation. Figure 3-16 shows the corresponding PSD of all milled powders, confirming the smaller average particle size for Neusilin® milled at 20,000 rpm. Figure 3-15 also supports the already established relationship between loading and release, as the loading increases, the release time increases.

A tableting study using impregnated Neusilin® was performed to understand the effect of tablet compression on dissolution profile. Figure 3-17 presents dissolution kinetics of tablets with various tensile strength and shape made from 20% impregnated Neusilin® (un-milled). Three conclusions can be made from comparison of all data. The first is that tableting increases drug release time from the formulation. For tablets with 0.27 MPa tensile strength, the release time for 80% drug was slightly above 12 minutes. The second conclusion is that release time is greatly affected by the compression force. For the same type of tablets, release times (for 80% drug) of 12, 21 and 63 minutes were observed at 0.27MPa, 0.50MPa and 2.34MPa tensile strength respectively. The third conclusion is that for the same tensile strength, larger tablets show slightly slower dissolution. A 0.27MPa tensile strength tablet of 270mg shows 12 minutes release of 80% of its API vs. 17 minutes for a 560mg tablet. It should be noted again that all tablet formulations contained 4% croscarmelose sodium as disintegrant. These effects on dissolution kinetics

are most likely due to the pore closure of the impregnated excipient due to the applied compression force during tableting. Because of the unfavorable effect on drug release, tableting of impregnated Neusilin® was not deemed favorable and hence was abandoned. This effect should be less pronounced (or could be entirely eliminated) if the excipient was also soluble in the dissolution media. In the case of extended release formulations, the above properties of impregnated and tableted excipients could be highly advantageous.

In an attempt to produce a feasible formulation of Fenofibrate using impregnated Neusilin® capable of delivering at least 48mg of drug (which is comparable to one of the current marketed formulations, TriCor® 48mg), impregnated Neusilin® at 30% loading and milled at 10,000rpm was filled in size 0 capsules. The reason 20,000rpm was not used despite its better release profile was due to its reduced flowability, however that does not exclude its application. Figure 3-18 shows dissolution profiles of these capsule formulations, with and without croscarmellose sodium as disintegrant. The corresponding release times for 80% API are 11 and 12 minutes respectively (three of which are due to capsule dissolution), suggesting that adding disintegrant has a small benefit. Due to the low bulk density of Neusilin®, the amount of impregnated powder at 30% loading that could be filled in size 0 capsules was not enough to give the desired 48mg of Fenofibrate. In order to achieve this goal, a 40% loaded Neusilin® was filled into size 0 capsules and its dissolution kinetics tested. Figure 3-18 shows that its drug release profile was slowed from 10 minutes to 20 minutes for 80% drug released. This behavior is expected based on earlier discussions where the relationship of release time and impregnation loading was established.

All dissolution data presented so far suggests that solute diffusion from the internal pores of the impregnated excipient is the rate-limiting step in the overall drug release process. In order to speed-up drug release, one would need to find ways to speed-up diffusion from the Neusilin® pores. Because of the hydrophobic nature of Fenofibrate (as it is the case with most poorly soluble drugs), dissolution from the impregnated pores is further reduced. It was assumed that if the wettability of the pores was improved somehow, that would result in an increase of the release profile. A common method for increasing wettability in conventional formulation is the addition of SLS (up to 1% by wt). As stated previously, one of the potential benefits of FB impregnation is its ability for co-impregnation of any additive (provided the additive has similar solubility in the solvent used) with the API into the excipient of interest. In an effort to improve drug release and demonstrate the feasibility of co-impregnation, Fenofibrate (at 40% loading) was co-impregnated with 1% SLS into Neusilin®. Figure 3-19 shows the dissolution profile of that formulation, compared to impregnated Neusilin® without SLS. The improvement in dissolution kinetics is significant, from 50 minutes for 80% released API the release time was reduced to 20 minutes. Further milling of the co-impregnated SLS formulation further improves the dissolution profile. Comparing milled impregnated formulations with and without SLS shows an improvement from above 9 minutes (no SLS) to less than 4 minutes when SLS is co-impregnated (Figure 3-19). This significant improvement in release kinetics, which initially was linked to the improved wettability of the impregnated pores, was in fact due to the change in physical state of the impregnated Fenofibrate. As already discussed and shown in Figure 3-9, the physical state of Fenofibrate is changed from crystalline to amorphous when co-impregnated with SLS in the small pores of

Neusilin®. The improvement in dissolution kinetics is mainly due to the amorphous state of Fenofibrate. Filling this SLS-containing formulation into capsules increases release time as expected. Figure 3-20 shows dissolution profile comparison of two capsule formulations, either meeting or exceeding the 48mg Fenofibrate dose target of the best marketed formulation. Co-impregnation of 1% SLS into the formulation reduces the release time of Fenofibrate from about 20 minutes to about 11 minutes, 3 minutes of which are due to capsule dissolution. Co-impregnation of Fenofibrate with SLS results in almost 100% improvement in release time making this formulation commercially viable.

In order to understand how the impregnation formulation relates to current marketed formulations, a comparison study was performed using TriCor® 48mg Fenofibrate tablets as the baseline. Figure 3-21 shows that TriCor® tablets exhibit very rapid release after tablet disintegration, resulting in a release time of 8 minutes for 80% of the drug. The Neusilin® co-impregnated Fenofibrate-SLS formulation results in a release time of 10 or 11 minutes depending on which size capsules have been used. Due to the larger size of 00 capsules and smaller degree of powder compaction in them, these capsules achieve 1 minute faster release time compared to size 0 capsules. The FB formulation shows on average 2-3 minutes slower release time compared to the marketed TriCor® tablets. It should be noted that those 2-3 minutes are due to the initial capsule dissolution, characteristic for all capsule formulation. The rate of release for both types of formulation is almost identical.

Several other attempts to impregnate Fenofibrate into porous carriers using different methods have been reported in the literature. In one of them [108], the authors report a method for impregnating Fenofibrate into mesoporous silica via a co-spray drying

method and solvent impregnation. The co-spray drying method consists of spray drying a slurry made by mixing the excipient carrier in ethanol solution of Fenofibrate. Upon spray drying the Fenofibrate dries and deposits inside the carrier. The solvent impregnation method consists of drying the above slurry on a hot plate instead of spray drying it. The resulting powders were filled into size 0 capsules and dissolution tests were performed in similar conditions as those presented in this paper, however omitting the initial time for capsule dissolution. The fastest release time they have reported was about 10 min for 80% of drug released for their co-spray dried formulation, noting that this time is after capsule dissolution. The release time of the FB formulation, excluding the initial capsule dissolution time, is 7 min for 80% drug, which is 30% better than what they have reported.

In another paper [109] the authors report impregnation of Fenofibrate into Neusilin[®] via three different methods: supercritical carbon dioxide methods, solvent evaporation methods and hot-melt impregnation methods. The first one involves super critical CO_2 as the impregnation media, which at the end of the process is vented out. The second method is similar to the process presented in [108] with the small difference of using a rotary evaporator as the drying equipment. The third method, as the name suggests, involves impregnating melted Fenofibrate into Neusilin[®] by mixing the two powders and heating the mixture above the melting point of the API. Dissolution of all formulations was tested in a powder form (no filling of capsules or tableting) under similar conditions to methods used in this study. The fastest release time that was reported is 5 minutes for an impregnated powder via the super critical CO_2 method (80% API release). In comparison, the release time for 80% of API from the 40% Fenofibrate formulation that

was co-impregnated with 1% SLS and pin-milled, is less than 4 minutes, which is 20% faster.

3.4   Conclusions

The study presented in this chapter demonstrated another application of the FB impregnation method for pharmaceutical solid dosage formulation. The API chosen for the investigational work was Fenofibrate and the porous carrier was Neusilin®. The study expanded on the applicability of the FB impregnation method and demonstrated its feasibility with other APIs and excipients. More specifically, it demonstrated the benefits of fluidized bed impregnation in increasing dissolution kinetics of poorly soluble drugs. It was shown that the specific surface area of the excipient has a direct influence on the dissolution profile of the final formulation. Impregnating Fenofibrate into Neusilin® up to 30% loading led to a significant improvement in release time compared to physical blends. Furthermore, it established the effect of milling on the dissolution profile of impregnated powders. Milling of impregnated Neusilin®, regardless of Fenofibrate loading, greatly improved release kinetics of the API. The study also demonstrated the feasibility of co-impregnation of APIs with other additives simultaneously onto the porous carrier. In particular, the feasibility of co-impregnation of Fenofibrate with 1% SLS, an additive surfactant commonly used to increase wettability of the formulation, was shown. Co-impregnation of SLS with Fenofibrate into the small pores of Neusilin® causes the drug to be deposited in its amorphous state, which was shown to be stable for at least a year and a half. This stabilization of the amorphous form of the API significantly increased its release time and made it possible to manufacture a capsule

formulation of Fenofibrate, comparable in its release profile to one of the current marketed formulations, TriCor® tablets (48mg Fenofibrate).

The work presented further strengthens the novelty of fluidized bed impregnation and its benefits as a manufacturing method for pharmaceutical solid dosage forms, which can be summarized as follows:

- FB impregnation is a fast, easy to implement, one-step process that is able to deliver final pharmaceutical material ready for formulation into capsules or tablets.

- It has the ability to deliver a final formulation with high blend uniformity independent of the API loading.

- Milling of impregnated material further improves blend uniformity and dissolution kinetics.

- The physical state of impregnated API inside the porous excipient can be tailored to be either crystalline or amorphous.

- The final properties of the impregnated materials (e.g. flow properties, dissolution kinetics) are governed almost exclusively by the physical properties of the excipient (e.g. flow properties, specific surface area).

3.5   Figures for Chapter 3
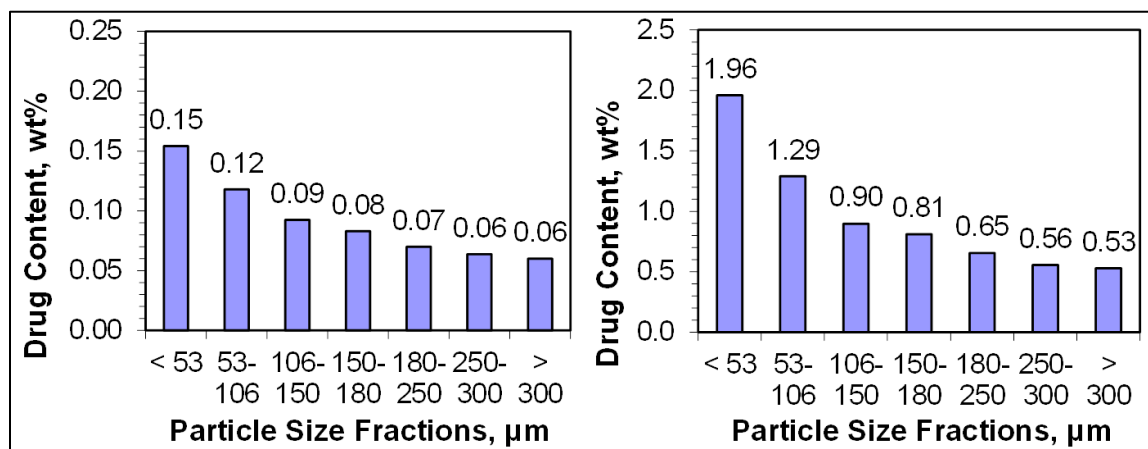
Figure 3-1: Griseofulvin loading of different size fractions: Run#1(left) and Run #2 (right).
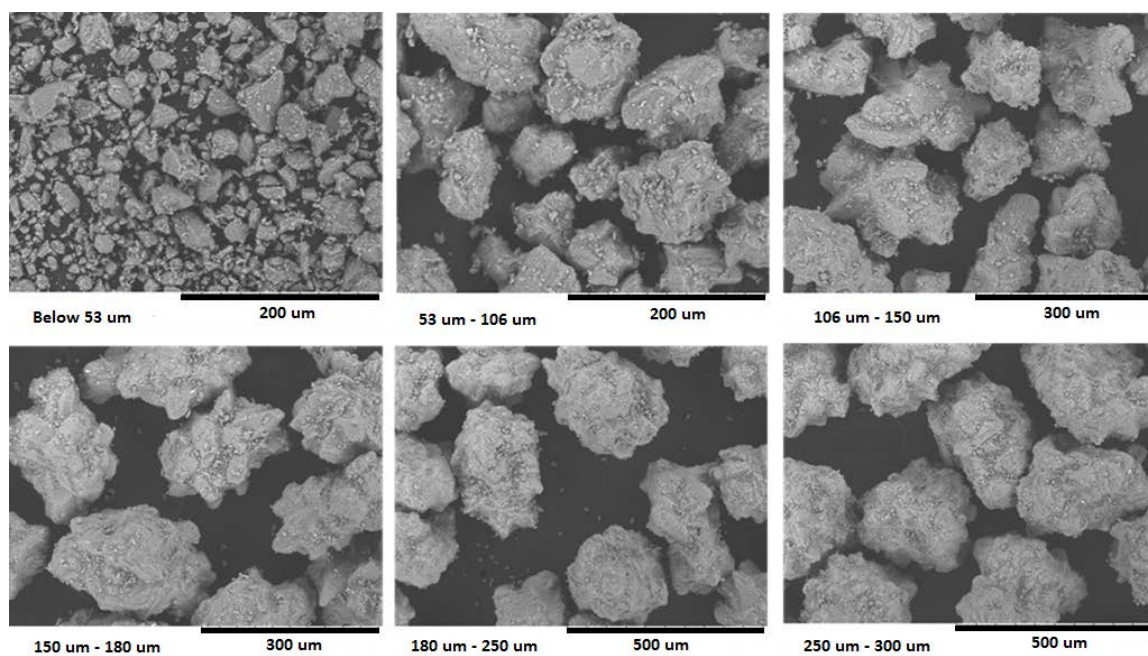
Figure 3-2: SEM pictures of various size fractions for Run #2.
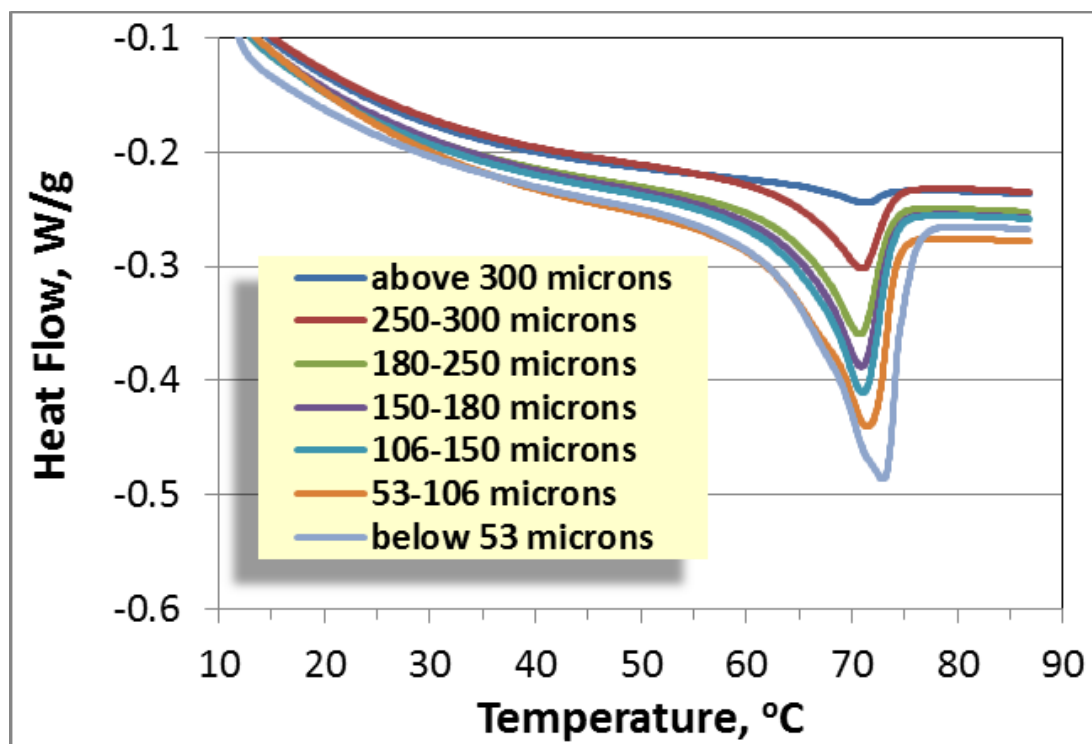
Figure 3-3: DSC test results for impregnated with Ibuprofen CaHPO₄.
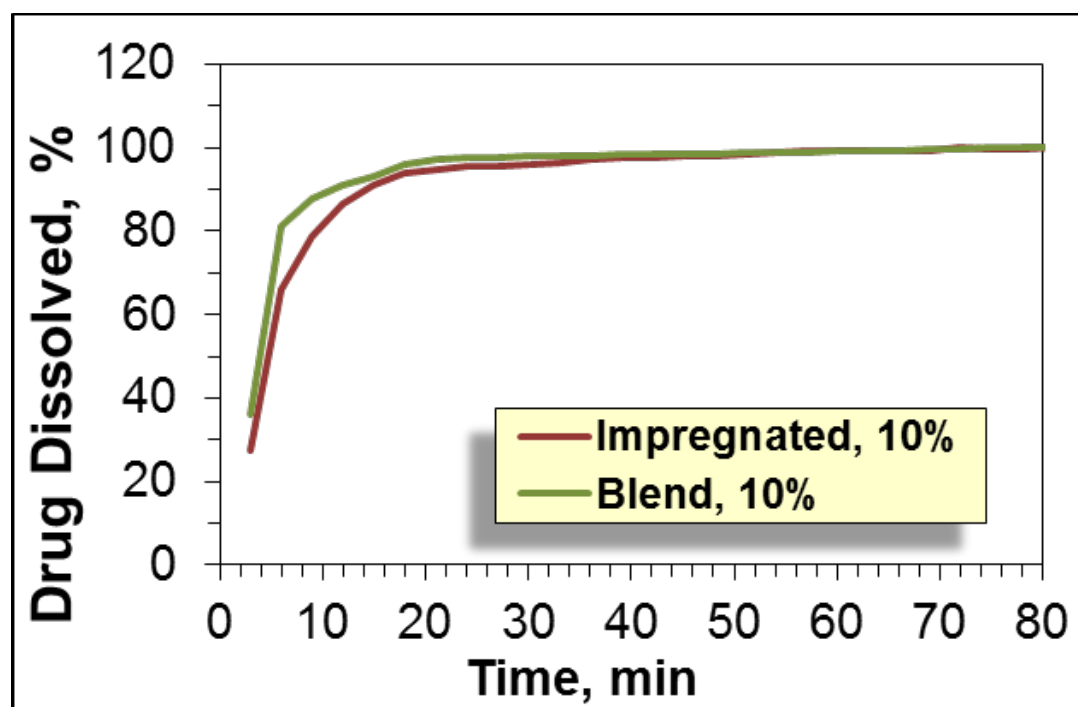
Figure 3-4: Dissolution profile of Ibuprofen (impregnated and blended) in phosphate buffer aqueous media (pH=7.2).
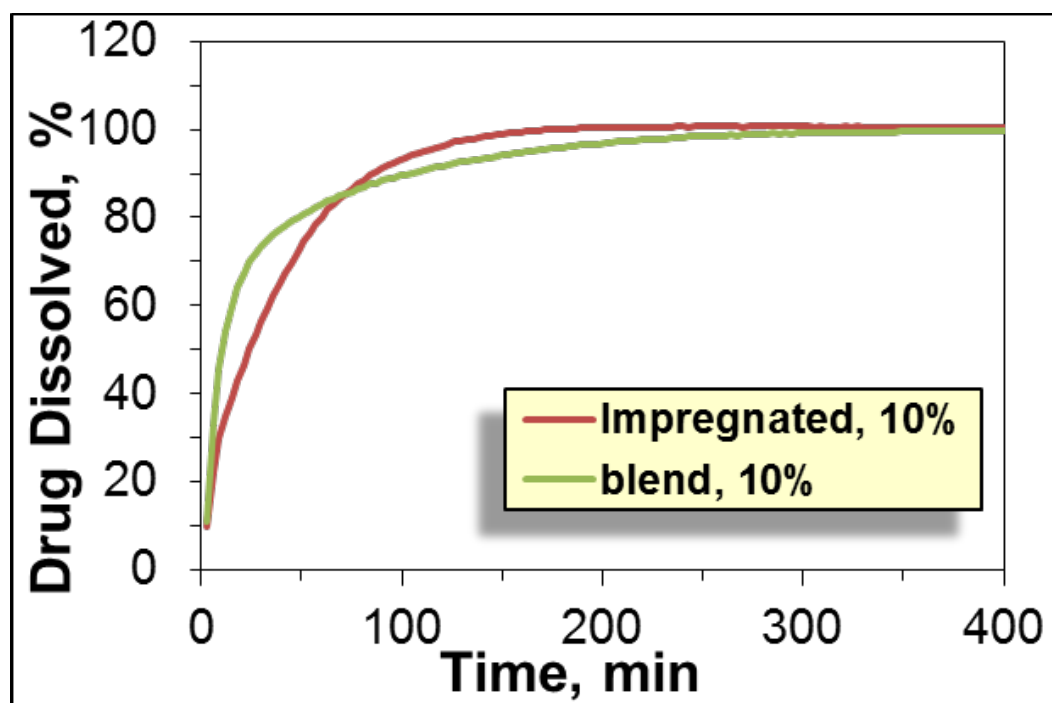
Figure 3-5: Dissolution profile of Ibuprofen (impregnated and blended) in 0.01N HCl aqueous media (pH=2).
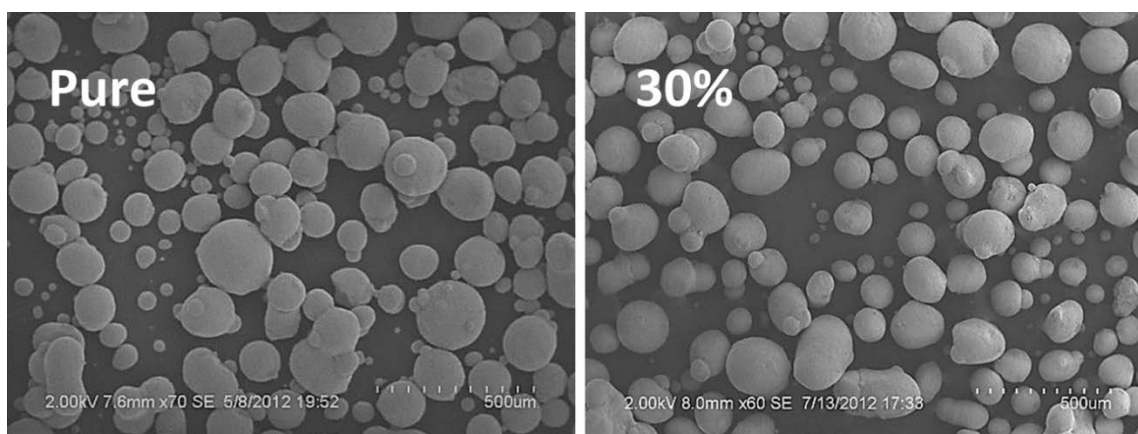
Figure 3-6: SEM Pictures of pure Neusilin® and impregnated with Fenofibrate at 30% loading.
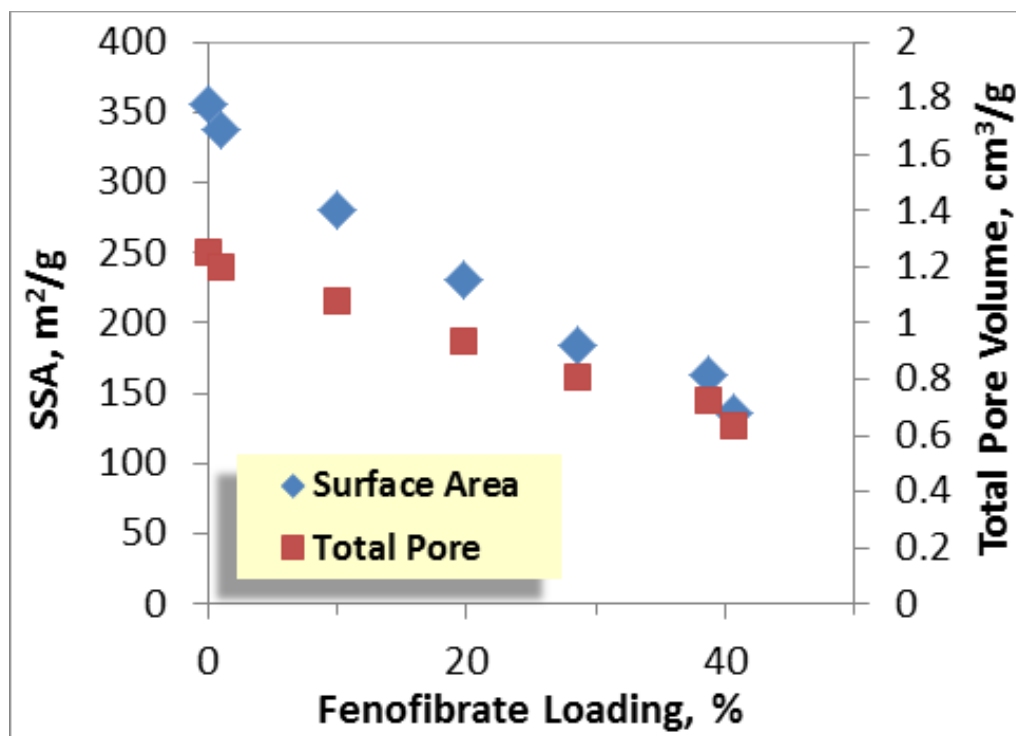
Figure 3-7: Specific surface area and total pore volume (for pores with d_{pore} < 120nm) as a function of actual Fenofibrate loading in Neusilin[®].
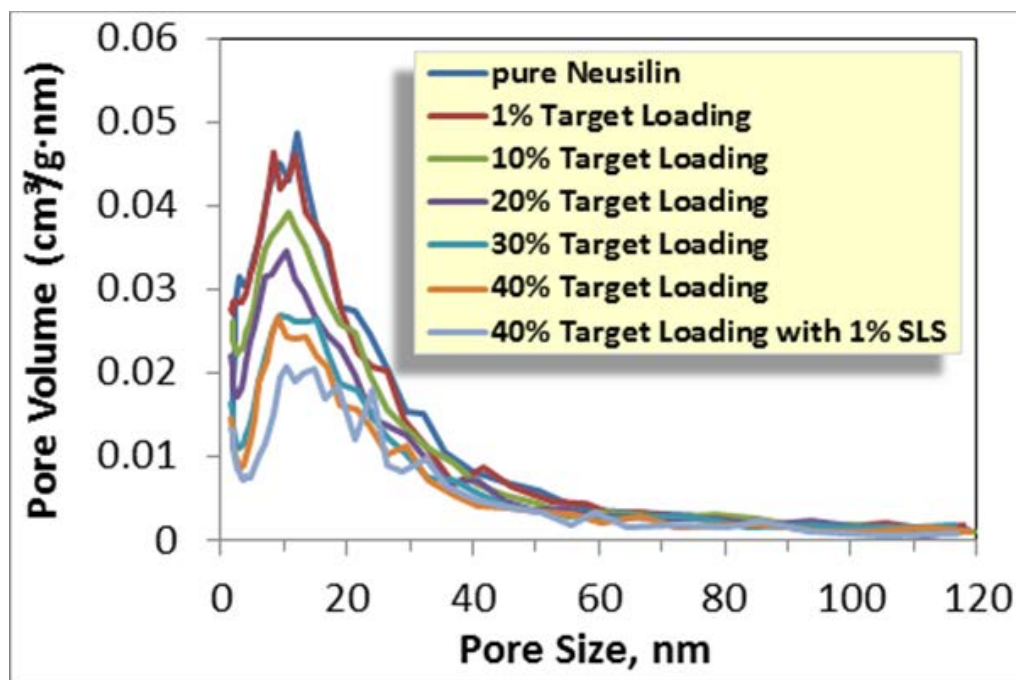
Figure 3-8: Pore size distributions (for pores with d_{pore} < 120nm) for various impregnated Neusilin® powders.
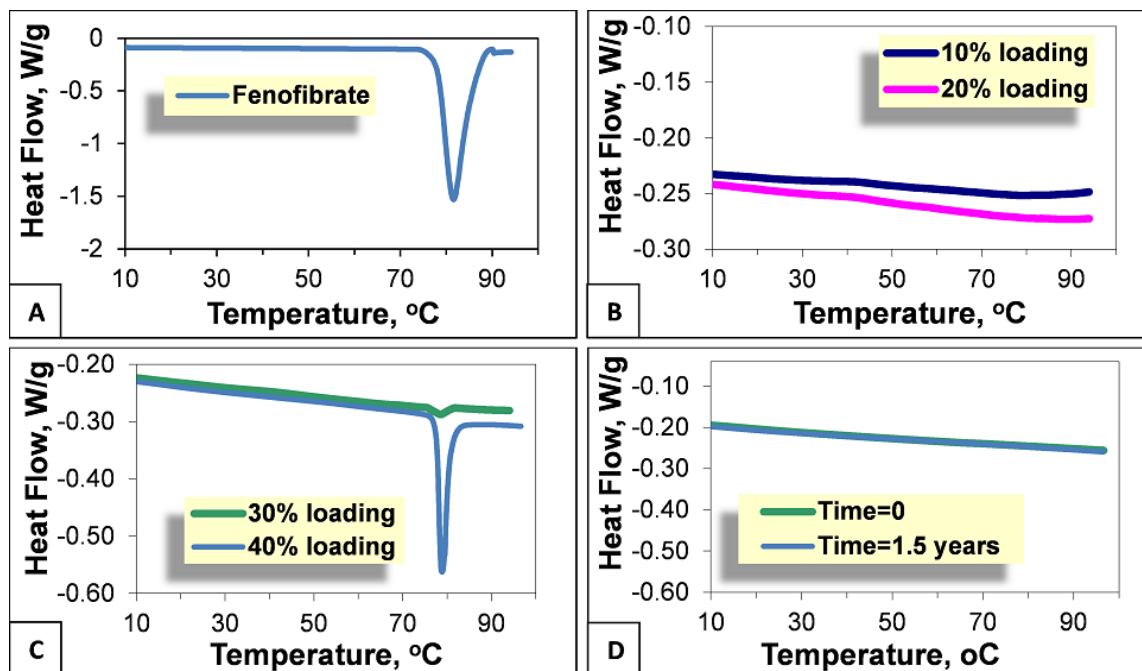
Figure 3-9: DSC scans for various impregnated with Fenofibrate Neusilin® powders: A) Pure Fenofibrate; B) 10% and 20% Fenofibrate loadings; C) 30% and 40% loadings; D) 40% loading with SLS at time zero and after 1.5 years after impregnation.
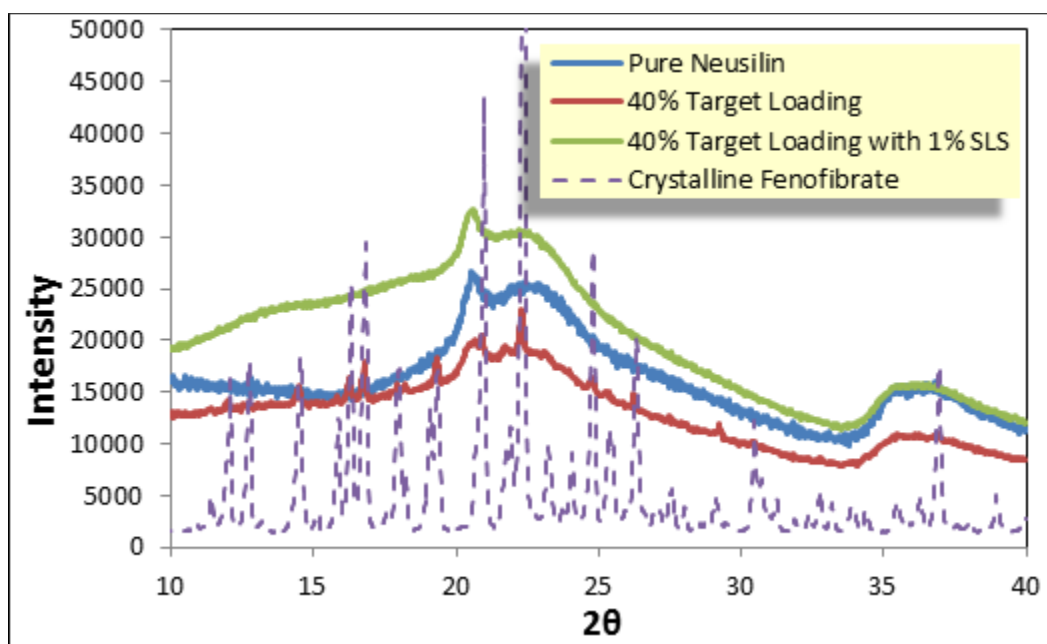
Figure 3-10: XRD pattern comparison between pure Neusilin®, pure Fenofibrate and impregnated Neusilin® at 40% loadings with and without SLS.
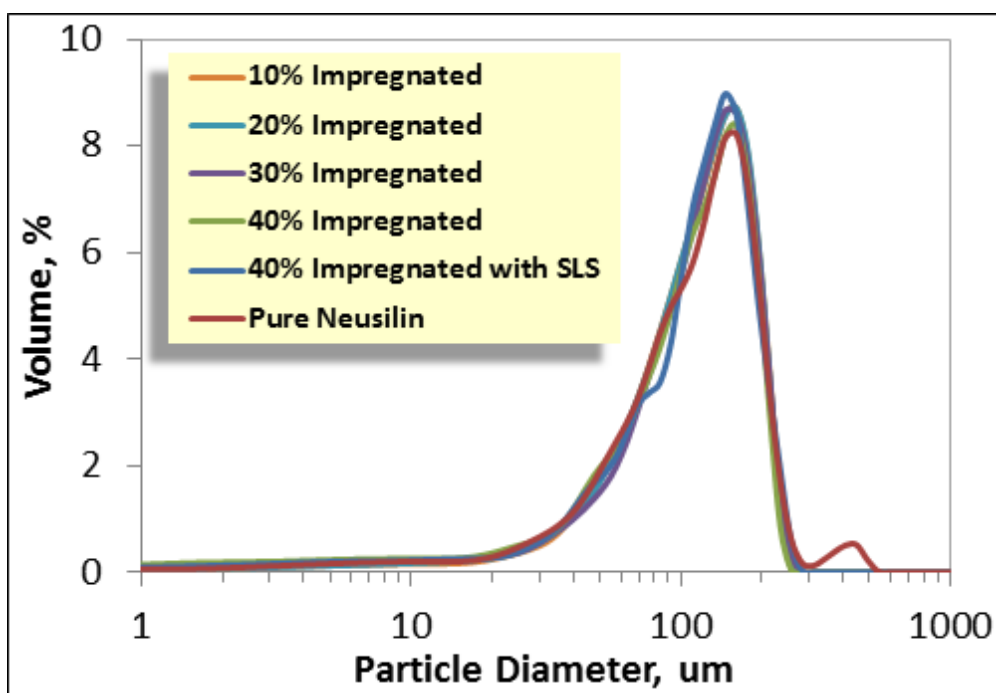
Figure 3-11: Particle size distribution comparison between pure and impregnated to various levels Neusilin®.
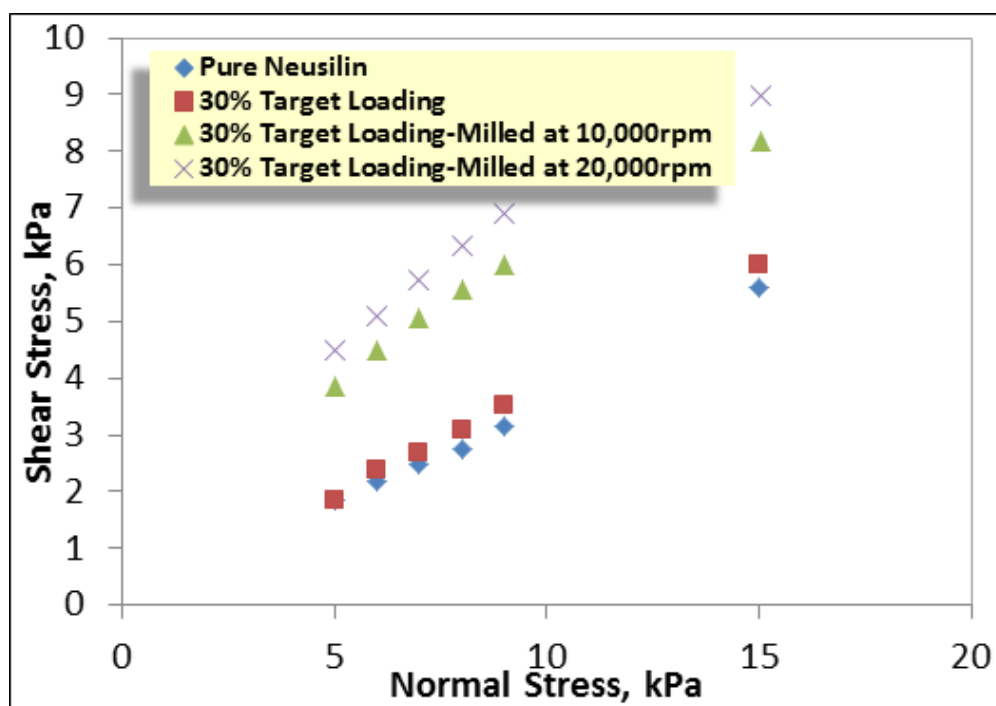
Figure 3-12: Shear cell measurements by FT4 of pure and impregnated Neusilin[®] (milled and un-milled).
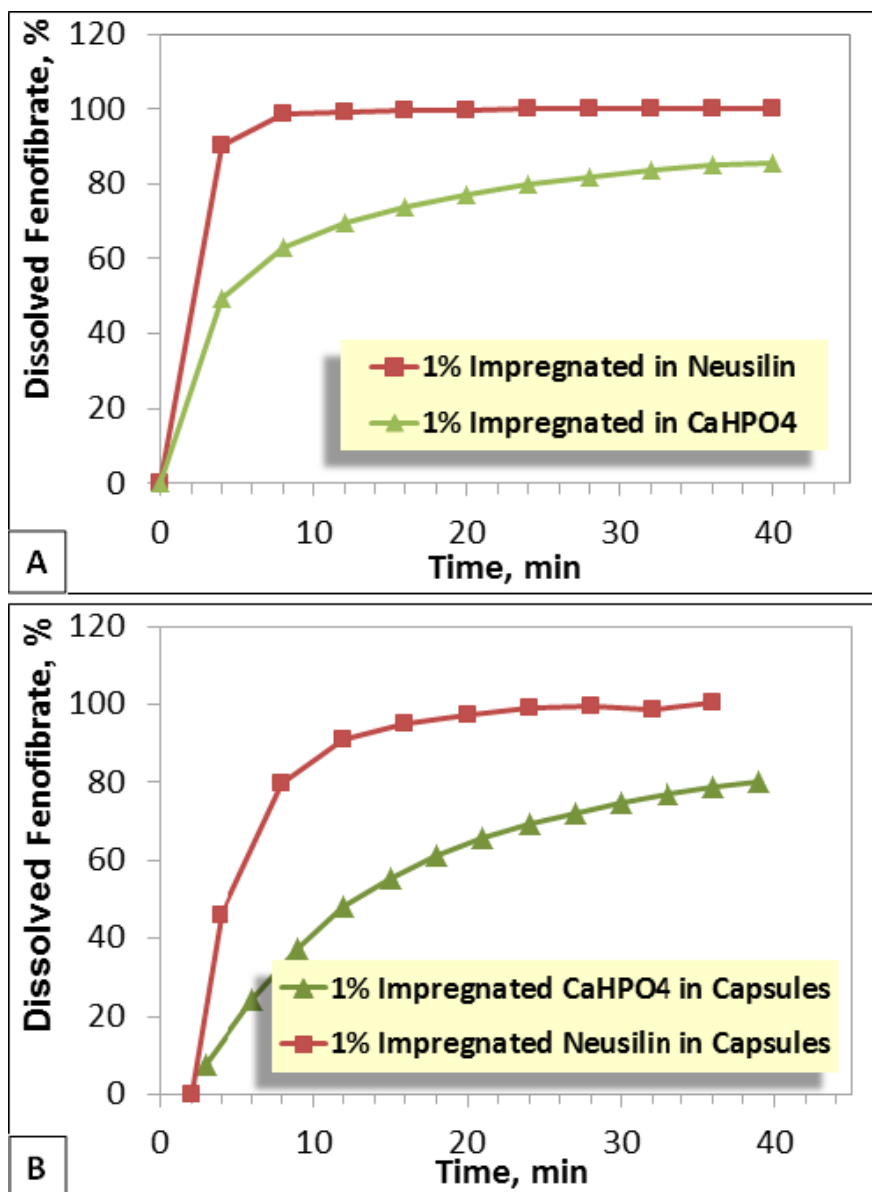
Figure 3-13: Dissolution kinetics impregnated CaHPO$_4$ and Neusilin$^{®}$ with 1% Fenofibrate: A) Powder test; B) Capsules filled with impregnated powder.
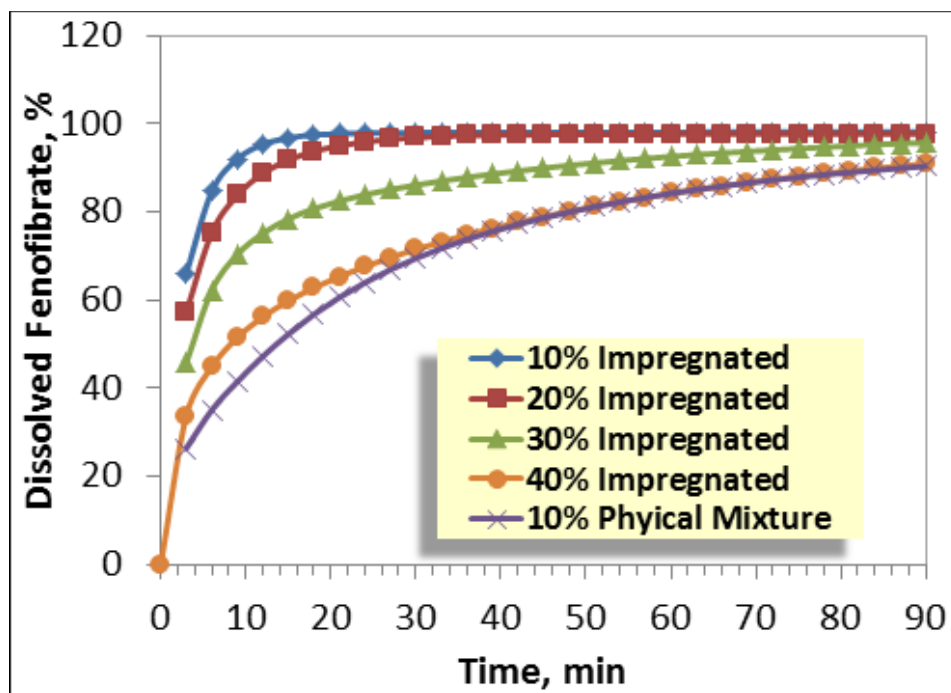
Figure 3-14: Dissolution kinetics of Fenofibrate-impregnated Neusilin® powders (un-milled).
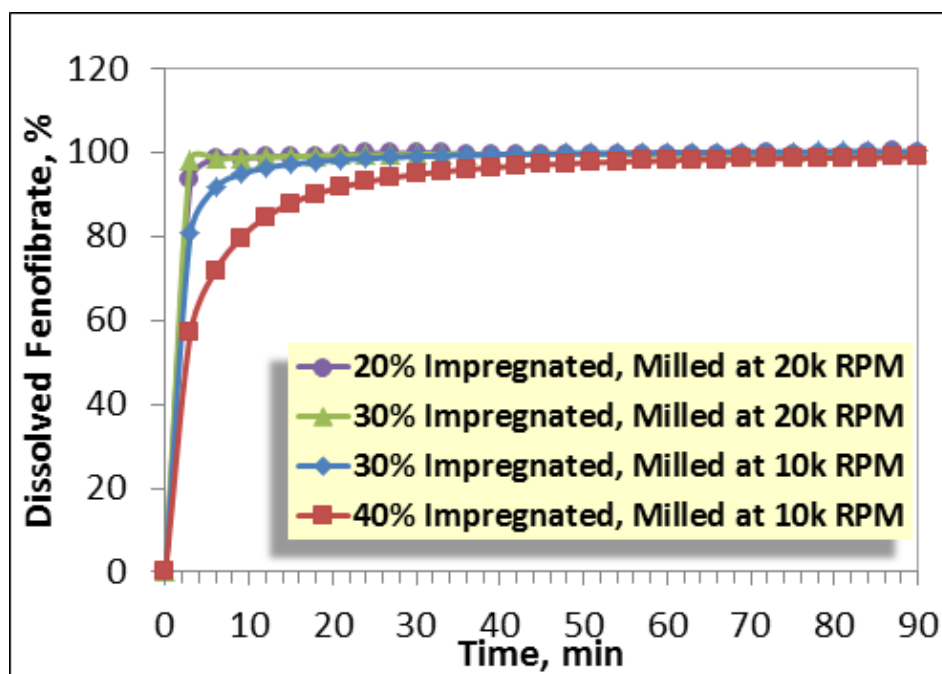
Figure 3-15: Dissolution kinetics of Fenofibrate-impregnated Neusilin® powders, milled at various mill speeds.
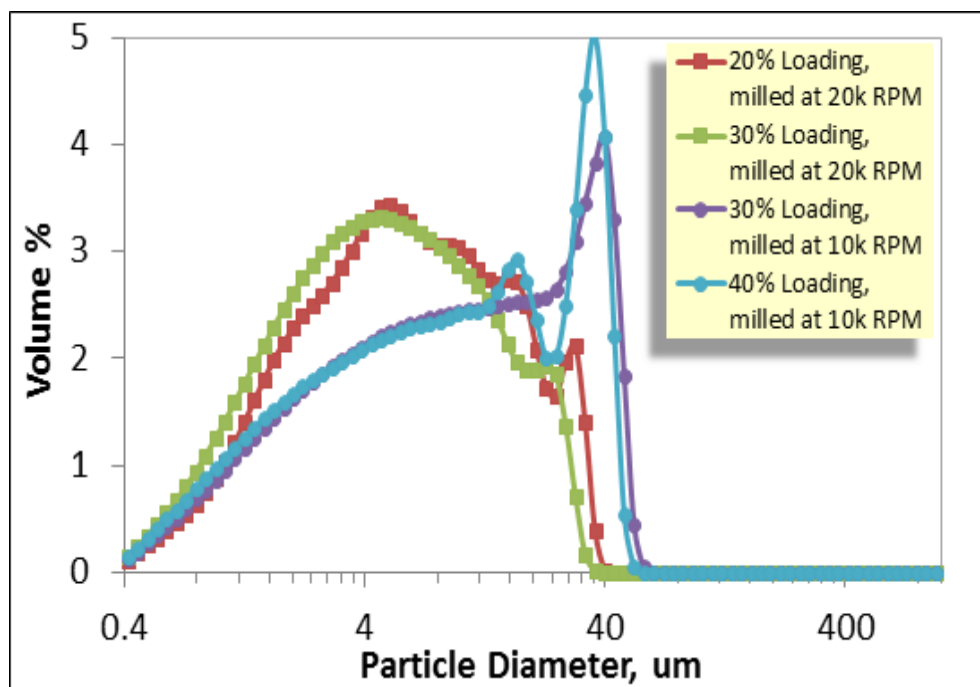
Figure 3-16: Particle size distribution various impregnated Neusilin® powders, pin-milled at 10,000 and 20,000 rpm.
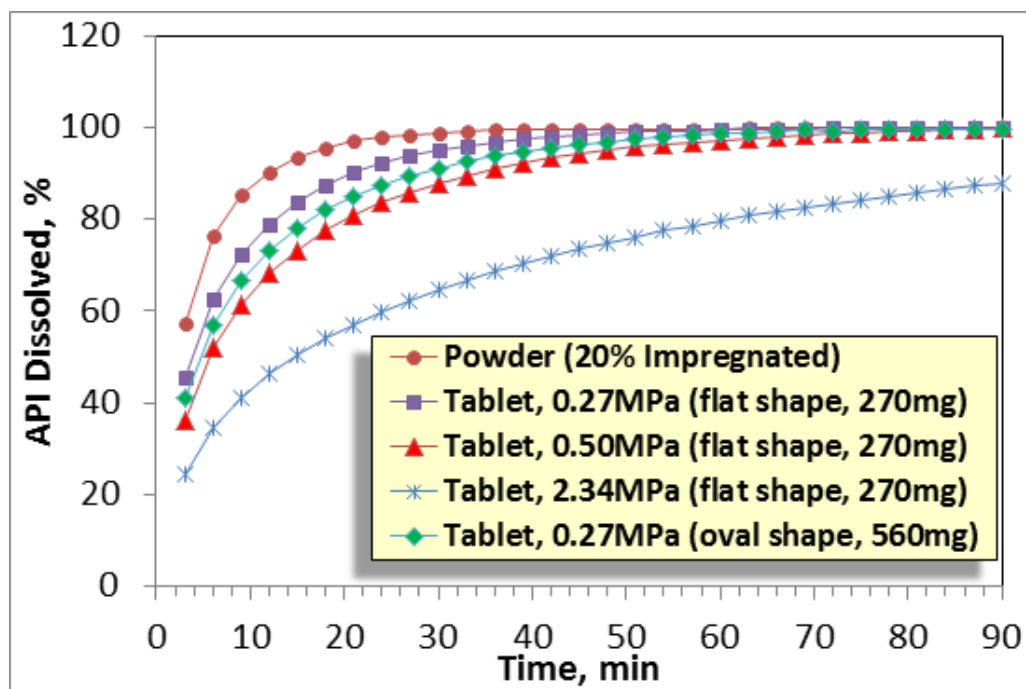
Figure 3-17: Dissolution kinetics of tablets with various tensile strength and weight/shape made from 20% impregnated Neusilin® (un-milled).
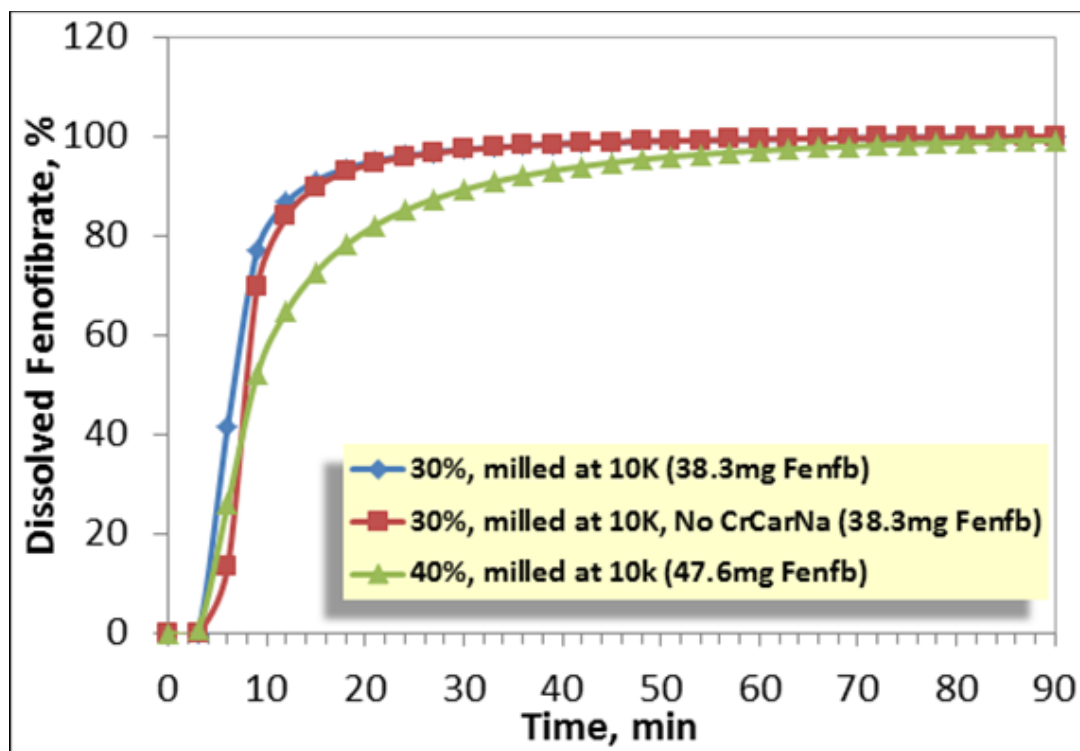
Figure 3-18: Dissolution kinetics of capsules filled with impregnated and milled Neusilin®.
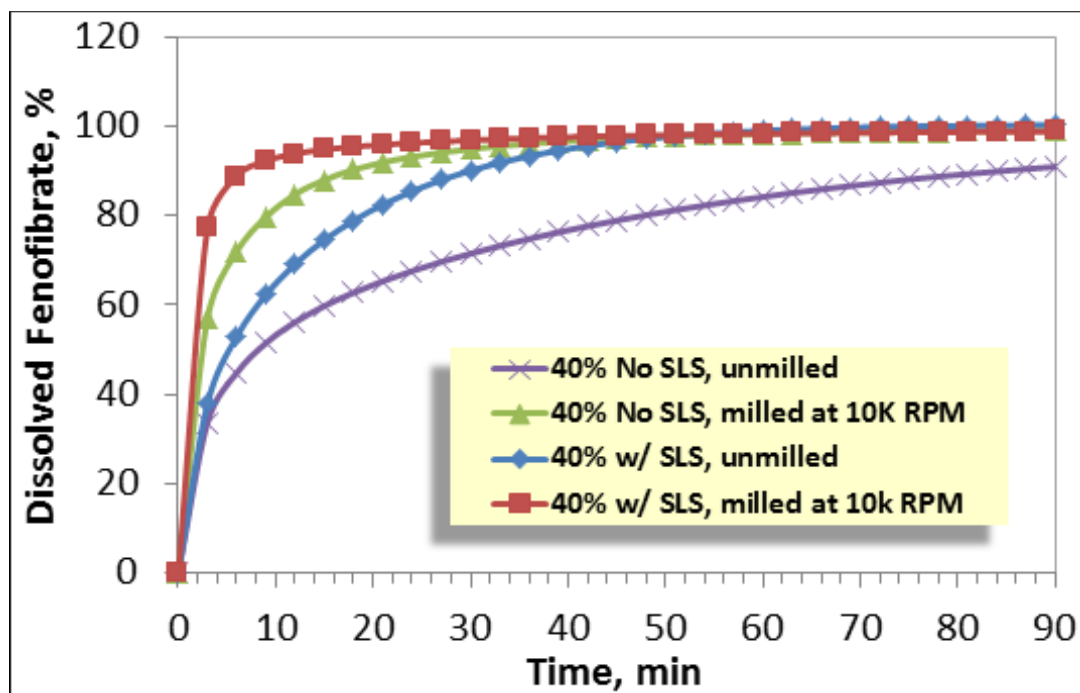
Figure 3-19: Dissolution kinetics improvement by co-impregnation of SLS and Fenofibrate in Neusilin®.
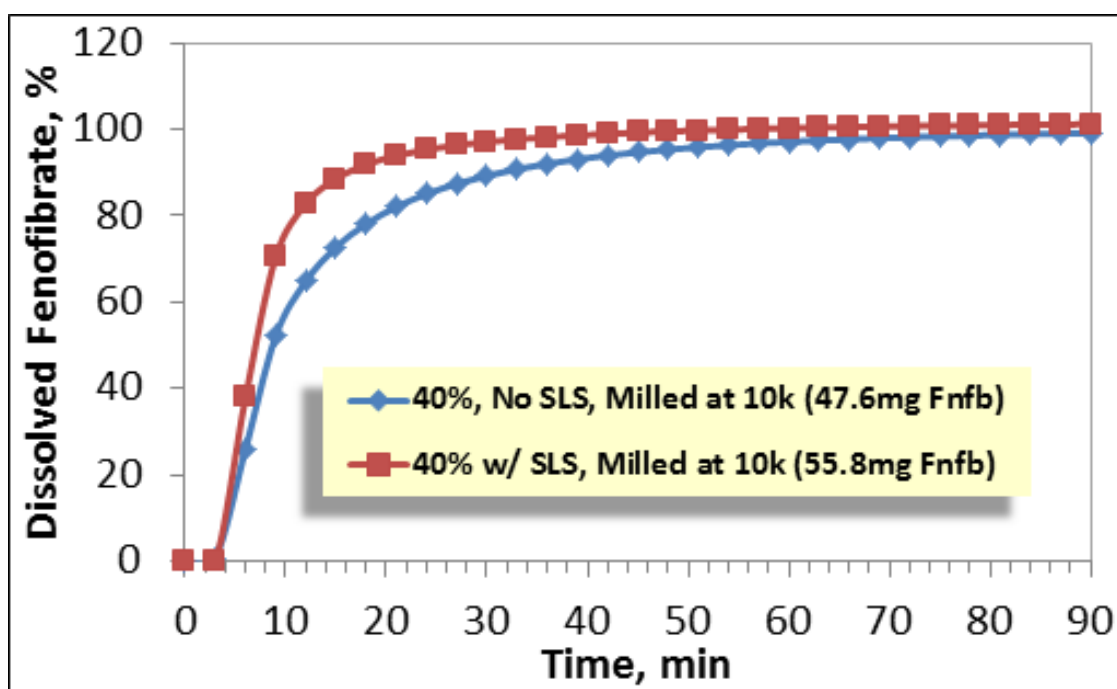
Figure 3-20: Effect of SLS co-impregnation on the dissolution kinetics of capsules filled with impregnated and milled Neusilin®.
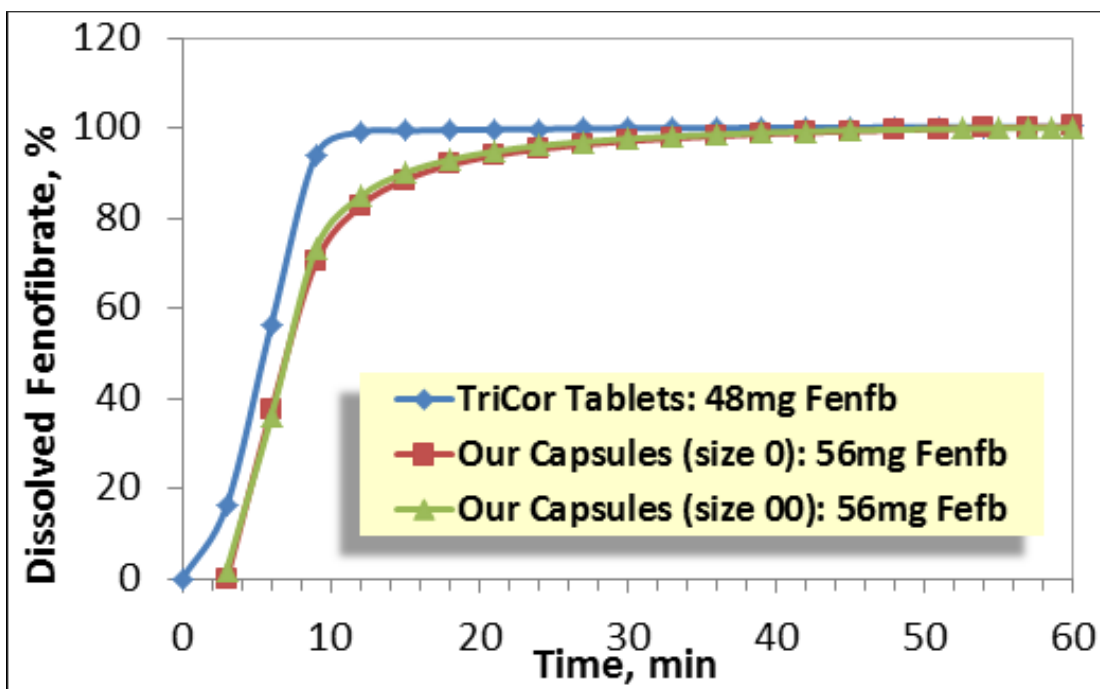
Figure 3-21: Comparison of dissolution kinetics between TriCor® tablets and capsule formulations (sizes "0" and "00") filled with Fenofibrate-impregnated Neusilin® (milled and co-impregnated with SLS).

3.6 Tables for Chapter 3

Impregnation Conditions	#1	#2
Weight of CaHPO$_4$, g	3900	3900
Solvent Used	Methanol	Acetone
APAP Solution Concentration, mg/ml	1.433	14.33
Spray Rate, ml/min	17	17
Spray Time, min	160	160
Inlet Gas Velocity, m/s	1.3-1.5	1.3-1.5
Atomization Pressure, bar	2	2
Inlet Temperature, ^{o}C	85	60
Product Temperature, ^{o}C	43-45	37-38

Table 3-1: Processing conditions for Griseofulvin impregnation runs.

Run #	Griseofulvin Loading, % w(API)/w(pure CaHPO$_4$)		Blend Uniformity, %RSD	
	Target	Actual	Un-milled	Pin milled
#1	0.1	0.095	1.173	0.777
#2	1.0	0.935	1.615	0.561

Table 3-2: Griseofulvin loading and blend uniformity for impregnated CaHPO$_4$ (un-milled and milled).

Process Parameters	#1
Weight of CaHPO$_4$, g	3900
Solvent Used	Methanol
APAP Solution Concentration, mg/ml	145.4
Spray Rate, ml/min	17
Spray Time, min	160
Inlet Gas Velocity, m/s	1.3-1.5
Atomization Pressure, bar	2
Inlet Temperature, ^{o}C	85
Product Temperature, ^{o}C	43-45

Table 3-3: Processing conditions for Ibuprofen impregnation runs.

Run #	Ibuprophen Loading, % w(API)/w(pure CaHPO$_4$)		Blend Uniformity, %RSD	
	Target	Actual	Un-milled	Pin milled
#1	10.14	10.28	1.19	0.875

Table 3-4: Ibuprophen loading and blend uniformity for impregnated CaHPO$_4$ (un-milled and milled).

Run #	Excipient Weight g	API Solution Concentration mg/ml	Spray Rate ml/min	Spray Time min	Inlet Gas Velocity m/s	Atomization Pressure bar	Temperature, °C Inlet	Temperature, °C Product
1	3900	14.3	17	160	1.3-1.5	2	80	35-37
2	877	3.2	17	160	1.0-1.3	2	80	39-42
3	220	44	4	125	0.9-1.0	1.2	80	42-44
4	220	44	4	250	0.9-1.0	1.2	80	41-42
5	220	44	4	375	0.9-1.0	1.2	80	41-43
6	220	44	4	500	0.9-1.0	1.2	80	40-42
7	220	44 (SLS - 1.1 mg/ml)	4	500	0.9-1.0	1.2	80	42-44

Table 3-5: Experimental conditions and process parameters for all impregnation experiments in fluidized bed.

Run #	Target Loading, %	Actual Loading, %	Blend Uniformity, %RSD	Excipient	Equipment
1	1%	0.98	0.45	CaHPO$_4$	Glatt GPCG 1
2	1%	0.92	1.41	Neusilin®	Glatt GPCG 1
3	10%	9.94	1.52	Neusilin®	MiniGlatt
4	20%	19.83	0.54	Neusilin®	MiniGlatt
5	30%	28.65	0.55	Neusilin®	MiniGlatt
6	40%	38.70	0.93	Neusilin®	MiniGlatt
7	40% with 1% SLS	40.76	0.28	Neusilin®	MiniGlatt

Table 3-6: Target Impregnation levels, actual loadings and blend uniformity of Neusilin® and CaHPO$_4$ impregnated with Fenofibrate.

Chapter 4 . Cross-sectional analysis of impregnated excipient particles by energy dispersive X-ray spectroscopy

4.1 Introduction

Impregnation is a process widely used in heterogeneous catalyst preparation [110, 111]. There are many advantages in placing catalyst molecules inside porous carriers: increasing total surface area available for reaction, improving overall reactivity, catalyst stabilization and reducing cost to name a few. As it has been demonstrated already, there are also several advantages of placing an API into a porous carrier to produce a dosage form: improvements to API uniformity, improvements to blend flowability and improvements to API release profile. The type of impregnation profile can influence the performance of the final product. In the case of catalysts, these effects have been firmly established [16, 112, 113]. There are several types of profiles that can be achieved during impregnation: uniform, egg-shell, egg-white or egg-yolk. Research in the field of catalysts has shown that these profiles can be affected by the processing conditions (impregnation and drying temperatures), the nature of the solute/carrier or their interaction [18-20]. In the case of pharmaceutical impregnated formulations, the API profile type could affect its release from the porous excipient, its long-term stability and the overall formulation efficacy.

The impregnation profile inside porous particles can be studied by numerous analytical techniques, once the cross-section of the particle is obtained and exposed for analysis. Available analytical methods today span the whole spectrum of electromagnetic radiation. The main categories include: radio-waves (NMR microscopy), microwaves

(EPR microscopy), infrared light (IR microscopy), visible and ultraviolet light (photography, light microscopy, UV-vis microscopy), infrared through ultraviolet light (Raman microscopy, fluorescent microscopy) and X-rays (X-ray microscopy, X-ray computed tomography) with many other subcategories [114, 115]. The choice of analytical tool depends on the information (qualitative or quantitative) and detail (sample size and spatial resolution) that are needed. Obtaining a cross-section for analysis is not generally a simple task. Heterogeneous catalysts are typically made of large cylindrical (or spherical) carries, several millimeters in size. Cutting such large carrier particles and exposing their cross-section area is usually not a problem. However, pharmaceutical excipients that are suited for impregnation normally are small spherical particles (up to 300-400um in diameter), which are much more difficult to handle and cut. Such particles need to be immobilized in place or embedded into a solid matrix before cutting. Popular materials for embedding solid particles are resins - liquid organic substances, which after polymerization provide a solid matrix with excellent optical properties [116, 117].

During the pre-digital age, impregnation profiles in catalysts were investigated using autoradiography [118] or photography [119-122]. Both analyses resulted in generating photographic negatives of the cross section of impregnated particles and analyzing them with a microdensitometer. This allowed one to determine the catalyst coverage as a function of position. Other optical methods involved directly measuring the impregnation profiles using a microdensitometer [123] or digital camera [112, 124]. In all cases, optical analyses required a very good contrast between the impregnated and the non-impregnated regions and relatively large particles (several millimeters in diameter).

Impregnation profiles in large enough pellets can also be analyzed using UV-vis micro-spectroscopy. This technique can be used to gain information on the spatial distribution of the catalyst [125], knowledge on its chemical structure [126] and changes during catalyst preparation [124]. The reported resolution of the method starts at 100 um and can potentially go down to 1-3 um [127]. It requires the impregnant to have an absorbance in the UV-vis region of the spectrum. UV-vis micro-spectroscopy is more sensitive than previously discussed optical methods for analysis but still has its limitations, depending on the chemical nature of the investigated substance. Chemical imaging techniques could also be used to map dynamic processes. Infrared spectroscopy has proven advantageous in studying dynamic adsorption processes inside supported catalysts [128, 129]. This method helps to gain understanding on process parameters that are affecting adsorption and ultimately the catalyst's performance. Very often, multiple analytical techniques are used simultaneously in order to significantly amplify the knowledge that could be obtained during the analysis. One such combination is atomic-force microscopy (AFM) coupled with IR spectroscopy. This approach combines the unique spatial resolution capabilities of AFM with the chemical analysis capabilities of IR spectroscopy, making it possible to capture IR spectra at the nanoscale [130, 131]. Raman imaging techniques can also be very powerful when characterizing impregnation profiles in catalysts during the impregnation or drying stages [132-134]. Water is almost invisible to Raman spectroscopy, which could be beneficial in some cases. Raman imaging has become very popular in drug product development and characterization[135]. Its applications have been proven very useful in determining API's content uniformity in various pharmaceutical formulations [136]. The ability of Raman spectroscopy to differentiate

different crystal forms of the same API makes it a powerful tool in determining the spatial distribution of polymorphs [137, 138]. It can be also used to determine how processing conditions (for example drying) influence API distribution in the individual particles of the final formulation [139]. Similar to UV-vis, Raman spectroscopy can be coupled with AFM to further increase its spatial resolution [140]. Computed X-ray tomography (knows as CAT scan in medicine) is a powerful imaging technique used to analyze the internal structure and porosity of various powder agglomerates and granules [141-143]. The technique can be also used to study dynamic processes, such as die compaction and mixing [144].

Nuclear magnetic resonance (NMR) spectroscopy is an analytical method routinely used by chemists for determining the physical and chemical properties of atoms or molecules. NMR spectroscopy relies on the acquisition of NMR spectra, which characterize local magnetic environments of nuclei possessing a non-zero spin (resonance frequency as a function of static magnetic field and gyromagnetic ratio) and makes it a great tool for qualitative (identification) or quantitative analyses. One very powerful variation of NMR spectroscopy is MRI (magnetic resonance imaging), where the magnetic field is intentionally made inhomogeneous and dependent on spatial coordinates (as opposed to NMR where the magnetic field is highly homogeneous). This allows MRI to produce 2D or 3D images of objects along with information about their chemical compositions. Besides its wide-spread as a diagnostic tool in modern medicine and other biomedical applications, MRI is getting attention as a powerful imaging technique in various engineering fields [145, 146]. In supported catalyst preparation, MRI has proven to be a powerful technique for imaging the spatial metal distribution during the impregnation and

drying stages [147, 148]. The technique can also be used to provide data in operating model reactors (internal structure, mass/heat transport, chemical conversion) [149, 150]. MRI has also found use in pharmaceutical applications for monitoring drug release [151-153]. Another imaging technique similar to MRI is electron paramagnetic resonance (EPR) imaging. In this case it is the spins of the electrons that are excited (vs. spins of atomic nuclei as in MRI). Materials under study must have unpaired electrons in order to be detected (metal complexes, organic radicals). Successful applications of this imaging technique include studies of diffusion processes in pharmaceutical drug delivery systems [154, 155].

Arguably, the most powerful imaging technique today is electron microscopy (EM), which is capable of achieving high magnifications to submicron levels and below [156]. EM relies on an accelerated beam of electrons to illuminate the sample and create an image. The original form of EM, called transmission electron microscopy (TEM), relies on the transmission of electrons through the sample in order to create an image. The technique requires a very high accelerating voltage (>100 keV) and a very thin sample (< 200nm) in order to achieve transmission [157]. TEM and its modification, STEM (scanning transmission electron microscopy), are the most powerful electron microscopy techniques, which can easily achieve nanometer and atomic level magnifications [158]. Scanning electron microscopy (SEM) is the other main form of EM, which relies on detecting emitted electrons from the sample's surface. It is not as powerful as TEM/STEM, but is still capable of achieving magnifications to micron and submicron levels. The advantage of SEM is that it does not require thin specimens and such high accelerating voltages (typically less than 30keV) as TEM. There are many signals

produced inside the EM by the interaction of the electron beam with the sample: secondary electrons (SE), back-scattered electrons (BSE), characteristic X-rays, etc. SEM relies on the detection of SE but also can operate in BSE mode.

Combining an electron microscope with a detector for characteristic X-rays, gives rise to energy-dispersive X-ray spectroscopy (EDS), another very powerful analytical method for quantitative and qualitative surface analysis. When the atoms in the sample get excited as a result of the electron beam/sample interaction, an electron from the inner electron shell can get ejected by the incident electrons, resulting in a vacant electron hole. The excited atom will immediately return to ground (unexcited) state by filling the hole with electrons from the outer electron shells, resulting in the emission of X-rays equivalent to the energy difference between the transfer shells (Figure 4-1). This energy difference is characteristic for each atom in the periodic table (excluding He and H), which allows EDS to measure the elemental composition of the sample. What makes EDS particularly useful is that the amount of emitted X-rays from each element is directly proportional to its concentration (mass or atomic fraction) in the sample. In order to construct the spatial distribution of elements, early EDS systems had to analyze the cross-section of the sample at different points and then plot signal intensity vs. distance [159, 160]. Further improvements in the EDS technology and increase in computational and storage power of computers has led to the development of a process known as X-ray mapping, where data about elemental composition and concentration can be used to construct an elemental map, overlaid on top of the sample's image. This powerful technique allows one to visualize the spatial distribution of all detected elements on the sample's surface [161, 162]. EDS systems can be coupled with both types of electron

microscopes, resulting in elemental maps with submicron (SEM/EDS) and nanoscale resolutions (TEM/EDS, STEM/EDS) [163-167].

Chapter 2 introduced the method for API impregnation in a fluidized bed, describing the many advantages it presents to pharmaceutical formulations. The method was capable of achieving impregnated formulations with very high homogeneity, independent of the drug loading, and with physical properties independent of the API's nature and loading. In Chapter 3 other benefits of FB impregnation were further investigated (improving dissolution kinetics of poorly-soluble drugs). There have been a lot of research efforts directed towards studying of impregnation profiles, however none of them (to our knowledge) have been focused on API-impregnated excipients produced in a FB. In most impregnation methods, particles are impregnated by immersing them into solutions, resulting in partial or complete liquid saturation. In all of these cases, liquid penetration takes place across the entire external surface of the particles. By contrast, FB impregnation is achieved by atomizing the impregnation solution into droplets, which in turn collide with the individual particles. This is followed by a drying period until the next time the particles enter the spray zone to get impregnated again. Therefore, the FB impregnation process consists of small impregnation increments, the frequency of which depend on processing conditions such as spray rate, droplet size, drying temperature and drying gas flow rate (or mixing). This difference in the impregnation mechanism could result in differences in the API profile inside the excipient carrier. The API profile can affect drug product performance. Drug release could be greatly impacted by the impregnation profile (egg-shell vs. uniform distribution for example).

This chapter aims to develop methods for analysis of the type of impregnation profile achieved during FB impregnation of APIs onto porous excipients. The analytical technique employed to analyze and map the cross-section of FB impregnated particles is SEM/EDS. The analysis presented here is intended to be purely qualitative (relative elemental distribution). Quantitative EDS analysis (absolute elemental concentrations) is usually not straightforward and many factors need to be taken into account before the concentration data obtained from the spectra can be reported. The work showcases different particle embedding techniques, various markers that could be used to analyze FB impregnation profiles, several cutting and polishing methods as well as the type of API profile (using Fenofibrate and Acetaminophen as model drugs) achieved during the FB impregnation process.

4.2   Materials, equipment and methods

4.2.1   Materials

Neusilin® US2 grade was purchased from Fuji Health Science Inc. (Burlington, NJ, USA). Methanol, B&J Brand® Multipurpose Grade (purity > 99%), was purchased from VWR International. Fenofibrate (purity >99%), potassium acetate (purity >99%), potassium iodide (purity >99%) and LR White embedding kit (including resin, accelerator and catalyst) were purchased from Sigma- Aldrich (St. Louis, MO, USA). Acetaminophen (APAP, purity >99%) was purchased from Mallinckrodt Pharmaceuticals. (Raleigh, NC, USA). SEM supplies (aluminum specimen mounts, double-coated conductive carbon tabs and high performance silicate-based nickel paste) were purchased from Ted Pella Inc. (www.tedpella.com). Micron graded wet/dry

polishing paper (37-948 Assortment 30-1 micron) was purchased from Zona Tool Co. (Bethel, CT USA).

4.2.2 Equipment

Impregnation experiments were carried out in a Mini-GLATT fluidized bed dryer/coater/granulator, equipped with a top spray nozzle (Glatt Inc., Ramsey, NJ, USA). Cross-sections of resin-embedded particles were obtained using Shandon AS 325 Microtome equipped with steel blade. SEM samples were sputtered with gold in an EMS 550 sputter coater (Electron Microscopy Sciences). All image and elemental analysis was done on Hitachi SU5000 Schottky Field-Emission Scanning Electron Microscope (Hitachi High Technologies America, Inc.) equipped with Oxford X-Max 80 EDS probe with silicon drift detector (Oxford Instruments Analytical Ltd.).

4.2.3 Methods

4.2.3.1 Impregnation

Fluidized bed impregnation of Neusilin® with Acetaminophen and Fenofibrate was carried out according to the general procedure outlined in Chapter 2/Chapter 3. Impregnating API solutions were prepared using methanol with the following concentrations: Acetaminophen – 128 mg/ml, Fenofibrate – 44 mg/ml. Drying gas temperature and velocities were $80^{o}C$ and 1 m/s respectively. Spray rate for both API formulations was 4 ml/min. The solution was sprayed until desired average API loading was achieved: Acetaminophen – 10%, Fenofibrate – 10% and 40% (expressed as wt(API)/wt(pure excipient)).

Impregnation of Neuslin® with potassium acetate (KAc) and potassium iodide (KI) was performed according to the common dry impregnation procedure. Separate solutions of KAc and KI in methanol were prepared at RT with concentration of 140 mg/ml and 70 mg/ml respectively (estimated average loading of 40% and 20% respectively based on Neusilin® porosity). Pure, sieved Neusilin® (above 180 μm fraction) was added to above solutions and slurries were agitated for 30 min to allow full impregnation. Impregnated Neusilin® was then filtered gently under vacuum and dried in oven at $30^{\circ}C$ overnight (no vacuum) with N_2 purge.

4.2.3.2   Particle embedding, cutting and polishing

<u>LR White Resin</u>

Cross-sections for some of the impregnated samples were obtained by embedding them in a resin. Impregnated samples were first sieved to separate the largest particles and those with sizes above 180 um were used for analysis. These particles were then dried under vacuum again to remove any surface moisture absorbed during storage. Particle embedding was done in LR White, a popular and widely used resin for immobilization of biological samples. LR White is a type of acrylic resin with low toxicity and ultra-low viscosity (8 cP). The resin can be cured by one of four methods: microwave, heat, UV light (365nm) and chemical (aromatic tertiary amine as accelerator). All LR White embedded samples presented in this work were cured using an accelerator. The resin was first mixed with the provided catalysts for 24 h to allow complete dissolution. About 20 ml of resin mixture was placed in a glass vial and sparged with N_2 for 1 h to remove all oxygen, and then capped. If oxygen is not removed, polymerization of the resin will not occur. The next steps were performed under N_2 atmosphere (glove box) to minimize O_2

inclusion. Two drops of the accelerator were added to the resin mixture and the vials were shaken vigorously for 10 seconds. Small glass vials (1cm in diameter with flat bottom) containing a small amount of the sieved impregnated particles were filed with about 2ml of resin/accelerator mixture, shaken gently to allow complete infiltration of the liquid within all solids and then capped. Vials were taken from the glove box and placed in an ice bath. The whole operation from adding the accelerator until the vials are placed on ice should be done in less than 10 min, as polymerization usually occurs between 10 to 20 minutes. It should be noted that small amounts of O_2 or other polymerization-inhibiting species can inhibit the polymerization process. For example, Neusilin$^®$ particles impregnated with KI or Acetaminophen could not be embedded using LR White resin as polymerization never took place (despite numerous attempts including UV-initiated polymerization). The glass vials were then left for 24 h to complete the polymerization process and then carefully cracked to remove the solid polymer. The embedded samples were mounted on microtome holders using epoxy resin as adhesive. The whole assembly was placed on a microtome and the sample was cut to the desired depth to produce a rough cross-sectional cut. All samples were then micro-polished using wet/dry polishing paper.

Cyanoacrylate Adhesive (Super Glue)

Because embedding with LR White resin was not always successful, a different approach was needed to prepare samples impregnated with KI and Acetaminophen. It was discovered that among its endless applications, Super Glue could also act as an embedding media. Impregnated Neusilin$^®$ with KI was sprinkled over aluminum specimen mounts with conductive carbon tabs to create a monolayer of particles. Super

glue was then slowly applied over the particles to completely cover the entire monolayer and left to dry for 24 h. Cross-sections of the particles were then obtained by polishing (as outlined next) the monolayer until a good cross-section was obtained by visual confirmation using an optical microscope.

Sample Polishing

Particle cross-sections for both LR White and Super Glue embedded samples were produced by polishing the surface using six different micron graded wet/dry polishing paper. Starting with the largest grading (30 microns) samples were polished using forward/backward movement until a satisfactory particle cross-section was achieved (as observed periodically under an optical microscope). Sample polishing continued using 15um, 9um, 3um, 2um and finally 1um size paper. The polishing direction was changed by rotating the sample 90° every time the paper was changed. This procedure yielded very smooth sample surfaces with almost mirror-like appearance.

4.2.3.3   Manually cutting particles

Cross-section exposure of impregnated Neusilin$^®$ particles was also successfully accomplished without any embedding media. An alternative procedure was developed involving a manual cut across a particle monolayer. This was achieved in two ways, differing in the type of adhesive used for anchoring of the particles. In the first method, aluminum discs with conductive carbon tape were sprinkled with impregnated sample. The powder was then gently pushed to ensure good adherence with the tape and any loose particles were lightly blown with N_2. The monolayer of particles was then cut manually by hand, using a microtome steel blade. The cut was done gently, making sure

the knife was parallel to the surface. For a successful cut, the knife had to be very close to the surface, almost touching the carbon tape. Neusilin® particles are firm enough not to crumble under the knife but at the same time soft enough to be cut manually. Upon optical microscope inspection it was revealed that not every particle was cut right through the middle (or cut at all). But due to the sheer volume of particles there were always particles that were cut right near their middle plane. The cross-section produced by manual cut exhibited higher degree of roughness compared to embedded and polished particles but was still good enough for analysis. The second method differed only in the type of adhesive used to anchor the particles. A non-carbon based, inorganic paste (silicate based) with Ni particles to enhance conductivity was used as adhesive. In the same described fashion, aluminum sample holders with a thin layer of Ni paste were sprinkled with impregnated powder. After removing the loose particles, the samples were left to dry for 24h at RT before they were cut manually as described above. The success rate in obtaining suitable cross-sections was similar to the one when carbon tape was used.

4.2.3.4   *Sputter coating*

In order to increase electrical conductivity of specimens, all resin-embedded samples were sputter coated with gold in an EMS 550 sputter coater. Sputter coating eliminates build-up of electrical charge and increases the amount of secondary electrons that are produced from the surface, ultimately improving the SEM picture quality by reducing the signal-to-noise ratio. The gold layer was estimated to be about 10-15nm in thickness. The coating process was performed in an argon atmosphere under reduced pressure ($1.5x10^{-1}$ mbar) for 2 minutes at 35 mA current.

4.2.3.5   Energy dispersive spectroscopy and SEM

Energy dispersive X-ray spectra for all samples were collected with an Oxford X-Max 80 EDS probe. Before proceeding with the analysis, all peaks were confirmed by comparison with a fitted theoretical spectrum using the "Fitted Spectrum Tool" in the Aztec software package based on pre-selected elements. The fitted theoretical spectrum is generated based on the specified elements that are thought to be present in the sample and theoretical first principles about their X-ray emission. If all elements that are truly present in the sample are identified correctly (automatic or manual identification) then all peaks in the map spectrum will match those in the fitted spectrum. The software also calculates average concentrations of all elements detected in the entire field view, displayed as weight percent (wt%) and the associated statistical error, displayed as σ (weight% sigma), which is the overall confidence figure for the analysis. Elements which are detected just above the statistical noise are displayed in red. All EDS maps were collected using the "TruMap" option in the software. In this mode, the maps are corrected for peak overlaps and any false variations due to X-ray background. Parameters for the EDS analysis were chosen such that the resulted "dead time" was less than 30%. This is the time when effectively the detector is switched-off and the software is integrating the data to minimize noise. Parameters for the EDS analysis included: high vacuum mode, accelerating voltage: 15 keV, spot intensity: 50, resolution 516 or 1024, process time: 4-6, and pixel dwell time: 150 μs. SEM pictures were collected using secondary electrons (SE) mode and slow scan. For samples that were not Au-coated, SEM pictures were collected using fast scan mode to allow for acceptable quality.

4.3 Results

EDS is a very powerful analytical technique for quantitative and qualitative elemental analysis of solid composite materials. The spatial resolution is high and depends on the accelerating voltage used in the analysis. The spatial resolution in EDS analysis also includes subsurface sample layers since X-rays have curtain penetration depth depending on their energy intensity. Structures in the range of 50 nm (length, width and depth) or less can be investigated using low accelerating voltage of 3 keV. As the voltage is increased, the spatial resolution is decreased and for 12 keV it goes up to 500 nm [168]. The number of X-ray counts produced is directly proportional to the accelerating voltage, which therefore could affect also the limit of detection of trace elements. Achievable limit of detection in modern SEM/EDS systems can reach 1000-3000 ppm (0.1-0.3 wt%)[117]. Therefore a balance between desired spatial resolution and limit of detection needs to be considered when choosing the optimal accelerating voltage.

The two APIs used in this work can be detected by the characteristic K-series produced from the chlorine and nitrogen atoms present in Fenofibrate and Acetaminophen respectively. The corresponding concentration of chlorine and nitrogen in the respective APIs (based on molecular weight) are 9.8wt% and 9.3wt% respectively. The lowest API loading in tested Neusilin impregnated samples was 10wt% (on average), which makes the concentration of chlorine and nitrogen in the samples to be 0.98wt% and 0.93wt% respectively. In order to achieve the desired limit of detection, the analysis in this work was performed using 15 keV. The resulting spatial resolution based on the used accelerating voltage was estimated to be less than 1 μm, which is more than adequate to

determine impregnation profiles differences in the 150-200 μm particles used in all analysis presented.

Embedding with Acrylic Resin

Figure 4-2 shows an SEM picture and EDS maps for corresponding elements present in pure Neusilin®, embedded in LR White resin and coated with gold. The analysis shown is for a polished cross-section of non-impregnated particle of about 200 μm. Neusilin® is a synthetic, amorphous form of magnesium aluminometasilicate with an empirical formula of $Al_2O_3 \cdot MgO \cdot 1.7SiO_2 \cdot xH_2O$. The embedding resin ($C_{27}H_{32}O_6$), catalyst ($C_{14}H_{10}O_4$) and accelerator ($C_9H_{13}N$) all have carbon, oxygen, hydrogen and nitrogen (accelerator only) as part of their molecules. The EDS maps show the spatial distribution of carbon (C), oxygen (O), aluminum (Al), silica (Si) and magnesium (Mg). The last three elements are characteristic only to Neusilin and the maps clearly show that (all are present in the particle substrate only). Larger pores and crevices seen in the SEM are also seen in the Al/Si/Mg maps confirming that these are empty spaces within the particles. This is clearly visible when EDS maps are overplayed on top of the SEM (picture not shown). These internal empty spaces are filled with resin during the embedding process as seen on the C-map. Carbon, which is characteristic only to the resin, is detected at a higher concentration between the particles as indicated by the more intense red color on the C-map. Due to its low viscosity, the resin quickly impregnates the entire particle and shows as less intense red color. Because Neusilin® particles are carbon-free, mapping of carbon could be another way of detecting and visualizing the spatial distribution of an API (or any other carbon-based impregnant). However, the impregnation of Neusilin® with the resin during sample preparation makes C-mapping inadequate for determining

impregnation profiles of organic compounds in porous particles. In these cases, API mapping could only be achieved if they possess another characteristic element in their molecule that could be detected. Oxygen, which is a common element to both the resin and Neusilin® is confirmed by the EDS analysis. Because it has higher levels in Neusilin® compared to the resin, oxygen shows with brighter green color within the particles and less intense green within the resin.

In order to test feasibility of profiling the spatial distribution of an impregnated API, Neusilin® particles impregnated with Fenofibrate (40wt% on average) were embedded in LR White resin (cut, polished and Au coated) and subjected to SEM/EDS analysis. Figure 4-3 shows the SEM picture, the EDS maps for corresponding elements present in Neusilin impregnated with Fenofibrate and the resulting X-ray spectrum. Because carbon could not be used to uniquely detect the API (as discussed above), the focus of the analysis was directed towards detecting the K series of the Cl atoms characteristic to Fenofibrate. The corresponding X-ray spectrum shows a distinct Cl-peak detected at 0.3 wt% with an adequate statistical significance (identified by the software by its white color in the table of detected elements). The EDS map shows chlorine as uniformly distributed throughout the entire sample (particles and surrounding resin). Despite originating from the impregnated particles, the API appears to be diffusing out into the resin. Upon further investigation it was discovered that Fenofibrate has appreciable solubility (> 50mg/ml at RT) in the liquid resin (determined before polymerization). This is enough to cause complete dissolution and redistribution of the API during the resin embedding process. This result showcases the inadequacy of the resin-embedding method to produce reliable results for detecting impregnated Fenofibrate and determining its

spatial distribution within a porous carrier. An attempt was made to repeat the analysis using Acetaminophen-impregnated Neusilin as this API did not have high solubility in the liquid resin and thus it should have been possible to map its distribution within the particles. However, it was discovered that Acetaminophen had an inhibiting effect on the resin polymerization reaction and particle embedding was unsuccessful.

LR White resin (or acrylic resins in general) is an excellent embedding media for producing a clean and polished cross-section of small particles for SEM/EDS analysis. When working with supported catalysts, the resin-embedding method can lead to excellent elemental mapping of the active metals, as the metals usually do not interact with the resin (exhibit no solubility or reactivity). When trying to map an impregnated API however, due to its more complex chemical structure, interactions with the resin may occur, which could hinder the EDS analysis producing unrealistic results. In order to still be able to study the impregnation profiles of APIs, other organic surrogates could be used in their place. These surrogate substances ideally should have some general properties as follows: be organic molecules (resemble organic APIs), have solubility in organic solvents (ability to be impregnated using same methods) and exhibit no solubility or reactivity with the resin. Another required property would be to have an element present in the molecule that gives a good, distinct X-ray signal, away from those already present in the composite sample coming from resin or porous excipient (C, O, Mg, Si, Al). A class of substances that can act as good surrogate impregnants and that could help in the study of impregnation profiles are the salts of organic acids. For example, there are many pharmaceuticals which are in the form of a potassium salt of a free acid. In general, they exhibit good solubility in water and organic solvents, which makes them ideal for

impregnation of excipients. The most important asset they have is the presence of a potassium atom in their molecule. This alkali metal produces a strong, distinct Kα peak at 3.3 keV, which is safely away from the other elements present in a Nesulin®/resin sample allowing for a clear detection.

One such candidate for a surrogate impregnant that could be used to study impregnation profiles in excipients is potassium acetate (KAc). It is soluble in water and alcohols, insoluble in LR White resin and does not interfere with the polymerization process of the resin. In order to test its feasibility in mapping the impregnation profile, Neusilin® particles (sieved, 150-200µm range) were impregnated with potassium acetate, embedded in resin and their cross section was analyzed by SEM/EDS. Figure 4-4 shows the EDS maps of all characteristic elements present in those samples. Maps for Si, Al and Mg clearly outline the excipient particle. Although KAc contains carbon in its molecule, the C-map is not a reliable indicator of its distribution since the C-based polymer has impregnated the particle during embedding. The strong and distinct potassium peak however is a good indicator of the KAc distribution within the particle. The K-map shows unambiguously that the impregnation profile is highly uniform. This is to be expected since the porous carrier (Neusilin®) in this case was impregnated by dry impregnation technique followed by slow drying. It has been shown in catalyst preparation that the impregnation profile can be greatly affected by the drying rate, with slow drying usually resulting in a uniform profile [20]. It is also clear from the K-map that potassium is only located in the impregnated particle, indicating that KAc is insoluble in the resin.

Potassium acetate (as well as many other potassium salts) is characterized as a deliquescent material. These are substances which are very hygroscopic and when exposed to ambient air absorb large amount of water to form an aqueous solution. Therefore, special care and handling should be employed when working with KAc impregnated excipients. Improper storage could result in completely solubilizing the salt inside the particles, which in turn will alter the original impregnation profile producing inaccurate results. In order to illustrate the possible outcome of improper storage, impregnated Neusilin® with KAc was left for several days exposed to ambient air to pick up moisture and then dried quickly in a vacuum oven. The corresponding cross-sectional EDS analysis of resulting impregnated particles embedded in resin is shown in Figure 4-5. Maps of Al, Mg and Si all show a uniform distribution, confirming that the impregnated particle has a homogeneous structure without any internal defects. The map for potassium however shows a completely different picture, where the distribution of the K signal is far from uniform. The resulting profile is a combination of egg-shell and egg-yolk type distributions, resulting in an annular region of low concentration. This profile can be explained by the deliquescent nature of KAc. When deposited KAc picks up moisture, it forms an aqueous solution inside the impregnated Neusilin® and becomes highly mobile. When fast drying is applied, the salt is redistributed towards the outer surface of the particle due to the fast convective flow generated during drying. This result showcases the ability of EDS analysis for detecting differences in the impregnation profile within impregnated excipients. Good solubility in water and organic solvents (alcohols) coupled with its strong Kα peak for detection and no interaction with the resin

make KAc a good indicator for studying impregnation profiles of resin-embedded particles by SEM/EDS analysis.

Embedding with Cyanoacrylate Adhesive

Studying impregnation profiles by EDS analysis relies on the detection of a characteristic element specific to the impregnated substance. The confidence in the detected impregnation profile determined by EDS therefore could be improved by increasing the number of detectable elements characteristic to the impregnated substance. Another good candidate for studying impregnation profiles could be potassium iodide (KI). Similar to KAc, it has good solubility in water and organic solvents (alcohols), which makes it applicable for impregnation studies. The added benefit is the presence of iodine (I), which gives a strong, distinct Lα peak at 3.9 keV, safely away from potassium and the other elements present in a Nesulin®/resin sample, allowing for a clear detection. The ability to identify the impregnated substance by two different elements increases the degree of confidence in the detected impregnation profile type. Unfortunately, attempts to embed KI-impregnated particles in LR White resin were unsuccessful and cyanoacrylate adhesive (Super Glue) was used instead. Figure 4-6 shows the SEM picture and EDS maps for all characteristic elements present in impregnated Neusilin® with KI embedded in Super Glue. To our knowledge, the technique of embedding particles in Super Glue followed by polishing to obtain cross-section for EDS analysis has not been reported previously. The quality of the cross-section produced by this technique (as evident by the SEM picture) is identical to the one obtained by using LR White resin. Embedding particles using Super Glue is much easier and less expensive than using acrylic resins (such as LR White). Although it dries quickly, the adhesive still had time to infiltrate the

particles as is evident by the C-map, where all the carbon detected internally is due to the glue itself. The impregnation profile of KI is detected by both the K and I signals and shows to be highly uniform. This again is to be expected due to the slow drying of the impregnating KI solution. The solubility in water and organic solvents (alcohols), the lower hygroscopicity than KAc and the presence of K and I signals for detection by SEM/EDS analysis makes potassium iodide a very good candidate for studying the dependence of impregnation profiles on processing parameters.

Embedding with Carbon Tape

Using carbon-based resins for particle embedding has the advantage of producing very smooth cross-sections for SEM/EDS analysis. A smooth and polished surface is highly desirable if a very accurate quantitative analysis is needed. As shown by other researchers, polishing the surface to different degrees of roughness can greatly influence the coefficient of variation of the quantitative results[169]. The drawbacks of using resins for analysis of API-impregnated excipients can be summarized as follows: 1) resins penetrate into the porous matrix and make carbon signals useless for API detection, 2) resins could solubilize the API, producing an erroneous impregnation profiles, 3) resins could be affected by the sample resulting in incomplete polymerization and 4) presence of resins could affect the X-ray signal generated from the samples and affect the limit of detection for some trace elements (which sometimes are the only markers for API detection). Embedding techniques are usually employed due to the very small size of the sample/particles to be analyzed. Ideally, if particles could be cut in half without introducing any other agents (resins or adhesives) then EDS results would be meaningful and the above disadvantages would be eliminated.

In order to eliminate the use of embedding resins, a procedure for manual cutting of Neusilin® particles with sizes above 150 μm was developed. Figure 4-7 shows the SEM/EDS cross-sectional analysis of impregnated Neusilin® particles (average 10% Fenofibrate loading) produced by manual cutting, without any resins; the samples were Au coated. The SEM picture reveals the quality of the resulting cross-section: right through the middle of a 180 um particle with uneven, rough surface. The nature of the surface is further confirmed by the EDS maps of all elements characteristic to Neusilin® elements: Mg, Si, Al and O (also characteristic to Fenofibrate). X-ray spectrum results reveal a more distinct Cl peak (peak area of 43934cps/eV), detected at a higher levels (0.5wt%) compared to the same peak in Figure 4-3 (0.3wt%, peak area of 32733.3cps/eV), despite the fact that here Fenofibrate loading is four times less (at 10% average loading vs. 40% average loading in Figure 4-3). These results show the effect of resin on the overall signal – the absence of embedding media improves the detection of trace elements. The Cl-map shows that the relative distribution of chlorine on the particle surface is highly uniform. This is the first clear indication of the API (Fenofibrate) distribution within the porous carrier (Neusilin®) obtained during fluidized bed impregnation. The ability of any impregnation process to deliver uniform distribution of the API is highly desirable as this will have a direct impact on both content uniformity and dissolution kinetics. Uniform distribution means that the API is deposited evenly over the entire available internal surface area of the excipient.

The spectrum also shows reduction in the carbon signal (40.7wt% vs. 69.6wt% in Figure 4-3), which is another direct consequence of the absence of carbon-based resin. The carbon signal in Figure 4-7 is coming from two sources: carbon tape used to immobilize

the particles and the API itself. The particle's cross-section and carbon tape are not in the same focal plane, with the electron beam being focused primarily on the sample surface. This leaves most of the carbon tape out of focus or in the shadow of the electron beam. As a result, most of the carbon signal should be coming from the analyzed particle surface with only a small fraction coming from the carbon tape. One way to determine if the carbon seen on the C-map is coming primarily from the API is to calculate the ratio of Cl/C. Based on the molecular formula of Fenofibrate ($C_{20}H_{21}ClO_4$), the theoretical Cl/C ratio is 14.8%. The X-ray spectrum in Figure 4-7 shows that this ratio is 1.2%. Despite the fact that there is no carbon-based resin, the Cl/C ratio is still much smaller that theoretical value, indicating that there is more carbon detected than there should be. One hypothesis is that during the Au sputtering process, carbon from the tape is re-deposited on all tested surfaces. This result suggests that Au sputtering should be avoided, if possible, in order to eliminate carbon contamination in the sample and to enable carbon detection from the API only. Another hypothesis is that in spite of the Carbon tape being out of focus it is still being picked up in the spectrum.

Figure 4-8 shows SEM/EDS analysis of impregnated Neusilin® with a different API, Acetaminophen (APAP) at a 10% average loading. Similar to the previous case, the particles were immobilized on carbon tape and manually cut to obtain a cross-section with the only difference being the absence of Au coating. Despite the lack of conductive coating, the SEM still produces enough detail (using fast scanning) to reveal the rough surface of the cross-section. The molecular formula for Acetaminophen ($C_8H_9NO_2$) reveals that the API can be detected using the nitrogen (N) Kα peak at 0.4 keV. In spite of being close to the carbon peak (Kα at 0.3 keV) and oxygen peak (Kα at 0.5 keV) the

SEM/EDS can still detect nitrogen in a statistically significant manner. This would not have been possible if there was an embedding resin of any type present in the sample, because that would have increased the C-peak and O-peak intensities and would have covered the N-peak that resides between the two. The EDS spectra also reveals that the amount of carbon detected (19.9wt%) is much less than the previous case of Fenofibrate impregnated in Neusilin® (40.7wt% in Figure 4-7), despite the fact that both APAP and Fenofibrate have roughly the same carbon content in their molecules (64% and 67% respectively) and the two formulations were both at 10% average loadings. This fact could be attributed to the lack of Au sputtering, which as mentioned may be redistributing carbon from the C-tape used as the particle adhesive. The N/C ratio calculated from the EDS spectra is 8.0%, which is closer to its expected theoretical ratio of 14.6% in APAP (compared to the Cl/C ratio in Figure 4-7 in the case of Fenofibrate). Since no Au sputtering was carried out for the APAP case, the extra carbon in the sample is coming from the C-tape detected in the background. This result shows that the C-peak is becoming more reliable for detection of the API and with some degree of caution, it could be used also to gauge the API distribution within the sample. Both the C-map and N-map show a uniform distribution of the Acetaminophen. This is another indication that the fluidized bed impregnation method has the ability to produce highly uniform distribution of APIs throughout the porous excipient. The fact that both formulations show uniform distributions of the APIs (Fenofibrate and Acetaminophen) supports previous claims that FB impregnation process is highly dependent on processing conditions (drying gas temperature and flow rate, spray rate and solvent nature) and less dependent on the nature of the API.

Embedding with Non-Carbon Based Adhesive

Since all APIs are organic compounds, they can in principle be detected by their carbon footprint in the impregnated excipient. As has already been shown, this is not always a straight-forward procedure due to the carbon contamination from the various resins or adhesives used during sample preparation. This contamination can be eliminated by switching to a non-carbon based adhesive. The only available inorganic-based (and carbon free) adhesives are sodium or potassium silicates. These are inorganic substances, usually supplied as an aqueous solution with low viscosity. Upon dehydration, the silicates rapidly increase their viscosity and when completely dry they become very hard, clear solids with glass resemblance (often called "water glass"). Since they are non-conductive, additives (in the form of powder metals such as Ag, Au or Ni) are needed in order to be used as adhesives in SEM sample preparation. Silicate-based carbon-free Ni paste, specially formulated for SEM use, was used as an adhesive to immobilize a monolayer of Neusilin® particles impregnated with Fenofibrate. Samples were left to dehydrate and harden under ambient conditions for 24 h. Heat was not used since Fenofibrate has a lower melting point (81.6 °C) than the temperature usually required for heat curing this silicate adhesive (93°C). Drying of the paste was enough to produce adequate hardness to allow the particles to be manually cut. Figure 4-9 shows the results from SEM/EDS analysis of the same Neusilin®/Fenofibrate formulation as in Figure 4-7, but embedded in Ni/silicate paste. The X-ray spectrum shows that the detected carbon content is at 13.3%, which is the lowest carbon reading among all previously presented results. This is a direct consequence of the carbon-free paste used for embedding. The Cl/C ratio of 4.5% however is still much lower than the theoretical value for Fenofibrate

(14.8%), indicating that there is more carbon present in the sample than expected. One possibility for this phenomenon is that during curing, the silicate reacted with CO_2 to form carbonate and carbon was trapped in the adhesive. When the electron beam was focused on a much smaller area (about 60μm x40μm) of the particle's cross section (Figure 4-10) the EDS analysis showed much lower carbon content (9.7wt%) and the Cl/C ratio increased to 12.4%, much closer to the theoretical value of 14.8. This result indicates that the particle itself has less carbon than the image of the particle and tape together (see Figure 4-9) suggesting that the inorganic adhesive did in fact "take in" carbon during cutting. AT the same time, most of the carbon detected in the cross-section in Figure 4-10 is coming primarily from the API itself. Therefore, the C-map in Figure 4-9 can be used as an indicator of the spatial distribution of Fenofibrate. Both the Cl-map and C-map confirm that the API distribution within the impregnated Neusilin® is highly uniform. This is a further evidence that fluidized bed impregnation of pharmaceuticals onto porous excipients can deliver a highly uniform API profile.

4.4   Conclusions

In this study, a method for cross-sectional analysis of impregnated excipient particles using energy dispersive x-ray spectroscopy has been presented. The aim of the work was to determine the methodology most suited for studying the impregnation profiles achieved during fluidized bed impregnation of APIs onto porous excipients. The focus of the analysis was to develop methods for determining the relative spatial distribution of the active ingredient within the impregnated particle rather than a fully quantitative analysis. The APIs chosen for the investigational work were Fenofibrate and

Acetaminophen and the porous carrier was Neusilin®. Two other candidates were introduced (KAc and KI) as potential surrogate substrates for impregnation studies.

Several particle embedding methods were demonstrated, highlighting their benefits and shortfalls. Acrylic resins (LR White) used for particle immobilization showed the ability to produce excellent cross-sections with a smooth surfaces. In the case of Fenofibrate, the EDS analysis of LR White embedded samples failed to produce the real API distribution due to the API's high solubility in the resin. In other cases (Acetaminophen and KI) the resin failed to polymerize due to a substrate/resin interaction. When KAc was embedded in LR White resin, the EDS analysis showed its full potential and ability to detect differences in the impregnation distributions (uniform vs. egg-shell/egg-yolk profiles). Cyanoacrylate adhesives (Super Glue) showed similar ability to produce high quality cross-sections without the drawback of a substrate/media interaction (lack of polymerization). A major disadvantage of using embedding media was its penetration within the porous particle during sample preparation.

The presence of carbon-based adhesive/resin inside the particles presented two major problems: 1) it impeded the detection of the API by its carbon signal and 2) it lowered the detection signal for the other characteristic elements (N or Cl) that could be used for analysis. In order to overcome these shortfalls, a different method for producing cross-sections of particles was introduced. This involved the immobilization of a particle monolayer onto carbon tape or non-carbon, silicate-based Ni paste, followed by manually cutting the particles. This technique produced cross-sections with a higher degree of roughness but without any embedding media inside or around the particles. This

improved the detection of trace elements from the API's molecule since glue did not penetrate the sample. In addition, the carbon in the sample from sources other than the API was significantly reduced, allowing its use for API detection. At the same time, the use of carbon had a number of drawbacks for use as an element for analysis. During the Au sputtering process, it appeared that carbon from carbon tape was re-deposited on all tested surfaces. Even when no Au sputtering was carried out for the carbon tape, it appeared that the C-tape was detected in the background. When work was carried out for a silicate-based carbon-free Ni paste it appeared that the paste took on carbon during curing. The detection of trace elements from the API's molecule was also improved. EDS analysis based on both carbon and trace elements (Cl for Fenofibrate and N for Acetaminophen) showed a uniform profile in both fluidized bed impregnation formulations, showcasing the potential of the impregnation process to produce highly desirable uniform API distributions.

4.5   Figures for Chapter 4
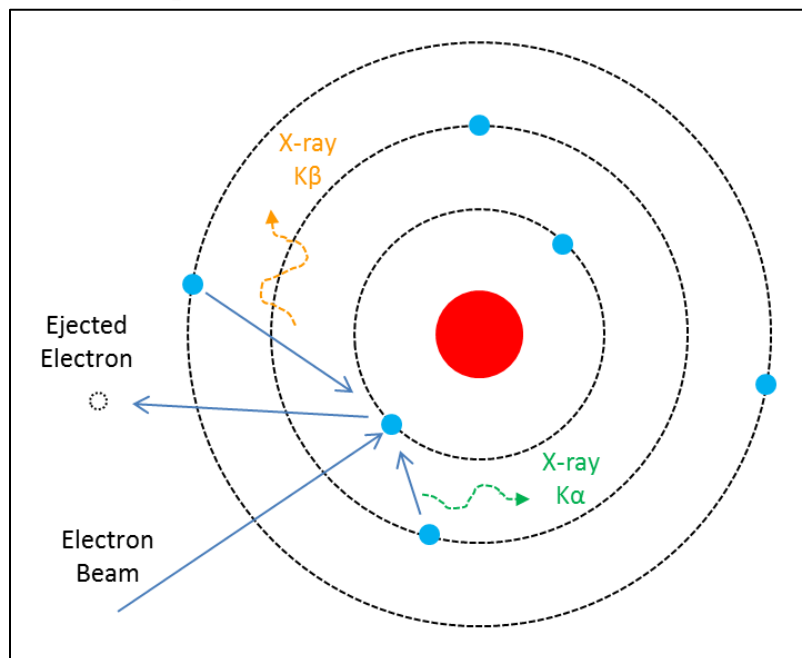
Figure 4-1: Mechanism of characteristic X-ray emission.
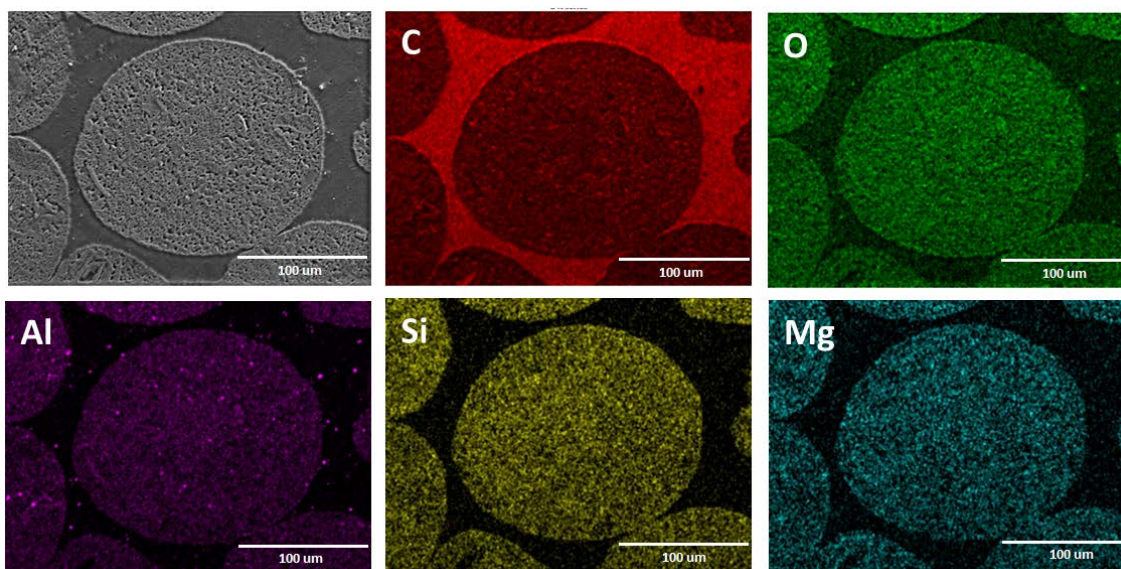
Figure 4-2: SEM picture and EDS maps for characteristic elements in pure Neusilin® embedded in LR White resin (Au coated).
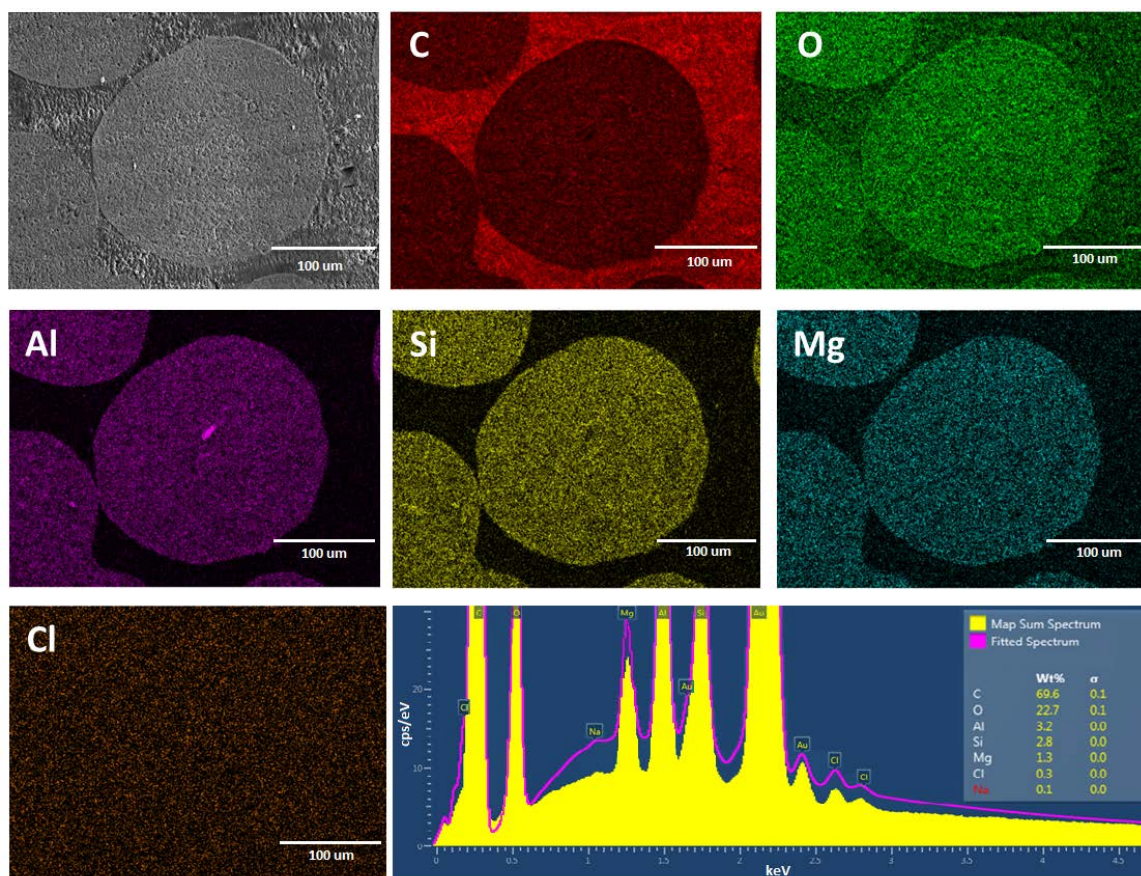
Figure 4-3: SEM picture, EDS maps and corresponding X-ray spectrum for characteristic elements in impregnated Neusilin® with Fenofibrate (40% average loading) embedded in LR White resin (Au coated).
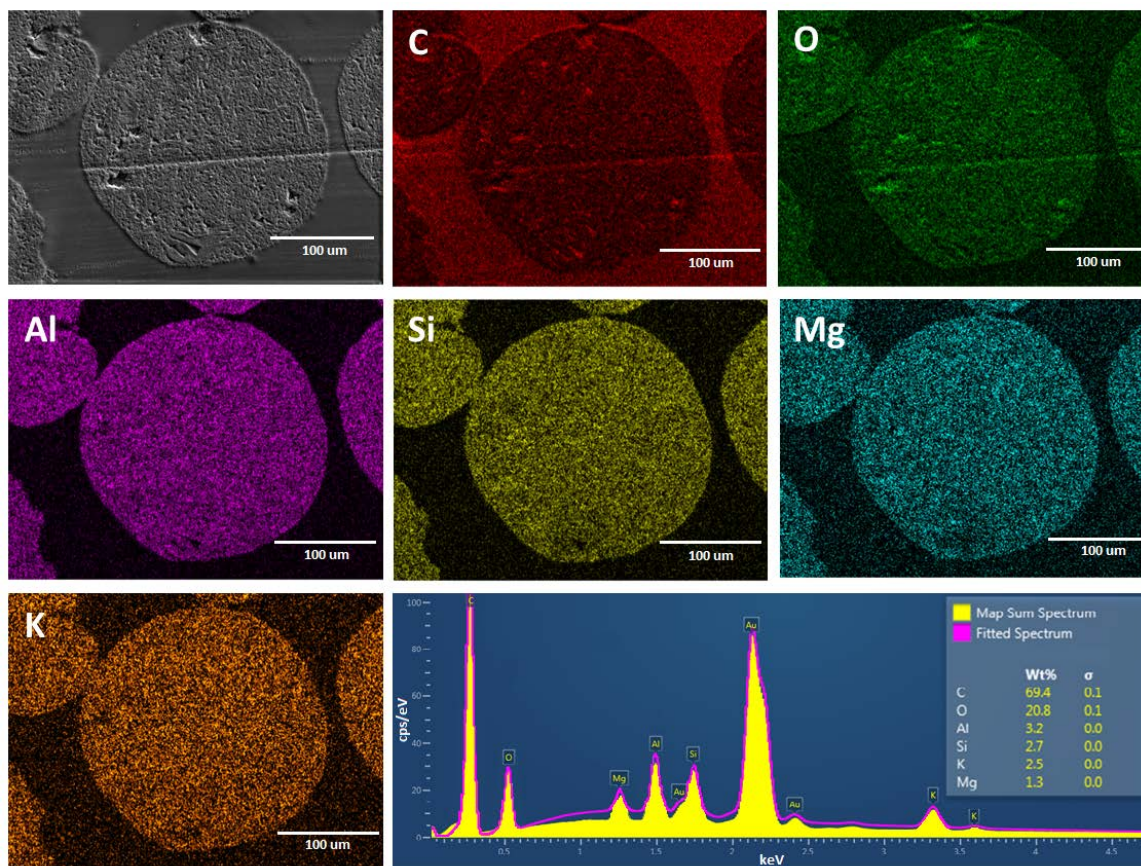
Figure 4-4: SEM picture, EDS maps and corresponding X-ray spectrum for characteristic elements in impregnated Neusilin® with Potassium Acetate embedded in LR White resin (Au coated).
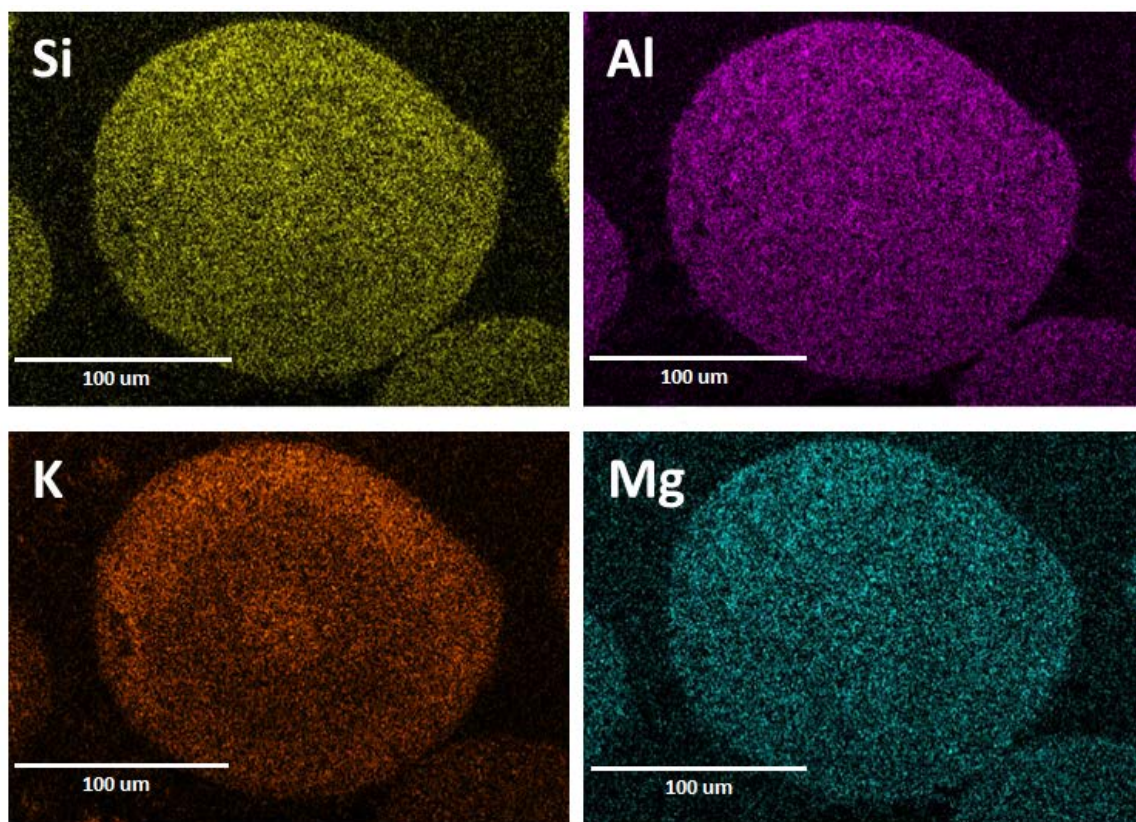
Figure 4-5: EDS maps for characteristic elements in impregnated Neusilin® with Potassium Acetate (fast dry) embedded in LR White resin (Au coated).
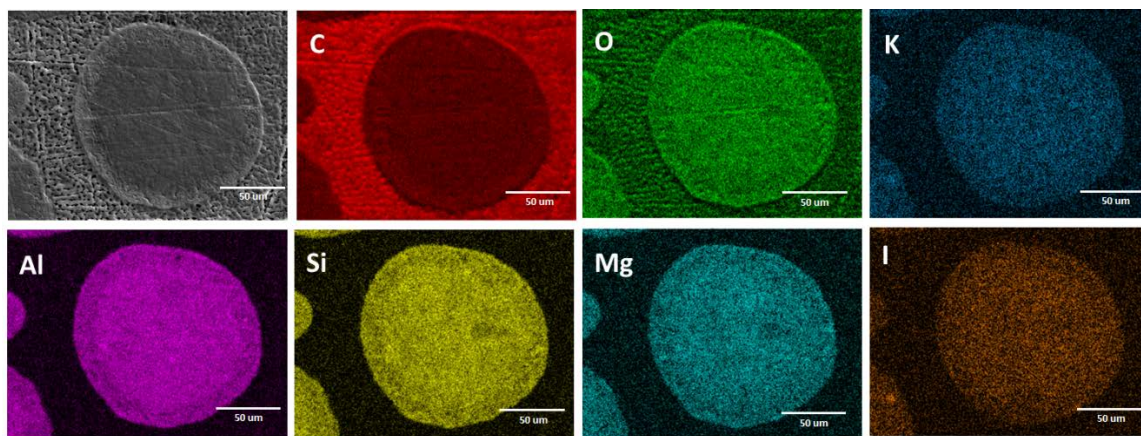
Figure 4-6: SEM picture and EDS maps for characteristic elements in impregnated Neusilin® with Potassium Iodide embedded in Super Glue (Au coated).
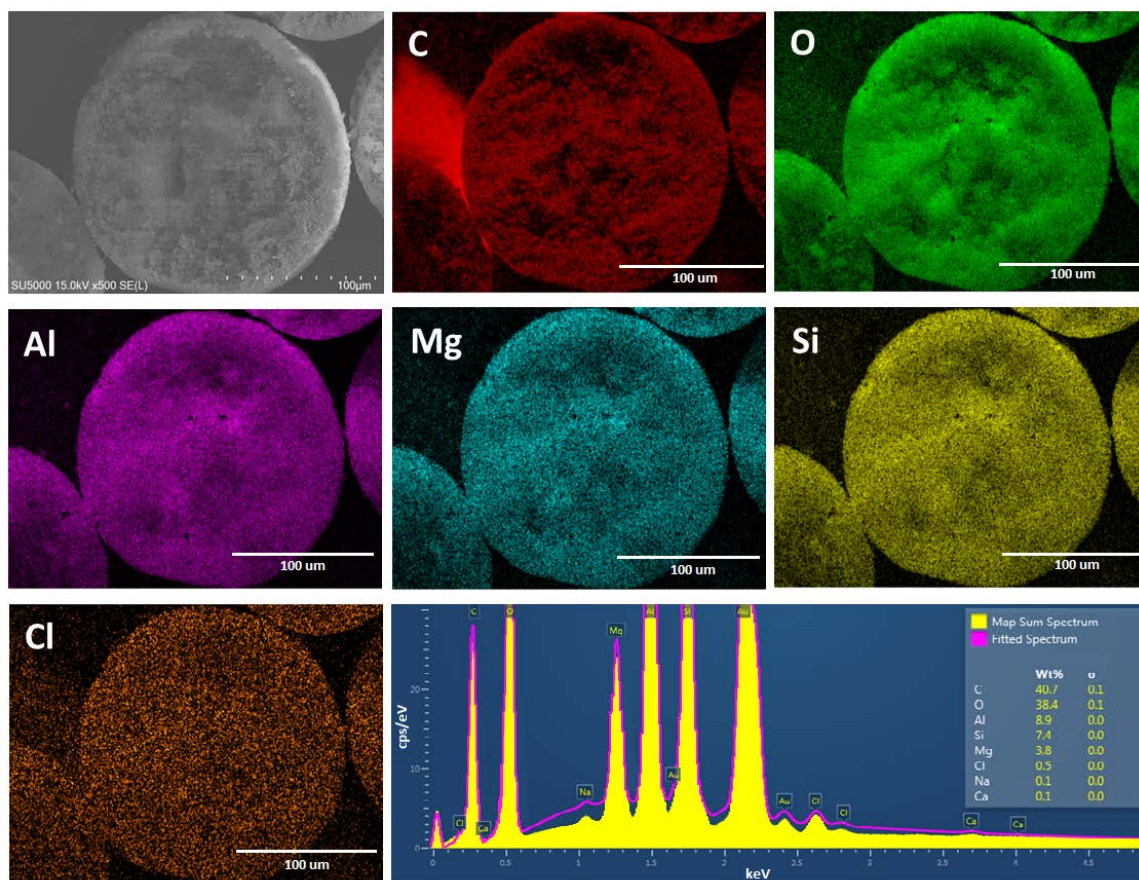
Figure 4-7: SEM picture, EDS maps and corresponding X-ray spectrum for characteristic elements in impregnated Neusilin® with Fenofibrate (10% average loading) on carbon tape, cut manually (Au coated).
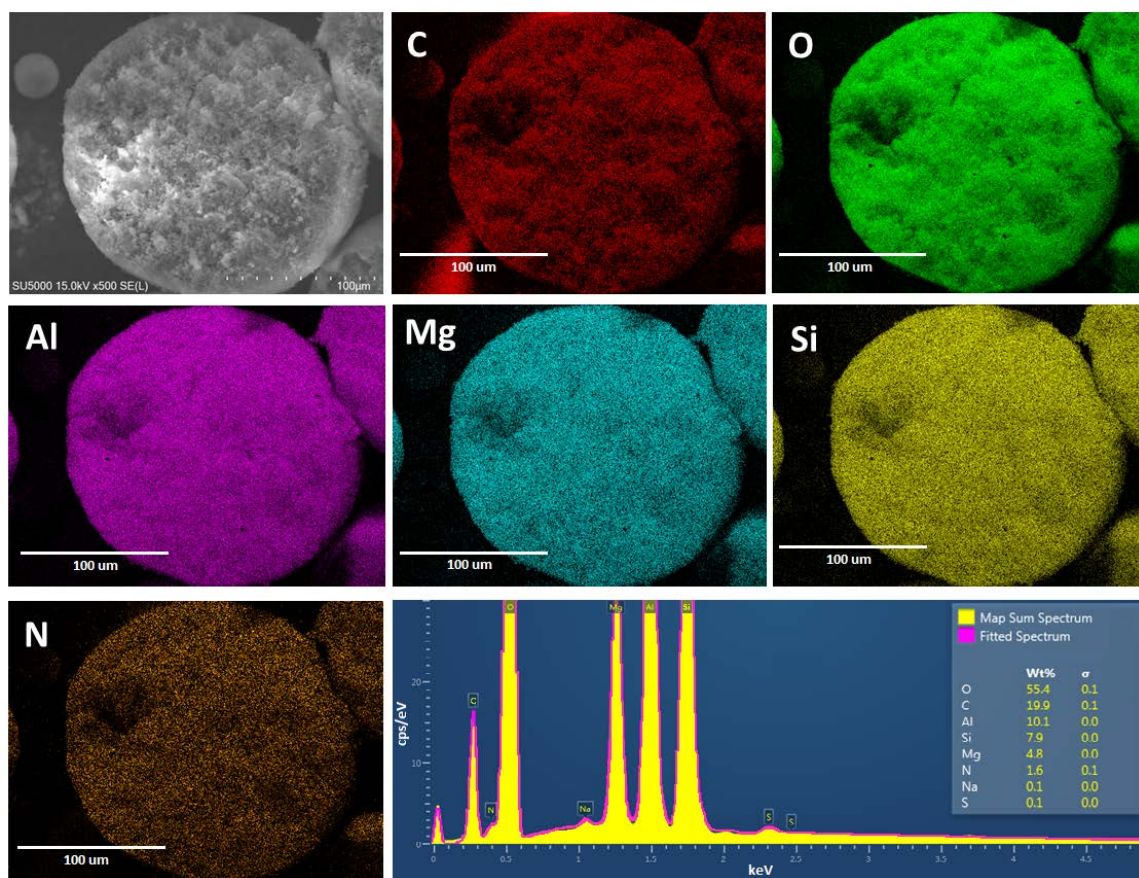
Figure 4-8: SEM picture, EDS maps and corresponding X-ray spectrum for characteristic elements in impregnated Neusilin® with Acetaminophen (10% average loading) on carbon tape, cut manually (without Au coating).
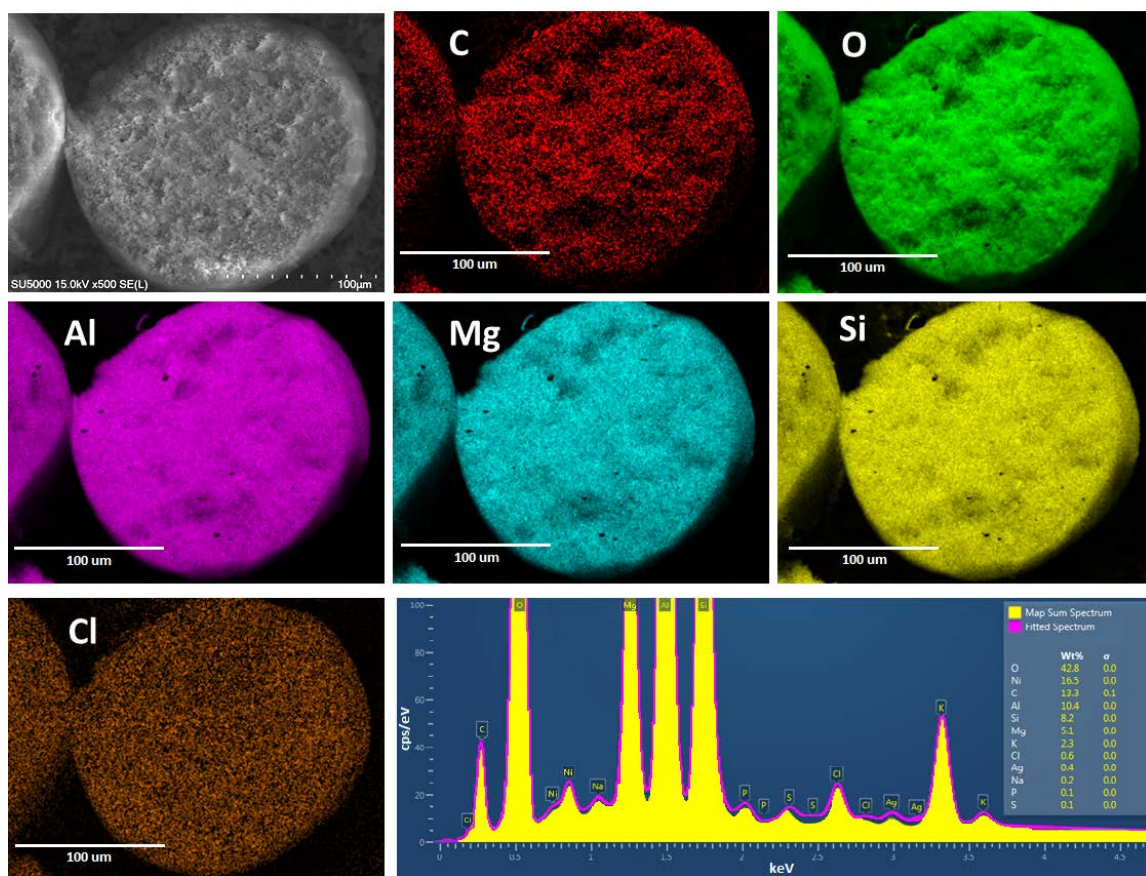
Figure 4-9: SEM picture, EDS maps and corresponding X-ray spectrum for characteristic elements in impregnated Neusilin® with Fenofibrate (10% average loading) on Ni paste, cut manually (without Au coating).
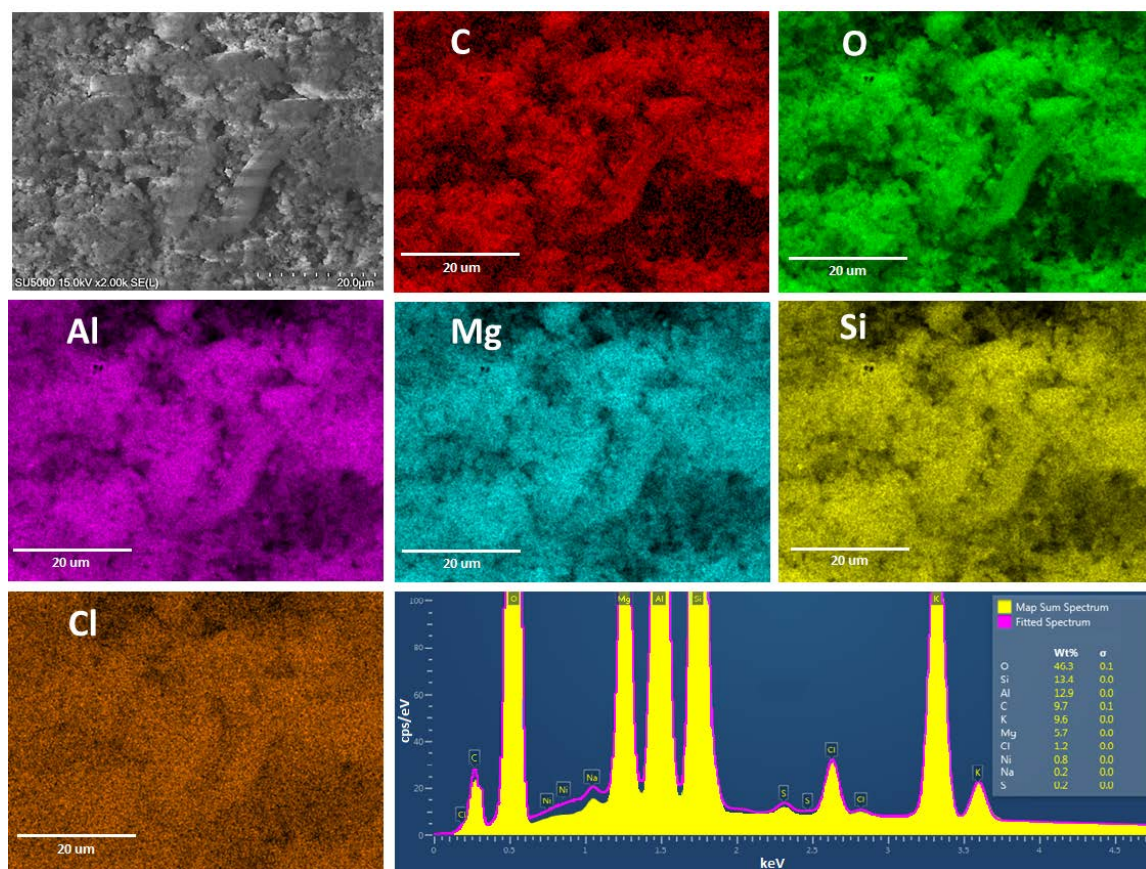
Figure 4-10: Zoomed-in SEM picture, EDS maps and corresponding X-ray spectrum for characteristic elements in impregnated Neusilin® with Fenofibrate (10% average loading) on Ni paste, cut manually (without Au coating).

Chapter 5 .   Establishing basic framework for mathematical modeling of FB impregnation process in a porous medium

5.1   Introduction

Mathematical modeling of chemical engineering systems can be a powerful tool to study the effect of processing parameters and material properties on the outcome of the physical process (heat/mass transfer, crystallization, reaction kinetics, drying, etc.). Models can be very useful in predicting a trend related to a specific parameter/property or in the design of chemical equipment (e.g. reactors, dryers, mixers, extractors). Impregnation is one of those processes that has greatly benefitted from mathematical modeling. Historically, the main application of impregnation has been in supported catalyst preparation, an area that has seen a steady increase in modeling development in the past 40 years. As previously described, the process consists of impregnating a porous carrier with a precursor solution and subsequent drying, leaving the active substance inside the support. The competition of several transport phenomena determines the final spatial distribution of the catalysts. These include convection, diffusion, adsorption and crystallization. There are several distinct types of catalyst profiles that can be generated depending on the processing conditions and materials used: uniform, egg-yolk, egg-shell and egg-white [16, 170]. The preference toward a certain profile depends on the particular catalyst application. It has been demonstrated that egg-yolk catalysts are advantageous for negative order reactions, where poisoning of the catalyst occurs or where catalyst attrition is a problem [16, 171, 172]. When reactions are diffusion-limited, the active catalysts should be deposited on the outer shell of the support in order to minimize diffusion, hence egg-shell profiles are preferred [16, 112, 113]. Minimizing

competitive reactions is also possible by using egg-shell catalysts [173]. There are limited cases, where a uniform catalyst profile would result in a better performance [174]. This includes the case where mass transfer of reactants and products is rapid and maximum metal dispersion is desirable [175, 176].

Similar to catalyst preparation, the final API profile inside the carrier will be controlled by the impregnation and drying steps. Limited information is available on the effect of processing conditions and material properties on the API profile. Work in Chapter 4 already demonstrated methods for cross-sectional imaging analysis and reported a uniform profile of Fenofibrate inside impregnated Neusilin® particles produced in FBs. Allgeier et al. report a uniform API profile also in Neusilin®, obtained via solvent impregnation [177]. It is not fully understood what impregnation profile is more preferred when it comes to API impregnated pharmaceutical formulations. One could argue that uniform profiles would be ideal in cases where high loadings are preferred, as that will allow for better utilization of the available internal pore volume. Uniform profiles would be also preferred when improving the dissolution kinetics is the goal, as they will result in higher internal surface area of the impregnated API (which will promote faster dissolution). Further work looking into the effect of impregnation and drying on the final API profile is needed in order to fully understand potential control parameters.

In the case of catalyst preparation, it was assumed initially that the precursor profile was affected primarily by the impregnation step. One of the early attempts to model the impregnation step and the resulting metal distribution was proposed by Vincent and Merrill [176]. The single pore model that they proposed was based on the Washburn equation for liquid penetration into a cylindrical capillary [178] and included a Langmuir

adsorption kinetic term. Their results showed that the relative capacity for adsorption was the most important parameter in regulating the metal distribution. The model was further applied to spherical porous particles [123]. Later models for dry impregnation assumed that the liquid motion was governed by the Darcy's law for flow through porous media [112]. Experimental work in the field had revealed that drying could considerably alter the initial impregnation profile [110, 123], especially when the interaction between support and metal ions is week [179].Neimark et al. [15, 180] were one of the first to propose theoretical treatment of the impregnation and drying phenomena and their effect on the resulting catalyst profiles. They characterized slow and fast drying via dimensionless numbers and showed limiting cases where different metal profiles are expected. During very rapid drying, vapor removal is much faster than liquid capillary flows, causing the drying front to move inside the particle. As a result, the metal does not have time to redistribute, forming a uniform profile. For the slow drying regime, convective liquid transport is faster than solvent removal and the final catalyst profile is determined by the competitive convection and diffusion. These results showed a good agreement with experimentally determined catalyst profiles for the two limiting drying cases [123]. Single capillary tube impregnation models were further improved to include drying. Lee and Aris coupled convective (described by Washburn equation) and diffusive transport with an energy balance for a single capillary to produce a model describing catalyst redistribution during the constant rate drying period [110]. They showed that drying has little effect on the catalyst distribution in the case of strong adsorption. On the contrary, if adsorption is weak, drying can broaden the originally sharp profile. They

suggested that intense drying would suppress catalyst redistribution during the drying step.

A more complete model was proposed by Lekhal et al., which included mass and energy balances on all phases and components present during the drying stages: solvent liquid, solvent vapor, drying gas and metal ions [19, 181, 182]. The model assumed Darcy's law for liquid flow, used the dusty gas model for gas phase diffusion, utilized the Nernst-Planck equation to describe electrostatic forces, accounted for adsorption with a Langmuir kinetic term and included an experimentally determined correlation for capillary pressure vs. saturation. The model was able to capture the pre-heating, constant-rate and falling-rate drying periods and describe evolution of catalyst profile as a function of various operating conditions and material properties. They re-confirmed that drying does not affect the catalyst distribution under strong adsorption conditions; in those cases, the profile is set during the impregnation step. They were able to show that egg-shell profiles formed when the drying rate is high (high drying temperature) leading to high convective flows. When permeability of the support was high (large permeability constant), egg-shell distributions were also dominant. Examples with large diffusivity of the metal ions (large diffusion constant) led to more produce more uniform profiles due to the stronger diffusive back-flow. By utilizing dimensionless analysis they were able to construct profile maps as a function of three dimensionless groups describing the relative strength of convection, diffusion and adsorption. In later work they were able to explore more the complicated situation of a two-component system with co-impregnant. The interplay between the relative adsorption and diffusion coefficients of the two species were among the main factors determining the final metal profile. By revising the

Langmuir adsorption term they were able to improve the model and study the influence of pH and ionic strength of the liquid solution. Simulation data suggested that for high pH the adsorption constant is higher, which in turn results in the metal profile being set during the impregnation stage with a minimal to no effect of the drying rate. Liu et al. took the model one step further by incorporating an impregnation module (to study dry and wet impregnation) and included a crystallization term, which permitted study of the effect of crystallization along with adsorption [18]. They found that for weak adsorption, the dry impregnation process is faster than the wet impregnation, while for strong adsorption both methods exhibit similar behaviors. The effect of crystallization on the final profile was found to be significant for high metal concentrations where predominantly egg-shell distributions were obtained. Further improvements to the model included film breakage in order to account for isolated liquid during later stages of drying, which was necessary to get good agreement with experimental data [20]. It was found that high initial metal concentrations in the solution promoted highly uniform catalyst distributions. Experimental work suggested that precursor concentration has an appreciable effect on the drying rate as the concentration is increased. This led to further improvement to the model to include correction for the solvent vapor pressure as a function of the metal concentration [183]. The updated model also included small corrections for the solution properties as a function of temperature (density, viscosity, surface tension and solubility). The simulation results showed that the constant-rate drying period is not observed when the initial metal concentration is very high. Metal precursors with low melting points were shown to produce nearly uniform profiles due to melting of the metal salt during drying. A first step toward understanding microwave

drying was undertaken through experimentation. Microwave drying is a process during in which the particles are heated volumetrically, which provides rapid and uniform drying within the support. The experimental results showed that microwave drying produces a significantly more uniform profile compared to oven drying.

All of the work mentioned above involves continuum models based on the volume-averaging approach. They all require knowledge of capillary pressure and absolute and effective permeabilities as a function of saturation. These depend strongly on the particular porous matrix and need to be obtained experimentally. An alternative approach to describing flows in porous materials is possible via discrete models, which use simplified geometries to represent the real system. The structural information included in the model depends on its complexity. Single pore models have successfully accounted for pore size distribution [184, 185]. This modeling approach was utilized to describe a convection drying with isothermal and non-isothermal conditions for mono- and bimodal pore size distributions [186]. Although with some limitations, the model was able to demonstrate the effect of pore size distributions on the drying kinetics. Porous media with bimodal distributions (having macro and micro pores) will dry more easily than media with narrow pore size distribution. The capillary network model is a more complex representation, where spatial connectivity and pore shape can be incorporated [187-190]. The porous matrix is represented as a series of interconnected individual pores and throats, both having different sizes expressed through some distribution law. The number of neighboring connections for each pore (the coordination number) can also be adjusted to represent more accurately the real porous media. The pores serve as a reservoir for the liquid and their size determines the overall porosity of the domain. The size of the throats

determines the magnitude of the various transport parameters: intrinsic permeability is set by their length and capillary pressure is determined by their radius [191].

Studies utilizing pore networks have been used to examine the influence of various pore structures on the drying behavior. It was demonstrated that bimodal pore distributions lead to higher drying rates with a longer constant rate drying period [192]. It was also shown that the spatial connectivity can influence drying: more favorable drying kinetics is characteristic for networks with lower coordination number and smaller throat length. Viscous effects have also been studied using 2D pore network modeling [193]. Results have shown that liquid viscosity plays a significant role only for narrow size distributions. Capillary effects dominate over viscous forces for broad or bimodal distributions. Extending the study to 3D structures with viscous and non-viscous liquids reconfirmed this effect [194]. Pore network models can be applicable for real systems only if they closely resemble the actual pore structure, which is often of irregular shape. Using powerful imaging techniques such as X-ray microtomography, more realistic 3D structural features can be incorporated into the model [195].

Discrete pore network models have been applied to study impregnation phenomenon alone. Work in the area has successfully adopted this approach to study impregnation of single droplets into porous medium [191, 196, 197]. The modeling approach, integrating a micro-force balance at the liquid free interface, was able to describe the two-step imbibition process: primary (droplet still present on the surface) and secondary (no fluid left at the surface) infiltration. Results show that secondary infiltration could proceed long after primary infiltration has been completed. The imprint radius continuously increases throughout the spread with the liquid infiltrating a large volume of the porous

medium. Pore network modeling has also been applied to drying of a solute-solvent saturated porous system. Drying of a sucrose solution was investigated to determine the effect of dissolved solute on drying rates and liquid/vapor/solute distributions [198]. The model only accounts for diffusion and does not account for convective transport. Despite the absence of convective transport, the model could still capture the main aspects of drying of liquids and solutions present in porous media.

Recently the pore network approach has been applied to study the effect of drying conditions, pore structure and solute concentration on the distribution profiles in various porous supports after drying [199]. The model incorporated convective and diffusive transport of the solute for more accurate representation. It was demonstrated that slow drying rates lead to more pronounced accumulation of the solute at the particle surface, while faster drying resulted in more uniform distribution. Results also showed that smaller pore size and narrower distribution width produced more uniform solid profiles. More pronounced egg-shell profiles were obtained with higher initial solute concentrations, whereas lower concentrations resulted in more uniform profiles. The discrete modeling approach can be also used to compute effective transport parameters, such as capillary pressure functions or effective permeabilities, which in turn can be used in continuous modeling methods [200]. Accuracy of pore network models would increase if they could represent the actual pore size of the structure. Describing and studying nano-porous materials at the actual nano-level is still a difficult task with this approach, as it requires an enormous number of equations to be solved, which is limited computationally. Work in the area continues and time will show which modeling approach describes porous materials more adequately, continuum or discrete.

This chapter demonstrates a multi-scale modeling approach for a fluidized bed impregnation process. The model is applied to the same API/excipient system that was studied previously in Chapter 3 and Chapter 4: Fenofibrate as the active ingredient and Neusilin® as the porous carrier. The goal was to develop a mathematical model that calculates API impregnation profiles under typical processing conditions and compare those with experimentally determined Fenofibrate distributions in Neusilin® presented in Chapter 4. The model was then used to study the effect of several material properties on the final impregnation profile. The rest of the chapter is organized as follows. The modeling approach starting with a mass and energy balances on the entire fluidized bed is described, which allows the calculation of several important processing parameters. A single-particle model is presented next, which is achieved by the separation of energy (calculates evaporative flux) and mass (calculates API and solvent distributions) balances. Following is a description of all parameters used in the model and methods for their calculation/estimation. The capillary pressure vs. saturation relationship is calculated from experimental mercury intrusion porosimetry data for Neusilin®. The chapter ends with a discussion of all the simulation results, followed by conclusions.

5.2   Modeling approach

Fluidized bed impregnation process can be viewed as the continuous occurrence of these two consecutive steps (as depicted in Figure 5-1):

- Impregnation of the solid particle as it moves into the wetting zone of the fluidized bed impregnator

- Drying of the wet particle as it moves around the bed (until it is impregnated again when it goes again through the wetting zone).

In this work, modeling of FB impregnation of a single particle will be divided into two separate models, which are solved sequentially: 1) modeling of particle impregnation with API solution and 2) modeling of particle drying using the impregnation profile form step 1. This approach is justifiable only if the following condition is met: the impregnation step is much faster than the drying step. It will be shown in Section 5.5.3 that this is true for excipients with small pore size and for typical drying conditions during FB impregnation. Impregnation and drying rates are determined by the nature of the support (particle size, pore size, porosity, permeability), the solvent (heat of vaporization, heat capacity, density, viscosity, surface tension, contact angle with solid) and the API (concentration and solubility in solvent) and by the impregnation and drying conditions in the FB (drying gas temperature and flow rate, liquid spray rate and droplet size), which all become model parameters of interest. Both the impregnation and drying steps are ran sequentially to complete a single impregnation/drying cycle. If necessary, the cycle can be repeated until a desired API loading is achieved. Another important model parameter is the extent and frequency of the impregnation/drying steps. This determines for how long the impregnation and drying models should be run before initiating a new cycle. Section 5.5.2 has a further discussion on this subject.

Modeling of droplet penetration into a spherical particle and subsequent drying of the particle in a 3D geometry could be a resource-intensive process. In this work, it is assumed the particle-droplet system has a spherical symmetry around the axis connecting

their centers. Moreover, it is assumed that the 3D geometry can be reduced into a 2D problem as depicted in Figure 5-2. This is a reasonable approximation as a first step to developing and solving a model to describe the process. The insights that are obtained from the simplified model can be used at a later stage to implement and solve a full 3D model. Because of the droplet-particle interface (red line in Figure 5-2, right) the problem in 2D does not have circular symmetry and cannot be reduced further into a 1D problem, as in the case of modeling the drying of a fully impregnated particle [19, 20]. All governing equations are expressed and solved in 2D Cartesian coordinates (Section 5.4).

Fluidized bed impregnation is a type of dry impregnation, where a liquid droplet penetrates a dry porous medium. The main driving force is capillary pressure, which is the pressure difference between the two fluids (gas and liquid) due to surface tension and curvature of the interface between them. Capillary pressure is expressed by the Young-Laplase equation [201]:

$$P_c = \frac{2 * \gamma * \cos(\theta)}{R_{pore}} \tag{5-1}$$

where γ is the surface tension between the two fluid phases, θ is the contact angle between the wetting phase and solid wall and R_{pore} is the radius of the pore. The particle-droplet interface during impregnation can be represented by two limiting cases: constant base radius or constant contact angle [202]. In the first case, the interface length remains constant but the contact angle between droplet and particle decreases during impregnation. This means that the droplet curvature increases with time causing a decrease in capillary pressure inside the droplet. In the second case, the contact angle

between droplet and particle remains constant but the interface length is decreasing. This translates to a decrease in droplet curvature radius and hence an increase in droplet capillary pressure. In the presented model the contribution of the droplet's capillary pressure is not taken into account. This is justified since the capillary pressure in the droplet is much smaller (droplet diameter of 20-40μm) than the capillary pressure inside the porous matrix (pore diameter 10-20nm). For simplicity, the first case of constant interface length is assumed when modeling droplet impregnation into a porous particle.

5.3 Model equations

The FB impregnation model is constructed in three parts: 1) energy/mass balance on the FB and evaporative flux calculation, 2) impregnation model for a single particle and 3) drying model for a single particle. The macroscopic mass and energy balance on the whole FB allows the calculation of several important processing parameters (e.g. bed temperature, solvent content in exit gas). The entire FB process is operated at a steady state (constant bed temperature), where the drying conditions are set by the operating process parameters: drying gas temperature, drying gas flow rate and liquid spray rate. This means that particle drying is not taking place in a dry gas at the inlet temperature but rather in a solvent-rich atmosphere at the resulting bed temperature (which is lower than the inlet gas temperature). The steady state operation during FB impregnation allows the separation of the energy and mass balance on the single particle. Performing a separate energy balance on the particle allows the calculation of particle temperature and solvent composition at the particle surface. These are needed for the calculation of the evaporative flux, which is used later in the drying model for a single particle.

5.3.1 Mass and energy balance on FB

Performing mass and energy balances on the fluidized bed allows the calculation of the resulting bed temperature T_{bed} and the mass fraction of solvent in the exit gas Y^{out} for a chosen inlet gas temperature T_{gas}^{in}, inlet gas mass flow rate $\dot{m}_{gas}$, mass fraction of solvent in the inlet gas Y^{in} and solvent spray rate $\dot{m}_{solvent}$. These parameters are needed later to calculate the evaporative solvent flux from the particle itself. Figure 5-3 shows a schematic of a FB impregnation process with all inlet and outlet streams. Several simplifying assumptions are made in order to derive the required relations:

- Perfect mixing inside the bed

  - Solvent content in the bed and outlet gas are the same

  - Temperature of the bed and outlet gas are the same

  - Bed temperature is uniform

- Steady state operation – no solvent accumulation

- Sprayed solution is represented by pure solvent

- Atomization gas contains no solvent

- The equipment is thermally insulated

Mass balance on the solvent leads to the following expression:

$$Solvent\ Mass_{in} - Solvent\ Mass_{out} = 0 \qquad (5\text{-}2)$$

$$\left(\dot{m}_{solvent} + \dot{m}_{gas} * Y^{in}\right) - \left(\dot{m}_{gas} + \dot{m}_{ato}\right) * Y^{out} = 0 \qquad (5\text{-}3)$$

The above equation allows the calculation of solvent content in the exit stream (Y^{out}). An energy balance on all species for a steady-state operation is performed as follows [203]:

$$E_{in} - E_{out} = 0 \tag{5-4}$$

$$\left[\dot{m}_{gas} * H_{gas}^{in} + \dot{m}_{ato} * H_{ato}^{in} + \dot{m}_{solvent} * H_{solvent}^{liquid} \right] - \left[\dot{m}_{gas} * H_{gas}^{out} + \dot{m}_{ato} * H_{gas}^{out} \right] = 0$$

$$\tag{5-5}$$

where H_{gas}^{in}, H_{gas}^{out}, H_{ato}^{in}, and $H_{solvent}^{liquid}$ are the enthalpies of the drying gas at the inlet and

outlet, the atomization gas and liquid solvent respectively. In order to calculate the

enthalpies, the following reference states are defined: for drying gas - T=273 K and P=1

atm; for solvent (liquid) - T=273 K and P=1 atm. The enthalpies of the drying gas at the

inlet and outlet are given below:

$$H_{gas}^{in/out} = H_{air} + H_{solvent}^{vapor} \tag{5-6}$$

$$H_{gas}^{in} = C_{p,air} * T_{gas}^{in} + Y^{in} * \left(\Delta H_{vaporization}^0 + C_{p,solvent}^{vapor} * T_{gas}^{in} \right) \tag{5-7}$$

$$H_{gas}^{out} = C_{p,air} * T_{gas}^{out} + Y^{out} * \left(\Delta H_{vaporization}^0 + C_{p,solvent}^{vapor} * T_{gas}^{out} \right) \tag{5-8}$$

where $C_{p,air}$, $C_{p,solvent}^{vapor}$ and $\Delta H_{vaporization}^0$ are the heat capacity for air, heat capacity for

solvent vapor and solvent enthalpy of vaporization at the reference state. The enthalpies

of the atomization gas and liquid solvent are given below:

$$H_{ato}^{in} = C_{p,ato} * T_{ato}^{in} \tag{5-9}$$

$$H_{solvent}^{liquid} = C_{p,solvent}^{liquid} * T_{solvent,liquid}^{in} \tag{5-10}$$

where $C_{p,ato}$ and $C_{p,solvent}^{liquid}$ are the heat capacities of the atomization gas (which will be

assumed to be air in the model) and liquid solvent respectively. Substitution of (5-7)

through (5-10) into (5-5) allows the calculation of the bed temperature (which equals the bed temperature, $T_{bed} = T_{gas}^{out}$) for a given inlet temperatures and flow rates of the drying gas, atomization gas and liquid solvent. The solvent content in the exit stream needed for the above calculation is obtained from the solvent mass balance given in (5-3). The opposite is also possible – to calculate drying gas temperature T_{gas}^{in} for a desired bed temperature.

In order to ensure steady state operation with no solvent accumulation inside the bed (which can lead to agglomeration, poor powder fluidization and eventual a complete halt to fluidization) the solvent spray rate must not exceed the drying capacity of the inlet gas. This condition is expressed by the following relation:

$$Y^{out} < Y^{Max} \tag{5-11}$$

The maximum possible solvent content in the exit gas is set by the thermodynamics of the system (bed pressure and temperature). This is the solvent content in the gas phase that corresponds to pure solvent in thermodynamic equilibrium with the drying gas at the specific bed temperatures and pressures. The value of Y^{Max} is given by the relation:

$$Y^{Max} = \frac{Mass_{solvent}^{max}}{Mass_{air}} = \frac{MW_{solvent} * mol_{solvent}^{max}}{MW_{air} * mol_{air}} = \frac{MW_{solvent} * P_{solvent}^{Vapor}}{MW_{air} * \left(P_{bed} - P_{solvent}^{Vapor}\right)} \tag{5-12}$$

where P_{bed} is the pressure inside the fluidized bed and $P_{solvent}^{Vapor}$ is the saturation vapor pressure of the solvent at specified bed temperature T_{bed}. The vapor pressure can be expressed as a function of temperature via the Antoine equation, which has the general form:

$$log\left(P_{solvent}^{Vapor}\right) = A - \frac{B}{C+T_{bed}} \tag{5-13}$$

The procedure for evaluation and calculation of the process parameters for fluidized bed impregnations is as follows:

- Choose $\dot{m}_{gas}$, $\dot{m}_{ato}$, $\dot{m}_{solvent}$ and Y^{in}

    o Y^{in} is usually zero when solvents are used and if the exit gas is not recycled back to the fluidized bed through a condenser to reduce solvent content

- Calculate solvent content Y^{out} in the outlet gas stream, equation (5-3)

- Calculate T_{bed} for given temperatures and flow rates of the drying gas, atomization gas and solvent, equation (5-5)

- Calculate Y^{Max} at the calculated T_{bed} and ensure that it is larger than Y^{out}, equation (5-12)

5.3.2 Evaporative flux

There are three distinct phases during drying of any porous solid material. The first phase is the heat-up or preheating period, where energy from the drying gas is used to increase the temperature of the solids. This period is generally faster compared to the other two and there is little evaporation. Fluidized bed impregnation is conducted at a steady state, when all solids have reached their drying temperature and therefore the heat-up phase is not included in the modeling work. The second phase is when most of the drying occurs, called the "constant rate" period. During this phase, energy from the drying gas is used entirely for solvent evaporation and the particle temperature remains constant. The solvent is transported to the particle surface due to capillary action, where it is evaporated

into the drying air. The solute, which is non-volatile will remain in the particle and diffuse back due to the concentration gradient generated by the removal of solvent. The third phase is called the "falling rate" period. During this phase, the internal capillary flows no longer can supply liquid fast enough to the surface to match the rate of heat supplied by the drying gas. The drying rate during this period is termed "mass transfer limited". As a result, the overall drying rate decreases causing an increase in the particle temperature.

The evaporative flux during the constant rate drying period depends on the solvent nature and drying conditions in the bed. It can be calculated using the fact that during that period, all the heat supplied to the particle is used for solvent removal (Figure 5-4). It is assumed that the gas phase is always in equilibrium with the liquid phase and that the only resistance to solvent mass transfer is in the gas phase. The procedure starts with performing a solvent mass balance on a fully wetted particle, leading to the following expression [204]:

$$-V_{particle} * \frac{\partial(\varepsilon_l * \rho_{solvent}^{liquid})}{\partial t} = k * A_p * \rho_{gas} * (Y_{surface} - Y^{out}) \qquad (5\text{-}14)$$

where k is the overall gas-side mass transfer coefficient for the solvent at the external surface of the particle, A_p is the external surface area of the particle, ρ_{gas} is the average density of the gas phase in the boundary layer, $V_{particle}$ is the porous particle total volume, ε_l is the liquid (solvent) volume fraction in the porous particle, $\rho_{solvent}^{liquid}$ is the density of the solvent inside the particle and $Y_{surface}$ is the mass fraction of solvent in the

gas phase at the particle surface. Energy balance on the same particle leads to the following expression:

$$-V_{particle} * \frac{\partial\left(\varepsilon_l * \rho_{solvent}^{liquid}\right)}{\partial t} * \Delta H_{vaporization} = h * A_p * \left(T_{gas}^{out} - T_p\right) \quad (5\text{-}15)$$

where h is the convective heat transfer coefficient, $\Delta H_{vaporization}$ is the vaporization enthalpy of the solvent and T_p is the average particle temperature. Combining the mass and energy balance leads to the following:

$$\frac{Y_{surface} - Y^{out}}{T_p - T_{gas}^{out}} = -\frac{h}{\rho_{gas} * k} * \frac{1}{\Delta H_{vaporization}} \quad (5\text{-}16)$$

Solvent on the particle surface is in thermodynamic equilibrium with the gas phase at the particle surface. Therefore, the solvent mass fraction in the gas phase at the surface of the particle $Y_{surface}$ is equal to the maximum solvent content Y^{Max} already given by equation (5-12), where $P_{solvent}^{Vapor}$ is a function of particle temperature T_p. The enthalpy of vaporization is given by the following:

$$\Delta H_{vaporization} = \Delta H_{vaporization}^0 + C_{p,solvent}^{vapor} T_{gas}^{out} - C_{p,solvent}^{liquid} T_p \quad (5\text{-}17)$$

The ratio of convective heat transfer coefficient and mass transfer coefficient can be obtained by the Chilton-Colburn analogy [204]:

$$\frac{h}{k} = \rho_{gas} * C_{p,gas} \left(\frac{\alpha_{air}}{D_{solvent/air}}\right)^{\frac{2}{3}} \quad (5\text{-}18)$$

where α_{air} and $D_{solvent/air}$ are the thermal diffusivity of air and the mass diffusivity of

the solvent in air respectively. Values of diffusivities can be obtained from various

sources [204, 205]. The heat capacity of the gas phase can be expressed as:

$$C_{p,gas} = C_{p,air} + Y^{out} * C_{p,solvent}^{vapor} \qquad (5\text{-}19)$$

Substituting equations (5-17), (5-18) and (5-19) into equation (5-16) yields the following

expression:

$$\frac{Y_{surface} - Y^{out}}{T_p - T_{gas}^{out}} = -\frac{\left(C_{p,air} + Y^{out} * C_{p,solvent}^{vapor}\right)\left(\frac{\alpha_{air}}{D_{solvent/air}}\right)^{\frac{2}{3}}}{\left(\Delta H_{vaporization}^{0} + C_{p,solvent}^{vapor} * T_{gas}^{out} - C_{p,solvent}^{liquid} * T_p\right)} \qquad (5\text{-}20)$$

The solvent saturation at the particle surface can be calculated in a similar way using

equation (5-12):

$$Y_{surface} = \frac{MW_{solvent} * P_{solvent}^{Vapor}}{MW_{air} * \left(P_{bed} - P_{solvent}^{Vapor}\right)} \qquad (5\text{-}21)$$

where this time the solvent vapor pressure is calculated at the particle temperature T_p,

similar to equation (5-13):

$$log\left(P_{solvent}^{Vapor}\right) = A - \frac{B}{C + T_p} \qquad (5\text{-}22)$$

Once Y^{out} and $T_{bed} = T_{gas}^{out}$ are calculated (as described in Section 5.3.1), then $Y_{surface}$

and T_p are calculated by solving the system of equations (5-20) and (5-21). The

evaporative flux (per unit area) can be calculated using the flowing equation:

$$Flux = k * \rho_{gas} * \left(Y_{surface} - Y^{out}\right) \tag{5-23}$$

The overall gas-side mass transfer coefficient k can be estimated by using known empirical relationship between Sherwood number (Sh), Reynolds number (Re) and Schmidt number (Sc) for a forced convection around a solid spherical particle as described by Cussler [204]:

$$\frac{k * d}{D_{sol/gas}} = 2 + 0.6 * \left(\frac{\rho_{gas} * d * V^{gas}}{\mu_{gas}}\right)^{1/2} * \left(\frac{\mu_{gas}}{\rho_{gas} * D_{sol/gas}}\right)^{1/3} \tag{5-24}$$

where d is the particle diameter, V_{gas} is the gas phase velocity moving pass the particles in the bed (assumed to be equal to the average drying air velocity in the bed), μ_{gas} and ρ_{gas} are the average viscosity and density of the gas phase in the boundary layer.

5.3.3   Impregnation/drying model for single particle

The derivation of the governing equations was done using the volume averaging approach as described by [206]. For simplicity, we only focus on transport phenomena involving the liquid phase (containing solvent and dissolved API) and exclude the gas phase (containing air and solvent vapor). It is assumed that the gas phase is always in equilibrium with the liquid phase. Transport of the saturated gas phase from inside the particle into the drying medium is a much slower process during the constant rate drying period and becomes significant only when capillary flows stop due to significant reduction in liquid content. Particle temperature is assumed to be uniform and constant during the drying process. This assumption could be partially justified as particles undergo impregnation/drying cycles continuously during FB impregnation, which is

operated at a steady state. It also allows the separation of energy transfer (solved by algebraic equations) from mass/momentum transfer (solved by partial differential equations, PDEs) phenomena when developing the model. Another assumption is that the liquid film is continuous during the entire drying process and film breakage is absent (isolated liquid domains within the particle do not form [53]. These assumptions allow for a simple, yet representative model describing the relationships between different processing parameters and how they affect the API distribution. In particular, it describes the convective and diffusive mass transfer of solvent and API, and the crystallization of the latter.

Mass balance on the solvent and API leads to the following PDEs:

$$\frac{\partial(\varepsilon_l C_{sol})}{\partial t} = -\nabla \cdot (N_{sol}) \tag{5-25}$$

$$\frac{\partial(\varepsilon_l C_{API})}{\partial t} = -\nabla \cdot (N_{API}) - \varepsilon_l R_{crys} \tag{5-26}$$

$$\frac{\partial(W_{API}^{crys})}{\partial t} = \varepsilon_l R_{crys} \tag{5-27}$$

where ε_l is the volume fraction of liquid phase in the particle, C_{sol} and C_{API} are the concentrations of solvent (assumed constant) and API respectively. N_{sol} and N_{API} are the mass fluxes of solvent and API respectively. The mass balance also accounts for crystallization, where R_{crys} is the rate of crystallization and W_{API}^{crys} is the mass of the crystallized API in the particle. Crystallization rate R_{crys} can be expressed using first order kinetics proposed by Mullin [207]:

$$R_{crys} = K_{crys} * (C_{API} - C_{API}^{sat})$$
(5-28)

where C_{API}^{sat} is the API's saturation concentration for the particular solvent and temperature and K_{crys} represents the coefficient of crystallization.

Liquid flow in porous media is described well by Darcy's law, where the liquid flux is proportional to the pressure gradient across the liquid. It is assumed that this law can also describe convective flow during impregnation and drying [208]:

$$N_{sol} = -C_{sol} \frac{KK_{eff}}{\mu_{sol}} \nabla P_l$$
(5-29)

where the proportionality constants K and K_{eff} are the absolute (intrinsic) and relative (effective) permeability of the porous medium respectively and μ_{sol} is the viscosity of the liquid phase. As mentioned already, the main driving force in impregnation is the capillary action that arises when any liquid is brought into contact with a small capillary. This driving force, the capillary pressure, is the difference between the pressure in the gas and liquid phases respectively. If we assume the gas phase pressure inside the particle is constant and always equal to the atmospheric pressure (pores open/vented to the environment) then equation (5-29) becomes:

$$N_{sol} = C_{sol} \frac{KK_{eff}}{\mu_{sol}} \nabla P_c$$
(5-30)

For a single capillary, the capillary pressure P_c as shown in equation (5-1), depends on the surface tension, contact angle and capillary size. Any porous material consists of pores with various sizes, characterized with a specific pore size distribution. Therefore,

the capillary pressure in any porous material will be also a function of the liquid saturation ($S = V_{void\ space}/V_{particle}$), which can be expressed as the ratio of the liquid fraction in the particle ($\varepsilon_l = V_{solvent}/V_{particle}$) to the particle porosity ($\varepsilon = V_{void}/V_{particle}$). It quickly drops as the saturation increase and eventually becomes zero for a completely saturated particle [209-211]. Many correlations between capillary pressure and liquid saturation have been developed and proposed over the years [212-215], with some recent modifications [216, 217]. Here, an experimentally determined mercury (Hg) porosimetry data for Neusilin® is used, which is then converted to Pc vs. saturation (see section 5.5.1). The relative and absolute permeability of the porous carrier are also calculated from experimental data (see section 5.5.1).

Transport of the API inside the particle is by both diffusion and convection. The mass flux of the API can then be expressed as follows:

$$N_{API} = C_{API}\frac{KK_{eff}}{\mu_{sol}}\nabla P_c - \varepsilon_l D_{API}\nabla C_{API} \qquad (5\text{-}31)$$

where D_{API} is the diffusion coefficient of the API in the solvent. Here, the effect of adsorption is neglected, assuming there is no interaction between the API and the support.

5.4 Numerical solution of the PDEs

The impregnation and drying of a single particle in FB is modeled by solving the system of partial differential equations (PDEs) consisting of equations (5-25), (5-26) and (5-27). These equations are solved using the method of lines [218], where the PDEs are converted into system of ODEs by discretization of the spatial derivatives only. The

discretization is achieved by utilizing the finite volume method (FVM) with an up-wind discretization scheme [219]. This method satisfies conservativeness, boundedness and transportiveness and as a result, provides physically realistic solutions to many engineering problems.

The entire 2D region (as depicted in Figure 5-2) is discretized in Cartesian coordinates. All cells that fall inside the circular particle region are assigned as "internal cells", cells that fall on the particle surface are assigned as "boundary cells", cells that fall on the particle-droplet interface are assigned as "interface cells" and all other cells are assigned as "outside cells". All governing equations are written in 2D Cartesian coordinates and solved for all cells except on the "outside cells". For the impregnation model with a single-droplet impregnation, all "boundary cells" are assigned with "no-flux" boundary condition (Neumann boundary condition) and all "interface cells" are assigned with a constant value (constant saturation, S=1) boundary condition (Dirichlet boundary condition). In the case of full impregnation (which is a complete impregnation of the particle with a liquid that is penetrating from the entire external particle surface), all "boundary cells" become "interface cells". For the drying model (regardless of impregnation mode, single-droplet or full), all cells at the particle surface become "boundary cells" (drying is taking place across the entire external surface of the particle) and are assigned a specific flux (Neumann boundary condition) for the solvent, depending on the drying conditions inside the fluidized bed, calculated using equation (5-23). The same "boundary cells" are assigned with "no-flux" for the API. All "outside cells" stay idle and no equations are solved there.

A custom MatLab program was written, utilizing its "ode113" subroutine as the primary ODE solver for the system above. The program was constructed in three distinct segments. The first part performs a mass and energy balance on the FB (per section 5.3.1) and calculates the solvent evaporative flux needed for the drying model (per section 5.3.2). This part also calculates all solvent thermodynamic properties needed in the model (density, viscosity, diffusion coefficients, etc.). The second part is the impregnation model, which calculates solution and API distribution within the porous particle assuming there is no drying. The model runs until all liquid from the droplet is impregnated (in the case of single droplet impregnation) or the entire particle is saturated (in the case of full saturation). The resulting solution/API profiles are then passed to the drying model (third part of the program). Using previously calculated solvent evaporative flux, this part of the model runs until a pre-determined liquid phase volume fraction is reached. It is assumed that convection and diffusion stop when the liquid fraction in the particle drops below 0.015 m^3/m^3. At the end of the simulation when diffusion and convection stops, any API still remaining in solution (which did not crystallize) is assumed to fully crystallize in its place. Together with the crystallized API, this forms the final impregnated API profile for that particular impregnation/drying cycle. If needed, the impregnation/drying cycle model is repeated starting with a fully dried particle containing the calculated API profile from the previous step, until a desired final drug loading is achieved.

5.5   Results and discussion

5.5.1   Modeling parameters

The developed FB impregnation model was applied to an API/excipient system that was already presented in Chapter 3. The model drug was Fenofibrate, the porous excipient was Neusilin® (US2 grade), the solvent used was methanol and the equipment for impregnation was MiniGlat. Typical FB impregnation conditions used in the model (spray rate, drying gas flow rate and temperature, etc.) used in the model are described in Chapter 3. Several other API/excipient properties needed for the model were either experimentally determined or calculated using known mathematical relations. The model could be easily extended to other API/excipient systems.

The mathematical expression for the capillary pressure as a function of liquid saturation was obtained using experimental data. Mercury porosimetry data [220] of Hg volume vs. Hg penetration pressure was converted to methanol capillary pressure vs. saturation [185]. This data was then fitted to a capillary pressure model proposed by Li and Horne [217] in order to obtain mathematical expression of Pc vs. S:

$$P_c = P_{c,max}(1 - bS)^{-\frac{1}{\lambda}} \qquad (5\text{-}32)$$

Here λ is a fitting parameter and b is a constant expressed as: $b = 1 - \left(P_{c,e}\middle/P_{c,max}\right)^{-\lambda}$,

where $P_{c,e}$ and $P_{c,max}$ are the entry and maximum capillary pressure of Neusilin respectively. Figure 5-5 (left) shows the experimentally obtained (after conversion) P_c vs. S for methanol/Neusilin® system along with the data fit using equation (5-32). The

parameters used for the data fit curve are as follows: λ=0.25, P$_{c, e}$=50320 Pa, P$_{c, max}$= 22596822 Pa.

The same experimental P_c vs. S data was used to obtain a mathematical expression for K_{eff} vs. saturation needed for the model. Following the Purcell approach [185, 217], the relative (or effective) permeability can be calculated by the following expression:

$$K_{eff} = \frac{\int_0^S dS/P_c^2}{\int_0^1 dS/P_c^2} \qquad (5\text{-}33)$$

Figure 5-5 (right) shows the corresponding K_{eff} vs. S curve after numerically integrating the experimental data of P_c vs. S according to equation (5-33). This data was then fitted with a power function of the form:

$$K_{eff} = S^\alpha \qquad (5\text{-}34)$$

Figure 5-5 (right) shows also the K_{eff} data fit with a fitting parameter $\alpha = 4$. Equations (5-32) and (5-34) with their corresponding fitting parameters were the final mathematical expressions used in the impregnation/drying model.

The diffusion coefficient of Fenofibrate in methanol was estimated using an expression relating D_{API} to its molecular radius (R_{API}) and the solvent's (μ_{sol}) and temperature (T) [204, 221]:

$$D_{API} = \frac{k_B T}{2\mu_{sol} R_{API}} \qquad (5\text{-}35)$$

where k_B is the Boltzmann constant. The diameter of Fenofibrate's molecule was taken to be 12.73 Å [222]. As a result, the diffusion coefficient of Fenofibrate in methanol at 300K estimated using equation (5-35) is $D_{API} = 6 \times 10^{-9}$ m^2/s.

The reported porosity of Neusilin® US2 grade is $\varepsilon = 0.85$ [177]. The intrinsic permeability of a porous media is dependent on its pore size distribution and can be estimated using the modified Ergun equation [20, 223]:

$$K = \sum_i \frac{3\varepsilon_{l,i} d_{p,i}^2}{200} \tag{5-36}$$

where $d_{p,i}$ is the average pore diameter for the ith group of pores and $\varepsilon_{l,i}$ is their combined volume fraction. Using porosimetry data reported by Allgeier [177] the intrinsic permeability of Neusilin® (US2 grade) was calculated to be $K = 8.6 \times 10^{-15}$ m^2.

Droplets produced by the atomizing (two-fluid) nozzle during impregnation are characterized with a specific size distribution, which depends on several process parameters (liquid/gas flow rate, temperature, solvent nature, solute concentration, nozzle configuration). Using reported performance data on MiniGlatt's atomization nozzle [224], a droplet size of 40 um was chosen for the simulation work. Most of Neusilin® particles are less than 200 um in size [225] which was chosen as the particle size used in the model.

Saturation solubility and its temperature dependence for Fenofibrate in methanol was measured experimentally using Crystal16 crystallization system (Technobis Crystallization Systems). Slurries with known amounts of API and solvent were

subjected to heat/cool cycles and the solubility temperature was determined by a turbidity sensor. Figure 5-6 shows the experimental results along with a data fit using Van't Hoff's equation [207]. The resulting mathematical expression for the solubility that is needed in equation (5-28) is: $C_{API}^{sat} = exp(36.16 - 9668.96/T)$, where T is in degrees Kelvin.

5.5.2   Frequency and extend of impregnation step in FB

When running the impregnation/drying model, it is very important to know the frequency and the extent of the impregnation step. That is, how often each particle goes through the wetting zone, how much solution does it receive and how long does it have to dry until it goes again through the wetting zone. This determines two important model parameters: amount of liquid a particle receives during impregnation (size/number of droplets it receives or is it fully impregnated) and the extent to which it dries (fully or partially dried before next impregnation). The amount of liquid that each particle receives as it passes through the wetting zone depends on the droplet size (or size distribution) produced by the spray nozzle, on the particle size itself and on the impact frequency between the particle and the droplets (mixing intensity in the FB). There are two possible scenarios, full and partial impregnations. The former could take place when small particles collide with much larger droplets or if particles collide with many droplets before leaving the wetting zone. The latter takes place when particles collide with one or several (but not enough to produce full impregnation) droplets.

In Chapter 2 (Section 2.5.2.1, Figure 2-14) it was demonstrated that the API loading correlates closely with the particle size: loading is reduced as particle size is increased. This result indicates that full impregnation is not taking place, i.e. not all particles

become fully saturated as they pass through the wetting zone, otherwise loading for all sizes would have been the same. Depending on the actual droplet size, small particles may receive full impregnation and larger particles will receive partial impregnation. Therefore, in the presented modeling, two limiting cases are studied: impregnation/drying cycle of a fully saturated (full impregnation) and a partially saturated (single droplet impregnation) particle. For the full impregnation case it is assumed that liquid penetration takes place across the entire external surface of the particle.

The frequency of impregnation (or average time interval between two consecutive single-droplet impregnations) could be roughly estimated if several simplifying assumptions are made: perfect mixing in the fluidized bed; all particles receive the same number of droplets; the porous excipient is of uniform particle size distribution; the atomized spray is of uniform droplet size distribution; cubic packing of particles when tap density is measured. These assumptions allow for the calculation of the total number of particles and droplets per unit of time during impregnation, which then can be used to calculate number of droplets each particle receives per unit time, or equivalently the time between two consecutive droplet impregnations. Table 5-1 shows calculated average times between consecutive single-droplet impregnations for typical Fenofibrate FB impregnation runs (as described in Section 3.3.1, Table 3-5, runs 3-7). While these results are gross estimates based on assumptions, they do show that particles will have sufficient time (see drying time in Section 5.5.3) to fully dry after impregnation, before the next droplet impact. This in turn justifies the claim that the model could be repeated if necessary (using random droplet impact location) until a desired final API loading in the modeled particle is achieved.

5.5.3 Simulation results

Performing energy and mass balances on the FB and single particle (as described in sections 5.3.1 and 5.3.2) allows the prediction of several processing parameters that are important for a successful impregnation. For example, temperatures of the drying particle and the exiting drying gas can be easily estimated for a given set of processing conditions. These are important in the case of unstable or low melting point APIs. Another example is the liquid spray rate of the API solution being impregnated. This parameter can greatly influence the quality of the impregnated product. If the spray rate is higher than the drying capacity of the FB for the given set of conditions, it will result in flooding of the FB, reducing powder mixing and ultimately leading to particle agglomeration. Figure 5-7 shows calculated maximum liquid spray rates vs. temperature and flow rate of the drying gas for methanol in a MiniGlatt system. The maximum spray rate is assumed to be reached when the solvent mass fraction in the bed is 10% lower than the solvent mass fraction at the particle surface. The condition for calculating the maximum spray rate is set as: "$(Y_{surface} - Y^{out})/Y^{out} = 0.1$". As expected, the maximum spray rate increases with temperature and gas flow rate. This relationship should be always determined for any solvent before its use in FB impregnation and the process should be operated away from those limiting values to ensure successful impregnation.

The FB impregnation process consists of repeated impregnation/drying cycles, which occur continuously until a final loading is achieved. In order to understand how processing conditions and material properties affect the final API distribution, the governing PDEs are solved over a single particle first in impregnation mode, followed by

a drying mode for a one complete cycle. All processing parameters used in the model describe a typical FB impregnation process as described in Section 3.3.1, Table 3-5, runs 3-7. Two limiting cases are presented: 1) full impregnation and drying; 2) partial (single-droplet) impregnation and drying. Figure 5-8 shows simulation results for a full impregnation of Neusilin[®] particle with methanol-Fenofibrate solution. Results for the average liquid fraction vs. time (top left) show that a full impregnation of this 200 um particle is completed within 9.5×10^{-4} seconds. As expected, the impregnation rate is very fast at the very beginning of the process and then gradually decreases as the particle reaches the maximum possible liquid fraction of 0.85 (equal to its porosity). This is a direct consequence of the P_c vs. saturation relationship given by equation (5-32) and the corresponding experimental data presented in Figure 5-5 (left). Figure 5-8 also shows the actual distribution of the liquid fraction within the particle at three distinct time points. The simulation results indicate that the impregnation front is non-uniform, represented by the liquid fraction gradient between completely wetted and completely dry areas. This behavior is a direct consequence of the pore size distribution within the Neusilin[®] particle, which is captured by the P_c vs. saturation relationship. The gradient represents filling of small pores first, followed by large ones. In an ideal case, where the material consists of pores with identical size, this liquid fraction gradient would not exist, resulting in a uniform impregnation front. At the other extreme case, where the porous material is characterized with a very broad pore size distribution (small and large pores) the liquid fraction gradient would have been much broader than the one shown in Figure 5-8. The relationship between P_c and liquid saturation (and corresponding K_{eff} vs. saturation) defines the magnitude of the convective flows within the porous particle

during impregnation and drying. The accuracy of the P_c vs. saturation relationship ultimately determines how well the resulting model represents the actual porous network. Therefore, it is extremely important to determine the P_c vs. saturation relationship experimentally for the particular porous material rather than use universal correlations for similar materials. The same is valid for the intrinsic permeability of the porous medium.

Since it is assumed that each impregnation cycle in the FB starts with a completely dry particle, the impregnation is governed solely by the convective liquid flow. Diffusion is not present because the impregnating liquid has a constant concentration. Crystallization is also not taking place due to the constant API solution concentration, which is below the saturation concentration. In the subsequent drying cycle, diffusion and crystallization start to play a role and in some cases, as it will be seen in later examples, may become important factors. In order to model drying, the same governing PDEs are solved with changed boundary conditions: constant flux for the solvent and no flux for the API. In the case of a fully saturated particle, the drying model is solved until a predetermined average liquid fraction in the particle is achieved (< 0.015 m^3/m^3). Figure 5-9 shows the mass balances for solvent and API during the entire drying period. Top left of Figure 5-9 displays the average liquid fraction in the particle as it changes during drying. The results show that the final dry state is achieved in 3.67 seconds. Most of the drying occurs during the "constant rate drying period", represented by the linear part of the drying curve. This result agrees with the observations by Chen et al., who report that FB drying of dibasic calcium phosphate takes place predominantly in the constant rate drying period [53]. This period is rather fast, ending in 0.42 seconds and resulting in an average liquid fraction of 0.064 m^3/m^3. This is a period during which, the drying is entirely controlled by the

constant solvent flux across the boundary. Convective flows deliver solvent to the surface of the particle, where the evaporative flux is the rate limiting step. As long as the convective flows can deliver solvent fast enough, the evaporative flux will be the controlling factor. The rest of the drying takes place in the "falling rate period", where the convective transport becomes the rate limiting step. Because liquid saturation within the particle falls, the effective permeability of the porous matrix significantly drops (as indicated by the K_{eff} vs. saturation relationship in Figure 5-5), reducing the magnitude of the convective liquid transport. The drying times mentioned above are much larger than the impregnation time (Figure 5-8), which justifies previous assumptions and validates the modeling approach: solving the PDEs for impregnation and drying separately. Moreover, these drying times are shorter than the average times between two consecutive single droplet impregnations as estimated in Table 5-1. This justifies another modeling assumption: if impregnation/drying cycles are to be repeatedly modeled, each consecutive impregnation cycle can start with a dry particle, only taking the API distribution/loading obtained from the previous cycle.

Figure 5-9 (bottom left) shows a mass balance of the API during the drying cycle. This data is shown just to illustrate that the total API is conserved during the calculation process. The results show that the overall API mass balance at the end of the simulation is closed within 1×10^{-4} %. This high degree of conservativeness is possible because of the finite volume method used for solving the system of governing equations. Previous attempts to solve the system of equations using finite difference methods had failed to close the API's mass balance (with losses as high as 30%). Figure 5-9 also displays the change in the amount of API remaining in solution (top right) as well as the amount of

API crystallized in the particle (bottom right) during the drying process. The change is linear, which is a direct consequence of the first order kinetics of the crystallization process as described by equation (5-28). The data shows that crystallization is absent at the beginning of the drying process and only start to take place when the local concentration exceeds the solubility limit. For this particular case, the difference between the initial solution concentration of 44 mg/ml and the solubility limit of 51 mg/ml (determined from Figure 5-6 for the particular drying conditions) is not very large and crystallizations starts to take place soon after the drying starts. The amount of crystallized API during the entire drying process is very small, only 0.2% of the total API. The rate of crystallization is dependent on the value of K_{crys}, the coefficient of crystallization. Here it is assumed a case of a slow crystallization with a value of 1×10^{-3} s^{-1}. This is probably the case since crystallization occurring in very small confined spaces (pores of the excipient particle) can be affected by their size [23]. The exact value of the coefficient of crystallization is difficult to measure and therefore another limiting case with fast crystallization is presented later.

Figure 5-10 shows the actual distribution of the liquid fraction within the particle at four distinct time points during the drying process. The results visually illustrate the difference between the "constant rate" and "falling rate" drying periods. Top left map at time t=0.23 seconds shows a uniform liquid profile, typical for the constant rate drying period. Once the drying enters the falling rate period (after t=0.42 seconds), a liquid gradient starts to appear due to the rate limiting effect of the convective transport at low liquid content. This gradient is the most pronounced at the beginning of the falling rate period and tends to get reduced towards the end of drying. Figure 5-11 shows several maps of the API

distribution within a fully impregnated Neusilin® particle at the end of its drying. Top left displays the API concentration of the remaining liquid phase within the particle with a relatively uniform distribution. The values are rather high due to the short drying times and slow crystallization, indicating that most of the API still did not have enough time to crystallize. This fact is also confirmed by the relatively small amount of crystallized API as shown on the top right map. The crystallized API shows a uniform profile. Most of the API still resides in the un-crystallized liquid as shown on Figure 5-11 (bottom left). Because at this point the particle is almost dry and all diffusion and convection effects have ceased to play a role, it is assumed that all of this API will just crystallize in place without any further re-distribution. Summing up the API that has already crystallized and the API that is about to crystallize gives the final total API distribution within the particle at the end of the drying cycle. This distribution is shown on Figure 5-11 (bottom right) and displays a relatively uniform profile. This is the model's prediction for the final API distribution after drying of a fully saturated Neusilin® particle with solution of Fenofibrate in methanol at the specific drying conditions.

Full impregnation is one possible outcome when a particle leaves the spray zone during FB impregnation, however this is not the case for all particles as it was already argued in Section 5.5.2. The highest probability for a full impregnation is when the smallest Neusilin® particles collide with the largest droplets. For the particular conditions for impregnation, most of the particles will most likely get partially impregnated, with a single-droplet impregnation having the highest frequency. Figure 5-12 shows simulation results for a 40 um single-droplet impregnation of a 200 um Neusilin® particle. Top right map displays the liquid fraction distribution at the end of impregnation. The space

occupied by the droplet is quite small relative to the size of the particle. The time for droplet impregnation is 1.15×10^{-5} seconds (top left plot), which is about 83 times faster than the one needed for a full impregnation. Wetted areas close to the particle's surface have almost full saturation, which quickly decrease towards the center. The solvent concentration after impregnation is shown on Figure 5-12 (bottom left). Because impregnation takes place in a fully dried particle, the concentration is uniform, equal to the initial API concentration. The covered area here is a bit larger than the one shown on the map above (for liquid fraction), where some of the points with very low liquid fraction are just not visible due to the scale. Figure 5-12 (bottom right) shows the total API distribution within the particle at the end of impregnation. This API loading profile follows closely the liquid fraction profile above. As evident from the results, most of the API resides at the surface of the particle where droplet impregnation had just taken place.

Immediately after the impregnation is completed, the drying process begins. Although there is no more liquid entering the particle, the solution that is already present inside continues to flow due to convective forces. Drying is a much longer process than impregnation and as a result, the impregnated liquid will be re-distributed further into the particle before convection stops. Figure 5-13 (top left) shows the final liquid fraction distribution within the particle at the end of drying. As expected, the solution has penetrated deep into the particle, reaching its center. It is to be expected that for lower drying temperatures the liquid will penetrate further into the particle. Following the same logic, higher drying temperatures will cause the liquid to penetrate less. While with impregnation convection is the only driving force (since there is no concentration gradient), during drying diffusion will start to play a role as well. Figure 5-13 (bottom

left) shows the distribution of API that is still present in the remaining liquid. In this particular case, it seems that convection and diffusion are of similar magnitudes because the resulting API profile is relatively uniform (very small API gradient is present). This is also evident from the profile of the crystallized API (top right), which also exhibits relative uniformity. Since this case is also assuming slow crystallization ($K_{crys} = 1x10^{-3}$ s^{-1}), the amount of crystallized API is very small relative to what is still present in solution. As a result, the final API profile at the end of drying (bottom right) is relatively uniform.

The simulation presented here for a single droplet could be repeated may times over with droplets impregnating the particle at random positions. The average API loading from this single-droplet impregnation is 0.35 kg(API)/m^3(particle). The density of a single Neusilin$^®$ particle can be calculated from its true density (2.2 g/ml) and its porosity (0.85 m^3/m^3) and was found to be 330 kg(particle)/m^3(particle). This means that if a 10% loading (as kg API/kg particle) is desired for example, the impregnation/drying simulation will need to be repeated 94 times. Each new impregnation will start with a dry particle, taking only the final API profile from the previous simulation. After several random single-droplet impregnations, the profile will start to look uniform throughout the entire particle, similar to the full impregnation case presented earlier. Both the full and single droplet impregnations showcased so far are two limiting cases of the potential impregnation mechanism taking place in a fluidized bed. Any combination of these two cases is also expected to produce a uniform API profile. In Chapter 4 it was presented a study regarding the type of Fenofibrate profile (as a result of FB impregnation onto Nesilin$^®$) by energy dispersive X-ray spectroscopy. There it was determined that the resulting API profile (for the same processing conditions used in the preceding two

simulations) is relatively uniform. The agreement between the experimental results there and the simulations results is good, which is an encouraging result towards validating the modeling approach presented in this work.

The crystallization rate is something that may be difficult to quantify, especially when it comes to porous media. In order to understand the effect of crystallization rate on the final API profile, a hypothetical case with fast crystallization kinetics is presented next. Figure 5-14 shows simulation results for a full (top) and a single-droplet (bottom) impregnation and drying of a 200 um Neusilin® particle. All simulation parameters are the same as in the previous examples (the base case) with the exception of the crystallization constant, which in this case was set to 1 s^{-1}. The results reveal that the amount of crystallized API is perceivably higher than before. In the full impregnation case, most of the API had crystallized and only a small amount remains still in solution (top left and middle). The crystallized API profile has the determining effect on the final API distribution. The final API profile exhibits a distinct "egg-shell" type (top right). For the single-droplet case the effect of crystallization rate is similar. The API tends to crystallize near the surface of the particle (bottom left). In this case however, the amount of crystallized API is comparable to the amount still in solution (bottom left and middle). This difference is mainly attributed to the fact that the single-droplet case dries faster than the full impregnation case and the API has less time to crystallize before the final liquid fraction content is reached and all convection/diffusion stops. Fast crystallization here also impacts the final API profile, which has an egg-shell appearance as well (bottom right). Repeating the single-droplet impregnation/drying cycle will lead eventually to an API profile with a similar egg-shell characteristic.

The effect of crystallization rate on the final API profile can be explained also by the use of dimensionless numbers. The Damköler number relates the crystallization rate to the transport rates inside the particle. The most common form of the Damköler number (Da), relates the crystallization rate to the convection rate, as given by the following equation [226]:

$$Da = \frac{crystallization\ rate}{convective\ transport\ rate} = \frac{K_{crys}*R_p}{v_0} \tag{5-37}$$

where R_p is the radius of the particle and v_0 is the theoretical liquid velocity during the constant rate period. This velocity can be calculated as $v_0 = Flux/C_{sol}$, where the flux is given by equation (5-23). The second Damköler number relates the crystallization kinetics to the diffusion transport and is given by the following relation [204]:

$$Da_{II} = \frac{crystallization\ rate}{diffusive\ transport\ rate} = \frac{K_{crys}*R_p^2}{D_{API}} \tag{5-38}$$

In the case of fast crystallization presented here, the values of the first and second Damköler numbers are 1.06 and 1.67 respectively. This means that the crystallization rate is comparable to the convection rate and slightly higher than the diffusion rate. In the previous example (base case) the two Damköler numbers are 0.001 and 0.002 respectively. When the crystallization rate is much smaller than the convective and diffusive transport, the liquid can move around and/or diffuse quickly before it has a chance to crystallize in place. When the numbers are above 1, the liquid can crystallize in place before it has a chance to move either by diffusion or convection. The relative magnitude of the crystallization rate to these two transport mechanisms ultimately determines its effect on the final API profile.

Fluidized bed impregnation is a versatile process that can be applied to other APIs, which could have larger molecular sizes than Fenofibrate. As a result, they may have smaller diffusion coefficients. In order to explore the effect of the diffusion coefficient on the final API profile, a hypothetical case of slow diffusion is presented next. All simulation parameters were kept the same as in the base case except the diffusion coefficient, which was set ten times smaller ($D_{API}=6x10^{-10}$ m^2/s). Figure 5-15 shows the simulation results for a full (top) and single-droplet (bottom) impregnation and drying of a 200 um Nesuilin$^{®}$ particle with a slow-diffusive API. The results show that the API tends to crystallize very close to the surface, in both the full (top left) and single-droplet (bottom left) impregnated particles due to its relatively slow diffusion rate. The amount of crystallized API is again very low relative to the amount remaining in solution in both cases (middle top and bottom). As indicated previously, this is due to the slow crystallization rate. The API remaining in solution after drying, which is expected to crystallize in place, shows an egg-shell type of profile. The resulting final API profile shows an identical egg-shell type profile for both full and single-droplet impregnations. Similar to the fast crystallization case, another way to look into the effect of diffusion on the final profile is through dimensionless numbers. Here the final profile is determined by the competitive convective and diffusive flows. The number that most accurately represents their relative magnitudes is the Péclet number defined by the following expression [204]:

$$Pe = \frac{convective\ transport\ rate}{diffusive\ transport\ rate} = \frac{v_0 * R_p}{D_{API}} \qquad (5\text{-}39)$$

where v_0 is the same liquid velocity as in equation (5-37). The Pe number for this slow diffusion case is 15.72. This value indicates that the convective transport rate is much higher than the diffusion transport rate. This means that points in the particle that see an increase in concentration due to the convective flows (directed towards the particle surface) cannot easily diffuse that concentration back towards the center. As a result of this difference in magnitudes of the two transport mechanisms, the final API profile shows an egg-shell type appearance. For comparison, the *Pe* number corresponding to the base case presented earlier (which exhibited relatively uniform profile) is 1.57. Values close to 1 indicate that both convection and diffusion have comparable magnitudes, resulting in uniform final API profile.

The FB impregnation process can be applied to other excipients as well, provided they possess enough internal porosity necessary for successful impregnation. In order to understand the effect of porosity on the final API profile, a hypothetical case of an excipient with low porosity is presented next. All processing parameters are the same as in the base case with the only difference being the porosity, which is set to 0.45. It should be noted that it is assumed that this low porosity material still follows the same P_c vs. saturation relationship as in the case of Neusilin[®]. This implies that the internal pore size distribution is the same with the only difference being in the total internal volume available for impregnation. Figure 5-16 shows the simulation results for a fully (top) and single-droplet (bottom) impregnated particle with low porosity. The crystallized API in both cases (left top and bottom) is a small fraction of the total API and is predominantly deposited close to the surface of the particle. Most of the API still remains in solution (middle top and bottom) at the end of the drying when convection and diffusion stops.

When it crystallizes in place it will determine the final API profile (right top and bottom). In both cases, the final API profile shows to be a well-defined egg-shell type. This result is a direct consequence of the lower porosity of the particle. In the case of a fully impregnated particle, low porosity translates to a lower absolute amount of impregnated liquid compared to the base case (where $\varepsilon=0.85$). As a consequence, the drying time is faster and the API has less time to diffuse back towards the particle center. In the case of single-droplet impregnated particle where the amount of liquid is the same as in the base case, low porosity translates to a higher wetted internal volume. Because the liquid is spread over a larger volume, the saturation at any given internal point is lower and on average the particle will need less time to reach the limit of saturation at which convection and diffusion stops. With a faster drying time, the API has less time to diffuse back towards the particle center resulting in an egg-shell type profile.

5.6   Conclusions

Fluidized bed impregnation of APIs onto porous excipients can be impacted by the processing conditions or by the properties of the materials used. In order to better understand their effect on the final API profile, a multi-scale FB impregnation/drying model was developed and presented in this chapter. The model consists of three main parts: 1) energy/mass balance on FB and evaporative flux calculation, 2) impregnation model of a single particle and 3) drying model of a single particle. Part one calculates several important processing parameters for a given set of operating conditions. For example, for a given drying gas temperature/flowrate and solvent spray rate it can calculate product temperature and exiting gas temperature. This is important to know if

dealing with thermally sensitive APIs. Another example includes calculation of the maximum liquid spray rate possible for a given drying conditions (drying gas temperature and flow rate) before the FB gets flooded. The variation of this parameter is also important to understand when trying to optimize the throughput and time cycle of the process. This part of the model also calculates the evaporative flux under steady state operation of the FB, which is used in the single-particle drying model (part 3). Part two of the model calculates the liquid profile during particle impregnation in full or single-droplet mode and the time scale for impregnation. It uses experimentally determined P_c and K_{eff} vs. saturation relationships to better represent the porous excipient (Neusilin) used in the model. Part three of the model accounts for convective and diffusive flows as well as for crystallization of the API (Fenofibrate). As a result it calculates the API distributions (crystallized and still in solution) during the drying process. Several cases were presented to better illustrate various possible FB impregnation scenarios. For each case, full and single-droplet impregnations are studied. The first case involves Fenofibrate impregnation onto Neusilin[®] with drying conditions identical to runs described in Section 3.3.1 (Table 3-5, runs 3-7). The results from the simulation showed that a uniform API should be obtained at the end of drying. This conclusion agrees very well with the experimental measurements of the API profile for the same formulations presented in Chapter 4. A second case was presented assuming a fast crystallization rate for the API. Simulation results reveal that when the crystallization rate is fast and comparable to convection and diffusion (as indicated by the Damköler number) a well pronounced egg-shell type of impregnation profile is obtained. APIs can come in various sizes, which could affect their diffusion rate within the liquid. In order to illustrate a slow

diffusion scenario, the third case presented involved a hypothetical API with lower diffusion coefficient than that of Fenofibrate. Simulation results indicate that the final API profile would exhibit more egg-shell like appearance, although not as pronounced as in the second case. The last case demonstrates the effect of low porosity on the final API profile, as many excipients may differ in their internal void volumes. Results indicate that the resulting API profile is strongly egg-shell shaped. These results are for a limited number of parameters and further work is needed to better understand the effect of process conditions and material properties on the API distribution profile. In addition, these results are for a 2D model and should be confirmed with a full 3D simulation. Further works is also needed to validate the model with more experimental case studies. The model can be further improved by incorporating gas phase diffusion during the falling rate drying period in order to make the model more representative for studying examples with high temperature drying. Another improvement would be to account for the solvent vapor pressure variation with the solute concentration. This will permit studying cases with high initial API concentration and its effect on the drying rate and the final distribution of the active ingredient.

5.7 Notation

A, B, C	Component-specific constants for Antoine Equation	-, K, K
A_p	External surface area of particle	m^2
C_{sol}	Solvent concentration in solution	kg/m^3
C_{API}	API concentration in solution	kg/m^3
C_{API}^{sat}	API saturation concentration (API solubility)	kg/m^3
$C_{p,air}$	Heat capacity of air	J/kg/K
$C_{p,gas}$	Heat capacity of gas phase	J/kg/K
$C_{p,ato}$	Heat capacity of atomizing gas	J/kg/K
$C_{p,solvent}^{liquid}$	Heat capacity of solvent (liquid)	J/kg/K
$C_{p,solvent}^{vapor}$	Heat capacity of solvent (vapor)	J/kg/K
d	Particle diameter	m
d_p	Average pore diameter	m
Da	First Damköler number	-
Da_{II}	Second Damköler number	-
D_{API}	Diffusion coefficient of API in solvent	m^2/s
$D_{solvent/air}$	Gaseous diffusion coefficient of solvent in air	m^2/s
$Flux$	Evaporative solvent flux across particle surface	$kg/m^2/s$
h	Convective heat transfer coefficient	$W/m^2/K$
H_{gas}^{in}	Enthalpy of drying gas at the inlet	J/kg
H_{gas}^{out}	Enthalpy of drying gas at the outlet	J/kg
H_{ato}^{in}	Enthalpy of atomization gas	J/kg
$H_{solvent}^{liquid}$	Enthalpy of solvent (liquid)	J/kg
$H_{solvent}^{vapor}$	Enthalpy of solvent (vapor)	J/kg
H_{air}	Enthalpy of air	J/kg
$\Delta H_{vaporization}$	Enthalpy of vaporization of solvent	J/kg
$\Delta H_{vaporization}^{0}$	Enthalpy of vaporization of solvent at reference state	J/kg
k	Solvent overall mass transfer coefficient in gas phase	m/s
K	Absolute (intrinsic) permeability	m^2
k_B	Boltzmann constant	$m^2*kg/s^2/K^2$
K_{crys}	Crystallization rate constant	1/s
K_{eff}	Relative (effective) permeability of the liquid phase	-

$\dot{m}_{ato}$	Atomization gas mass flow rate	kg/s
$\dot{m}_{gas}$	Drying gas mass flow rate	kg/s
$\dot{m}_{solvent}$	Solution/solvent mass flow rate	kg/s
MW_{air}	Molecular weight of air	kg/mol
$MW_{solvent}$	Molecular weight of solvent	kg/mol
N_{sol}	Mass flux of solvent	kg/m^2/s
N_{API}	Mass flux of API	kg/m^2/s
P_{bed}	Pressure inside fluidized bed	Pa
P_c	Capillary pressure	Pa
$P_{c,e}$	Entry capillary pressure during mercury porosimetry test	Pa
$P_{c,max}$	Maximum capillary pressure during mercury porosimetry test	Pa
Pe	Péclet number	-
P_l	Pressure in the liquid phase	Pa
$P_{solvent}^{Vapor}$	Vapor pressure of pure solvent	Pa
R_{crys}	Crystallization rate	kg/m^3/s
R_{API}	API's molecular radius	m
R_p	Particle radius	m
R_{pore}	Pore radius	m
S	Liquid saturation	m^3/m^3
T_p	Particle temperature	K
T_{bed}	Temperature of fluidized powder bed	K
T_{gas}^{in}	Temperature of drying gas	K
T_{gas}^{out}	Temperature of exiting gas	K
$T_{solvent,liquid}^{in}$	Temperature of sprayed liquid solution/solvent	K
V_{gas}	Average drying gas velocity in the bed	m/s
$V_{particle}$	Volume of particle	m^3
W_{API}^{crys}	Amount of API deposited in particle via crystallization	kg/m^3
Y^{in}	Solvent mass fraction in entering drying gas	kg/kg
Y^{out}	Solvent mass fraction in exiting gas	kg/kg
$Y_{surface}$	Solvent mass fraction in gas phase at particle surface	kg/kg
Y^{Max}	Maximum possible solvent mass fraction in drying gas	kg/kg

Greek Letters

α	Fitting parameter for K_{eff}	-
α_{air}	Thermal conductivity of air	W/m/K
ε_l	Volume fraction of liquid phase in particle	m³/m³
ε	Particle porosity	m³/m³
γ	Surface tension for liquid/air system	N/m
μ_{sol}	Viscosity of liquid phase (solvent or API solution)	kg/m/s
μ_{gas}	Average viscosity of gas phase in boundary layer (solvent vapor and air)	kg/m/s
$\rho_{solvent}^{liquid}$	Density of liquid solvent	kg/m³
ρ_{gas}	Average density of gas phase in boundary layer (solvent vapor and air)	kg/m³
θ	Contact angle between liquid and solid	deg
λ	Fitting parameter for P_c *vs.* S relationship	-
υ_0	Theoretical liquid velocity during the constant rate period.	m/s

5.8   Figures for Chapter 5
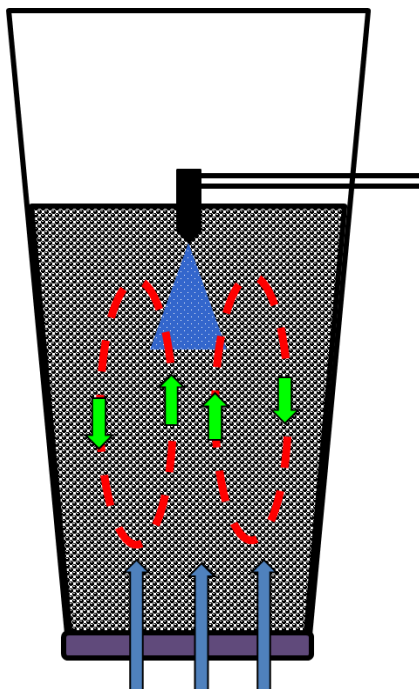
Figure 5-1: Spray zone and particle movement during FB impregnation.
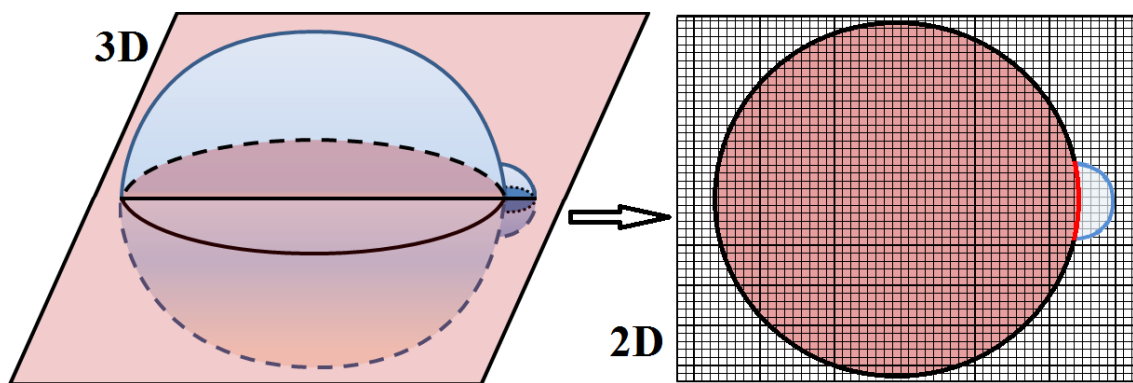
Figure 5-2: Reducing 3D into 2D problem with Cartesian discretization.
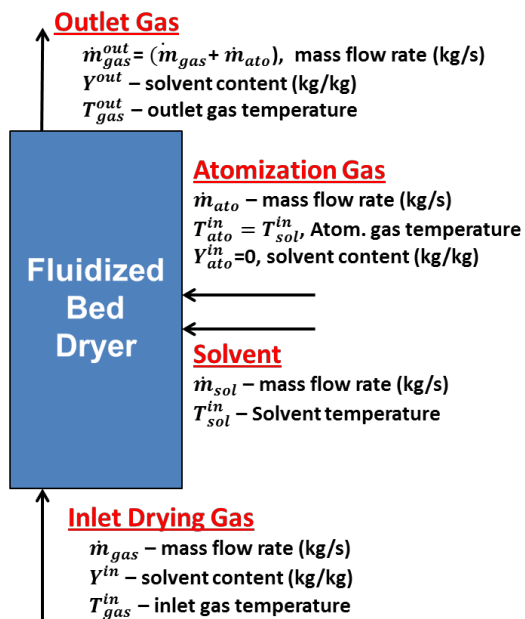
Figure 5-3: Fluidized bed mass/energy balance.
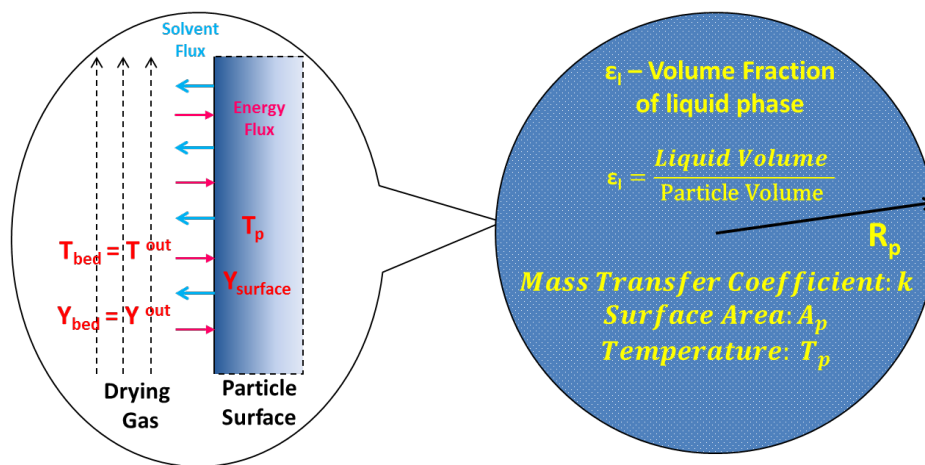
Figure 5-4: Single particle drying.
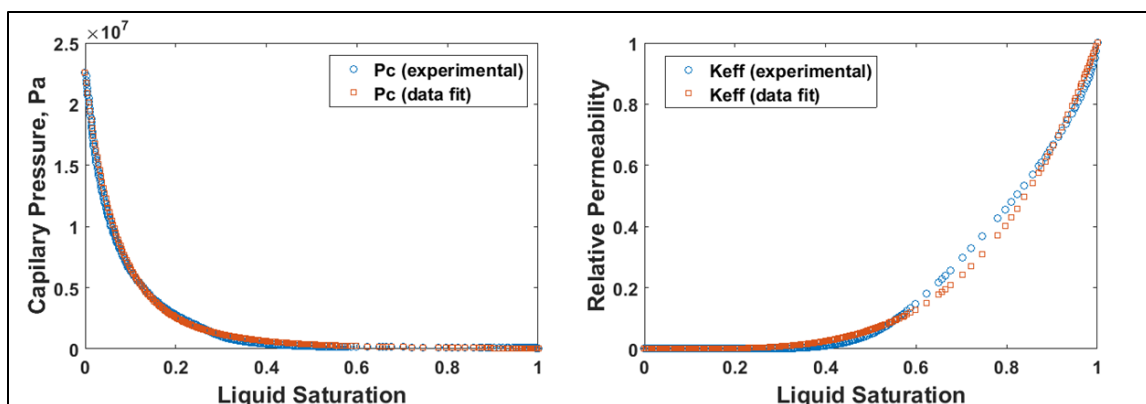
Figure 5-5: Capillary pressure (left) and relative permeability (right) vs. saturation for methanol/Neusilin® (US2 grade) system
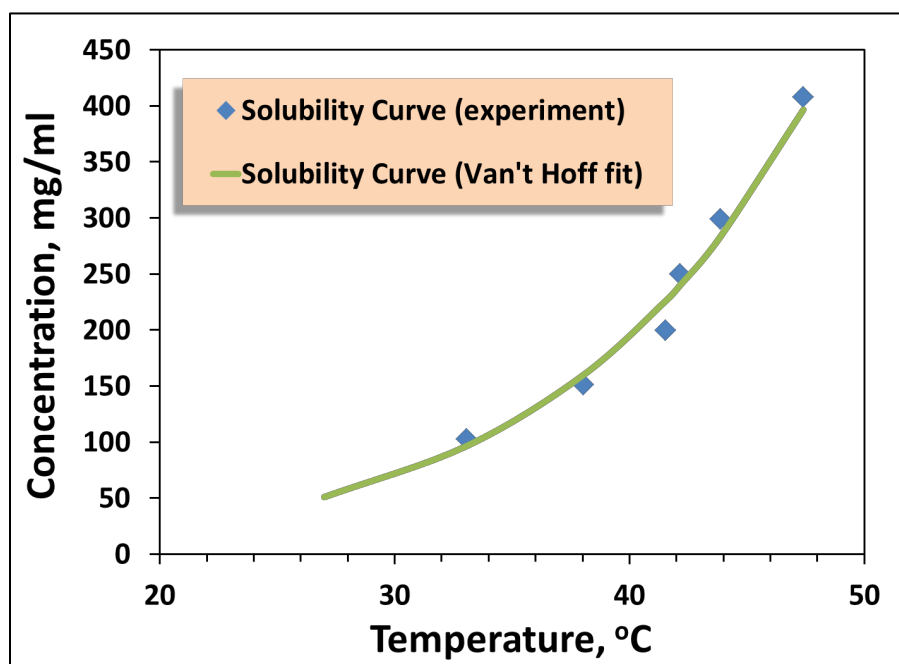
Figure 5-6: Fenofibrate solubility in methanol: experimental results and Van't Hoff data fit.
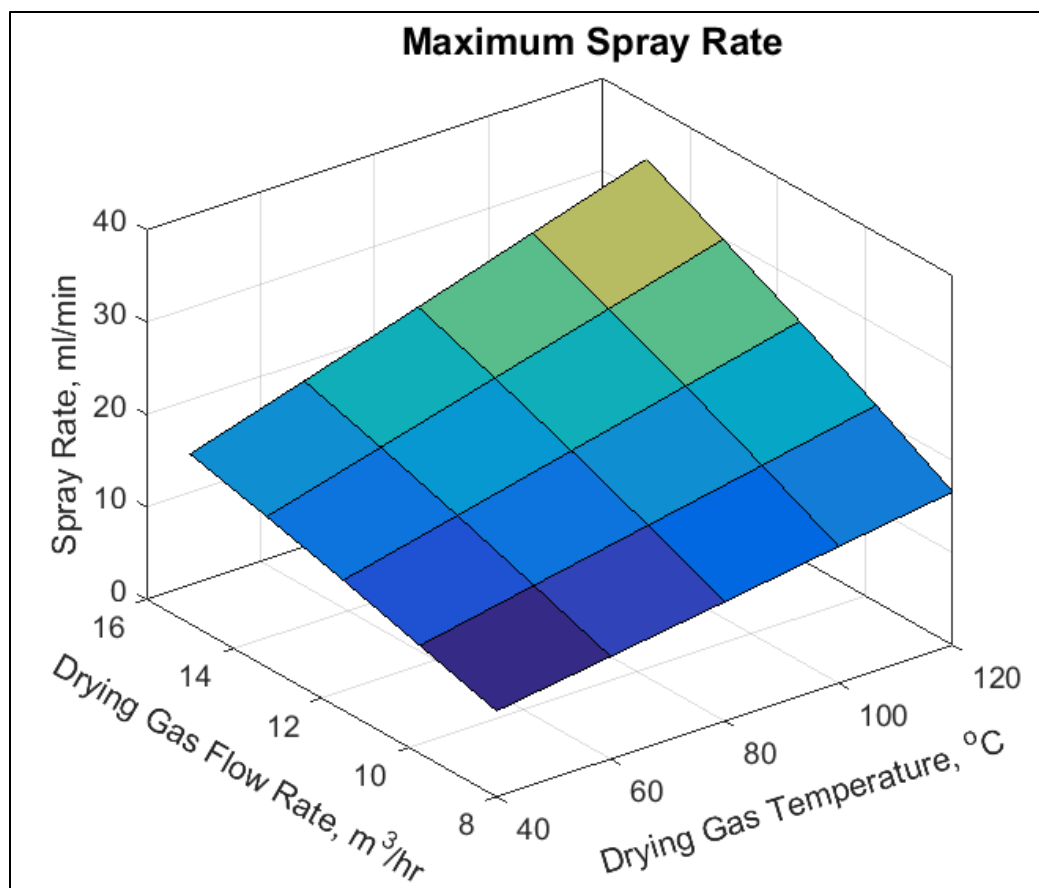
Figure 5-7: Calculated maximum liquid (methanol) spray rate vs. drying conditions (drying gas flow rate and temperature) that is achievable during FB impregnation in MiniGlatt.
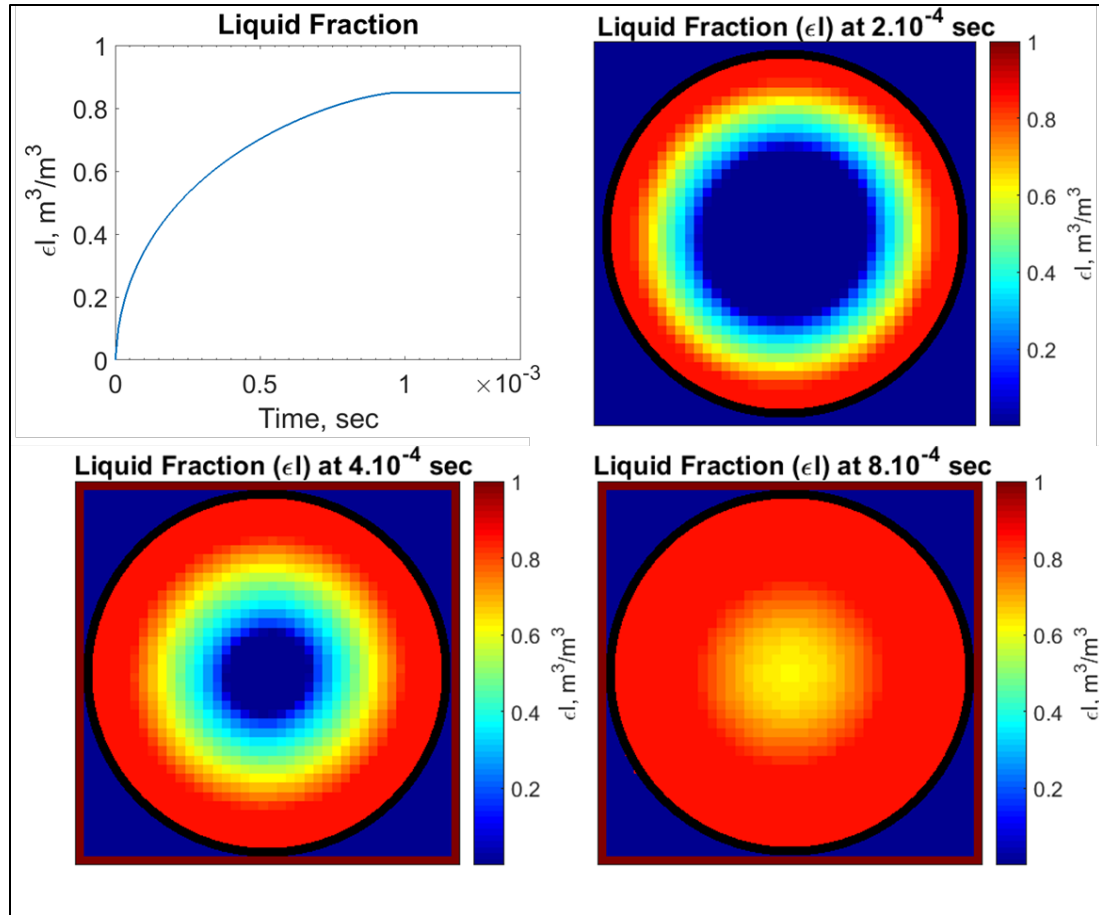
Figure 5-8: Liquid fraction vs. time during a full impregnation of Neusilin® particle with methanol solution of Fenofibrate in fluidized bed: D_p=200 um, K=8.6x10^{-15} m^2, ε=0.85 m^3/m^3, D_{API}=6x10^{-9} m^2/s, K_{cryst}=1x10^{-3} s^{-1}, $T_{drying\ gas}$=80 ^{o}C, Q_{soln}=4 ml/min, $Q_{drying\ gas}$=9 m^3/h, C_{API}=44 mg/ml.
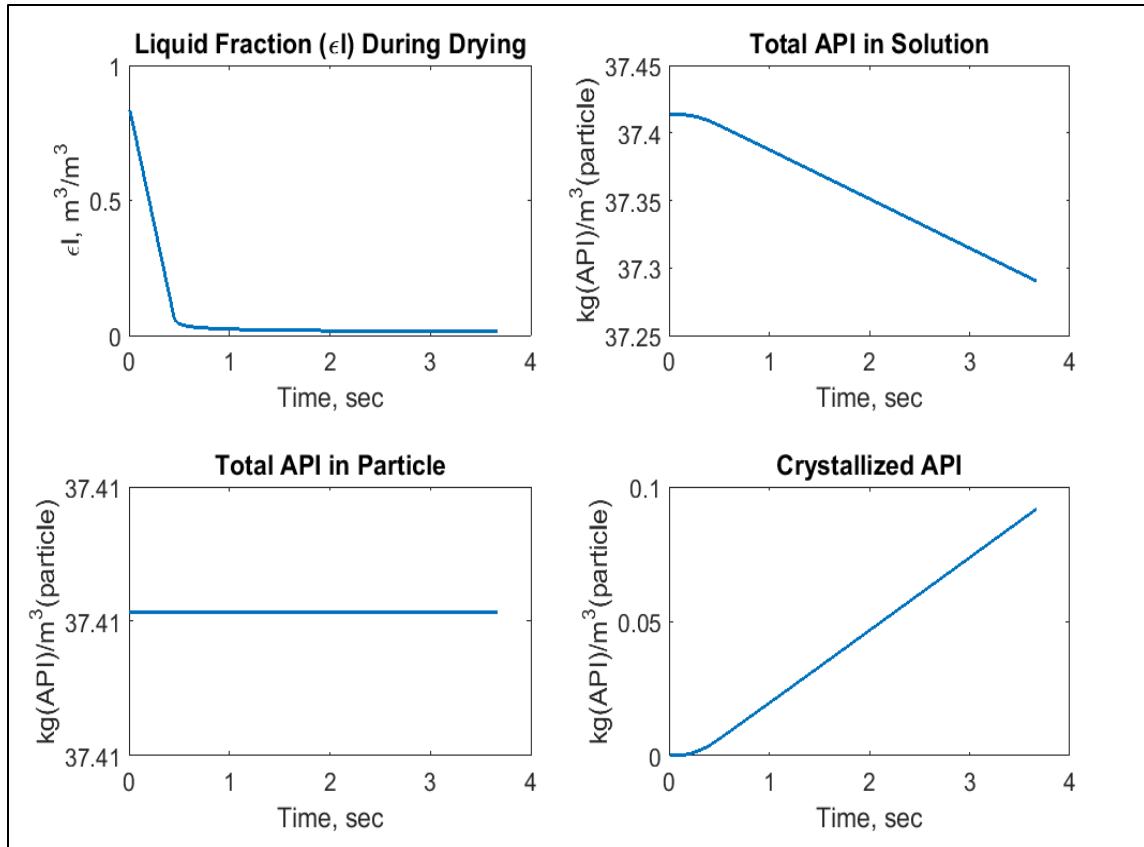
Figure 5-9: Mass balances for solvent and API during drying of a fully impregnated Neusilin® particle with methanol solution of Fenofibrate in fluidized bed: D_p=200 um, K=8.6x10^{-15} m^2, ε=0.85 m^3/m^3, D_{API}=6x10^{-9} m^2/s, K_{cryst}=1x10^{-3} s^{-1}, $T_{drying\ gas}$=80 °C, Q_{soln}=4 ml/min, $Q_{drying\ gas}$=9 m^3/h, C_{API}=44 mg/ml.
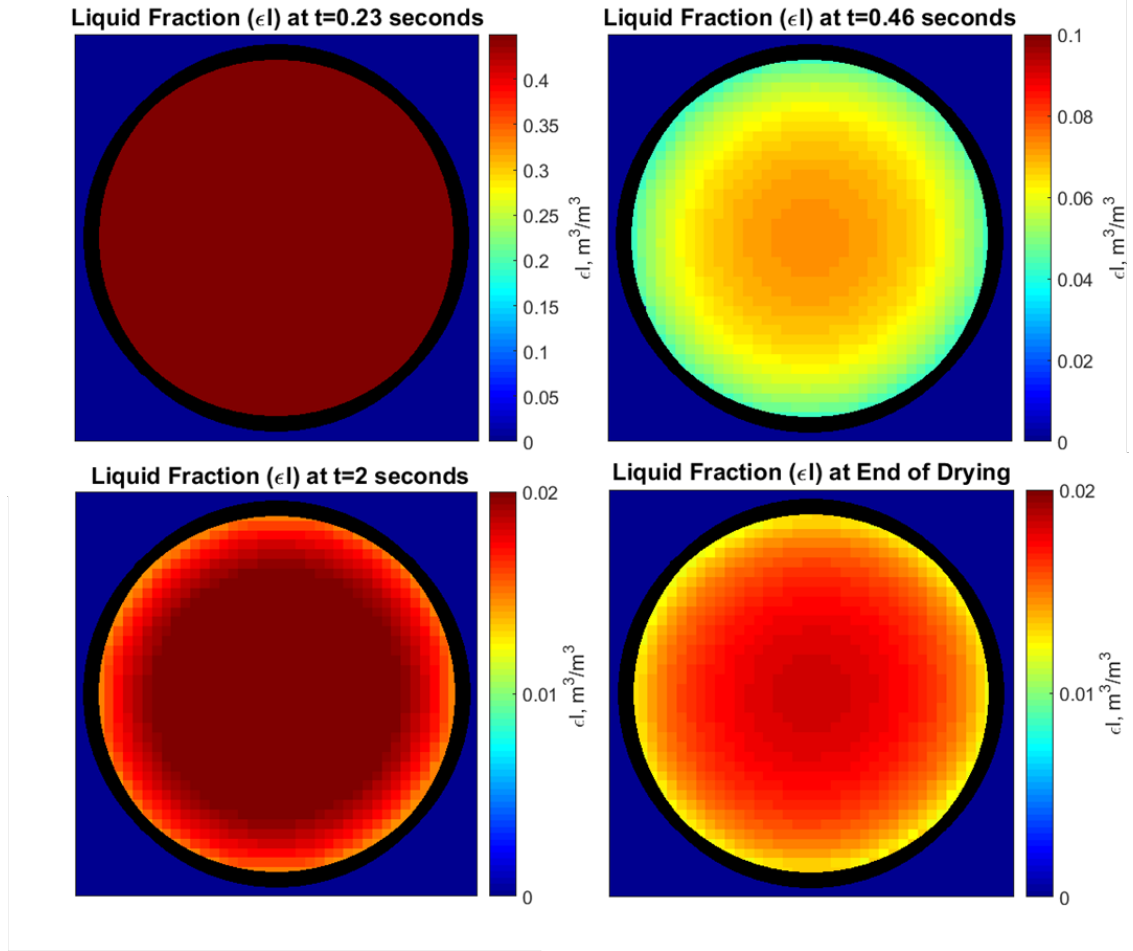
Figure 5-10: Liquid fraction vs. time during drying of a fully impregnated Neusilin® particle with methanol solution of Fenofibrate in fluidized bed: D_p=200 um, K=8.6x10^{-15} m^2, ε=0.85 m^3/m^3, D_{API}=6x10^{-9} m^2/s, K_{cryst}=1x10^{-3} s^{-1}, $T_{drying\ gas}$=80 °C, Q_{soln}=4 ml/min, $Q_{drying\ gas}$=9 m^3/h, C_{API}=44 mg/ml.
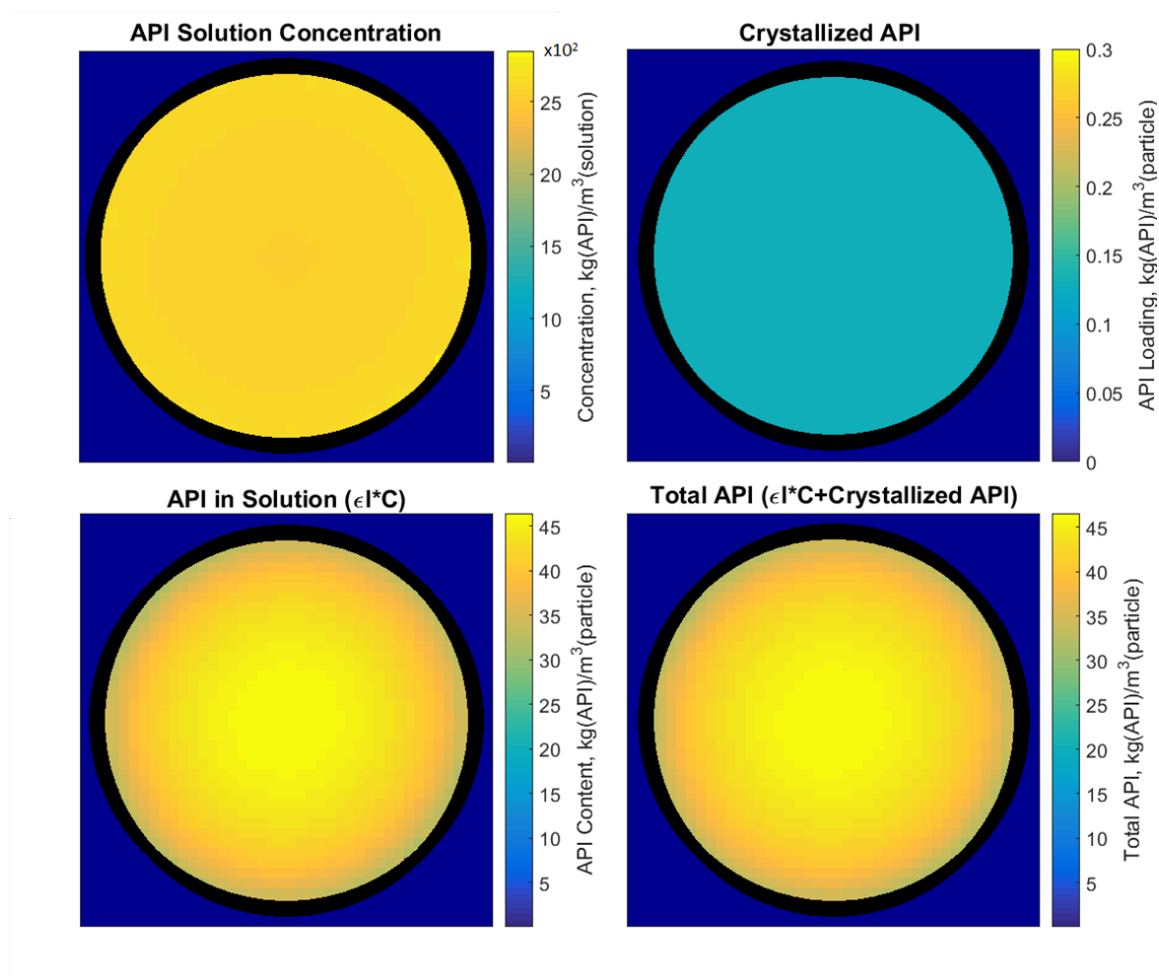
Figure 5-11: API distribution within a fully impregnated Neusilin® particle with methanol solution of Fenofibrate at the end of fluidized bed drying: D_p=200 um, K=8.6x10^{-15} m^2, ε=0.85 m^3/m^3, D_{API}=6x10^{-9} m^2/s, K_{cryst}=1x10^{-3} s^{-1}, $T_{drying\ gas}$=80 ^{o}C, Q_{soln}=4 ml/min, $Q_{drying\ gas}$= 9 m^3/h, C_{API}=44 mg/ml.
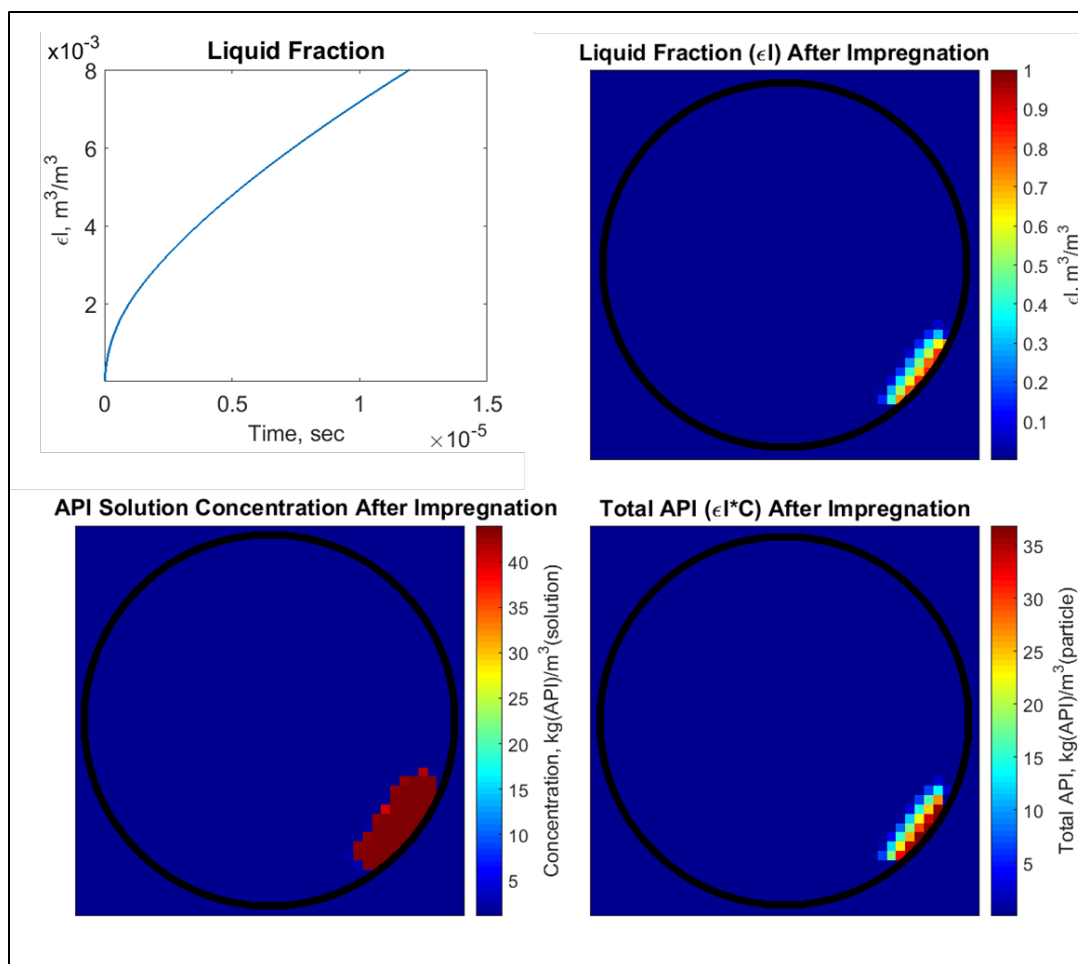
Figure 5-12: Liquid fraction during fluidized bed impregnation of a partially impregnated (single droplet) Neusilin® particle with methanol solution of Fenofibrate: $D_{droplet}$=40um, $D_{particle}$=200 um, K=8.6x10^{-15} m^2, ε=0.85 m^3/m^3, D_{API}=6x10^{-9} m^2/s, K_{cryst}=1x10^{-3} s^{-1}, $T_{drying\ gas}$=80 ^{o}C, Q_{soln}=4 ml/min, $Q_{drying\ gas}$=9 m^3/h, C_{API}=44 mg/ml.
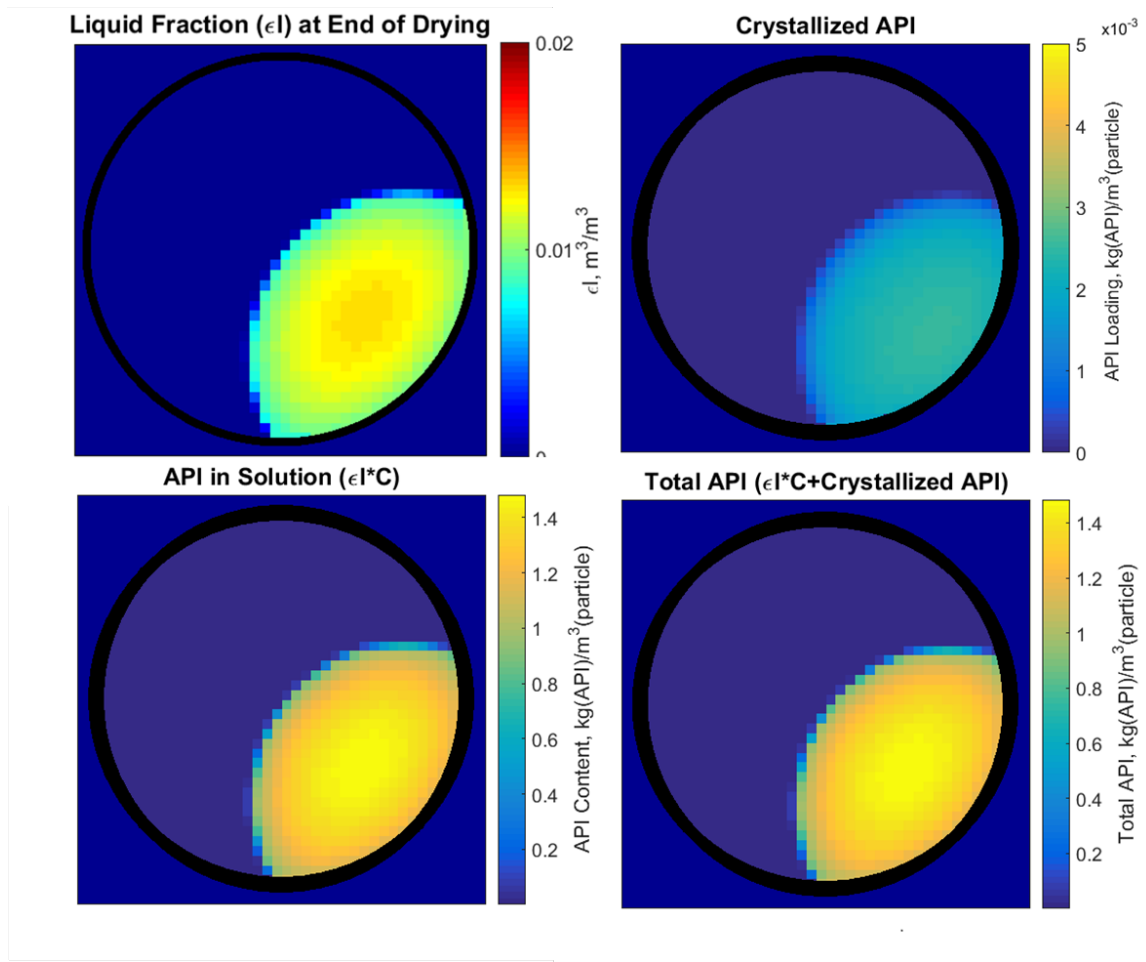
Figure 5-13: Liquid fraction and API distributions within a partially impregnated (single droplet) Neusilin® particle with methanol solution of Fenofibrate at the end of fluidized bed drying: $D_{droplet}$=40um, $D_{particle}$=200um, K=8.6x10^{-15} m^2, ε=0.85 m^3/m^3, D_{API}=6x10^{-9} m^2/s, K_{cryst}=1x10^{-3} s^{-1}, $T_{drying\ gas}$=80 ^{o}C, Q_{soln}=4 ml/min, $Q_{drying\ gas}$=9 m^3/h, C_{API}=44 mg/ml.
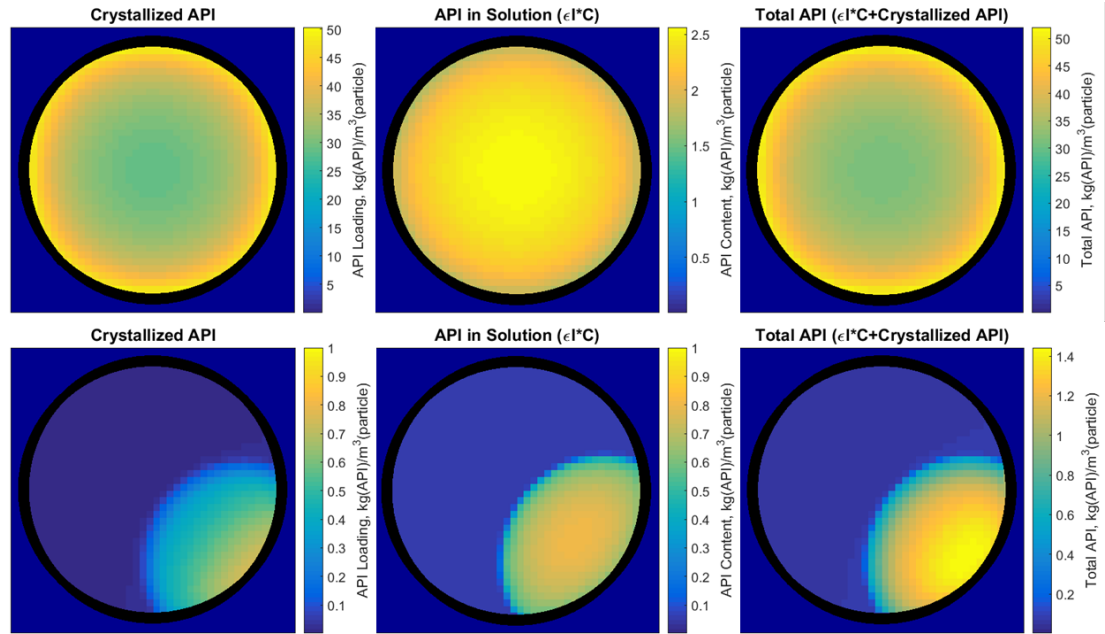
Figure 5-14: Fast Crystallization Case - API distribution within a fully impregnated (top) and partially (single droplet) impregnated (bottom) Neusilin® particle at the end of fluidized bed drying: $D_{droplet}$=40um, $D_{particle}$=200um, K=8.6x10^{-15} m^2, ε=0.85 m^3/m^3, D_{API}=6x10^{-9} m^2/s, $\underline{K_{cryst}=1\ s^{-1}}$, $T_{drying\ gas}$=80 ^{o}C, Q_{soln}=4 ml/min, $Q_{drying\ gas}$=9 m^3/h, C_{API}=44 mg/ml.
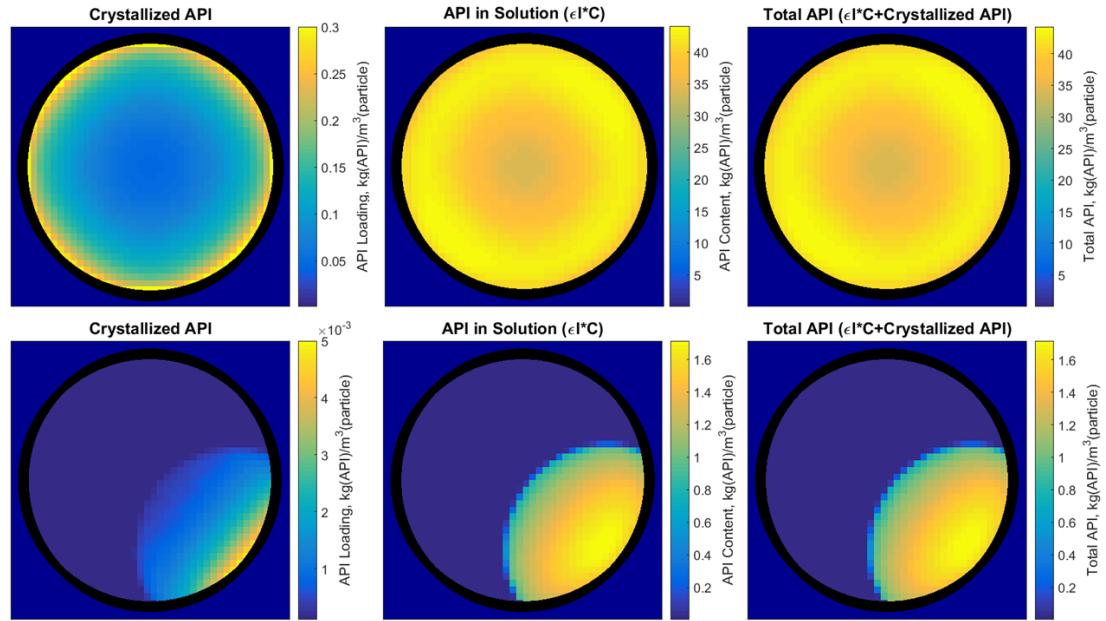
Figure 5-15: Slow Diffusion Case - API distribution within a fully impregnated (top) and partially (single droplet) impregnated (bottom) Neusilin® particle at the end of fluidized bed drying: $D_{droplet}$=40um, $D_{particle}$=200um, K=8.6x10^{-15} m^2, ε=0.85 m^3/m^3, <u>D_{API}=6x10^{-10} m^2/s,</u> K_{cryst}=1x10^{-3} s^{-1}, $T_{drying\ gas}$=80 ^{o}C, Q_{soln}=4 ml/min, $Q_{drying\ gas}$=9 m^3/h, C_{API}=44 mg/ml.
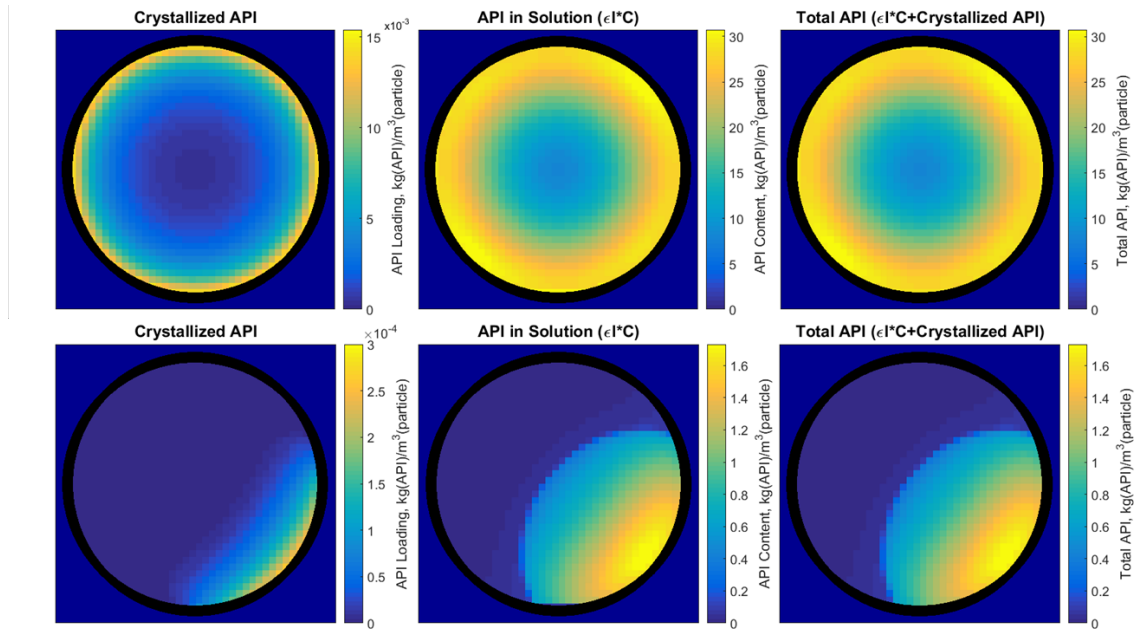
Figure 5-16: Low Porosity Case - API distribution within a fully impregnated (top) and partially (single droplet) impregnated (bottom) porous particle with low porosity at the end of fluidized bed drying: $D_{droplet}$=40um, $D_{particle}$=200um, K=8.6x10^{-15} m^2, ε=0.45 m^3/m^3, D_{API}=6x10^{-9} m^2/s, K_{cryst}=1x10^{-3} s^{-1}, $T_{drying\ gas}$=80 ^{o}C, Q_{soln}=4 ml/min, $Q_{drying\ gas}$=9 m^3/h, C_{API}=44 mg/ml.

5.9   Tables for Chapter 5

Droplet Size μm	Time Between Impregnation Cycles, s	
	100 μm Particle	200 μm Particle
20	72.8	9.1
30	245.5	30.7
40	582	72.8
Spray Rate: 4 ml/min; Neusilin: 220g Neusilin tap density: 0.19 g/ml **[227]**		

Table 5-1: Estimated average times between consecutive single-droplet impregnations for different sizes of liquid droplets and Neusilin® particles.

Chapter 6 .   Conclusions and recommendations

The work presented in this dissertation focused on fluidized bed impregnation of APIs onto porous excipients as a novel method for manufacturing pharmaceutical products. Through several case studies it was demonstrated the feasibility of the method and its many advantages over conventional solid dosage formulation techniques. A methodology for the complete characterization of the impregnated material was developed by employing commonly used analytical techniques. It was shown experimentally that fluidized bed impregnation can deliver highly uniform impregnation profile. Finally, a mathematical modeling tool box was developed capable of calculating several process parameters and the final API profile as a function of material properties and processing conditions. This chapter summarizes all presented work in the dissertation and describes several recommendations for future work.

6.1   Conclusions

The first specific aim focused on achieving a successful impregnation of pharmaceutical excipients with APIs and the complete characterization of the impregnated product and final solid dosage formulation. Chapter 2 of the dissertation outlined a comprehensive analysis of all material and equipment properties necessary for an effective impregnation. Several excipients, solvents and equipment types were identified as potential candidates. An array of analytical methods was presented that is necessary for the complete characterization of the final impregnated product. These methods can be categorized into six groups: visual examination (SEM microscopy), solid state analysis (DSC, pXRD), structural analysis (SSA, pore size distribution), drug content (HPLC), bulk powder characterization (bulk/tap densities, PSD, shear cell measurements) and final drug product analysis (dissolution testing,

tableting and compressibility). Chapter 2 continued with several preliminary studies comparing the performance of two impregnation methods. The first method was a traditional dry impregnation (full powder impregnation followed by drying) carried in a conventional granulating equipment (needed to provide adequate powder and liquid mixing). The second method was a dry impregnation carried in a fluidized bed dryer/coater/granulator, where liquid impregnation and drying occur continuously. Results showed that FB impregnation is superior because it preserves the physical properties of the excipient (PSD), eliminates particle agglomeration and is capable of achieving higher drug loadings in one-step operation. At the end of Chapter 2, a complete case study of FB impregnation using Acetaminophen as the model drug and anhydrous calcium phosphate as the porous excipient was presented. This study described in detail the methodology for a successful FB impregnation and the complete analysis of the final product. The study confirmed several important claims about impregnating APIs (using APAP as model drug) into porous excipients (using anhydrous $CaHPO_4$ as model porous excipient) utilizing fluidized bed:

- Successful proof of concept.

- Ability of the process to deliver final product with high blend uniformity (as expressed in % RSD), independent of the API loading

- Milling of the impregnated material further improves blend uniformity.

- Physical state of impregnated APAP inside porous excipient is crystalline

- FB impregnation process by design preserves the final bulk physical properties and flow properties of the impregnated materials compared to those of the pure excipient

- Impregnated APAP acts as a binder during tableting, making harder tablets when compared to physical blends

- FB impregnation does not slow down the dissolution profile of APAP

The second specific aim focused on expanding the applicability of FB impregnation to other drugs and excipients in order to show its robustness as a method for solid dosage pharmaceutical manufacturing. It also established some important benefits of FB impregnation to drug formulations consisting of poorly water soluble APIs. The first part of Chapter 3 of the dissertation described two studies using different APIs (Griseofulvin and Ibuprofen) and solvents (acetone and methanol) for FB impregnation. The results showed a successful impregnation and further reinforced the claim that FB impregnation is a suitable manufacturing technique for other APIs. The study also showed that the process mostly depends on the solvent used. The final impregnated product exhibited high blend uniformity and subsequent milling further improved homogeneity of the drug. The second part of Chapter 3 expanded the application of FB impregnation furthermore by introducing a new porous excipient with a very high internal surface area and porosity. The study focused on investigating the effects that FB impregnation and excipient have on the final formulation of a poorly-soluble drug. The API chosen for the investigational work was Fenofibrate and the porous carrier was Neusilin®. It was shown that the specific surface area of the excipient has a direct influence on the dissolution profile of the final formulation. Impregnating Fenofibrate into Neusilin® led to a significant improvement in release time compared to physical blends. The study also discovered another benefit of milling the final impregnated excipient (besides its effect on the final blend uniformity). Milling of impregnated Neusilin®, regardless of Fenofibrate loading, greatly improved release kinetics of the API. Additionally, the study demonstrated the feasibility of co-

impregnation of APIs with other additives simultaneously onto the porous carrier. The additive was SLS, a surfactant that is commonly used to increase the wettability of pharmaceutical formulations. Co-impregnation of SLS with Fenofibrate into the small pores of Neusilin® caused the drug to be deposited in its amorphous state. Furthermore, it was shown that Neusilin® stabilized the amorphous state of the API for an average shelf-life of a typical solid dosage formulation. This amorphization of the impregnated API significantly shortened its release time and made it possible to manufacture a capsule formulation of the drug, comparable in its release profile to one of the current marketed formulations, TriCor® tablets. The work presented in Chapter 3 helped to further reinforce the novelty of fluidized bed impregnation process and established several additional benefits as a manufacturing method for pharmaceutical solid dosage forms, which can be summarized as follows:

- Demonstrated further expansion of the applicability of the impregnation process to other APIs, solvents and excipients.

- Reconfirmed the ability of FB impregnation process to achieve very high blend uniformity regardless of the API loading, its nature or that of the solvent or excipient used. Milling additionally improves blend uniformity.

- Dissolution kinetics of poorly soluble APIs can be greatly influenced by the properties of the excipient used: high internal surface area speeds-up API release.

- Milling of impregnated material further improves dissolution kinetics.

- Co-impregnation with additives (or other APIs) is feasible.

- The physical state of impregnated API inside the porous excipient can be tailored to be either crystalline or amorphous.

- Amorphization of the impregnated API further improves dissolution kinetics

- Impregnated amorphous APIs can be stabilized for a long period of time in excipients with high internal surface area.

The third specific aim focused on determining the type of impregnation profile (egg-shell, egg-yolk, egg-white or uniform) that is obtained during FB impregnation of porous excipients with APIs. Chapter 4 outlined a method for cross-sectional analysis of impregnated excipient particles using energy dispersive x-ray spectroscopy along with several approaches for successful sample preparation. The goal of the study was to determine the relative API distribution inside the particles instead of a fully quantitative analysis, which usually is not straightforward and many factors need to be taken into account before the concentration data obtained from the spectra can be reported. Two FB impregnated formulations of Fenofibrate and Acetaminophen onto Neusilin$^\circledR$ were analyzed. Additionally, two other candidates were introduced (KAc and KI) as potential surrogate substrates for impregnation studies. Several particle embedding methods were demonstrated, highlighting their benefits and shortfalls. Acrylic resins worked great for particle immobilization and showed ability to produce excellent cross-sections with smooth surfaces. However, their polymerization is not always guaranteed as it depends on the nature of the impregnated substrate. Additionally, a high solubility of the API in the resign can alter the impregnation profile within the particle (as was the case with Fenofibrate). When there is no interaction between the resin and substrate (as was the case with KAc), the full potential of EDS and its ability to detect differences in the impregnation distributions (uniform vs. egg-shell/egg-yolk profiles) was revealed. Substrate/media interactions were eliminated by using cyanoacrylate adhesives, which

proved to be a great media for particle immobilization, producing quality cross-sections. The high level of resign/adhesive penetration within the porous particle during sample preparation proved to be a major disadvantage for two reasons. All types of resins/adhesives are carbon-based and their presence inside the particle prohibits mapping of the API by its own carbon signal. When an API can be detected by other characteristic elements (Cl or N), the impregnated resign showed to saturate the EDS signal and lowered its ability for meaningful detection. These shortfalls were eliminated by developing an alternative method for sample preparation: immobilization of particle monolayer onto carbon-tape or inorganic (carbon free) silica-based adhesive, followed by manually cutting the particles. This method improved the detection of trace elements and reduced significantly the carbon signal from non-relevant sources, allowing its use primarily for API detection. EDS analysis based on both carbon and trace elements showed a uniform profile in both (Fenofibrate and Acetaminophen) FB impregnation formulations, proving the ability of the impregnation process to produce highly desirable uniform distributions.

It is anticipated that the type of the API profile will be a function of the processing conditions (drying gas temperature and flow rate, spray rate, etc.) and material parameters (solvent nature, excipient porosity and pore size distribution, API diffusion constant, etc). The fourth specific aim focused on developing a mathematical model capable of describing the FB impregnation process and the resulting API distribution profile within the porous excipient. Chapter 5 described in detail the derivation of a multi-scale FB impregnation/drying model from first principles linking and how can be used to calculate important process parameters and final impregnation profiles. There were three distinct

parts to the model, each describing different aspects of the FB impregnation process. The first part performs energy/mass balance on the entire fluidized bed along with calculation of the evaporative flux from a single particle. For a given set of operating conditions, this part determines several important processing parameters such as product temperature, exiting gas temperature or maximum liquid spray rate possible. This part of the model also calculates the evaporative flux under steady state operation of the FB, which is used later in the single-particle drying model. Part two of the model calculates the liquid profile during particle impregnation in full or single-droplet mode and the time scale for impregnation. It uses experimentally determined P_c and K_{eff} vs. saturation relationships to better represent the porous excipient (Neusilin) used in the model. Part three of the model accounts for convective and diffusive flows as well as for crystallization of the API (Fenofibrate) and calculates the API distributions (crystallized and still in solution) during the drying process. The model was first applied to the same Fenofibrate/Neusilin$^{®}$ formulation that was investigated in Chapter 4 in terms of its API distribution. The results from the model predicted a uniform drug profile in a single Neusilin$^{®}$ particle, which was in agreement with the experimental results obtained in Chapter 4 using EDS analysis and in turn validated the general approach that was used to model FB impregnation. Several other hypothetical cases were investigated, where important material properties of the API/excipient system were varied. These included a fast crystallization case, a slow diffusion case and a low excipient porosity case. In all these cases, the model predicted an egg-shell type of impregnation profile.

6.2   Recommendations for future work

Although the work presented in this dissertation established FB impregnation as a viable method for manufacturing of pharmaceutical solid dosage formulations and demonstrated its many advantages, there are several potential areas for future study and improvements to the technology. Seven specific examples are detailed here.

6.2.1   Expanding FB impregnation technology to other excipient/API/solvent systems

Fluidized bed impregnation was successfully demonstrated using two excipients (dibasic calcium phosphate and Neusilin®), four APIs (Acetaminophen, Ibuprofen, Griseofulvin and Fenofibrate) and two organic solvents (methanol and acetone). The applicability of the novel formulation method can be further reinforced by testing it with different excipient/API/solvent combinations. A good excipient candidate for FB impregnation is Fujicalin®, a trade name for a different variation of dibasic calcium phosphate. The manufacturing process for Fuijicalin® is specially designed to produce highly spherical particles (similar to Neusilin®) with a higher internal surface area and total porosity, great flowability and compressibility [228]. Particles of this excipient have a reported specific surface area of 40 m^2/g, which is the highest reported for any variation of CaHPO$_4$. This could lead to dissolution kinetics improvement for some poorly-soluble APIs. Mapping of impregnated drug profiles by EDS should be performed as part of any future experiments to further understand the capabilities of FB impregnation in delivering highly uniform distributions. Comparing experimental API distributions within the excipient particles with the ones predicted by the model can further shed light on important aspects of the impregnation process. Mercury porosimetry characterization of

Fujicalin® should be performed to obtain realistic model predictions for this particular excipient. Using other organic solvents to deliver the API during FB impregnation will expand the available possibilities for impregnation. Good candidates are tetrahydrofuran, ethyl acetate, methyl-tert-butyl ether and ethanol as they have relatively low boiling points. Water could be also tested in the case of some water soluble API such as salts. There are many APIs that could be good candidates for further studies. There are several types of APIs that could be particularly valuable for further FB impregnation development. These include poorly water-soluble (study drug release improvements), amorphous (study drug release improvements and amorphous stabilization) or APIs in a salt form (impregnate with water as a solvent if solubility is high enough).

6.2.2 Investigation of other modes of FB impregnation

All impregnation studies presented in this dissertation were achieved using two different scales of fluidized bed dryer/granulator/coater, both operated in the same top-spray mode. Appropriate inserts available to both pieces of equipment can convert them for a bottom-spray operation. As already discussed in Chapter 1, bottom-spray or Wurster type FB equipment is used primarily for coating. It has been determined that this type of operation delivers more uniform coating to the particles. Wurster type FB should be able to successfully achieve impregnation and further studies could reveal other unforeseen benefits. Full testing of the impregnated powder will be needed (as described in Chapter 2 and Chapter 3) in order to adequately compare bottom-spray to top-spray mode of impregnation. Characterization of its drying capabilities will reveal if bottom-spray is more or less efficient, information needed to determine the economics of the

impregnation process. Other types of FB equipment types, such as tangential spray, could also be tested for impregnation.

6.2.3   Application of FB impregnation method to continuous manufacturing

All described work involved FB impregnation in a batch mode - a fixed amount of impregnated powder (set by the size of the equipment) is produced each time. Although the pharmaceutical industry has traditionally operated in a batch mode, recently there has been a large interest in moving towards continuous manufacturing of final drug formulations. Continuous manufacturing can have many advantages, including smaller equipment footprint, reduced capital expenses, variable (on demand) batch size and elimination of scale up. Historically FB technology has been used successfully for continuous processing, with pharmaceutical applications being drying, granulation and coating [229-231]. Future work could include adopting FB impregnation to continuous production of pharmaceuticals. In order for this to be successful, some preliminary studies need to be conducted. All FB impregnation experiments described in this dissertation involved relatively slow liquid spray rates, resulting in longer processing times (several hours). These spray rates were chosen to ensure success, as no prior information existed regarding FB impregnation of pharmaceuticals. In order for the technology to be successfully implemented in a continuous mode, the processing times need to be shortened and be comparable to typical residence times of common excipients inside a continuous fluidized bed. Further investigation is needed to determine the maximum achievable liquid spray rates during FB impregnation. Their effect on critical product attributes (blend uniformity and absence of coating/agglomeration to name a few) will determine FB impregnation applicability as a continuous process.

6.2.4   Further improvements to dissolution kinetics of poorly-soluble APIs

Work presented in Chapter 3 demonstrated the advantages FB impregnation can offer to poorly water-soluble APIs. It was shown that when large surface area excipients were impregnated with such APIs, the dissolution kinetics of the formulation was significantly improved (speed-up drug release). The impregnating process distributes the API over a large surface area inside the particles, which is proportional to the effective dissolution rate. Further increase in dissolution was achieved by additional milling of the impregnated powders. All of these formulations used water-insoluble excipient (Neusilin®), which suggests that part of the overall drug dissolution process was diffusion from inside the particles towards the bulk solution. If the excipient carrier was a water-soluble substance (such as salts or sugars) the expectation is that the drug release would have been even a faster process. Future FB impregnation studies using water-soluble excipients could shed more light on ways to further improve drug dissolution. Such excipients currently exist, however, their porosity and internal surface area are not very high. There have been reported methods for manufacturing relatively high surface area mannitol [232] and lactose [233-235] by spray drying with templating agents. Using water soluble excipients could also be beneficial to tableting of impregnated formulations. Upon compression during tablet preparation, the internal voids of the non-water-soluble porous carrier are compacted, which traps the drug material inside and as a result the diffusion and the overall drug release rate are reduced. These effects can be eliminated when using water-soluble excipients for impregnation.

6.2.5 Expand application of FB co-impregnation with additives and APIs

An interesting effect was reported in Chapter 3, where co-impregnation of an API (Fenofibrate) and an additive (SLS) resulted in a complete amorphization of the impregnated API. It is highly desirable to understand if this effect is applicable to other types of APIs or it is only specific to Fenofibrate. Co-impregnation with other types of additives, such as polymers, could offer additional possibilities for tailoring the drug release profile. Such additives could be beneficial for developing slow-release formulations. An example of a pharmaceutical polymer often used in solid dosage formulations for delaying drug release is HPMC (hydroxypropyl methylcellulose) with many others having similar effect. Often pharmaceutical formulations comprise of two APIs in combination. Co-impregnation of two or more APIs could be achieved by FB impregnation using a common solution of the drugs. It could be also achieved by a impregnating the APIs individually in a sequential fashion. Dissolution testing of the resulting formulation will reveal what is the effect of co-impregnation of the individual drug release profiles. The possibilities for tailoring pharmaceutical formulation by FB co-impregnation are endless. One could expect that a formulation prepared by co-impregnation of an API, followed by a polymer, followed by another API would have the effect of a fast dissolution of the second API and a control release for the first.

6.2.7 Mathematical modeling

The mathematical model presented in Chapter 5 aimed to study effects of material properties and processing conditions have on the resulting API profile. The time span between consecutive impregnations was roughly estimated based on several broad assumptions. A discrete element modeling (DEM) coupled with computational fluid

dynamic (CFD) modeling could be very useful in understanding the motion of particles during the FB impregnation process. Such modeling could help estimate the average residence time the excipient particles are spending in the spray and drying zones [236, 237]. It was demonstrated in Chapter 2 and Chapter 3 that FB impregnation was capable of achieving high degree of blend uniformity. This is due to the high degree of powder mixing in the FB coupled with the high dispersion of the spraying liquid into micron-sized droplets. Therefore, it is expected that the blend uniformity will depend on the drying gas velocity, particle and droplet sizes and liquid spray rate. Modeling the impregnation process using DEM could demonstrate important relationships between the processing conditions and the resulting blend uniformity [238].

The model presented in Chapter 5 can be further improved by incorporating gas phase diffusion during the falling rate drying period in order to make the model more representative for studying examples with high drying temperature. Another improvement would be to account for the solvent vapor pressure variation with the solute concentration. This will permit studying cases with high initial API concentration and its effect on the drying rate and the final distribution of the active ingredient.

References

1. Nickerson, B., *Sample Preparation of Pharmaceutical Dosage Forms: Challenges and Strategies for Sample Preparation and Extraction*. 2011, American Association of Pharmaceutical Scientists. p. 145.

2. Zheng, J., *Formulation and Analytical Development for Low-Dose Oral Drug Products*. 2009, Hoboken: John Wiley & Sons, Inc.

3. FDA, *Guidance for Industry: Powder Blends and Finished Dosage Units - Stratified In-Process Dosage Unit Sampling and Assessment*. (2003), http://www.fda.gov/downloads/Drugs/GuidanceComplianceRegulatoryInformation/Guidances/ucm070312.pdf.

4. FDA. *The Biopharmaceutics Classification System (BCS) Guidance*. Available from: http://www.fda.gov/AboutFDA/CentersOffices/OfficeofMedicalProductsandTobacco/CDER/ucm128219.htm.

5. Benet, L.Z., *The role of BCS (biopharmaceutics classification system) and BDDCS (biopharmaceutics drug disposition classification system) in drug development*. Journal of Pharmaceutical Sciences, 2013. 102(1): p. 34-42.

6. Chaumeil, J., *Micronization: a method of improving the bioavailability of poorly soluble drugs. PG - 211-5*. Methods and Findings in Experimental and Clinical Pharmacology, 1998. 20(3): p. 211-215.

7. Sinha, B., R.H. Muller, and J.P. Moschwitzer, *Bottom-up approaches for preparing drug nanocrystals: Formulations and factors affecting particle size*. International Journal of Pharmaceutics, 2013. 453(1): p. 126-141.

8. Keck, C. and R. Muller, *Drug nanocrystals of poorly soluble drugs produced by high pressure homogenisation*. European Journal of Pharmaceutics and Biopharmaceutics, 2006. 62(1): p. 3-16.

9. Serajuddin, A.T.M., *Salt formation to improve drug solubility*. Advanced Drug Delivery Reviews, 2007. 59(7): p. 603-616.

10. Babu, N.J. and A. Nangia, *Solubility Advantage of Amorphous Drugs and Pharmaceutical Cocrystals*. Crystal Growth & Design, 2011. 11(7): p. 2662-2679.

11. Murdande, S., et al., *Solubility Advantage of Amorphous Pharmaceuticals: II. Application of Quantitative Thermodynamic Relationships for Prediction of Solubility Enhancement in Structurally Diverse Insoluble Pharmaceuticals*. Pharmaceutical Research, 2010. 27(12): p. 2704-2714.

12. Murdande, S.B., et al., *Solubility advantage of amorphous pharmaceuticals: I. A thermodynamic analysis*. Journal of Pharmaceutical Sciences, 2010. 99(3): p. 1254-1264.

13. Lee, S.Y. and R. Aris, *The Distribution of Active Ingredients in Supported Catalysts Prepared by Impregnation*. Catalysis Reviews-Science and Engineering, 1985. 27(2): p. 207-340.

14. Komiyama, M., *Design and Preparation of Impregnated Catalysts*. Catalysis Reviews-Science and Engineering, 1985. 27(2): p. 341-372.

15. Neimark, A.V., L.I. Kheifets, and V.B. Fenelonov, *Theory of preparation of supported catalysts*. Industrial & Engineering Chemistry Product Research and Development, 1981. 20(3): p. 439-450.

16. Gavriilidis, A., A. Varma, and M. Morbidelli, *OPTIMAL DISTRIBUTION OF CATALYST IN PELLETS.* Catalysis Reviews-Science and Engineering, 1993. 35(3): p. 399-456.

17. Maatman, R.W. and C.D. Prater, *Adsorption and Exclusion in Impregnation of Porous Catalytic Supports.* Industrial & Engineering Chemistry, 1957. 49(2): p. 253-257.

18. Liu, X., J.G. Khinast, and B.J. Glasser, *A Parametric Investigation of Impregnation and Drying of Supported Catalysts.* Chemical Engineering Science, 2008. 63(18): p. 4517-4530.

19. Lekhal, A., B.J. Glasser, and J.G. Khinast, *Impact of drying on the catalyst profile in supported impregnation catalysts.* Chemical Engineering Science, 2001. 56(15): p. 4473-4487.

20. Liu, X., J.G. Khinast, and B.J. Glasser, *Drying of Supported Catalysts: A Comparison of Model Predictions and Experimental Measurements of Metal Profiles.* Industrial & Engineering Chemistry Research, 2010. 49(6): p. 2649-2657.

21. Mellaerts, R., et al., *Physical state of poorly water soluble therapeutic molecules loaded into SBA-15 ordered mesoporous silica carriers: A case study with itraconazole and ibuprofen.* Langmuir, 2008. 24(16): p. 8651-8659.

22. Van Speybroeck, M., et al., *Ordered Mesoporous Silica Material SBA-15: A Broad-Spectrum Formulation Platform for Poorly Soluble Drugs.* Journal of Pharmaceutical Sciences, 2009. 98(8): p. 2648-2658.

23. Rengarajan, G.T., et al., *Stabilization of the amorphous state of pharmaceuticals in nanopores.* Journal of Materials Chemistry, 2008. 18(22): p. 2537-2539.

24. Ji, C.D., et al., *The development of a dense gas solvent exchange process for the impregnation of pharmaceuticals into porous chitosan.* International Journal of Pharmaceutics, 2010. 391(1-2): p. 187-196.

25. López-Periago, A., et al., *Impregnation of a biocompatible polymer aided by supercritical CO2: Evaluation of drug stability and drug–matrix interactions.* The Journal of Supercritical Fluids, 2009. 48(1): p. 56-63.

26. Verraedt, E., et al., *Controlled release of chlorhexidine from amorphous microporous silica.* Journal of Controlled Release, 2010. 142(1): p. 47-52.

27. Chevalier, E., et al., *Ibuprofen-loaded calcium phosphate granules: Combination of innovative characterization methods to relate mechanical strength to drug location.* Acta Biomaterialia, 2010. 6(1): p. 266-274.

28. Ugaonkar, S., T.E. Needham, and G.D. Bothun, *Solubility and partitioning of carbamazepine in a two-phase supercritical carbon dioxide/polyvinylpyrrolidone system.* International Journal of Pharmaceutics, 2011. 403(1-2): p. 96-100.

29. Banchero, M., et al., *Supercritical solvent impregnation of piroxicam on PVP at various polymer molecular weights.* Journal of Supercritical Fluids, 2009. 49(2): p. 271-278.

30. Beiner, M., et al., *Manipulating the crystalline state of pharmaceuticals by nanoconfinement.* Nano Letters, 2007. 7(5): p. 1381-1385.

31. Desportes, S., et al., *Production of supported asymmetric catalysts in a fluidised bed.* Powder Technology, 2005. 157(1-3): p. 12-19.

32.   Barthe, L., et al., *Dry impregnation in fluidized bed: Drying and calcination effect on nanoparticles dispersion and location in a porous support.* Chemical Engineering Research & Design, 2008. 86(4A): p. 349-358.

33.   Barthe, L., et al., *Metallic salt deposition on porous particles by dry impregnation in fluidized bed: Effect of drying conditions on metallic nanoparticles distribution.* Chemical Engineering Research & Design, 2009. 87(7A): p. 915-922.

34.   McCabe, W.L., J.C. Smith, and P. Harriott, *Unit Operations of Chemical Engineering.* 7 ed. 2004, New York: McGraw-Hill Higher Education.

35.   Geldart, D., *Types of gas fluidization.* Powder Technology, 1973. 7(5): p. 285-292.

36.   Chen, Y.H., et al., *Fluidization of coated group C powders.* Aiche Journal, 2008. 54(1): p. 104-121.

37.   Mujumdar, A.S., *Handbook of Industrial Drying, Fourth Edition.* Vol. Fourth edition. 2015, Boca Raton: CRC Press.

38.   Yang, W.-c., *Handbook of fluidization and fluid-particle systems.* 2003: CRC press.

39.   Zhu, H.Y. and J. Zhu, *New investigation in regime transition from bubbling to turbulent fluidization.* Canadian Journal of Chemical Engineering, 2008. 86(3): p. 553-562.

40.   Potter, O.E. and A.J. Keogh, *Drying high-moisture coals before liquefaction or gasification.* Fuel Processing Technology, 1981. 4(2): p. 217-227.

41.   Niamnuy, C. and S. Devahastin, *Drying kinetics and quality of coconut dried in a fluidized bed dryer.* Journal of Food Engineering, 2005. 66(2): p. 267-271.

42.   Strumiłło, C., et al., *Simulation of fluidized bed drying of biosynthesis products.* Chemical Engineering and Processing: Process Intensification, 1989. 26(2): p. 139-145.

43.   Türker, M., et al., *Drying of baker's yeast in batch fluidized bed.* Chemical Engineering and Processing: Process Intensification, 2006. 45(12): p. 1019-1028.

44.   Şahin, Ö. and A.N. Bulutcu, *Dehydration kinetics of sodium perborate tetrahydrate to monohydrate in a fluidized-bed drier.* Chemical Engineering Science, 1999. 54(1): p. 115-120.

45.   Wurster, D.E., *Air-Suspension Technique of Coating Drug Particles *.* Journal of Pharmaceutical Sciences. 48(8): p. 451-454.

46.   Scott, M.W., et al., *Continuous production of tablet granulations in a fluidized bed I. Theory and design considerations.* Journal of Pharmaceutical Sciences, 1964. 53(3): p. 314-320.

47.   Rankell, A.S., et al., *Continuous production of tablet granulations in a fluidized bed II. Operation and performance of equipment.* Journal of Pharmaceutical Sciences, 1964. 53(3): p. 320-324.

48.   Swarbrick, J. and J.C. Boylan, *Encyclopedia of pharmaceutical technology.* Vol. 6. 1992, New York: M. Dekker.

49.   Kristensen, J., T. Schaefer, and P. Kleinebudde, *Direct pelletization in a rotary processor controlled by torque measurements. I. Influence of process variables.* Pharmaceutical Development and Technology, 2000. 5(2): p. 247-256.

50.   Srivastava, S. and G. Mishra, *Fluid bed technology: Overview and parameters for process selection.* International Journal of Pharmaceutical Sciences and Drug Research, 2010. 2(4): p. 236-246.

51.   Glatt. *Fluidized Bed Processes*. Available from: https://www.glatt.com/en/processes/.

52.   Briens, L. and M. Bojarra, *Monitoring Fluidized Bed Drying of Pharmaceutical Granules.* AAPS PharmSciTech, 2010. 11(4): p. 1612-1618.

53.   Chen, H., et al., *Fluidized bed drying of a pharmaceutical powder: A parametric investigation of drying of dibasic calcium phosphate.* Drying Technology, 2017. 35(13): p. 1602-1618.

54.   Dixit, R. and S. Puthli, *Fluidization technologies: Aerodynamic principles and process engineering.* Journal of Pharmaceutical Sciences, 2009. 98(11): p. 3933-3960.

55.   Loh, Z.H., et al., *Spray granulation for drug formulation.* Expert Opinion on Drug Delivery, 2011. 8(12): p. 1645-1661.

56.   Glatt. *Fluid Bed Systems*. Available from: https://www.glatt.com/fileadmin/user_upload/content/pdf_downloads/WS_EN_7221_301.pdf.

57.   Parikh, D.M., *Handbook of Pharmaceutical Granulation Technology*. 2 ed. 2005, Boca Ration: Taylor & Francis.

58.   Daud, W.R.W., *Fluidized Bed Dryers - Recent Advances.* Advanced Powder Technology, 2008. 19(5): p. 403-418.

59.   Syahrul, S., F. Hamdullahpur, and I. Dincer, *Energy analysis in fluidized-bed drying of large wet particles.* International Journal of Energy Research, 2002. 26(6): p. 507-525.

60.   Augsburger, L.L. and S.W. Hoag, *Pharmaceutical Dosage Forms: Tablets*. Vol. 1,2,3. 2008, New York: Informa Healthcare USA.

61.   Gibson, M., *Pharmaceutical preformulation and formulation: a practical guide from candidate drug selection to commercial dosage form*. 2009, New York: Informa Healthcare USA.

62.   ICH. *International Council for Harmonisation - Quality*. Available from: http://www.ich.org/home.html.

63.   Clayton, J., *Reviewing Current Practice in Powder Testing.* Organic Process Research & Development, 2015. 19(1): p. 102-109.

64.   Faqih, A., et al., *An experimental/computational approach for examining unconfined cohesive powder flow.* International Journal of Pharmaceutics, 2006. 324(2): p. 116-127.

65.   Freeman, R., *Measuring the flow properties of consolidated, conditioned and aerated powders - A comparative study using a powder rheometer and a rotational shear cell.* Powder Technology, 2007. 174(1-2): p. 25-33.

66.   Pharmacopea, U.S. *711 DISSOLUTION*.

67.   Doldán, C., et al., *Dicalcium phosphate dihydrate and anhydrous dicalcium phosphate for direct compression: A comparative study.* International Journal of Pharmaceutics, 1995. 124(1): p. 69-74.

68. Alcoutlabi, M. and G.B. McKenna, *Effects of confinement on material behaviour at the nanometre size scale.* Journal of Physics - Condensed Matter, 2005. 17(15): p. R461-R524.

69. Qi, S., et al., *An investigation into the effects of thermal history on the crystallisation behaviour of amorphous paracetamol.* European Journal of Pharmaceutics and Biopharmaceutics, 2008. 69(1): p. 364-371.

70. Vasilenko, A., B.J. Glasser, and F.J. Muzzio, *Shear and flow behavior of pharmaceutical blends - Method comparison study.* Powder Technology, 2011. 208(3): p. 628-636.

71. Martinez, M.N. and G.L. Amidon, *A Mechanistic Approach to Understanding the Factors Affecting Drug Absorption: A Review of Fundamentals.* The Journal of Clinical Pharmacology, 2002. 42(6): p. 620-643.

72. Yu, L., *An Integrated Model for Determining Causes of Poor Oral Drug Absorption.* Pharmaceutical Research, 1999. 16(12 DO - 10.1023/A:1018911728161): p. 1883-1887 LA - English.

73. Shaikh, M.I., N.D. Derle, and R. Bhamber, *Permeability Enhancement Techniques for Poorly Permeable Drugs: A Review.* Journal of Applied Pharmaceutical Science, 2012. 2(7): p. 34-39.

74. Dokoumetzidis, A. and P. Macheras, *A century of dissolution research: From Noyes and Whitney to the Biopharmaceutics Classification System.* International Journal of Pharmaceutics, 2006. 321(1-2): p. 1-11.

75. Vogt, M., K. Kunath, and J.B. Dressman, *Dissolution enhancement of fenofibrate by micronization, cogrinding and spray-drying: Comparison with commercial preparations.* European Journal of Pharmaceutics and Biopharmaceutics, 2008. 68(2): p. 283-288.

76. Berti, D. and G. Palazzo, *Colloidal Foundations of Nanoscience.* 1st ed. 2014: Elsevier.

77. Peltonen, L. and J. Hirvonen, *Pharmaceutical nanocrystals by nanomilling: critical process parameters, particle fracturing and stabilization methods.* Journal of Pharmacy and Pharmacology, 2010. 62(11): p. 1569-1579.

78. Ostwald, W., Lehrbuch der Allgemeinen Chemie, 1896. 2(1).

79. Keck, C.M. and R.H. Muller, *Drug nanocrystals of poorly soluble drugs produced by high pressure homogenisation.* European Journal of Pharmaceutics and Biopharmaceutics, 2006. 62(1): p. 3-16.

80. Hancock, B. and M. Parks, *What is the True Solubility Advantage for Amorphous Pharmaceuticals?* Pharmaceutical Research, 2000. 17(4): p. 397-404.

81. Chiou, W.L. and S. Riegelman, *Pharmaceutical applications of solid dispersion systems.* Journal of Pharmaceutical Sciences, 1971. 60(9): p. 1281-1302.

82. Janssens, S. and G. Van den Mooter, *Review: physical chemistry of solid dispersions.* Journal of Pharmacy and Pharmacology, 2009. 61(12): p. 1571-1586.

83. Kaushal, A.M., P. Gupta, and A.K. Bansal, *Amorphous Drug Delivery Systems: Molecular Aspects, Design, and Performance.* Critical Reviews™ in Therapeutic Drug Carrier Systems, 2004. 21(3).

84. Leuner, C. and J. Dressman, *Improving drug solubility for oral delivery using solid dispersions.* European Journal of Pharmaceutics and Biopharmaceutics, 2000. 50(1): p. 47-60.

85.   Vasconcelos, T., B. Sarmento, and P. Costa, *Solid dispersions as strategy to improve oral bioavailability of poor water soluble drugs.* Drug Discovery Today, 2007. 12(23-24): p. 1068-1075.

86.   Ahuja, N., O.P. Katare, and B. Singh, *Studies on dissolution enhancement and mathematical modeling of drug release of a poorly water-soluble drug using water-soluble carriers.* European Journal of Pharmaceutics and Biopharmaceutics, 2007. 65(1): p. 26-38.

87.   Masuda, T., et al., *Cocrystallization and amorphization induced by drug-excipient interaction improves the physical properties of acyclovir.* International Journal of Pharmaceutics, 2012. 422(1-2): p. 160-169.

88.   Laitinen, R., et al., *Emerging trends in the stabilization of amorphous drugs.* International Journal of Pharmaceutics, 2013. 453(1): p. 65-79.

89.   Xu, W., J. Riikonen, and V.-P. Lehto, *Mesoporous systems for poorly soluble drugs.* International Journal of Pharmaceutics, 2013. 453(1): p. 181-197.

90.   Qian, K.K. and R.H. Bogner, *Application of mesoporous silicon dioxide and silicate in oral amorphous drug delivery systems.* Journal of Pharmaceutical Sciences, 2012. 101(2): p. 444-463.

91.   Van Speybroeck, M., et al., *Ordered mesoporous silica material SBA-15: A broad-spectrum formulation platform for poorly soluble drugs.* Journal of Pharmaceutical Sciences, 2009. 98(8): p. 2648-2658.

92.   Patil, A., et al., *Encapsulation of water insoluble drugs in mesoporous silica nanoparticles using supercritical carbon dioxide.* Journal of Nanomedicine and Nanotechnology, 2011. 2(3).

93.   Belhadj-Ahmed, F., et al., *Impregnation of vitamin E acetate on silica mesoporous phases using supercritical carbon dioxide.* The Journal of Supercritical Fluids, 2009. 51(2): p. 278-286.

94.   Nokhodchi, A., O. Amire, and M. Jelvehgari, *Physico-mechanical and dissolution behaviours of ibuprofen crystals crystallized in the presence of various additives.* DARU : Journal of Faculty of Pharmacy, Tehran University of Medical Sciences, 2010. 18(2): p. 74-83.

95.   Lee, T., C.S. Kuo, and Y.H. Chen, *Solubility, Polymorphism, Crystallinity, and Crystal Habit of Acetaminophen and Ibuprofen by Initial Solvent Screening.* Pharmaceutical Technology, October 2006.

96.   Shaw, L.R., et al., *The effect of selected water-soluble excipients on the dissolution of paracetamol and Ibuprofen.* Drug Dev Ind Pharm, 2005. 31(6): p. 515-25.

97.   Ling, H., J.T. Luoma, and D. Hilleman, *A Review of Currently Available Fenofibrate and Fenofibric Acid Formulations.* Cardiology Research, 2013. 4(2): p. 47-55.

98.   Jamzad, S. and R. Fassihi, *Role of surfactant and pH on dissolution properties of fenofibrate and glipizide - A technical note.* AAPS PharmSciTech, 2006. 7(2): p. E17-E22.

99.   Adkins, J. and D. Faulds, *Micronized Fenofibrate - A review of its Pharmacodynalic Properties and Clinical Efficacy in the Management of Dyclipidaemia.* Drugs, 1997. 54(4): p. 615-633.

100. Guichard, J.P., P. Blouquin, and Y. Qing, *A New Formulation of Fenofibrate: Suprabioavailable Tablets.* Current Medical Research and Opinion®, 2000. 16(2): p. 134-138.

101. Guivarc'h, P.-H., M.G. Vachon, and D. Fordyce, *A new fenofibrate formulation: results of six single-dose, clinical studies of bioavailability under fed and fasting conditions.* Clinical Therapeutics, 2004. 26(9): p. 1456-1469.

102. Bosselmann, S. and R.O. Williams, *Has nanotechnology led to improved therapeutic outcomes?* Drug Development and Industrial Pharmacy, 2011. 38(2): p. 158-170.

103. Shegokar, R. and R.H. Muller, *Nanocrystals: Industrially feasible multifunctional formulation technology for poorly soluble actives.* International Journal of Pharmaceutics, 2010. 399(1-2): p. 129-139.

104. FDA. *Drug approval package: Tricor (fenofibrate) tablets-application 021656.* November 5, 2004.

105. Dwyer, L.M., et al., *Confined crystallization of fenofibrate in nanoporous silica.* CrystEngComm, 2015. 17(41): p. 7922-7929.

106. Hou, D., et al., *The production and characteristics of solid lipid nanoparticles (SLNs).* Biomaterials, 2003. 24(10): p. 1781-5.

107. Schulze, D., *Powders and Bulk Solids.* 1 ed. Behavior, Characterization, Storage and Flow. 2008: Springer-Verlag Berlin Heidelberg.

108. Hong, S., et al., *High drug load, stable, manufacturable and bioavailable fenofibrate formulations in mesoporous silica: a comparison of spray drying versus solvent impregnation methods.* Drug Delivery, 2014: p. 1-12.

109. Cha, K., et al., *Enhancement of the dissolution rate and bioavailability of fenofibrate by a melt-adsorption method using supercritical carbon dioxide.* International Journal of Nanomedicine., 2012. 7: p. 5565-5575.

110. Lee, S.-Y. and R. Aris, *The Distribution of Active ingredients in Supported Catalysts Prepared by Impregnation.* Catalysis Reviews, 1985. 27(2): p. 207-340.

111. Munnik, P., P.E. de Jongh, and K.P. de Jong, *Recent Developments in the Synthesis of Supported Catalysts.* Chemical Reviews, 2015. 115(14): p. 6687-6718.

112. Galarraga, C., E. Peluso, and H. de Lasa, *Eggshell catalysts for Fischer–Tropsch synthesis: Modeling catalyst impregnation.* Chemical Engineering Journal, 2001. 82(1–3): p. 13-20.

113. Horvath, C. and J.-M. Engasser, *Pellicular Heterogeneous Catalysts. A Theoretical Study of the Advantages of Shell Structured Immobilized Enzyme Particles.* Industrial & Engineering Chemistry Fundamentals, 1973. 12(2): p. 229-235.

114. Buurmans, I.L.C. and B.M. Weckhuysen, *Heterogeneities of individual catalyst particles in space and time as monitored by spectroscopy.* Nat Chem, 2012. 4(11): p. 873-886.

115. Zaeraand, F. and Z. Ma, *Chapter 1. Characterization of Heterogeneous Catalysts*, in *Surface and Nanomolecular Catalysis*, R. Richards, Editor. 2006, CRC Press. p. 1-38.

116. Echlin, P., *Handbook of Sample Preparation for Scanning Electron Microscopy and X-Ray Microanalysis.* 2009, New York: Springer. 330.

117. Joseph I. Goldstein, D.E.N., Patrick Echlin & David C. Joy,, *Scanning Electron Microscopy and X-Ray Microanalysis, 3rd Edition*. 2005, New York: Springer. 820.

118. Harriott, P., *Diffusion effects in the preparation of impregnated catalysts.* Journal of Catalysis, 1969. 14(1): p. 43-48.

119. Heise, M.S. and J.A. Schwarz, *Preparation of metal distributions within catalyst supports. I. Effect of ph on catalytic metal profiles.* Journal of Colloid and Interface Science, 1985. 107(1): p. 237-243.

120. Heise, M.S. and J.A. Schwarz, *Preparation of metal distributions within catalyst supports: II. Effect of ionic strength on catalytic metal profiles.* Journal of Colloid and Interface Science, 1986. 113(1): p. 55-61.

121. Heise, M.S. and J.A. Schwarz, *Preparation of metal distributions within catalyst supports: III. Single component modeling of pH, ionic strength, and concentration effects.* Journal of Colloid and Interface Science, 1988. 123(1): p. 51-58.

122. Schwarz, J.A. and M.S. Heise, *Preparation of metal distributions within catalyst supports: IV. Multicomponent effects.* Journal of Colloid and Interface Science, 1990. 135(2): p. 461-467.

123. Komiyama, M., R.P. Merrill, and H.F. Harnsberger, *Concentration profiles in impregnation of porous catalysts: Nickel on alumina.* Journal of Catalysis, 1980. 63(1): p. 35-52.

124. van de Water, L.G.A., et al., *Spatially resolved UV–vis microspectroscopy on the preparation of alumina-supported Co Fischer–Tropsch catalysts: Linking activity to Co distribution and speciation.* Journal of Catalysis, 2006. 242(2): p. 287-298.

125. van de Water, L.G.A., et al., *UV−Vis Microspectroscopy: Probing the Initial Stages of Supported Metal Oxide Catalyst Preparation.* Journal of the American Chemical Society, 2005. 127(14): p. 5024-5025.

126. Zandbergen, M.W., A.M. Beale, and I.B.M. Weckhuysen, *On the Microdistributions of Cr-Ion Complexes within mm-Sized γ-Al 2O 3 Catalyst Bodies upon Impregnation as Studied by UV/Vis and Raman Microspectroscopy.* ChemCatChem, 2012. 4(2): p. 217-227.

127. Weckhuysen, B.M., *Chemical Imaging of Spatial Heterogeneities in Catalytic Solids at Different Length and Time Scales.* Angewandte Chemie International Edition, 2009. 48(27): p. 4910-4943.

128. Qin, F. and E.E. Wolf, *Spatially resolved infrared spectroscopy: a novel technique for in situ study of spatial surface coverage during CO oxidation on supported catalysts.* Catalysis Letters, 1996. 39(1): p. 19-25.

129. Stavitski, E. and B.M. Weckhuysen, *Infrared and Raman imaging of heterogeneous catalysts.* Chemical Society Reviews, 2010. 39(12): p. 4615-4625.

130. Dazzi, A. and C.B. Prater, *AFM-IR: Technology and Applications in Nanoscale Infrared Spectroscopy and Chemical Imaging.* Chemical Reviews, 2017. 117(7): p. 5146-5173.

131. Centrone, A., *Infrared Imaging and Spectroscopy Beyond the Diffraction Limit*, in *Annual Review of Analytical Chemistry, Vol 8*, R.G. Cooks and J.E. Pemberton, Editors. 2015. p. 101-126.

132. Bergwerff, J.A., et al., *Influence of the preparation method on the hydrotreating activity of MoS2/Al2O3 extrudates: A Raman microspectroscopy study on the genesis of the active phase.* Journal of Catalysis, 2006. 243(2): p. 292-302.

133. Bergwerff, J.A., et al., *Envisaging the Physicochemical Processes during the Preparation of Supported Catalysts: Raman Microscopy on the Impregnation of Mo onto Al2O3 Extrudates.* Journal of the American Chemical Society, 2004. 126(44): p. 14548-14556.

134. Espinosa-Alonso, L., A.M. Beale, and B.M. Weckhuysen, *Profiling Physicochemical Changes within Catalyst Bodies during Preparation: New Insights from Invasive and Noninvasive Microspectroscopic Studies.* Accounts of Chemical Research, 2010. 43(9): p. 1279-1288.

135. Paudel, A., D. Raijada, and J. Rantanen, *Raman spectroscopy in pharmaceutical product design.* Advanced Drug Delivery Reviews, 2015. 89: p. 3-20.

136. Stewart, S., et al., *Raman Imaging*, in *Annual Review of Analytical Chemistry, Vol 5*, R.G. Cooks and E.S. Yeung, Editors. 2012. p. 337-360.

137. Henson, M.J. and L. Zhang, *Drug characterization in low dosage pharmaceutical tablets using Raman microscopic mapping.* Applied Spectroscopy, 2006. 60(11): p. 1247-1255.

138. Lin, W.Q., et al., *Characterization of chloramphenicol palmitate drug polymorphs by Raman mapping with multivariate image segmentation using a spatial directed agglomeration clustering method.* Analytical Chemistry, 2006. 78(17): p. 6003-6011.

139. Schrank, S., et al., *Impact of Drying on Solid State Modifications and Drug Distribution in Ibuprofen-Loaded Calcium Stearate Pellets.* Molecular Pharmaceutics, 2014. 11(2): p. 599-609.

140. Łojewska, J., et al., *Topography and morphology of multicomponent catalytic materials based on Co, Ce and Pd oxides deposited on metallic structured carriers studied by AFM/Raman interlaced microscopes.* Catalysis Today, 2013. 216: p. 11-17.

141. Farber, L., G. Tardos, and J.N. Michaels, *Use of X-ray tomography to study the porosity and morphology of granules.* Powder Technology, 2003. 132(1): p. 57-63.

142. Dadkhah, M., M. Peglow, and E. Tsotsas, *Characterization of the internal morphology of agglomerates produced in a spray fluidized bed by X-ray tomography.* Powder Technology, 2012. 228(Supplement C): p. 349-358.

143. Pashminehazar, R., A. Kharaghani, and E. Tsotsas, *Three dimensional characterization of morphology and internal structure of soft material agglomerates produced in spray fluidized bed by X-ray tomography.* Powder Technology, 2016. 300(Supplement C): p. 46-60.

144. Yang, C.-Y. and X.-Y. Fu, *Development and validation of a material-labeling method for powder process characterization using X-ray computed tomography.* Powder Technology, 2004. 146(1): p. 10-19.

145. Gladden, L.F. and P. Alexander, *Applications of nuclear magnetic resonance imaging in process engineering.* Measurement Science and Technology, 1996. 7(3): p. 423-435.

146. Hardy, E.H., *Magnetic Resonance Imaging in Chemical Engineering: Basics and Practical Aspects.* Chemical Engineering & Technology, 2006. 29(7): p. 785-795.

147. Lysova, A.A., et al., *Magnetic resonance imaging as an emerging tool for studying the preparation of supported catalysts.* Applied Catalysis A: General, 2010. 374(1–2): p. 126-136.

148. Koptyug, I.V., *MRI of mass transport in porous media: drying and sorption processes.* Prog Nucl Magn Reson Spectrosc, 2012. 65: p. 1-65.

149. Koptyug, I.V., *Chapter 1 Magnetic resonance imaging methods in heterogeneous catalysis*, in *Spectroscopic Properties of Inorganic and Organometallic Compounds: Volume 45*. 2014, The Royal Society of Chemistry. p. 1-42.

150. Müller, C.R., et al., *Magnetic Resonance Imaging of fluidized beds.* Powder Technology, 2008. 183(1): p. 53-62.

151. Melia, C.D., A.R. Rajabi-Siahboomi, and R.W. Bowtell, *Magnetic resonance imaging of controlled release pharmaceutical dosage forms.* Pharmaceutical Science & Technology Today, 1998. 1(1): p. 32-39.

152. Richardson, J.C., et al., *Pharmaceutical applications of magnetic resonance imaging (MRI).* Advanced Drug Delivery Reviews, 2005. 57(8): p. 1191-1209.

153. Mantle, M.D., *NMR and MRI studies of drug delivery systems.* Current Opinion in Colloid & Interface Science, 2013. 18(3): p. 214-227.

154. Lurie, D.J. and K. Mäder, *Monitoring drug delivery processes by EPR and related techniques—principles and applications.* Advanced Drug Delivery Reviews, 2005. 57(8): p. 1171-1190.

155. Kempe, S., H. Metz, and K. Mäder, *Application of Electron Paramagnetic Resonance (EPR) spectroscopy and imaging in drug delivery research – Chances and challenges.* European Journal of Pharmaceutics and Biopharmaceutics, 2010. 74(1): p. 55-66.

156. Datye, A.K., *Electron microscopy of catalysts: recent achievements and future prospects.* Journal of Catalysis, 2003. 216(1–2): p. 144-154.

157. Rao, D.S., K. Muraleedharan, and C. Humphreys, *TEM specimen preparation techniques.* Microscopy: Science, Technology, Applications and Education, 2010: p. 1232-1244.

158. Su, D.S., B. Zhang, and R. Schlögl, *Electron microscopy of solid catalysts - Transforming from a challenge to a toolbox.* Chemical Reviews, 2015. 115(8): p. 2818-2882.

159. Fujiyama, T., et al., *Control of the impregnation profile of Ni in an Al2O3 sphere.* Journal of Catalysis, 1987. 104(2): p. 323-330.

160. Chen, H.-C. and R.B. Anderson, *Concentration profiles in impregnated chromium and copper on alumina.* Journal of Catalysis, 1976. 43(1): p. 200-206.

161. Knoke, S., et al., *Early Stages of Propylene Bulk Phase Polymerization with Supported Metallocene Catalysts.* Macromolecular Chemistry and Physics, 2003. 204(4): p. 607-617.

162. Sobanska, S., et al., *Resolving the internal structure of individual atmospheric aerosol particle by the combination of Atomic Force Microscopy, ESEM–EDX, Raman and ToF–SIMS imaging.* Microchemical Journal, 2014. 114: p. 89-98.

163. Laskin, A. and J.P. Cowin, *Automated Single-Particle SEM/EDX Analysis of Submicrometer Particles down to 0.1 μm.* Analytical Chemistry, 2001. 73(5): p. 1023-1029.

164. Herzing, A.A., et al., *Energy dispersive X-ray spectroscopy of bimetallic nanoparticles in an aberration corrected scanning transmission electron microscope.* Faraday Discussions, 2008. 138(0): p. 337-351.

165. Słowik, G., M. Greluk, and A. Machocki, *Microscopic characterization of changes in the structure of KCo/CeO2 catalyst used in the steam reforming of ethanol.* Materials Chemistry and Physics, 2016. 173: p. 219-237.

166. Tran, T.-H., et al., *Micromeritic properties and instrumental analysis of physical mixtures and solid dispersions with adsorbent containing losartan: Comparison of dissolution-differentiating factors.* Powder Technology, 2015. 272(Supplement C): p. 269-275.

167. Wei, Q., et al., *Facile one-step synthesis of mesoporous Ni-Mg-Al catalyst for syngas production using coupled methane reforming process.* Fuel, 2018. 211(Supplement C): p. 1-10.

168. Burgess, S., X. Li, and J. Holland, *High spatial resolution energy dispersive X-ray spectrometry in the SEM and the detection of light elements including lithium.* Microscopy and Analysis, 2013. 6: p. S8-S13.

169. Newbury, D.E. and N.W. Ritchie, *Is scanning electron microscopy/energy dispersive X-ray spectrometry (SEM/EDS) quantitative?* Scanning, 2013. 35(3): p. 141−168.

170. Shyr, Y.-S. and W.R. Ernst, *Preparation of nonuniformly active catalysts.* Journal of Catalysis, 1980. 63(2): p. 425-432.

171. Becker, E.R. and J. Wei, *Nonuniform distribution of catalysts on supports.* Journal of Catalysis, 1977. 46(3): p. 365-371.

172. Becker, E.R. and J. Wei, *Nonuniform distribution of catalysts on supports.* Journal of Catalysis, 1977. 46(3): p. 372-381.

173. Lin, T.-B. and T.-C. Chou, *Selective hydrogenation of isoprene on eggshell and uniform palladium profile catalysts.* Applied Catalysis A: General, 1994. 108(1): p. 7-19.

174. Roth, J. and T. Reichard, *Determination and effect of platinum concentration profiles in supported catalysts.* JOURNAL OF THE RESEARCH INSTITUTE FOR CATALYSIS HOKKAIDO UNIVERSITY, 1972. 20(2): p. 85-94.

175. Benesi, H.A., R.M. Curtis, and H.P. Studer, *Preparation of highly dispersed catalytic metals: Platinum supported on silica gel.* Journal of Catalysis, 1968. 10(4): p. 328-335.

176. Vincent, R.C. and R.P. Merrill, *Concentration profiles in impregnation of porous catalysts.* Journal of Catalysis, 1974. 35(2): p. 206-217.

177. Allgeier, M.C., et al., *Isolation and Physical Property Optimization of an Amorphous Drug Substance Utilizing a High Surface Area Magnesium Aluminometasilicate (Neusilin® US2).* Journal of Pharmaceutical Sciences, 2016. 105(10): p. 3105-3114.

178. Washburn, E.W., *The Dynamics of Capillary Flow.* Physical Review, 1921. 17(3): p. 273-283.

179. Santhanam, N., et al., *Nature of metal catalyst precursors adsorbed onto oxide supports.* Catalysis Today, 1994. 21(1): p. 141-156.

180. Neimark, A.V., V.B. Fenelonov, and L.I. Heifets, *Analysis of the drying stage in the technology of supported catalysts.* Reaction Kinetics and Catalysis Letters, 1976. 5(1): p. 67-72.

181. Lekhal, A., J.G. Khinast, and B.J. Glasser, *Predicting the Effect of Drying on Supported Coimpregnation Catalysts.* Industrial & Engineering Chemistry Research, 2001. 40(18): p. 3989-3999.

182. Lekhal, A., B.J. Glasser, and J.G. Khinast, *Influence of pH and ionic strength on the metal profile of impregnation catalysts.* Chemical Engineering Science, 2004. 59(5): p. 1063-1077.

183. Liu, X., J.G. Khinast, and B.J. Glasser, *Drying of supported catalysts for low melting point precursors: Impact of metal loading and drying methods on the metal distribution.* Chemical Engineering Science, 2012. 79: p. 187-199.

184. Childs, E.C. and N.C. George, *Soil geometry and soil-water equilibria.* Discussions of the Faraday Society, 1948. 3(0): p. 78-85.

185. Purcell, W.R., *Capillary Pressures - Their Measurement Using Mercury and the Calculation of Permeability Therefrom.* 1949.

186. Metzger, T. and E. Tsotsas, *Influence of Pore Size Distribution on Drying Kinetics: A Simple Capillary Model.* Drying Technology, 2005. 23(9-11): p. 1797-1809.

187. Fatt, I., *The Network Model of Porous Media.* 1956, Society of Petroleum Engineers.

188. Lenormand, R., E. Touboul , and C. Zarcone *Numerical Models and Experiments on Immiscible Displacement in Porous Media.* Vol. 189. 1988. 165-187.

189. Prat, M., *Percolation model of drying under isothermal conditions in porous media.* International Journal of Multiphase Flow, 1993. 19(4): p. 691-704.

190. Yiotis, A.G., et al., *A 2-D pore-network model of the drying of single-component liquids in porous media.* Advances in Water Resources, 2001. 24(3): p. 439-460.

191. Markicevic, B. and H.K. Navaz, *Primary and Secondary Infiltration of Wetting Liquid Sessile Droplet into Porous Medium.* Transport in Porous Media, 2010. 85(3): p. 953-974.

192. Metzger, T., A. Irawan, and E. Tsotsas, *Influence of pore structure on drying kinetics: A pore network study.* AIChE Journal, 2007. 53(12): p. 3029-3041.

193. Metzger, T., A. Irawan, and E. Tsotsas, *Isothermal Drying of Pore Networks: Influence of Friction for Different Pore Structures.* Drying Technology, 2007. 25(1): p. 49-57.

194. Metzger, T. and E. Tsotsas, *Viscous stabilization of drying front: Three-dimensional pore network simulations.* Chemical Engineering Research and Design, 2008. 86(7): p. 739-744.

195. Wang, Y., et al., *Pore Network Drying Model for Particle Aggregates: Assessment by X-Ray Microtomography.* Drying Technology, 2012. 30(15): p. 1800-1809.

196. Markicevic, B., et al., *Infiltration time and imprint shape of a sessile droplet imbibing porous medium.* Journal of Colloid and Interface Science, 2009. 336(2): p. 698-706.

197. Markicevic, B., T. G. D'Onofrio, and H. Navaz, *On spread extent of sessile droplet into porous medium: Numerical solution and comparisons with experiments*. Vol. 22. 2010.

198. SanMartin, F.A., J.B. Laurindo, and L.A. Segura, *Pore-Scale Simulation of Drying of a Porous Media Saturated with a Sucrose Solution.* Drying Technology, 2011. 29(8): p. 873-887.

199. Börnhorst, M., et al., *Influence of pore structure and impregnation–drying conditions on the solid distribution in porous support materials.* Drying Technology, 2016. 34(16): p. 1964-1978.

200. Nowicki, S.C., H.T. Davis, and L.E. Scriven, *Microscopic Determination of Transport Parameters in Drying Porous Media.* Drying Technology, 1992. 10(4): p. 925-946.

201. Finn, R., *Capillary surface interfaces.* Notices AMS, 1999. 46(7): p. 770-781.

202. Denesuk, M., et al., *Capillary Penetration of Liquid Droplets into Porous Materials.* Journal of Colloid and Interface Science, 1993. 158(1): p. 114-120.

203. Kyle, B.G., *Chemical and Process Thermodynamics*. 1999: Prentice Hall PTR.

204. Cussler, E.L., *Diffusion*. 2 ed. Mass Transfer in Fluid Systems. 1997: Cambridge University Press.

205. Bird, B.R., W.E. Stewart, and E.N. Lightfoot, *Transport Phenomena*. 2 ed. 2002: John Wiley & Sons, Inc.

206. Whitaker, S., *Simultaneous Heat, Mass, and Momentum Transfer in Porous Media: A Theory of Drying.* Advances in Heat Transfer, 1977. 13: p. 119-203.

207. Mullin, J.W., *Crystallization*, in *Crystallization (Fourth Edition)*. 2001, Butterworth-Heinemann: Oxford.

208. Dullien, F.A.L., *Porous media : Fluid transport and pore structure (2nd ed.)*. 1992.

209. Reeves, P.C. and M.A. Celia, *A Functional Relationship Between Capillary Pressure, Saturation, and Interfacial Area as Revealed by a Pore-Scale Network Model.* Water Resources Research, 1996. 32(8): p. 2345-2358.

210. O'Carroll, D.M., et al., *Prediction of two-phase capillary pressure–saturation relationships in fractional wettability systems.* Journal of Contaminant Hydrology, 2005. 77(4): p. 247-270.

211. Joekar-Niasar, V., S.M. Hassanizadeh, and A. Leijnse, *Insights into the Relationships Among Capillary Pressure, Saturation, Interfacial Area and Relative Permeability Using Pore-Network Modeling.* Transport in Porous Media, 2008. 74(2): p. 201-219.

212. Brooks, R.H. and A.T. Corey, *Hydraulic properties of porous media.* Hydrology Papers, 1964. 3.

213. Leverett, M.C., *Capillary Behavior in Porous Solids.* 1941.

214. Thomeer, J.H.M., *Introduction of a Pore Geometrical Factor Defined by the Capillary Pressure Curve.* 1960.

215. Bentsen, R.G. and J. Anli, *A New Displacement Capillary Pressure Model.* 1976.

216. Li, K. and R.N. Horne, *An Experimental and Analytical Study of Steam/Water Capillary Pressure.* SPE Reservoir Evaluation & Engineering, 2001. 4(6): p. 477-482.

217. Li, K. and R.N. Horne, *Universal capillary pressure and relative permeability model from fractal characterization of rock.* PROCEEDINGS, Twenty-Ninth Workshop on Geothermal Reservoir Engineering, 2004. Stanford University, Stanford, California, January 26-28, 2004.

218. Constantinides, A. and N. Mostoufi, *Numerical Methods for Chemical Engineers with MATLAB Applications with Cdrom.* 1999: Prentice Hall PTR. 608.

219. Patankar, S.V., *Numerical heat transfer and fluid flow.* Series in computational methods in mechanics and thermal sciences. 1980, Washington : New York: Hemisphere Pub. Corp. ; McGraw-Hill.

220. Choudhari, Y., et al., *Comparative evaluation of porous silica based carriers for lipids and liquid drug formulations*, in *Mesoporous Biomaterials*. 2014.

221. Glasstone, S., K.J. Laidler, and H. Eyring, *The Theory of Rate Processes: The Kinetics of Chemical Reactions, Viscosity, Diffusion and Electrochemical Phenomena.* 1941: McGraw-Hill Book Company, Incorporated.

222. Cha, K.-H., et al., *Enhancement of the dissolution rate and bioavailability of fenofibrate by a melt-adsorption method using supercritical carbon dioxide.* International Journal of Nanomedicine, 2012. 7: p. 5565-5575.

223. Innocentini, M.D.M., et al., *Prediction of ceramic foams permeability using Ergun's equation.* Materials Research, 1999. 2: p. 283-289.

224. Chen, Y., et al., *Granulation of cohesive Geldart group C powders in a Mini-Glatt fluidized bed by pre-coating with nanoparticles.* Powder Technology, 2009. 191(1): p. 206-217.

225. Grigorov, P.I., B.J. Glasser, and F.J. Muzzio, *Improving dissolution kinetics of pharmaceuticals by fluidized bed impregnation of active pharmaceutical ingredients.* AIChE Journal, 2016. 62(12): p. 4201-4214.

226. Fogler, S.H., *Elements of Chemical Reaction Engineering.* 3 ed. 1999, Upper Saddle River, NJ: Published by Prentice Hall PTR.

227. FujiChemicalIndustries, *General Properties of Neusilin.* Available at: http://www.neusilin.com/product/general_properties.php. Accessed July 28, 2017.

228. FujiChemicalIndustries, *General Properties of Fujicalin.* Available at: http://www.fujicalin.com/product/general_properties.php Accessed July 28, 2017.

229. Heinrich, S., et al., *Analysis of the start-up process in continuous fluidized bed spray granulation by population balance modelling.* Chemical Engineering Science, 2002. 57(20): p. 4369-4390.

230. Hampel, N., et al., *Continuous pellet coating in a Wurster fluidized bed process.* Chemical Engineering Science, 2013. 86(Supplement C): p. 87-98.

231. Chen, H., F. Muzzio, and B. Glasser. *Continuous Fluidized Bed Drying of Pharmaceutical Materials*. in *2017 AIChE Annual Meeting*. 2017. Minneapolis, MN: AIChE.

232. Saffari, M., A. Ebrahimi, and T. Langrish, *Highly-porous mannitol particle production using a new templating approach.* Food Research International, 2015. 67(Supplement C): p. 44-51.

233. Ebrahimi, A., M. Saffari, and T. Langrish, *Developing a new production process for high-porosity lactose particles with high degrees of crystallinity.* Powder Technology, 2015. 272(Supplement C): p. 45-53.

234. Ebrahimi, A., M. Saffari, and T. Langrish, *Spray drying and post-processing production of highly-porous lactose particles using sugars as templating agents.* Powder Technology, 2015. 283(Supplement C): p. 171-177.

235. Ebrahimi, A., M. Saffari, and T. Langrish, *The use of CTAB and citric acid as templating agents in production of highly-porous lactose particles.* Journal of Food Engineering, 2015. 156(Supplement C): p. 59-66.

236. Fries, L., et al., *DEM–CFD modeling of a fluidized bed spray granulator.* Chemical Engineering Science, 2011. 66(11): p. 2340-2355.

237. Börner, M., A. Bück, and E. Tsotsas, *DEM-CFD investigation of particle residence time distribution in top-spray fluidised bed granulation.* Chemical Engineering Science, 2017. 161(Supplement C): p. 187-197.

238. Shen, Y., W.G. Borghard, and M.S. Tomassone, *Discrete element method simulations and experiments of dry catalyst impregnation for spherical and cylindrical particles in a double cone blender.* Powder Technology, 2017. 318(Supplement C): p. 23-32.